Characterization of Light Scattering Point Defects in High-Performance Mirrors for Gravitational Wave Detectors

Sihem Sayah

THÈSE de DOCTORAT DE L'UNIVERSITÉ CLAUDE BERNARD LYON 1

École Doctorale : n°52
Physique et Astrophysique

Discipline : Physique des matériaux et Optique

Soutenue publiquement le 01/12/2022, par :

Sihem SAYAH

Characterization of Light Scattering Point Defects in High-Performance Mirrors for Gravitational Wave Detectors

---

Devant le jury composé de :

GASCON Jules,	Professeur des Universités, Université Lyon 1	Président du Jury
TOURNEFIER Edwige,	Directrice de Recherche, CNRS Annecy	Rapportrice
ZERRAD Myriam,	Ingénieure de recherche-HDR, Aix Marseille Université	Rapportrice
BONDU François,	Directeur de Recherche, CNRS Rennes	Examinateur
SORDINI Viola,	Chargée de Recherche-HDR, CNRS Lyon	Directrice de thèse
SASSOLAS Benoît,	Ingénieur de Recherche, CNRS Lyon	Co-directeur de thèse
MASENELLI-VARLOT Karine,	Professeure des Universités, INSA Lyon	Examinatrice

Abstract

Résumé de la thèse

Les miroirs haute réflectivité des détecteurs d'ondes gravitationnelles Advanced LIGO & Advanced Virgo présentent dans le revêtement de nombreux défauts de taille micrométrique qui diffusent la lumière dans l'interféromètre. Cette lumière diffusée induit une perte de puissance du laser de l'ordre de quelques dizaines de parties par million (ppm) et un bruit de phase à cause de la recombinaison avec le faisceau principal après réflexion sur les parois du tube. Ce phénomène limite la sensibilité du détecteur et a un impact sur la capacité à détecter des événements astrophysiques. Une réduction de la lumière diffusée est donc nécessaire afin d'améliorer les performances optiques des revêtements des nouveaux miroirs de l'Advanced LIGO et de la mise à niveau d'Advanced Virgo+. À cette fin, une ligne de recherche dédiée est en cours au LMA depuis 2018. Nous avons étudié les défauts ponctuels séparément dans les deux matériaux utilisés pour les revêtements réfléchissants des miroirs des détecteurs d'ondes gravitationnelles : le pentoxyde de tantale et la silice séparément avec des monocouches déposées sur des substrats micropolis de silice fondue. Nous avons analysé l'impact de différents paramètres, comme l'épaisseur, ainsi que l'effet d'un recuit post-dépôt sur le nombre de défauts. Les échantillons ont été mesurés avec un système de détection en champ sombre afin d'étudier la densité et la distribution de taille des défauts. Nous avons constaté que même si un matériau présente une densité de défauts beaucoup plus importante, les deux matériaux présentent des similitudes. De plus, nous avons remarqué une amélioration remarquable de la qualité du revêtement grâce au recuit post-dépôt. L'étude a été ensuite portée sur le phénomène de la diffusion en mesurant les échantillons à l'aide du diffusomètre afin de connaître l'impact des défauts et des différents paramètres testés sur la lumière diffusée. Il s'avère que le recuit post-dépôt améliore également la quantité de lumière diffusée qui diminue, mais on ne remarque pas d'effet lié à l'épaisseur du dépôt ou à la densité de défauts. Par ailleurs, afin de comprendre l'impact des défauts sur la lumière diffusée, des simulations optiques d'un cas simple d'un défaut localisé ont été réalisées avec le logiciel COMSOL.

Mot-clés: *Ondes gravitationnelles, Advanced Virgo, Couches minces, Défauts ponctuels, lumière diffusée, Instrumentation, optique, Miroirs, Advanced LIGO*

Thesis asbtract

The high reflectivity mirrors of the Advanced LIGO & Advanced Virgo gravitational wave detectors have many micrometer size defects in the coating which scatter the light in the interferometer. This scattered light induces a laser power loss of the order of a few tens of parts per million (ppm) and a phase noise due to recombination with the main beam after reflection on the tube walls. This phenomenon limits the sensitivity of the detector and has an impact on the ability to detect astrophysical events. A reduction of the scattered light is therefore necessary to improve the optical performance of the coatings for the new mirrors for Advanced LIGO and Advanced Virgo+ upgrade. To this end, a dedicated line of research has been underway at LMA since 2018. We have studied the point defects separately for the two materials typically used for mirrors coating in gravitational waves experiments: tantalum pentoxide and silica, with monolayers deposited on micropolished fused silica substrates. We analyzed the impact of different parameters, such as thickness, as well as the effect of post-deposition annealing on the number of defects. The samples were measured with a dark field detection system to study the density and size distribution of the defects. We found that even though one material has a much higher defect density, the two materials have similarities. In addition, we noticed a remarkable improvement in the quality of the coating due to post-deposition annealing. The study was then focused on scattered light by measuring the samples with the scatterometer. We assess the impact of the defects and the different parameters on the scattered light. It turns out that the post-deposition annealing also improves the quantity of scattered light which decreases but we do not notice any effect related to the thickness or the density of defects. Moreover, in order to understand the impact of defects on the scattered light, optical simulations of a simple case of a localized defect have been performed with the COMSOL software.

Key-words : *Gravitational waves, Scattering light, Advanced Virgo, Advanced LIGO, Point defects, Mirrors, Instrumentation, Thin films*

Acknowledgment

Je tiens à remercier en premier lieu Laurent PINARD, directeur du LMA d'avoir facilité les démarches et de m'avoir fait confiance pour ce sujet inédit de thèse malgré les difficultés rencontrées. Je souhaite remercier également Imad LAKTINEH, enseignant chercheur et responsable de Master Physique Subatomique pour son soutien et son aide tout au long de mon parcours.

Merci à Edwige TOURNEFIER et Myriam ZERRAD d'avoir fait l'honneur d'accepter de juger mon travail et merci pour nos échanges. Merci aux autres membres du jury François BONDU, Karine MASENELLI-VARLOT et à Jules GASCON d'avoir présidé mon jury.

Je voudrais remercier chaleureusement Viola et Benoît, mes deux directeurs de thèse. Chef Benoît, je ne peux pas t'accorder une page de remerciements à toi tout seul (comme tu me l'as demandé) mais saches que je suis très reconnaissante de t'avoir eu à mes côtés depuis le stage de M2 et pendant ces 3 ans et demi de thèse. Merci pour ta grande disponibilité, ton humour, ton aide et tes corrections infinies. Cheffe Viola, merci pour toutes nos discussions, ta bienveillance et ta fraicheur. Grâce à vous deux, j'ai été libre d'explorer mon sujet même si les contraintes expérimentales et le timing m'ont forcé à me concentrer sur une ligne de conduite plus précise.

Je remercie également tous les membres du LMA et particulièrement Eleonore ma "marraine du LMA". Merci pour ton souci, ta bienveillance et pour les blagues à l'encontre de Benoît. Merci à Danièle pour ton aide précieuse au CASI. Grâce à toi, j'ai pu me concentrer sur la rédaction du manuscrit et finir dans les temps. Merci à Mathieu pour les 93 échantillons nettoyés et envoyés au recuit. Merci à Jérôme pour ta curiosité et pour ta passion pour la vulgarisation scientifique que tu m'as transmises. Merci à Christophe, Julien, Bernard, Lorenzo, Massimo, Clément, et David mon collègue de bureau avec qui ce fut un plaisir de discuter chaque jour. Merci également aux mains discrètes du LMA qui prenaient soin de remplir ma bonbonnière pour que je ne manque jamais de sucre :)

Je remercie sincèrement toute l'équipe MANOIR (la meilleure équipe de recherche de l'IP2I !) pour leur soutien depuis mon stage de M1, les pauses déjeuner qui me permettaient de sortir de ma grotte qu'était la salle blanche. Et je remercie encore plus et du fond du coeur Maryvonne De Jesus d'avoir été ma marraine de thèse et de loin la meilleure. Merci pour ton souci, d'avoir eu de l'inquiétude dans les moments difficiles, d'avoir su m'encourager, briefer dès le début de la thèse et pour les coups de pieds quand j'en avais besoin. Je sais que j'étais ta première filleule et certainement la dernière :) Je remercie aussi Corinne Augier qui a également été ma marraine de thèse de l'ombre (#DarkMarraine) car qui dit Maryvonne dit Corinne et la réciproque est vraie. Merci car j'ai été très chanceuse de vous avoir toutes les deux avant et pendant ma thèse.

Je remercie tout particulièrement Impanga Anissa pour ton soutien, ta présence et ta patience face aux galères d'une doctorante en détresse. J'espère que la petite Assia deviendra une chercheuse brillante comme sa Tata Sihem ;) Un grand merci à mes Queens Assia, Fatima, Hajer, Hanane, Khadija, Sahra, Sarra et Sihem et une mention spéciale pour Selma la plus belle, notre chirurgienne. Merci pour les évasions, les randonnées, votre amitié et vos lumières.

J’exprime ma plus grande gratitude pour mes parents et leur soutien indéfectible qu’ils m’ont exprimé depuis mon enfance. A mes frères Ilyes et Jaber et ma petite soeur Joumana.

Merci à Celui sans qui rien de tout cela n’aurait été possible.

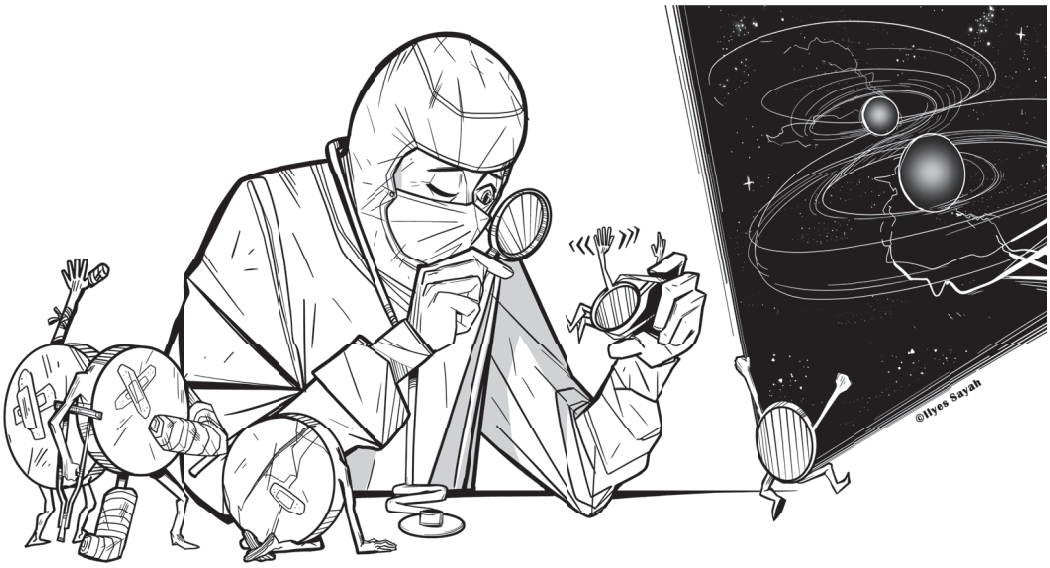

Miroir, Oh mon beau miroir, dis-moi qui est la plus belle ? Des miroirs pour se voir ? Non. Des miroirs pour entendre les chuchotements de l'espace-temps ? Oui. Eh bien miroirs, racontez-nous ce qu'il s'est passé dans l'Univers. Attention ! Ils ne vous raconteront pas les contes de Grimm ou de la rue Broca mais valideront les théories d'Einstein et l'histoire de l'Univers. Les sons transmis par l'espace-temps voyagent à la vitesse de la lumière alors observer loin, nous informe sur le passé. Ainsi, plus on entend loin, plus on entend les évènements survenus tôt dans l'histoire du cosmos. Les miroirs sur lesquels je travaille, ne pourront pas vous dire si vous êtes la plus belle, ou le plus beau ; non ; car ces miroirs réfléchissent seulement dans l'infrarouge, une lumière invisible, contrairement à vos miroirs de salle de bain. En revanche, une fois installée dans un détecteur géant, situé en Italie, les miroirs détectent les signaux qui parcourent l'Univers sur plusieurs millions d'années lumières avant de nous parvenir.

Imaginez l'espace-temps comme un océan et des vagues. Vous y êtes ? Il est immense, peuplé d'objets massifs. Quelque part, au fin fond de cet océan, se produisent de magnifiques spectacles de danses : les valses cosmiques. A chaque fin de valse, entre deux trous noirs, une union cosmique se produit déclenchant alors une secousse de l'espace-temps. Cette secousse est une vague imperceptible qui va se propager jusqu'à nos miroirs. La forme de cette vague est extrêmement précieuse pour les astrophysiciens; et pour permettre la détection il faut que ces miroirs soient le plus parfait possible. La moindre imperfection du miroir crée de la lumière diffusée. Cette lumière est donc perdue et on cherche à la réduire pour gagner en sensibilité. Si les miroirs sont moins sensibles, ils ont moins d'histoires à raconter !

C'est là que j'interviens. Le but de ma thèse est d'étudier leur « têtes » ; plus précisément, j'étudie 2 phénomènes; les défauts des miroirs et la diffusion de la lumière par les défauts. Au laboratoire, on dépose à l'aide d'une machine unique, une fine couche de matériau sur des blocs de verre ultra pur ce qui donne au miroir sa réflectivité quasi-parfaite. Pour ma thèse, on produit de nombreux échantillons tests qui sont des « bébés miroirs » avec des paramètres de dépôt différents que je caractérise. Ils sont bien plus faciles à manipuler que leurs parents qui pèsent 40kg. Pour la partie diffusion, je crée des simulations pour prédire l'interaction de ces défauts avec la lumière. Je suis docteur, enfin bientôt ! Je soigne les miroirs. Mais pour bien les soigner, j'examine les défauts pour comprendre leur origine et identifier les paramètres qui entrent en jeu dans leur formation. Comprendre l'origine des défauts permettra d'améliorer la qualité des futurs miroirs, d'entendre encore plus loin dans les abysses de l'océan cosmique et mieux connaître les sources émettrices de ces tangos de trous noirs mortels. Finalement, les miroirs sont comme les humains, ce sont leurs défauts qui les rendent intéressants.

French version of Three Minute Thesis - Third price Lyon 2021

Contents

Introduction

The year 2015 was marqued by the first direct detection of a gravitational wave signal. This was a striking confirmation of the theory of general relativity developed by Albert Einstein one century ago. It was followed by several other detections that have been observed coming from violent events, such as the coalescence of black holes and neutron stars, occurring billions of light years from our solar system. This validation of Einstein's theory, offers us a new way to observe and understand the Universe around us and the combined observation of the electromagnetic spectrum, cosmic rays, neutrinos and gravitational waves is called multi-messenger astronomy.

These detections have been possible thanks to the three interferometric gravitational wave detectors, Advanced LIGO-Handford and Advanced LIGO-Livingston in the USA and Advanced Virgo in Italy. The Laboratoire des Matériaux Avancés de Lyon (LMA) in Lyon is the world leader in the fabrication of very low-loss optical components for gravitational wave detection experiments. It carries out the surface treatment and metrology of the large mirrors which compose the interferometers. These are among the best reflective mirrors in the world, allowing all the laser light to be reflected. These dielectric mirrors are made of stacks of thin layers of Ta_2O_5 and SiO_2 with minimal optical and mechanical losses.

According to the technical specifications of Advanced Virgo and Advanced LIGO, the mirrors for gravitational wave detectors were characterized by measuring the wavefront, absorption, roughness, defect density, the reflectance and the scattering light with the different characterization instruments present at LMA. According to the specification, the arm cavity round trip losses must be less than 75 ppm. During the O2 observation run, excess of optical losses were observed in the detectors. Indeed after the standard characterizations of the mirrors (i.e. absorption, transmission, scattering, flatness) at LMA, the total losses are expected to be about 35-40 ppm. However the losses measured in the interferometer reach 50-60ppm. This discrepancy points out that some contributions to the scattered light are not taken into account. Although the specifications constrain the overall optical losses, in order to reduce them, it is crucial to understand their microscopic source. It has been observed that mirrors have point-like defects in the thin layers that scatter the light. The standard scattering map produced at LMA over the mirrors might not be able to catch the typical signature of such defects and then would underestimate the overall scattering budget. The presence of scattered light in the cavity has two effects: a loss of optical power and the addition of phase noise when the scattered light is recombined with the main beam after reflection on the walls of non-seismically insulated vacuum tubes. These two phenomena limit the sensitivity of the detector and imply that we detect fewer astrophysical events. The scattered light is generally acknowledged as a major issue for the Advanced Virgo + upgrade, where laser power will be increased (as well as the mirrors size) to gain sensitivity. The reduction of optical losses is at the heart of the ongoing research for this upgrade, and the study of the defects presented here fits perfectly in this perspective .

This research effort is essential to build the mirrors of the future and to benefit all precision experiments where optical losses are critical. These obviously include the future upgrades of existing ground-based gravitational waves detectors as well as the next (third) generation ones, but also quantum optics experiments that need high finesse cavities.

This thesis documents the meticulous investigations work performed at LMA to understand the formation and the origin of these defects presents in optical thin films as a first step towards

founding a way to reduce them. The impact of the point defects on the scattering light and optical loss is also studied.

Outline of the Thesis

- **Chapter 1** gives an introduction to the history of the gravitational waves quest from Albert Einstein to the current gravitational waves detectors which made the discovery possible.
- **Chapter 2** presents the principle of gravitational wave interferometric detectors and their limits. The mirrors and the different steps from the substrate choice to the deposition process using Ion Beam Sputtering (IBS) technique are also detailed.
- **Chapter 3** describes the instrumental setups used for this thesis work. An overview of the optical profilometer and scatterometer used for the study of defects and their charactrization and methods is given.
- **Chapter 4** presents the study of scattering point defects. Different tests have been performed on the deposition machines of LMA in order to understand the origin of these defects according to the materials and deposition parameters.
- **Chapter 5** presents the scattering theory and all the measurements of scattering light on different samples, as well as simulations performed with the code COMSOL.
- **Chapter 6** presents the results of the studies carried out to determine the chemical nature and structure of the defects, using different observation techniques.

Chapter 1

The begining of gravitational astronomy

Contents

1.1 Gravitational astronomy

From Isaac Newton to Albert Einstein, our understanding of gravitation has evolved a lot across the centuries. Gravitation changed first from an instantaneous force that acted in a mysterious way between two bodies at a distance d of each other to the general relativity theory where gravitation is no longer a force but is linked to space and time together. This relation between space and time defines a four-dimensional continuum called space-time that is influenced by the presence of masse or energy EINSTEIN [1905, 1916]. The presence of a mass will curve the space-time represented by a 2-dimensional grid in Figure 1.1. According to the General Relativity the gravitation is then a consequence of the curvature of the space-time where disturbances could propagate at the speed of light : it is the gravitational wave EINSTEIN [1916, 1918]. Thus, any object in the path of these waves, will locally see a change in space time. The amplitude of these waves is extremely small, which is why we have waited for a century before a direct detection. If we compare the 4 fundamental interactions that govern the Universe, the gravitational interaction is the weakest of all. Compared to the strong interaction that governs the cohesion of electrons in the atom, the intensity of the gravitational interaction is 10^{-39} times lower. The length variation due to a gravitational wave is defined as follows :

$$\delta L = \frac{1}{2} h L \tag{1.1}$$

Where L is the length between 2 free falling masses and h the gravitational wave amplitude of the order of 10^{-22} m.

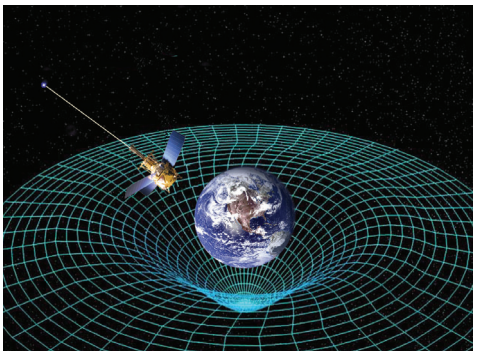

Figure 1.1: Distortion of the space-time due to the mass of the earth.

One purpose of gravitational research is to improve our knowledge on the first moments of the Universe, billions of years ago. Unlike electromagnetic waves which interact with matter, gravitational waves can travel over great distances without being attenuated, absorbed or modified. There are many places in space that still remain an enigma for astrophysicists and astronomers as shown in figure 1.2. Detecting events that took place early in the Universe allows us to understand the past of the Universe . The current means of observation do not allow yet to pierce them because the instruments of terrestrial detection and space telescopes do not reach a sufficient sensitivity and are not free from terrestrial noises. This is where gravitational astronomy becomes very advantageous because the properties of gravitational waves allow us to look further into space. Electromagnetic waves allow to go back up to 380 000 years after the Big Bang whereas gravitational waves at less than 10^{-32} seconds after the Big Bang. Theses waves are Universe traces from the past. In this way, detecting such signals enhance our understanding of the Universe creation.

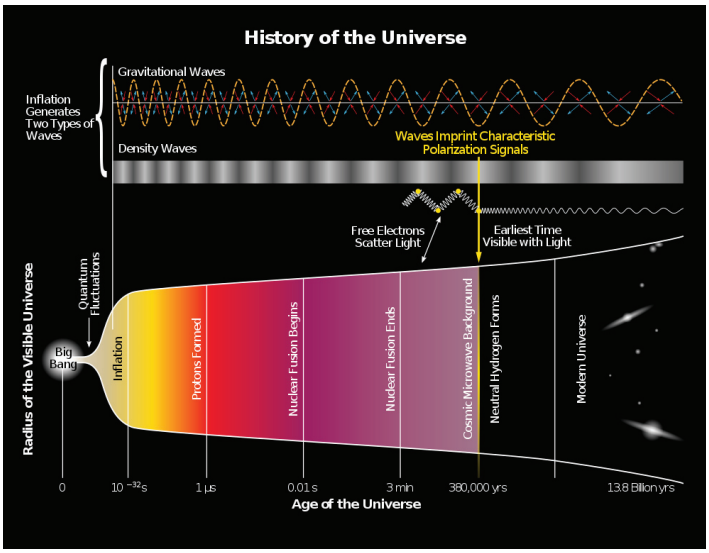

Figure 1.2: Timeline of the history of the Universe and location of gravitational waves in time. Credit : National Science Foundation.

1.2 The Astrophysical sources of gravitational waves

Albert Einstein demonstrated that only cataclysmic astrophysical phenomena that have a quadrupole moment can emit detectable gravitational waves EINSTEIN [1918]. The quadrupole moment quantifies the deviation from spherical symmetry. There are several sources of astrophysical objects emitting gravitational waves. Among the most favorable candidates, we can find four kinds of different sources depending on the frequency signal.

Binary Coalescence :

Two massive celestial objects like two black holes (BH-BH), two neutron stars (NS-NS) or a black hole and a neutron star (BH-NS) orbiting one around the other generate gravitational waves at frequencies equal to twice their orbital frequency. While the waves take away part of the energy of the system, the orbital frequency increases and the two objects will get closer together and will eventually merge. In 1974, Hulse and Taylor discovered the existence of a binary system composed of a pulsar and a neutron stars named PSR B1913+16 HULSE et TAYLOR [1975]. By observing the radio pulses and the orbital period of the pulsar they noticed the decrease of the orbital period as a function of time, consistent with the prediction of general relativity for such a binary system that lose energy due to gravitational radiation. This indirect hint to the existence of gravitational waves will be rewarded of a Nobel Prize in 1993 TAYLOR et WEISBERG [1989]. Since then, the search for a direct detection of these waves was the most expected event until the miracle year 2015.
GW150914 is the first direct observation of gravitational waves from 2 binary black holes of masses 29 and 36 times the solar mass that merged 1.3 billion years ago. Then, on August 17, 2017 occurred the fourth direct detection named GW170817 ABBOTT et AL [2017b]. This wave is due to the merger of two neutron stars which resulted in a kilonova located at 130 million years from the Earth. This event, detected simultaneously by the 3 detectors Advanced LIGO (aLIGO) and Advanced Virgo is the first event to also have an electromagnetic counterpart, with a gamma-ray burst detected by Fermi and INTEGRAL and observations by different telescopes, from radio to X-ray wavelengths, over the following hours to weeks. The collected information was crucial to improve our understanding of the kilonova process, highlighting for example the associated production of heavy elements ABBOTT et AL [2017a]. GW170817 marks the birth of multi-messenger astronomy.

Continuous Waves :

Continuous sources relate to stars with a constant rotation frequency like pulsars. These are

neutron stars in rapid rotation around their axis and which emit electromagnetic waves of frequency equal to their rotation frequency of the order of a second (up to 1 kHz). Pulsars periods make them very easy to detect. Such objects could emit detectable gravitational waves signals in the case of any asymmetry in their structure, fot this reason the search for gravitational waves emission associated to pulsars allows the researchers to constrain their structure and composition.

Gravitational Wave Bursts :
These searches target any transient unmodelled gravitational waves emission, typically associated with supernovae or the deexcitation of black holes. Supernovae explosions are extremely rare, about 1 per century and per galaxy. Moreover their amplitude are very low, $h \sim 10^{-23}$, what makes them less detectable than other events. Their mechanism is not well known and for this reason they are difficult to simulate and model .

Stochastic Background :
The stochastic gravitational waves background is the superposition of GW emitted by a large number of independent events combining to create a cosmic gravitational wave background. Such background could also contain the relic gravitational waves from the early evolution of the Universe, similarly to the Cosmic Microwave Background. Besides, some theories beyond the standard model physics suggest the existence of supersymmetric strings that can extend and compress throughout the Universe KIBBLE [1976]. These cosmic (super) strings also produce a stochastic background of gravitational waves. Studies are made on the accessibility of this type of sources to current and planned gravitational wave detectors SIEMENS et collab. [2007].

During my PhD I have witnessed great improvements in the detector sensitivity. For example in the latest observing run (2019-2020), the gravitational waves network of interferometers has detected on average rouchly one event per week.

Now publications are catalogs presenting the classification of the detected events after analysis of the data in the different observation runs. Other kinds of binary system have been detected like the one composed of a black hole and a neutron star, whose coalescence is at the origin of the GW200105 and GW200115 events ABBOTT et AL [2021].

1.3 History of gravitational waves experimental searches

Gravitational astronomy was born thanks to the theory of general relativity. In the 1920's to 1960's, questions about gravitation were debated by many physicists who tried to solve them mostly mathematically. Thus, the scientific debate was mostly focused on theory aspects. It was only in the 1960's and thanks to the emergence of detectors that the quest to detect gravitational waves could begin. The construction of the first detectors allowed the search and the detection of gravitational waves from extreme phenomena hidden in the Universe. We will see that the starting point of the construction of the very first gravitational wave detector is closely linked to the Chapel Hill Conference in 1957, marking a turning point in this domain.

1.3.1 Sticky bead

The existence of gravitational waves has been much debated and Albert Einstein has also hesitated about the existence of these waves, changing his mind several times EINSTEIN et ROSEN [1937]. He started to question his own solutions to the field equations published in 1916. The discussion around their existence can be summarised by the question wether gravitational waves have a real and physical existence or if they were only the result of a gauge effect.

Among the physicists who have studied the problem of gravitation, Felix Pirani, a student and later a colleague of Hermann Bondi at King's College (London), has demonstrated waves effects on matter and that the acceleration of binary object can be associated with the Riemann curvature

tensor PIRANI [2009]. Mathematically it expresses the evolution and the behavior of two geodesic [1] as a function of the curvature of the space-time.

Later, Hermann Bondi suggested an experimental idea. By connecting two masses by a piston, the energy of the wave could be absorbed and transformed into heat. It is the so called *Sticky Bead argument* PRESKILL et THORNE [2000]. That means that gravitational wave are real. The credits of this idea are given to the three physicists Felix Pirani, Hermann Bondi and Richard Feynmann who had suggested the idea anonymously.

1.3.2 The Chapel Hill Conference

The beginning of the experimental research on gravity is strongly tied to the Chapel Hill conference in January 1957 which took place at the University of North Carolina for six days, with the participation of 37 leading physicists from several countries (among them Richard Feynman, Frederick Ernst, and Joseph Weber). The conference was about *The Role of Gravitation in Physics* and it was organised with different sessions working group to discuss cosmology and problems on still unsolved enigmas about the theory of gravitation, at this time DEWITT [2011].

Joseph Weber and John Wheeler were working on the existence of gravitational waves and they published an article (probably begun before the conference) after the Chapel Hill conference and explained why gravitational waves exist WEBER et WHEELER [1957].

During this conference, Felix Pirani presented his work concerning measurement of classical gravitation fields and gravitational fields of an axially symmetric system. After Felix Pirani and Hermann Bondi talks, Joseph Weber, electrical engineer by training, understood what type of detector will be able to bring to light this exitence of this kind of waves. This marked the beginning of the instrumental development and the quest for gravitational waves detection.

1.3.3 Resonant Mass Antennas : Weber Bars

The first gravitational wave detector was designed by Joseph Weber WEBER [1960]. After studying Einstein equations he came to the conclusion that a gravitational wave will deform any object that it would passe through. Inspired and really stimulated by the Chapel Hill Conference, he decided to build in Maryland campus the first resonant detector to try to detect them.

> *"In 1958, I was able to prove , using Einstein's equations that a gravitational wave would change the dimensions of an extended body."* WEBER [1979]

Weber bars is a large massive suspended aluminium cylinder on which he fixed many piezoelectric sensors that are used to convert mechanical energy vibration of the cylinder into an electrical signal. Weighing 1.5 ton, the cylinder of 2 meters long and 1 meter in diameter, is suspended by steel wires from an arch on acoustic filters as shown in Figure 1.3a. This experiment has two limits that reduce the sensitivity of the detection : the first one is the detection frequency range which is limited around the cylinder resonance frequency 1660 Hz so anything could make the cylinder in resonance like close shocks around the detector and the second one is the sensitivity which is limited by seismic and thermal noise.

Later Weber built a second receiver at Argonne National Laboratory near Chicago, placed about 1000 kilometers from the first. The idea was make correlations between the observations of the two detectors.

If the same signal was detected simultaneously on both receivers, it was reasonable to assume that the signal was of non local origin. In a very famous article published in 1969 WEBER [1969], Weber claimed that he had detected coincidences corresponding to gravitational waves between them that could be explained by an emission from the center of our Galaxy and due to the pic amplitude the emitting source is 10^{10} solar masses (figure 1.3b). The experiment was repeated by other teams but they did not confirm Weber's results. As it was never verified, the article was refuted.

[1] Local characteristics of a curve drawn on a surface.

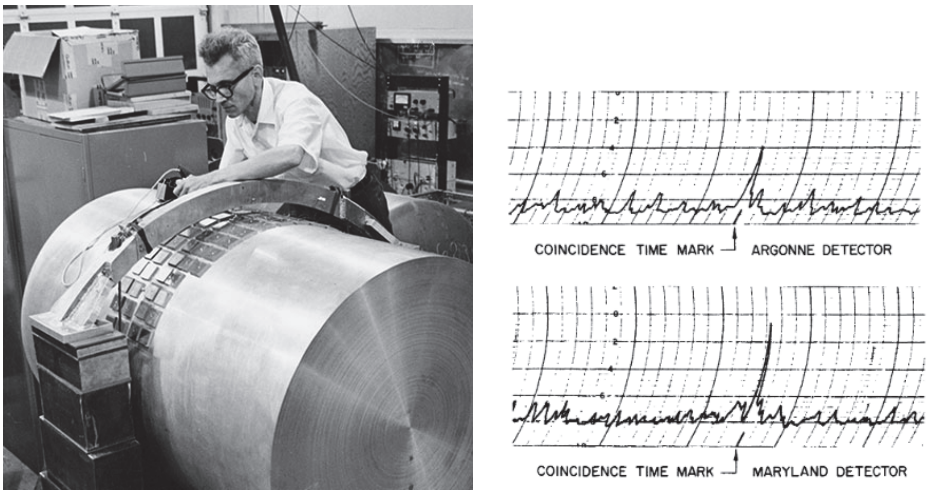

(a) (b)

Figure 1.3: (a) Picture of Joseph Weber working on the Resonant Mass Antenna, the first gravitational wave detector. Credit : Special Collections/University of Maryland Libraries. (b) Argonne National Laboratory and University of Maryland detector coincidence from WEBER [1969].

Following the first detectors of Joseph Weber, a second generation of resonant mass detectors was born around the world in the 90's. They had been significantly improved since the first bar. Unlike the first generation of Weber detectors at room temperature, these new detectors were cooled to cryogenic temperatures of the order of 4 K to reduce thermal noise and isolate the bar from unwanted noise. The table 1.1 presents some resonant bars antennas which operates between 1997s and 2010s AGUIAR [2010].

Seismic isolation was ensured by placing the detector in a cryogenic vacuum chamber, alternative materials and much more sensitive sensors were used.

The International Gravitational Event Collaboration (IGEC) regroups all the different bar observatory. These gravitational wave observatory consists of five cryogenic bar detectors EXPLORER, ALLEGRO, AURIGA, NAUTILUS and NIOBE PRODI et collab. [2000]. The main characteristics of detectors are listed in table 1.1. Detectors are cooled with liquid helium at temperature below 1K and the sensibility are near 10^{-21} $Hz^{-1/2}$ (unit of the spectral density in signal amplitude). In the years 2000', another kind of detectors projects that can be considered as third generation detectors, like the experiments MiniGrail detector (Leiden, Netherlands) DE WAARD et collab. [2003], Sfera (Frascati Italy) FAFONE [2006] and Shenberg (Sao Paulo, Brazil) AGUIAR et collab. [2005]. There were spherical detectors (between 1-100 tons weight) placed in a cryostat with a silent mixing chamber and a cryogenic vessels decoupled from the detector to reduce vibrations. The resonance frequency was 3 kHz and the sensitivity was significantly improved and reached 10^{-23} to 10^{-24} $Hz^{-1/2}$ (that correspond to $h \sim 10^{-21}$ - 10^{-22} respectively).

Table 1.1: Outlines of detectors. Main physical parameters of the five resonant mass detectors around the world in 1997-1998 PRODI et collab. [2000].

Project	Bar Material	Bar Masse M [kg]	Bar T^o [K]	Frequency [Hz]
ALLEGRO *Louisiana (USA)*	Al	2296	4.2	[895 ; 920]
EXPLORER *Geneva (Switzerland)*	Al	2270	2.6	[905 ; 921]
AURIGA *Padova (Italy)*	Al	2230	0.25	[912 ; 930]
NAUTILUS *Rome (Italy)*	Al	2260	0.1	[908 ; 924]
NIOBE *Perth (Australia)*	Nb	1500	5	[694 ; 713]

1.3.4 The first interferometric laser detectors

A forgotten paper in the history about gravitational waves but which is now recognized in the gravitational wave community is the one written and published in 1962 by two soviet physicists Michael Gertsenshtein and Vladislav Pustovoit from Moscow. After studying the works and papers of Joseph Weber, they demonstrated that the deformation of an object due to the passage of a gravitational wave was an extremely small variation. They concluded that the use of optical interferometers with 10 meters arms and the study of correlations between them could possibly detect theses waves with a sensitivity better than 10^{-16} $Hz^{-1/2}$ in the low frequency range GERTSENSHTEĬN et PUSTOVOĬT [1963].

In this case, the detection of gravitational waves was no longer done by measuring vibrations of a cylinder but by measuring the light interference between two laser beams reflected by mirrors placed at the ends of the arms of a Michelson interferometer. A gravitational wave will induce a differential arm length change between the 2 arms (equation (1.1)), and Michelson interferometers are particularly adapted to measure a differential change in length of the two arms. Several similar proposals came over the following years with the arms of the interferometer and the laser power constantly being increased in order to improve the shot noise limited sensitivity S at high frequency of the instrument which varie as :

$$S \propto \frac{1}{L * \sqrt{P}} \tag{1.2}$$

This equation link two quantities L the arms length and P the incident laser power. In fact the gravity antennas allows to measure the differential displacement and not a deformation contrary to the bars. Then they offers a better sensitivity for the detection of gravitational waves over a broad frequency range.

Three physicists, G.E.Moss, L.R.Miller and Robert Forward (a former student of Joseph Weber), focused on the construction of this kind of detector (see figure 1.4a). They built and tested the first free mass antenna interferometry with a laser at Hughes Research Laboratories (Malibu, California) MOSS et collab. [1971]. Shortly after, in the 1970s, Robert Forward built another prototype of a laser interferometer at Hughes Research Laboratories based on the previous work. The arms length was 2 meters and he used roof prisms mirrors placed in a cylindrical vacuum tank FORWARD [1978]. The system presented in figure 1.4b is significantly improved with respect to the one in figure 1.4a and the optical path of the beam too. It is composed of a single mode laser 6328 Å He-Ne 160 µW, two mirrors, a beamsplitter and several reflectors allowing to reflect the beam and to cancel some optical errors. The laser beam circulates in aluminum tubes under vacuum (<0.1 mbar) where high quality reflectors are placed. The beamsplitter and the reflectors are maintained in support blocks to avoid internal mechanical resonances below 25 kHz. The mirrors used are coupled to piezoelectric transducers in order to keep constant the optical's path length at low frequency. These kind of mirrors were used because they create a stable radio frequency and so they are most stable in the cavity. Therefore with this configuration the effective length covered by the beam in each arm is 4.25 m. This is the equivalent of an interferometer of 8.5 m long.

At the same period, in 1972, Reiner Weiss at Massachusetts Institute of Technology (MIT), was also working on an optical interferometer detector. In figure 1.5, the optical path of the laser light is entirely under vacuum, they are 4 mirrors and no more reflectors, one at each end of the arms and the corner mirrors have been replaced by spherical mirrors. Besides, Rainer Weiss is the first to have made a detailed study of a real interferometer system, proposed an antenna design and describes the different sources of noise that would be critical for the detection such as : amplitude noise in the laser output power, laser phase noise or frequency instability, mechanical thermal noise in the antenna, radiation-pressure noise from the laser light, seismic noise, thermal-gradient noise, cosmic-ray noise, gravitational-gradient noise, electric field and magnetic field noise WEISS [1972].

With the work of these pioneers in the experimental search for gravitational waves a new era was born, they have shown the path of the first observatories dedicated to the detection of space-

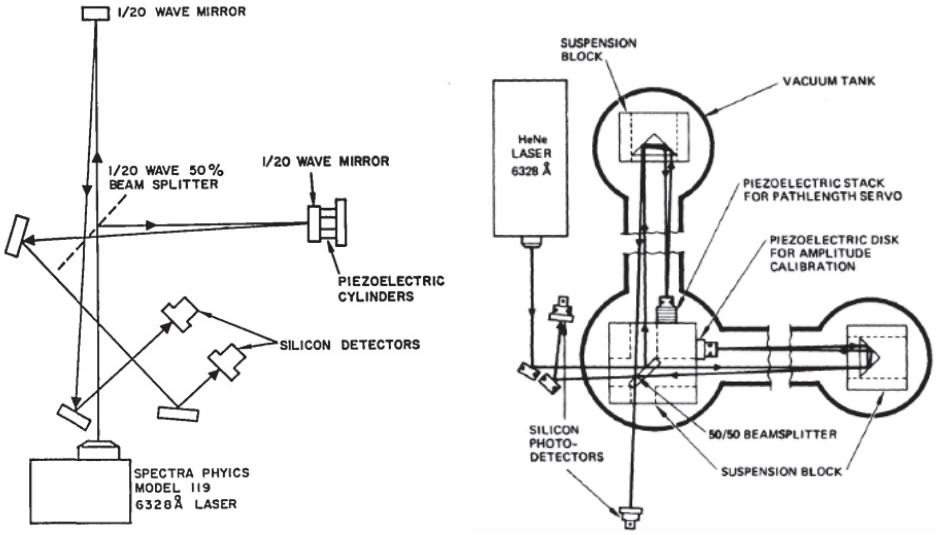

(a) (b)

Figure 1.4: (a) Scheme of the proposed interferometer by G.E.Moss, L.R.Miller and R.L.Forward MOSS et collab. [1971] (b) Scheme of the optical path in the interferometer optimized by R.L.Forward FORWARD [1978]. The major differences were the light source, the arms lenght, the cylindrical vaccum tank system and the reflector mirror added by R.Forward.

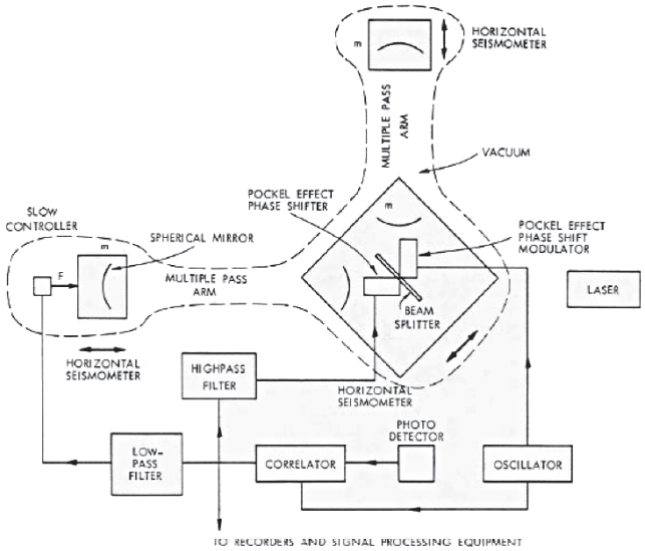

Figure 1.5: The first prototype interferometer by Reiner Weiss WEISS [1972].

time vibrations.

1.4 Gravitational Wave Observatories

Thanks to the remarkable work of all these physicists and all their contributions, a network of gravitational wave detectors has been built as is described in section 1.4.1. By now, different projects for the construction of future generation gravitational wave detectors are being negotiated in section 1.4.2 and 1.4.3. Whether it is on the Earth surface, underground or even in Space, the technological challenges keep growing and the future of gravitational wave research promises to be bright.

1.4.1 First and second generation detectors

Since 1989, four big projects proposal of giant observatories have taken shape. The first project was Laser Interferometer Gravitational-Wave Observatory (LIGO) supported by Caltech-MIT led by Rainer Weiss, Kip Thorne and Ronald Drever. There are two interferometers : one in Hanford and the other in Livingston (USA) whose construction lasted from 1994 to 2002. The second one is named Virgo () whose construction started in 1994 near Pisa in Italy. Interferometers are L-shape detectors, with two arms cooled at cryogenics temperatures. From 2010 to 2011 there was an upgrade to improve the sensitivity of the LIGO and Virgo detectors which became Advanced LIGO and Advanced Virgo. The quality of the mirrors has been improved, and the laser power increased. This has allowed a significant gain in sensitivity, and eventually the detection of gravitational waves. The figure 1.6 shows the sensitivity curves of the different gravitational waves experiments.

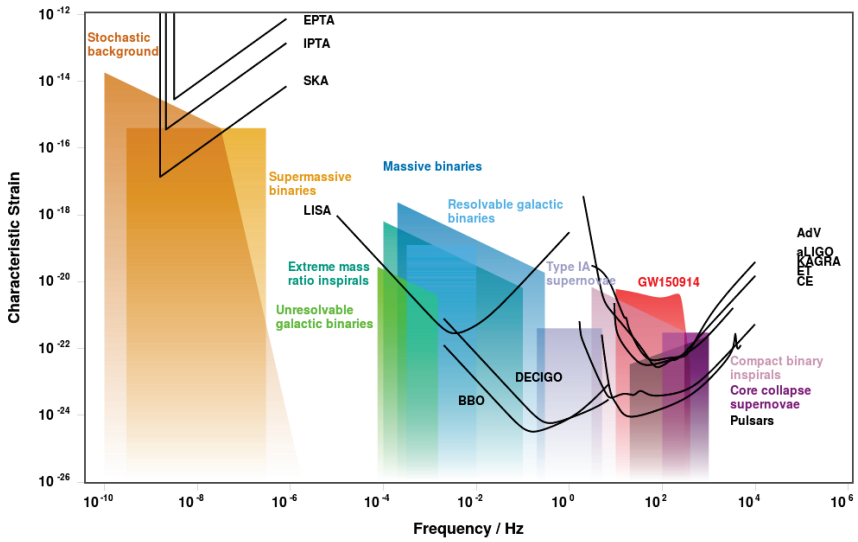

Figure 1.6: Sensitivity curves of the different gravitational waves detectors. The gravitational waves spectrum spans several orders of magnitude in frequency and is constrained by different experimental observations, from Pulsar Timing Arrays to GW space-based and terrestrial interferometers. The plot shows the physical phenomena contributing to the GW emission in the different frequencies, together with the sensitivity curves of experimental existing and future facilities. Credit : Christopher Moore, Robert Cole and Christopher Berry, formerly of the Gravitational Wave Group at the Institute of Astronomy, University of Cambridge (http://gwplotter.com/). The figure shows the sensitivity of the different instruments but we focus on aLIGO and AdV which are respectively the upgrade of the LIGO and Virgo detectors.

LIGO and Virgo work together to maximize the chances of detection. They have been sharing data access and analysis since 2007. The interferometer network also allows to determine the position of the source by using triangulation. The calculation is based on the measurement of the time difference of arrival of the signal at the three different detectors. In the case of an interesting confident event detection, alerts are sent to the different terrestrial and space telescopes in order to orient the observing instruments in the direction of interest to measure the eventual

Table 1.2: Informations about differents gravitational waves observatories around the world.

Observatories	LIGO Livingstone	LIGO Handford	VIRGO	KAGRA
Lenght arm [km]	4km	4 km	3 km	3 km
Optics ø[cm]	34	34	35	22
Material	Fused silica	Fused-silica	Fused-silica	Sapphire
Vaccum [mbar]	10^{-9}	10^{-9}	$<10^{-9}$	$<10^{-8}$
Frequency range[Hz]	[10 - 1000]	[10 - 1000]	[10 - 1000]	[100 - 1000]
Sensibility	$h \sim 10^{-22}$	$h \sim 10^{-22}$	$h \sim 10^{-21}$	$h \sim 10^{-19}$

(a) LIGO Livingston

(b) LIGO Hanford

(c) Virgo

(d) Credit ICRR, Univ. of Tokyo

Figure 1.7: Pictures of the large network of second generation gravitational wave detectors. Credit : Caltech/MIT/LIGO Lab.

electromagnetic counterparts of the event. Coincidences are also searched for with detections by neutrino detector experiments like Antares or IceCube.

The detection of the first gravitational wave in 2015 marked a turning point in the search for them. With the work of optimizing the detectors, we went to 100 coalescences of objects listed in a third catalog of gravitational wave detections ABBOTT et collab. [2021]. Rainer Weiss work in instrumental research he was awarded of the 2017 Nobel Prize in Physics shared with Barry C. Barish and Kip S. Thorne for their decisive contributions to the LIGO detectors and the first direct observation of gravitational waves.

The fourth gravitational wave detector to join the network is a Japanese observatory built in Kamioka called Kamioka Gravitational Wave Detector (KAGRA). This project is under the direction of the Institute for Cosmic Ray Research of the University of Tokyo. KAGRA uses the same technology as its three big brothers but has some peculiarities. It is the first to be installed underground (figure.1.7d), so to benefit from a very low seismic environment away from the noise of human activity. The detector is L-shaped and consists of two 3 kilometer long vacuum arms and uses sapphire mirrors cooled to 20 K. Cryogenic temperature reduces the thermal noise which is a major contributor at low frequencies. KAGRA whose construction started in 2010 is operational since late 2019. It officially joined the LIGO-Virgo collaboration in October 2019 and having a fourth interferometric detector in this network will improve the precision of the location of gravitational waves sources in the sky by triangulation.

1.4.2 Third generation detectors

Based on the success and experience gained on the second generation detectors Advanced Virgo and Advanced LIGO, new projects of ground-based interferometers arise for the future in Europe and the USA. Einstein Telescope (E.T.), recently endorsed by the European Strategic Forum for Research Infrastructures (ESFRI) Roadmap 2021, is the third generation of gravitational waves detectors scheduled for 2035. There are five countries that support the project, including Italy, Belgium, Poland, Spain and the Netherlands. Currently two sites are under study, the first in Sardinia and the second in Maastricht.

E.T will also be a giant laser interferometer with a xylophone configuration with three nested detectors at 250 meters under ground to avoid surface seismic noise (see figure 1.8a). Each one will comprise one cryogenic interferometer especially sensitive to the low frequency range of gravitational waves spectrum, thanks to the reduction of thermal noise, and one room temperature/high laser power interferometer for the high-frequency part HILD et collab. [2009]. According to the preliminary scheme of this project, developed in the last 10 years, arms will be 10 km long. Quantum technologies will be used to reduce light's fluctuation. The injection of squeezed light can reduce quantum noise by a factor of 2 in gravitational wave detectors AASI et collab. [2013]. In this way, E.T will be 10 times more sensitive than the current detectors, reaching sensitivity to a strain of the order of $h \sim 10^{-22}$. Thanks to its original geometry, ET will be equally sensitive to both polarizations and will provide a more isotropic antenna pattern than traditional L-shaped interferometers, and a better single-detector sky localisation.

Another project of third generation gravitational wave detectors called Cosmic Explorer (C.E.) is proposed to National Science Foundation (NSF) by the American gravitational wave community. The C.E. design is the same as the second generation detector apart from a significant elongation of the arms length which will be 5 to 10 times longer ensuring better sensitivity. This project will include two sites with 40 km and 20 km L-shaped interferometers. Third generation detectors will allow us to explore a large part of the Universe and to shed light on many topics including EVANS et collab. [2021]:

1. Black holes and neutron stars throughout cosmic time : With their significant increase of sensitivty, third generation detectors would detect stellar mass black hole mergers from the youngest years of the Universe (less than 500 million years old).

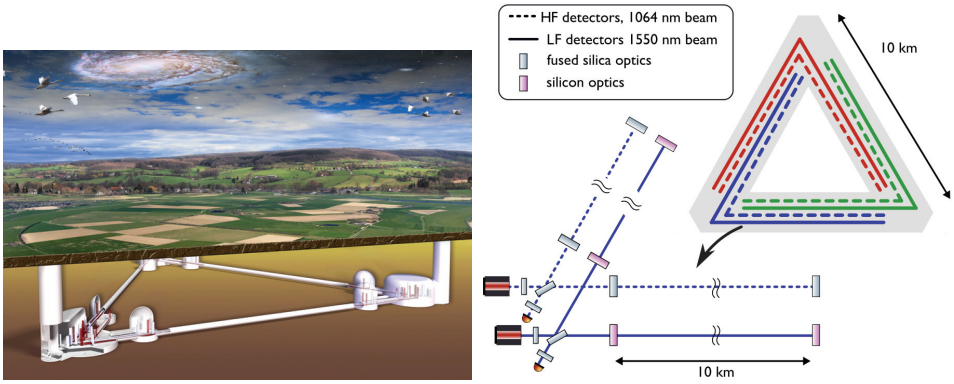

(a) Artist view (b)

Figure 1.8: (a) An artist view of Einstein Telescope, credit Marco Kraan (Nikhef) (b) Einstein Telescope Optical Layout showing an overview of the observatory with the 3 detectors forming triangular shape. The other layout show one detector composed of two intererometers, one for high frequencies (HF) and the other for low frequencies (LF) ROWLINSON et collab. [2021].

2. Dynamics of dense matter: Determining the internal structure and composition of neutron stars, explore new regions in the phase diagram of quantum chromodynamics and map heavy element nucleosynthesis in the Universe through counterpart kilonovae and distant mergers.

3. Extreme Gravity and fundamental Physics : The aim is to answer this question *"What is the nature of the strongest gravity in the Universe, and what does that nature reveal about the laws of physics ?"* by the revelation of potential new physics with the discoveries of new compact objects not detected untill now, probing the nature of strong gravity, the nature of dark matter and dark energy.

1.4.3 Space-based Observatories

The Laser interferometer Space Antenna (LISA) space project is the first space-based gravitational-wave observatory. This future mission of European Space Agency (ESA), in collaboration with National Aeronautics and Space Administration (NASA) aims to detect gravitational waves at low frequency from space between 0.1 mHz and 1 Hz. As we have learnt from the first and second generation detectors, it is necessary to get rid of terrestrial noise to reduce the noise level considerably BABAK et collab. [2017]. Being in space allows to be free of all the seismically induced noises, to increase detectors sizes and to explore the early universe from signals that are not detectable from the earth. LISA configuration will be composed of three spacecrafts forming an equilateral triangle separated by 2,5 million kilometers and placed in Earth orbits (figure 1.9). LISA will not use the same technology as terrestrial Michelson interferometers but will use digital interferometers Time Delay Interferometry (TDI). Indeed, laser beams cannot be recombined in space because of the large distances between satellites. The use of the TDI will allow thanks to algorithms to recombine the beams numerically. According to the figure 1.6 the sensitivity of LISA will be $h \sim 10^{-22}$. For now the launch is planned for 2037.

Another space gravitational wave antenna project is DECi-hertz Interferometer Gravitational wave Observatory (DECIGO) a future Japanese detector. The configuration is similar to LISA, there is three drag-free spacecraft separated by 1000 km using laser interferometry KAWAMURA et AL [2008]. According to projections it will be more sensitive than LISA and operate in the 0.1 to 10 Hz frequency band with $h \sim 10^{-25}$. DECIGO will detect gravitational waves from supermassive black holes, stochastic background and from a large number of neutron stars at the same time.

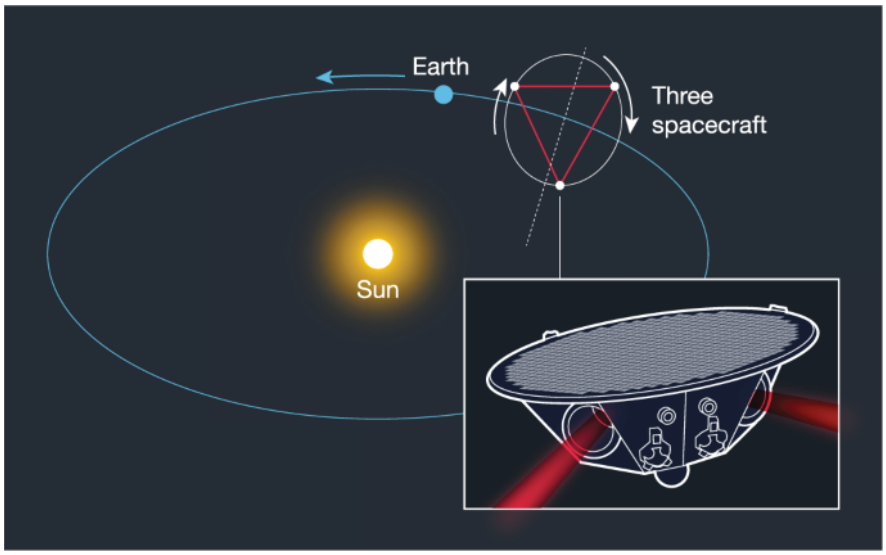

Figure 1.9: Unlike ground-based detectors, such as LIGO and Virgo, in LISA the stations are free-floating test masses in orbit around the Sun. Figure adapted from (Springer Nature).

Since Joseph Weber and his first gravitational wave antenna, our knowledge, technology and know-how have clearly evolved giving way now to detectors with innovative configurations and much better performances. By now and for the next years, we are able to probe the Universe using gravitational waves, and combine these observations with others based on cosmic rays, electromagnetic radiation and neutrinos. This is the recent and very promising field of multi-messenger astronomy.

1.5 References

AASI, J., J. ABADIE, B. P. ABBOTT, R. ABBOTT, T. D. ABBOTT, M. R. ABERNATHY, C. ADAMS, T. ADAMS, P. ADDESSO, R. X. ADHIKARI et ET AL. 2013, «Enhanced sensitivity of the ligo gravitational wave detector by using squeezed states of light», *Nature Photonics*, vol. 7, 8, doi:10.1038/nphoton.2013.177, p. 613–619, ISSN 1749-4893. URL http://dx.doi.org/10.1038/nphoton.2013.177. 14

ABBOTT et AL. 2017a, «Multi-messenger observations of a binary neutron star merger», *The Astrophysical Journal*, vol. 848, 2, doi:10.3847/2041-8213/aa91c9, p. L12. URL https://doi.org/10.3847/2041-8213/aa91c9. 5

ABBOTT, R. et AL. 2017b, «Gw170817: Observation of gravitational waves from a binary neutron star inspiral», *Phys. Rev. Lett.*, vol. 119, doi:10.1103/PhysRevLett.119.161101, p. 161 101. URL https://link.aps.org/doi/10.1103/PhysRevLett.119.161101. 5

ABBOTT, R. et AL. 2021, «Observation of gravitational waves from two neutron star black hole coalescences», vol. 915, 1, doi:10.3847/2041-8213/ac082e, p. L5. URL https://doi.org/10.3847/2041-8213/ac082e. 6

ABBOTT, R. et collab.. 2021, «GWTC-3: Compact Binary Coalescences Observed by LIGO and Virgo During the Second Part of the Third Observing Run», . 14

AGUIAR, O. D. 2010, «Past, present and future of the resonant-mass gravitational wave detectors», *Research in Astronomy and Astrophysics*, vol. 11, 1, doi:10.1088/1674-4527/11/1/001, p. 1–42. URL https://doi.org/10.1088/1674-4527/11/1/001. 8

AGUIAR, O. D. et collab.. 2005, «The Brazilian gravitational wave detector Mario Schenberg: Progress and plans», *Class. Quant. Grav.*, vol. 22, doi:10.1088/0264-9381/22/10/011, p. S209–S214. 8

BABAK, S., J. GAIR, A. SESANA, E. BARAUSSE, C. F. SOPUERTA, C. P. L. BERRY, E. BERTI, P. AMARO-SEOANE, A. PETITEAU et A. KLEIN. 2017, «Science with the space-based interferometer lisa. v. extreme mass-ratio inspirals», *Phys. Rev. D*, vol. 95, doi:10.1103/PhysRevD.95.103012, p. 103 012. URL https://link.aps.org/doi/10.1103/PhysRevD.95.103012. 15

DEWITT, C. 2011, *WADC Technical Report 57-216, in : C. DeWitt (Ed.),Conference on the Role of Gravitation in Physics at the University of North Carolina, 1957*, Éditeur. 7

EINSTEIN, A. 1905, «Zur elektrodynamik bewegter körper», *Annalen der Physik*, vol. 10, p. 891–921. 4

EINSTEIN, A. 1916, «Die grundlage der allgemeinen relativitätstheorie», *Annalen der Physik*, vol. 7, p. 769–822. 4

EINSTEIN, A. 1918, «Uber gravitationswellen», *Gesamtsitzung*, vol. 14, p. 154. 4, 5

EINSTEIN, A. et N. ROSEN. 1937, «On gravitational waves», *Journal of the Franklin Institute*, vol. 223, 1, doi:https://doi.org/10.1016/S0016-0032(37)90583-0, p. 43–54, ISSN 0016-0032. URL https://www.sciencedirect.com/science/article/pii/S0016003237905830. 6

EVANS, M., R. X. ADHIKARI, C. AFLE, S. W. BALLMER, S. BISCOVEANU, S. BORHANIAN, D. A. BROWN, Y. CHEN, R. EISENSTEIN, A. GRUSON, A. GUPTA, E. D. HALL, R. HUXFORD, B. KAMAI, R. KASHYAP, J. S. KISSEL, K. KUNS, P. LANDRY, A. LENON, G. LOVELACE, L. MCCULLER, K. K. Y. NG, A. H. NITZ, J. READ, B. S. SATHYAPRAKASH, D. H. SHOEMAKER, B. J. J. SLAGMOLEN, J. R. SMITH, V. SRIVASTAVA, L. SUN, S. VITALE et R. WEISS. 2021, «A horizon study for cosmic explorer: Science, observatories, and community», URL https://dcc.cosmicexplorer.org/public/0163/P2100003/007/ce-horizon-study.pdf. 14

FAFONE, V. 2006, «Developments in resonant-mass detectors», vol. 23, 8, doi:10.1088/0264-9381/23/8/s28, p. S223–S229. URL https://doi.org/10.1088/0264-9381/23/8/s28. 8

FORWARD, R. L. 1978, «Wideband laser-interferometer graviational–radiation experiment», *Phys. Rev. D*, vol. 17, doi:10.1103/PhysRevD.17.379, p. 379–390. URL https://link.aps.org/doi/10.1103/PhysRevD.17.379. 9, 10

GERTSENSHTEĬN, M. E. et V. I. PUSTOVOĬT. 1963, «On the detection of low-frequency gravitational waves», *Soviet Journal of Experimental and Theoretical Physics*, vol. 16, p. 433. 9

HILD, S., S. CHELKOWSKI, A. FREISE, J. FRANC, N. MORGADO, R. FLAMINIO et R. DESALVO. 2009, «A xylophone configuration for a third-generation gravitational wave detector», *Classical and Quantum Gravity*, vol. 27, 1, doi:10.1088/0264-9381/27/1/015003, p. 015 003. URL https://doi.org/10.1088/0264-9381/27/1/015003. 14

HULSE, R. A. et J. H. TAYLOR. 1975, «Discovery of a pulsar in a binary system», *The Astrophysical Journal*, vol. 195, p. L51–L53. 5

KAWAMURA, S. et AL. 2008, «The japanese space gravitational wave antenna - DECIGO», *Journal of Physics: Conference Series*, vol. 122, doi:10.1088/1742-6596/122/1/012006, p. 012 006. URL https://doi.org/10.1088/1742-6596/122/1/012006. 15

KIBBLE, T. W. B. 1976, «Topology of cosmic domains and strings», *Journal of Physics A: Mathematical and General*, vol. 9, 8, doi:10.1088/0305-4470/9/8/029, p. 1387–1398. URL https://doi.org/10.1088/0305-4470/9/8/029. 6

MOSS, G. E., L. R. MILLER et R. L. FORWARD. 1971, «Photon-noise-limited laser transducer for gravitational antenna», *Appl. Opt.*, vol. 10, 11, doi:10.1364/AO.10.002495, p. 2495–2498. URL http://www.osapublishing.org/ao/abstract.cfm?URI=ao-10-11-2495. 9, 10

PIRANI, F. A. E. 2009, «Republication of: On the physical significance of the riemann tensor», *General Relativity and Gravitation*, vol. 41, 5, doi:10.1007/s10714-009-0787-9, p. 1215–1232. 7

PRESKILL, J. et K. THORNE. 2000, «Foreword to feynman lectures on gravitation», . 7

PRODI, G. A., V. MARTINUCCI, R. MEZZENA, A. VINANTE, S. VITALE, I. S. HENG, Z. A. ALLEN, W. O. HAMILTON, W. W. JOHNSON, M. P. MCHUGH et ET AL. 2000, «Initial operation of the international gravitational event collaboration», *International Journal of Modern Physics D*, vol. 09, 03, doi:10.1142/s0218271800000219, p. 237–245, ISSN 1793–6594. URL http://dx.doi.org/10.1142/S0218271800000219. 8

ROWLINSON, S., A. DMITRIEV, A. W. JONES, T. ZHANG et A. FREISE. 2021, «Feasibility study of beam-expanding telescopes in the interferometer arms for the einstein telescope», *Physical Review D*, vol. 103, 2, doi:10.1103/physrevd.103.023004, ISSN 2470-0029. URL http://dx.doi.org/10.1103/PhysRevD.103.023004. 15

SIEMENS, X., V. MANDIC et J. CREIGHTON. 2007, «Gravitational–wave stochastic background from cosmic strings», *Phys. Rev. Lett.*, vol. 98, doi:10.1103/PhysRevLett.98.111101, p. 111 101. URL https://link.aps.org/doi/10.1103/PhysRevLett.98.111101. 6

TAYLOR, J. H. et J. M. WEISBERG. 1989, «Further experimental tests of relativistic gravity using the binary pulsar psr 1913+16», , vol. 345, doi:10.1086/167917, p. 434. 5

DE WAARD, A., L. GOTTARDI, J. A. VAN HOUWELINGEN, A. E. SHUMACK et G. FROSSATI. 2003, «Minigrail, the first spherical detector», *Classical and Quantum Gravity*, vol. 20. 8

WEBER, J. 1960, «Detection and generation of gravitational waves», *Phys. Rev.*, vol. 117, doi:10.1103/PhysRev.117.306, p. 306–313. URL https://link.aps.org/doi/10.1103/PhysRev.117.306. 7

WEBER, J. 1969, «Evidence for discovery of gravitational radiation», *Phys. Rev. Lett.*, vol. 22, doi:10.1103/PhysRevLett.22.1320, p. 1320–1324. URL https://link.aps.org/doi/10.1103/PhysRevLett.22.1320. 7, 8

WEBER, J. 1979, «Gravitational waves», *Crown Publishers*, vol. New York. 7

WEBER, J. et J. A. WHEELER. 1957, «Reality of the cylindrical gravitational waves of einstein and rosen», *Rev. Mod. Phys.*, vol. 29, doi:10.1103/RevModPhys.29.509, p. 509–515. URL https://link.aps.org/doi/10.1103/RevModPhys.29.509. 7

WEISS, R. 1972, «Electromagnetically coupled broadband gravitational antenna», *Quarterly Reports of the Research Laboratory of Electronics MIT 105*, vol. 14, p. 54. 9, 10

Chapter 2

Gravitational-wave interferometric detectors

Contents

2.1 Configuration of detectors

2.1.1 Interferometer working principle

The optical layout of the instrument Advanced Virgo is shown in figure 2.1. There are two input mirrors (IM), two output mirrors (EM) and a beam splitter. Each arm of the interferometer is a Fabry-Perot cavity to increase the laser power circulating in the long arms. A laser with a wavelength of 1064 nm is injected inside the interferometer, then separated in two by the beamsplitter (BS). Each beam travels in a 3 km long arm. The beams make a large number of round trips between the entrance and exit mirror proportionally to the finesse of the cavity. The two beams are recombined again, at the level of the beamsplitter. The beam is then directed to a detector which measures the interference pattern between the two beams. The system is adjusted so that in the absence of a gravitational wave the interference is destructive (dark fringe). The passage of the gravitational wave will change the phase shift and can be detected from the interference pattern.

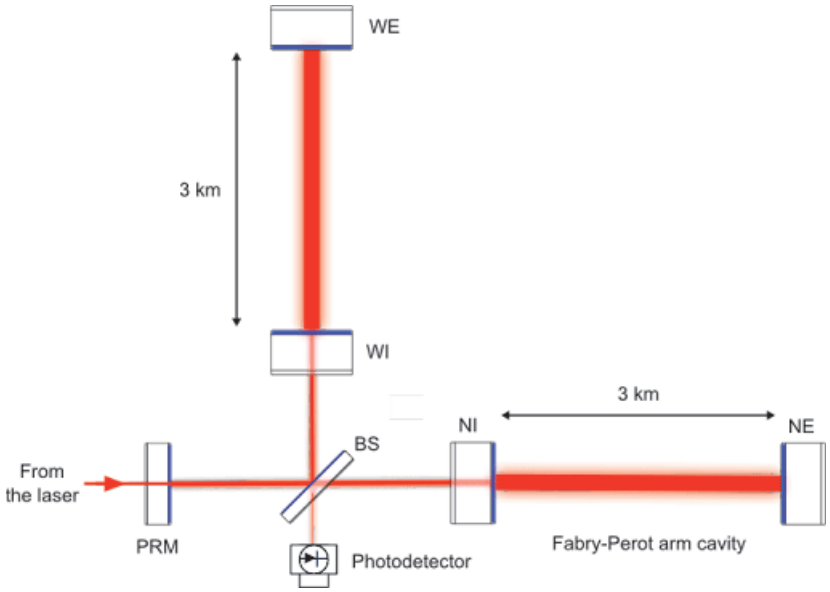

Figure 2.1: Configuration of the interferometer. Credit: Virgo collaboration

2.1.2 Fabry Perot Cavities

The 3 km arms of Virgo play an important role and are in fact Fabry-Perot optical resonators in which there are two mirrors, one facing the other, separated by a distance L. A monochromatic light beam circulates inside as a plane wave creating light interference inside the cavity, increasing or cancelling the electric field between the two mirrors. Thanks to the large number of round trips of the laser light within such a cavity, the equivalent distance covered by the laser light is higher than 3 km. The equation (2.1), connecting the sensitivity (S) to the length of the arms (L) and the laser power (P) explain why using the cavities are interesting.

$$S \propto \frac{1}{L * \sqrt{P}} \tag{2.1}$$

Within a cavity, the light makes an average of 280 round trips, which corresponds to an average distance of 1600 km. The design of these cavities is such that the mirror at the end of the arm should reflect all the light at 100%. By comparing ideal cavities and real ones, there are losses that are noticed. The Round Trip Losses (RTL), are one of the most critical parameters in the arm cavity, defined as :

$$RTL = \frac{P_{in} - P_t - P_r}{P_{circ}} \tag{2.2}$$

The physical quantities P_{in}, P_{circ} P_r and P_t are the input power, the circulating power inside the cavity, the reflected power and the transmitted power of the cavity respectively STRANIERO et collab. [2015].

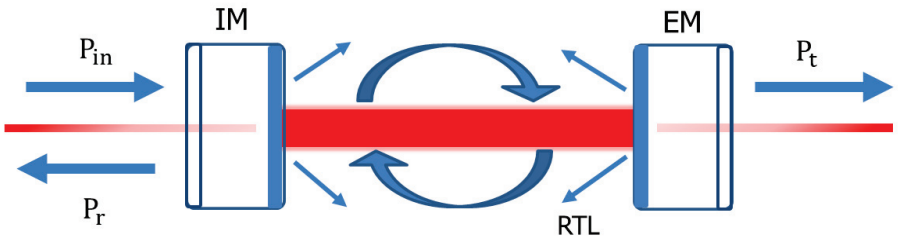

Figure 2.2: Fabry Perot representation.

For better understanding of the RTL impact, here are two simple examples, in the theoretical case where 1 W power laser is sent in the cavities. In the absence of loss, sending 1 W of laser on a perfect reflective surface, one recovers 1 W in reflection of the cavity which returns on the beamsplitter so the RTL will be 0 ppm. In the second case, let's assume the RTL are about 50 ppm (experimental measurements on the Virgo site YAMAMOTO [2015]), the majority of which is related to scattering, absorption and transmission losses. The 50 ppm are multiplied by the number of round trips of the light. Therefore, when sending 1 W of laser on a polishing and coated surface, one recovers only 0.978 W in reflection of the cavity and that means that RTL = 75 ppm. This implies an overall loss of 2% of the laser power in the cavity. These examples show how the Fabry-Perot cavities amplify the signal but also amplify the losses, so that the optical losses, even if very small, are enough to decrease sensibly the reflection of the cavity.

2.2 Limits of interferometers sensitivity

2.2.1 Different noise sources

There are various technical or fundamental noises that limit the sensitivity of the instrument such as fluctuations in the intensity or frequency of the laser source, thermal noise of suspensions and mirrors, or quantum noise of light. There is also the seismic noise affecting the low frequencies, as the high sensitivity of the interferometer makes it a very good optical seismograph. The sensitivity curve of Advanced Virgo, with the different components, is presented in figure 2.3.

To reduce the seismic noise of the detectors, a mechanical decoupling system, an inverted pendulum, on which the mirrors are placed, allows to limit the propagation of vibrations BROOKS et collab. [2021]. To isolate the interferometer from acoustic noise, the detectors are placed in a vacuum at a pressure of 10^{-9} mbar. This is the largest ultra-high vacuum installation in Europe in terms of volume. This also limits the fluctuations in the optical path of the laser arising from scattering by particles in the air and from the change in refractive index. The subject of this work is the phase noise generated by the scattered light.

Another noise source which is one of the major problems at low frequencies is the thermal noise. At the atomic scale, the atoms on the surface moves and induces a phase noise. Many research are being conducted trying to reduce this noise source by looking for new materials with better performance GRANATA et collab. [2019]. Others fundamental noises that limit the detectors are :

Quantum noise

This is one of the major sources of noise described at low frequency by the radiation pressure noise and at high frequency by the shot noise above 100 Hz. To limit the radiation pressure noise, generated by the quantum laser power fluctuations, the mass of the mirrors was increased from 21 kg to 42 kg for Advanced Virgo and to 100 kg for Advanced Virgo+. The shot noise can be reduced by increasing the power circulating inside the interferometer but not too high otherwise it would

degrade the sensitivity at low frequency because of the radiation pressure noise.

Gravity gradient

This concerns the fluctuations of terrestrial gravity at high frequencies, which are environmental noise that must be attenuated to improve sensitivity HUGHES et THORNE [1998].

Suspension thermal noise

The thermal noise of the suspension of the mirrors limits the sensitivity in the frequency band below 50 Hz due to some relaxation phenomenon in the suspension chain affecting the movement of mirrors. In order to overcome this problem and to reduce the thermal noise, monolithic fused silica suspensions have been installed LORENZINI [2010].

Brownian noise

This is one of the first noise identified as a problem for gravitational wave detectors. It is related to the thermal intrinsic noise produced by internal friction of both coating and substrate having the same spectral density. It is related to the surface using the fluctuation-dissipation theorem that produce phase noise GORODETSKY [2008].

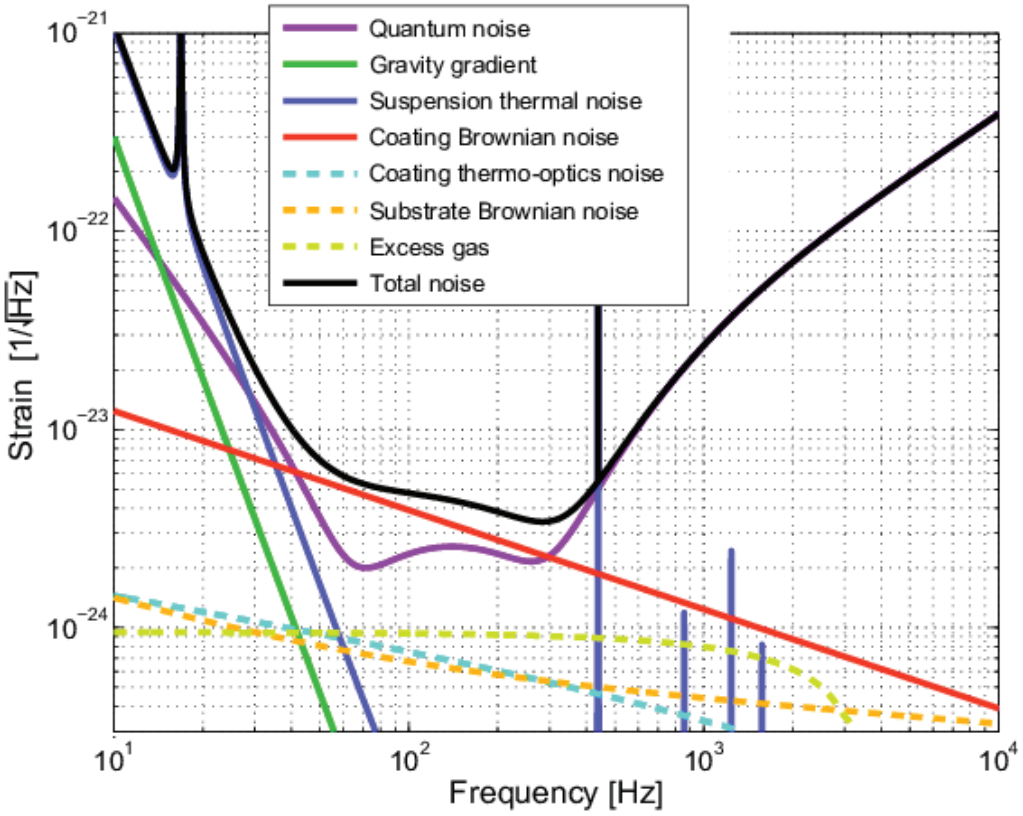

Figure 2.3: The Advanced Virgo sensitivity curve of the different noises limiting the detectors plotted as the equivalent strain amplitude detectable as a function of the frequency ACERNESE et AL [2014]. The black curve is the total sensitivity which envelop all the different noise sources.

2.2.2 Coating optical losses

Besides the technical and fundamental noises that limit the sensitivity, the interferometer is also impacted by the loss of the circulating power inside the cavity. Optical losses in the Fabry-Perot cavity, introduced in 2.1.2, can have different origins as presented in figure 2.4.

- Transmission : Light transmission through the output mirrors (ETM).
- Absorption : Absorption by the thin films, that can be caused by the cleaning, the nature of the substrate, the contaminations, and the technique of deposition used. Absorber points have been observed in the coatings. These points of the size of a hundred micrometers deform the surface of the mirror and reduce the circulating laser power which limits the sensitivity of the detectors BROOKS et collab. [2021]. Studies are currently underway to try to reduce them.
- Wave Front Error (WFE) distorsion : The surface figure error (SFE) corresponds to the deviation from the ideal wavefront curvature to ensure the resonance and stability of the cavity.
- Scattering : Light scattering by the high spatial frequency defects of the mirrors.

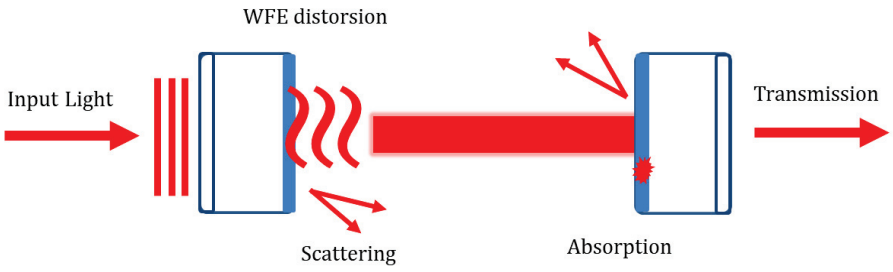

Figure 2.4: The different optical losses in the interferometer.

2.2.3 Focus on the scattered light

The scattered light is one of the main sources of noise under study for the Advanced Virgo upgrade. Light loss has two consequences : a loss of optical power in the interferometer arm amplified by the arm cavity gain and the addition of a phase noise when the scattered light is recombined to the main beam after reflection on the walls of the vacuum tubes. Both of these phenomena limit the sensitivity of the detector impacting the ability to detect astrophysical events. To try and mitigate the impact of scattering, Advanced Virgo and Advanced LIGO have installed light traps around the mirrors ACERNESE et AL. [2018]. They allow the scattered light to be absorbed to prevent it from returning to the interferometer and recombining with the main beam. Below are described the two main sources of scattered light :

Substrate surface roughness of the mirrors

Part of the scattering noise is attributed to the surface roughness which contributes to the scattering losses. Roughness corresponds to the topographic relief of a surface, and can be affected by polishing marks on optical surfaces, dust particles or machining marks BENNETT et MATTSSON [1999]. Such surface defects are at high spatial frequency (spatial period <0.1mm). When light impinges on this type of defects, it is scattered at large angles and is therefore lost. The amount of lost light is directly proportional to the RMS of the surface according to the law of total integrated scattering (TIS) STOVER [2012]. Indeed $\mathscr{L}$, the amount of light scattered by a mirror of roughness with RMS = σ (figure 2.5) and for a light wavelength λ, is given by the following relationship :

$$\mathscr{L} = \left(\frac{4\pi\sigma}{\lambda}\right)^2 \tag{2.3}$$

In this study the roughness of the chosen substrates is very good and its impact is negligible compared to the defects studied. The scattering of the uncoated substrate is then negligible.

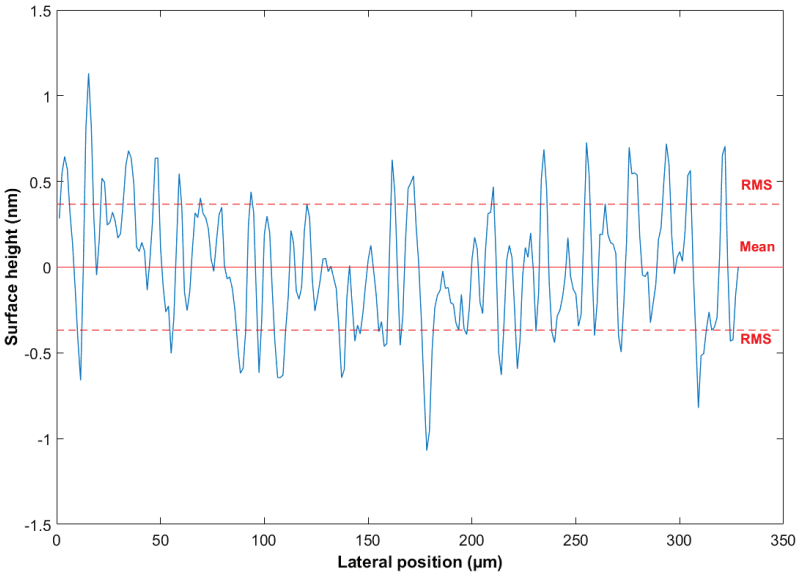

Figure 2.5: Schematic representation of a simulation of a rough surface showing statistical parameters. The surface height (in nm) is shown as a function of the lateral position (in µm).

Point defects in thin films due to the deposition technique

Despite the high quality of the optical coating, the performance of the mirrors is altered by the scattered light induced by the presence of micrometer-size defects in the coating layers. This induces a loss of the laser power in the cavity of the order of a few tens of parts per million. The three photos presented in figure 2.6 show an image with an infrared camera of the mirror placed in the Advanced Virgo interferometer at the end of the West arm. The pictures were taken (at an incident angle of about 10° where for perfect mirrors, no light should be collected) for different increasing laser powers from (a) to (c). Note that we observe exactly the same effect on the North end mirror. We can clearly see all the imperfections of the coating highlighted by the incident beam. Imperfections participate in the scattering. The more the defects, the more the scattering and the more the power loss. The problem of scattering points is a subject treated by other groups on the LIGO community side CAPOTE et collab. [2021]; VANDER-HYDE et collab. [2015].

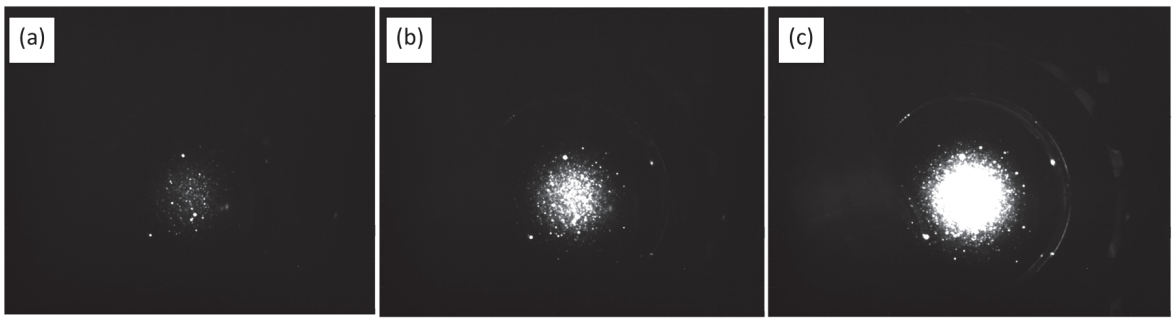

Figure 2.6: Photos of the end mirror of the West arm of the Advanced Virgo interferometer under different laser powers. The laser power is in around 0.1 kW in (a) 10 kW in (b) and 80 kW in (c). Credits: Jérôme Degallaix.

The work presented in this thesis is an investigation of the origin and nature of the defects in order to reduce their density. This research effort is essential to improve the optical performance of the mirrors in view of the next generation of coating. To understand this phenomenon, we will study in detail the scattering caused by the point defects in the high reflectivity coatings, their

relation with the deposition parameters and the behaviour of different materials like tantala and silica, used for the thin films.

2.3 The cavity mirrors : The heart of interferometers

At the heart of gravitational waves detectors there are mirrors with the lowest absorption in the world (0.14 ppm on a 5 ppm transmission stack is the record among the large optics coated by LMA). The detector core mirrors have very low wavefront distortion (2 nm peak-to-valley on 150 mm diameter) after coating deposition. Such outstanding results could be achieved thanks to two majors elements : high quality substrates and high quality coating.

2.3.1 Procurement of the large substrates

The choice of the good substrate is based on a material which has low optical losses (low mechanical loss, low absorption and low scattering). Substrates are large blocks of ultra pure fused silica (Heraeus 3001 et 312 Suprasil) produced in Germany by Heraeus see Figure 2.7. After the substrate choice, the second step is the micropolishing, performed in the USA by ZYGO Corp DEGALLAIX et collab. [2019], that guarantees a surface roughness with an RMS value down to 0.5 Å.

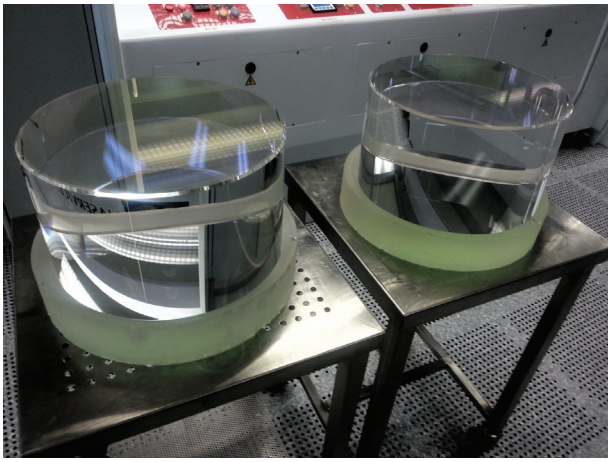

Figure 2.7: Pictures of Advanced Virgo substrates in the cleanroom of LMA after polishing and before coating. Crédit LMA/CNRS.

2.3.2 Coating structure

The last step is the responsibility of the LMA, in charge of the optical treatment by deposition of thin layers of materials on the surface substrate PINARD et collab. [2017]. All the mirrors that compose the optical cavities of the different observatories in the world have been coated at LMA. The thin film depositions for the Advanced Virgo and Advanced LIGO mirrors are identical. The large mirrors of Gravitational Waves detectors are dielectric mirrors allowing to reflect all the power of the laser light in the interferometer. The surface coating structure is a stack of thin optical layers, alterning two materials of different refractive index (see figure 2.8). The two materials used for the coatings are Ta_2O_5 doped with Titania (high refractive index n_H = 2.09 at 1064 nm) and SiO_2 (low refractive index n_L = 1.45 at 1064 nm) and the mirrors are 99.9995% reflective for a 1064 nm wavelength AMATO et collab. [2019].

The overall configuration was optimised in order to reduce the total thickness of Titania, the one with higher mechanical losses, in order to reduce the thermal noise. No more quarterwave layers, the high index layer total thickness decrease and we have the same spectral properties as quaterwave design. The formula of a thin film stack is expressed as follow :

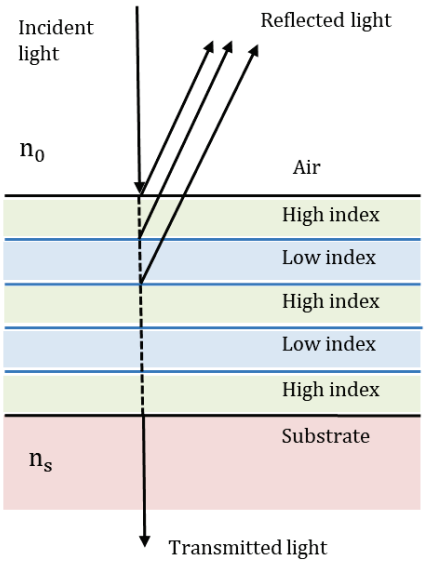

Figure 2.8: Layout of a multilayer coating. The arrows of the reflected light are shown with an incident angle different from zero for visibility.

$$a\mathrm{H}(b\mathrm{L}c\mathrm{H})^x d\mathrm{L} \tag{2.4}$$

with a, $c < 1$ and b, $d > 1$ are optimized coefficients, x the number of periods, H the optical thickness of a quarterwave layer at 1064 nm of Titania doped tantala (High index) and L the optical thickness of a quarterwave layer at 1064 nm of silica (Low index).

We consider a stack of x pairs of doublets homogeneous, linear and isotrope thin layers of index n_H and n_L and on a semi infinite substrate of index n_s. The incident light is an electromagnetic wave plane arriving at normal incidence and a wavelength λ (see figure 2.8), the expression of the reflectivity and transmission coefficients of the stack can be written as follow Born et Wolf [1999]:

$$\mathrm{R} = \left| \frac{n_s - \left(\frac{n_\mathrm{H}}{n_\mathrm{L}}\right)^{2\mathrm{N}}}{n_s + \left(\frac{n_\mathrm{H}}{n_\mathrm{L}}\right)^{2\mathrm{N}}} \right|^2 \simeq 1 - 4n_s \left(\frac{n_\mathrm{L}}{n_\mathrm{H}}\right)^{2\mathrm{N}} \tag{2.5}$$

The figure 2.9 shows the reflectivity as a function of the wavelength for different values of N. It highlights how the reflectivity varies depending on the configuration of the layer. The more layers, the more the reflectivity. Besides, the greater the refractive index contrast, the greater the reflectivity. In the case of negligible absorption and scattering, the transmissivity is written as follows :

$$\mathrm{T} = 1 - \mathrm{R} = 4n_s \left(\frac{n_\mathrm{L}}{n_\mathrm{H}}\right)^{2\mathrm{N}} \tag{2.6}$$

Based on this study, and in the aim of reducing the amount of material (in particular tantala) to minimise the thermal noise, the optimal number of layer pairs for Advanced Virgo mirrors has been chosen to be optimal.

2.3.3 Coating process for cavity mirrors

Ion beam sputtering deposition (IBS)

LMA has developed a large IBS coating machine called the Grand Coater Cimma et collab. [2006a], the unique and largest deposition machine in the world (dimensions 2.2 m x 2.2 m x 2.2 m shown

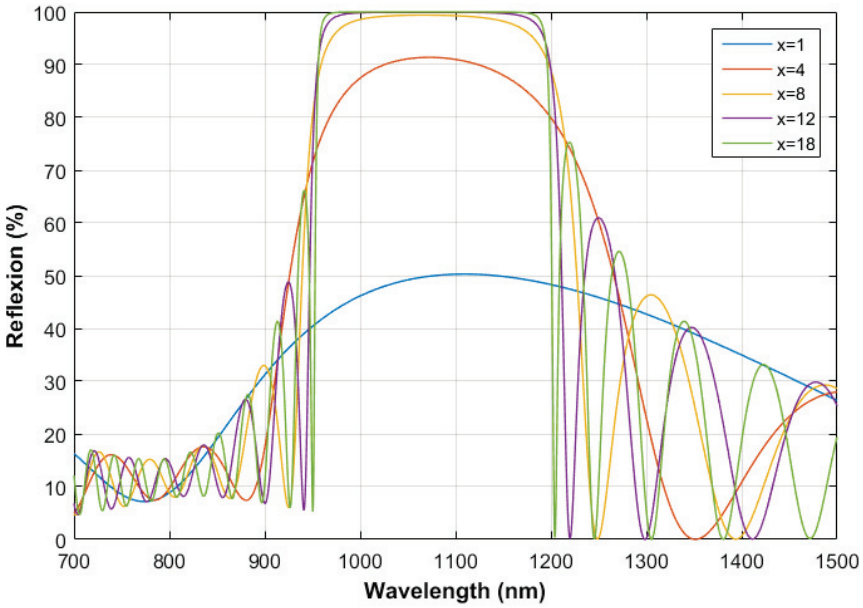

Figure 2.9: Reflexion as a function of the wavelength with different number of layer pairs (x, shown in the legenda).

in Figure 2.11) able to coat simultaneously two ∅ 350 mm mirrors using the ion beam sputtering (IBS) process. The LMA is also equipped with a smaller deposition machine called DIBS (0.6 m x 0.6 m x 0.8 m) that works with the same process. It was developed and used in the 90s at LMA as a prototype for the development of the Grand Coater. Another deposition machine using IBS process called SPECTOR (dimensions 1.1 m x 0.9 m) from IonTech (Veeco) is also installed at LMA (Figure 2.11).

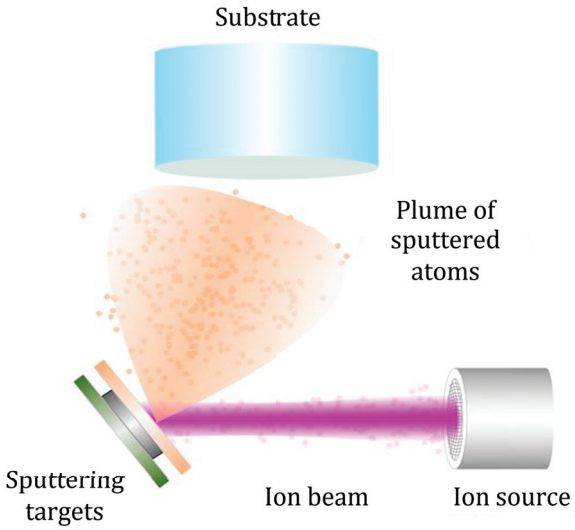

Figure 2.10: Principle of the deposition technique by Ion Beam Sputtering.

Radio-Frequency Ion Source

The IBS machine is composed of an Radio-Frequency (RF) ion source, a sputtering target (a plate made of the material to be sputtered), a neutralizer and a substrate holder. The figure 2.10, is a

(a) Spector

(b) DIBS

(c) Grand Coater

Figure 2.11: (a) The SPECTOR (b) The little IBS coating machine DIBS in the cleanroom at LMA (c) Grand Coater (GC). Credit Cyril Fresillon/CNRS

simplified schematic of the machine, which operates under vacuum at a base pressure of 10^{-8} mbar.

A Radiofrequency field allows to create a gas plasma by excitation of Ar atoms . Then the Ar+ ions are accelerated through a grid assembly biased at several hundreds of volts. The multiple extracted beamlets through the grids apertures combine into a broad monoenergetic ion beam (see 2.13). The schematic of the ion source presented in figure 2.12 shows the operating principle of the source. The ion beam impinges the target of the material, that is to say Ta_2O_5 and SiO_2, to deposit on the surface of the substrate.

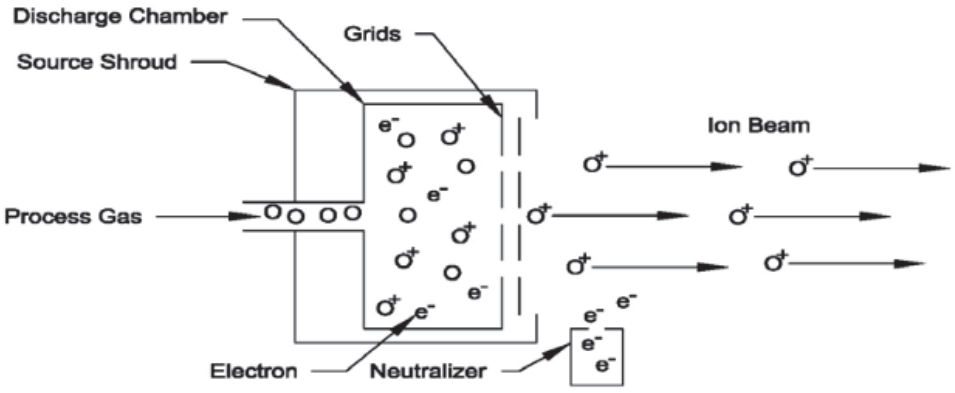

Figure 2.12: Schematic of an ion beam source BUCHHOLTZ [2000].

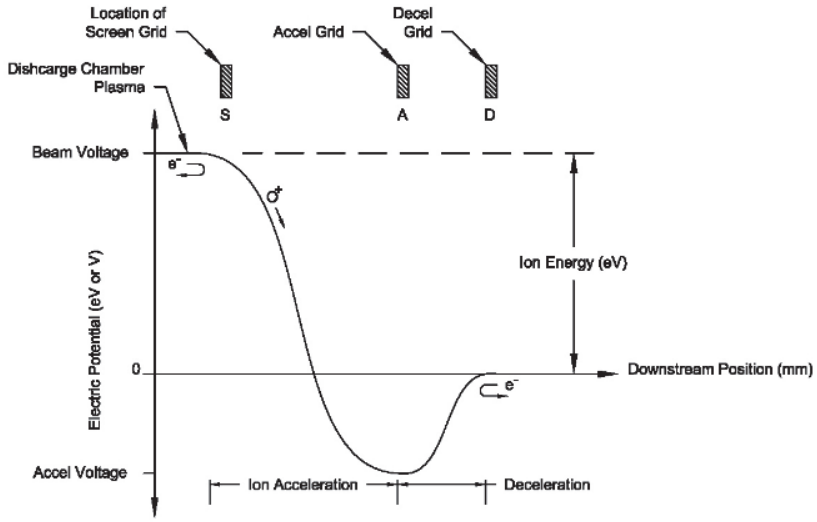

Figure 2.13: Schematic of the ion acceleration process BUCHHOLTZ [2000].

The Figure 2.13 explains how the ion source works. There are 3 grids. The energy of the ions is given by the first grid called screen grid (which allows to isolate the plasma) which is put at the potential V_b. This grid is positively polarized which allows to bend the electric field so that the ions feel the gradient and arrive at the second grid with energy.

Then we have the accelerating grid (which is negatively polarized) which allows to extract the ions and then a decelerating grid which brings back the ions to the potential of the chamber. The ions have a very high energy, of the order of keV, sufficient to sputter the atoms of the target by cascades of collisions. The sputtered material forms a plume above the target at a certain angle and then deposits on the rotating substrate for a more homogeneous deposition (Figure 2.10).

Control by quartz crystal

In order to control the thickness of the deposited layers, a piezoelectric material is used. It deforms when subjected to an electric field and starts to vibrate when excited at a frequency close to its resonance frequency. This quartz microbalance is placed vertically close to the substrate. As the material is deposited on the quartz and the substrate at the same time, its oscillation frequency decreases. A formula makes it possible to make the link between the frequency of oscillation of the quartz and the quantity of deposited material in order to obtain the thickness Lu et Czanderna [1984].

$$\frac{M_f}{M_q} = \frac{\Delta F}{F_q} \tag{2.7}$$

Where M_f is the mass of the material deposited on the surface of the quartz, M_q is the mass of the uncoated quartz crystal, ΔF is the variation of the quartz resonance frequency with $\Delta F = F_q - F_c$, where F_q is the resonance frequency of quartz without deposit and Fc the resonance frequency of quartz with deposit.

This formula describes in a simple way the relation between the quantity of deposited material and the oscillation frequency read by the acquisition electronics.

Deposition parameters

There are many deposition parameters that can impact the thin film structure : source parameters such as ion kinetic energy and ion angle of incidence, sputtering rate, the intensity of the ion beam I_b which represents the number of projectiles sent by the source per unit of time and V_b the voltage of the beam which represents its energy (see Table 2.1). There is also the substrate temperature that can impact the deposition process.

The Figure 2.14 show an exemple of the substrate temperature during coating deposition of a tantala sample. Before beginning the deposition a pre-heating of about three hours is done first.

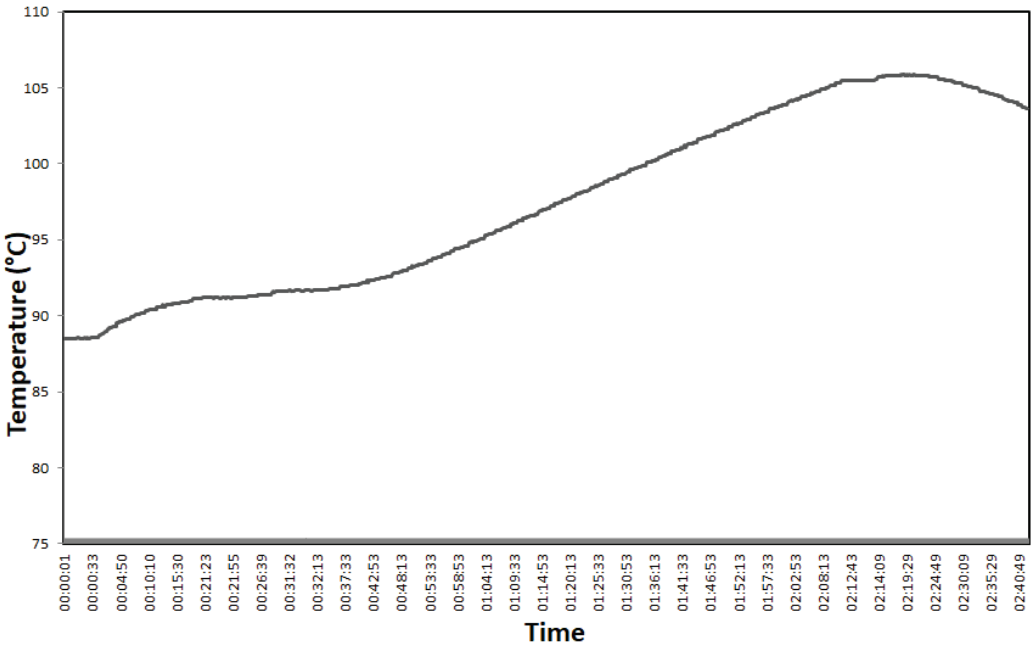

Figure 2.14: This curve represents a temperature measurement made by a probe that is far from the substrate. This is not a direct measurement of the temperature of the substrate, but in the hypothesis that we are in thermalised regime, is an indication of the substrate temperature.

Table 2.1: **Source parameters. Standard cubic centimeters per minute (SCCM) is a unit used to quantify the flow rate of a fluid.**

Material	Ib (mA)	Vb (V)	Vacc V (V)	Ie (mA)	θ (°)	Ar source sccm	N2 source sccm	Ar RFN sccm	O2 sccm
Ta_2O_5	200	1250	200	225	45	12 sccm	0 sccm	5 sccm	20 sccm

Some phenomena taking place during this deposition process can be at the origin of the creation of imperfections present in the thin layers. This is what we will study in the next chapter.

2.3.4 Optical characterization and properties of mirrors

After the deposition of thin films on the mirrors comes a large battery of tests to control the performance of the mirrors. LMA has at its disposal several metrology instruments for this purpose. This control step is crucial to determine if the final coated optic process is compliant with the specifications summarised in Table 2.2.

Table 2.2: Core optics requirements and specification about coating mirror on 35 cm diameter given for 1064 nm DEGALLAIX et collab. [2019] and based on coating characterization reports of LMA PINARD [2014].

Substrate	Absorption [ppm/cm]	Scattering [ppm]	Defect Density defect/mm²
Coating	< 2	< 50	< 1 per 4 mm²
Input Mirror IM	0.2	5.5	1.55
Endput Mirror EM	2.3	5.5	0.66

Here is a list of quantities that are measured at LMA, together with the experimental machines used to perform the measurement:

- Reflexion, Transmission and Scattering light with scatterometer bench called CASI. Possibility to use 633 nm and 1064 nm wavelength PINARD et collab. [2017]. it allows to measure ∅ 25.4 mm 350 mm and 550 mm optics. See more details in chapter 3.
- Absorption : Absorption bench PDS (Photothermal Deflection System) at 633 nm and 1064 nm. The sample is irradiated by a laser light and when the light is absorbed it heat the regions increasing the temperatures LORIETTE et BOCCARA [2003]. The instrument can gives absorption map on ∅ 400 mm.
- Flatness: Several interferometers (ZYGO, Phase Shift...) using wavelength shifting technique coupled with an 18 inch (1064 nm) beam expander, 450 mm pupil diameter and flatness below 0.5 nm RMS CIMMA et collab. [2006b].
- Roughness and Defect density : Optical profilometer MICROMAP (see more details in chapitre 3). It allows to measure roughness surface and to detect defects of Advanced Virgo and LIGO mirrors on ∅ 350 mm, 100 mm and 200 mm of width PINARD et collab. [2017]. The sensitivity of the Micromap is about 0.2 Å rms.

2.4 References

ACERNESE, F. et AL. 2014, «Advanced virgo: a second-generation interferometric gravitational wave detector», *Classical and Quantum Gravity*, vol. 32, 2, doi:10.1088/0264-9381/32/2/024001, p. 024 001. URL https://doi.org/10.1088/0264-9381/32/2/024001. 22

ACERNESE, F. et AL. 2018, *Status of the Advanced Virgo Gravitational Wave Detector*, p. 1–12, doi:10.1142/9789813231801_0001. URL https://www.worldscientific.com/doi/abs/10.1142/9789813231801_0001. 23

AMATO, A., S. TERRENI, V. DOLIQUE, D. FOREST, G. GEMME, M. GRANATA, L. MERENI, C. MICHEL, L. PINARD, B. SASSOLAS et collab.. 2019, «Optical properties of high-quality oxide coating materials used in gravitational-wave advanced detectors», *Journal of Physics: Materials*, vol. 2, 3, p. 035 004. 25

BENNETT, J. et L. MATTSSON. 1999, *Introduction to Surface Roughness and Scattering*, Optical Society of America, ISBN 9781557526090. URL https://books.google.fr/books?id=CnxjvwEACAAJ. 23

BORN, M. et E. WOLF. 1999, *Principles of Optics: Electromagnetic Theory of Propagation, Interference, and Diffraction of Light*, Cambridge University Press, London., ISBN 9781139644181. URL http://dx.doi.org/10.1017/CBO9781139644181. 26

BROOKS, A., G. VAJENTE, H. YAMAMOTO, R. ABBOTT, C. ADAMS, R. ADHIKARI, A. ANANYEVA, S. APPERT, K. ARAI, J. AREEDA, Y. ASALI, S. ASTON, C. AUSTIN, A. BAER, M. BALL et S. BALLMER. 2021, «Point absorbers in advanced ligo», *Applied Optics*, vol. 60, doi:10.1364/AO.419689. 21, 23

BUCHHOLTZ, B. 2000, «Physics of ion beam sources», . 29

CAPOTE, E. M., A. GLECKL, J. GUERRERO, M. REZAC, R. WRIGHT et J. R. SMITH. 2021, «In-vacuum measurements of optical scatter versus annealing temperature for amorphous ta2o5 and tio2:ta2o5 thin films», *J. Opt. Soc. Am. A*, vol. 38, 4, doi:10.1364/JOSAA.415665, p. 534–541. URL http://opg.optica.org/josaa/abstract.cfm?URI=josaa-38-4-534. 24

CIMMA, B., D. FOREST, P. GANAU, B. LAGRANGE, J.-M. MACKOWSKI, C. MICHEL, J.-L. MONTORIO, N. MORGADO, R. PIGNARD, L. PINARD et A. REMILLIEUX. 2006a, «Ion beam sputtering coatings on large substrates: toward an improvement of the mechanical and optical performances», *Applied optics*, vol. 45, p. 1436–1439. URL http://hal.in2p3.fr/in2p3-00025834. 26

CIMMA, B., D. FOREST, P. GANAU, B. LAGRANGE, J.-M. MACKOWSKI, C. MICHEL, J.-L. MONTORIO, N. MORGADO, R. PIGNARD, L. PINARD et A. REMILLIEUX. 2006b, «Ion beam sputtering coatings on large substrates: toward an improvement of the mechanical and optical performances», *Appl. Opt.*, vol. 45, 7, doi:10.1364/AO.45.001436, p. 1436–1439. URL http://opg.optica.org/ao/abstract.cfm?URI=ao-45-7-1436. 31

DEGALLAIX, J., C. MICHEL, B. SASSOLAS, A. ALLOCCA, G. CAGNOLI, L. BALZARINI, V. DOLIQUE, R. FLAMINIO, D. FOREST, M. GRANATA, B. LAGRANGE, N. STRANIERO, J. TEILLON et L. PINARD. 2019, «Large and extremely low loss: the unique challenges of gravitational wave mirrors», *J. Opt. Soc. Am. A*, vol. 36, 11, doi:10.1364/JOSAA.36.000C85, p. C85–C94. URL http://www.osapublishing.org/josaa/abstract.cfm?URI=josaa-36-11-C85. 25, 31

GORODETSKY, M. L. 2008, «Thermal noises and noise compensation in high-reflection multilayer coating», *Physics Letters A*, vol. 372, 46, doi:https://doi.org/10.1016/j.physleta.2008.09.056, p. 6813–6822, ISSN 0375-9601. URL https://www.sciencedirect.com/science/article/pii/S0375960108014692. 22

GRANATA, M., A. AMATO, G. CAGNOLI, M. COULON, J. DEGALLAIX, D. FOREST, L. MERENI, C. MICHEL, L. PINARD, B. SASSOLAS et J. TEILLON. 2019, «Progress in the measurement and reduction of thermal noise in optical coatings for gravitational-wave detectors», dans *Optical Interference Coatings Conference (OIC) 2019*, Optical Society of America, p. FA.1, doi:10.1364/OIC.2019.FA.1. URL http://www.osapublishing.org/abstract.cfm?URI=OIC-2019-FA.1. 21

HUGHES, S. A. et K. S. THORNE. 1998, «Seismic gravity-gradient noise in interferometric gravitational-wave detectors», *Phys. Rev. D*, vol. 58, doi:10.1103/PhysRevD.58.122002, p. 122 002. URL https://link.aps.org/doi/10.1103/PhysRevD.58.122002. 22

LORENZINI. 2010, «The monolithic suspension for the virgo interferometer», *Classical and Quantum Gravity*, vol. 27, 8, doi:10.1088/0264-9381/27/8/084021, p. 084 021. URL https://doi.org/10.1088/0264-9381/27/8/084021. 22

LORIETTE, V. et C. BOCCARA. 2003, «Absorption of low-loss optical materials measured at 1064 nm by a position-modulated collinear photothermal detection technique», *Appl. Opt.*, vol. 42, 4, doi:10.1364/AO.42.000649, p. 649–656. URL http://opg.optica.org/ao/abstract.cfm?URI=ao-42-4-649. 31

LU, C. et A. CZANDERNA. 1984, *Applications of Piezoelectric Quartz Crystal Microbalances, Volume 7*, ELSEVIER, ISBN 9780444596482. URL https://www.elsevier.com/books/applications-of-piezoelectric-quartz-crystal-microbalances/lu/978-0-444-42277-4. 30

PINARD, L. 2014, «Advanced virgo input mirror characterization report- im04 (coatings c14081+c14087)», VIR-0544A-14 Virgo. 31

PINARD, L., C. MICHEL, B. SASSOLAS, L. BALZARINI, J. DEGALLAIX, V. DOLIQUE, R. FLAMINIO, D. FOREST, M. GRANATA, B. LAGRANGE, N. STRANIERO, J. TEILLON et G. CAGNOLI. 2017, «Mirrors used in the ligo interferometers for first detection of gravitational waves», *Appl. Opt.*, vol. 56, 4, doi:10.1364/AO.56.000C11, p. C11–C15. URL http://www.osapublishing.org/ao/abstract.cfm?URI=ao-56-4-C11. 25, 31

STOVER, J. C. 2012, *Optical Scattering: Measurement and Analysis, Third Editions*, CRC press, doi:10.1117/3.975276. 23

STRANIERO, N., J. DEGALLAIX, R. FLAMINIO, L. PINARD et G. CAGNOLI. 2015, «Realistic loss estimation due to the mirror surfaces in a 10 meters-long high finesse fabry-perot filter-cavity», *Opt. Express*, vol. 23, 16, doi:10.1364/OE.23.021455, p. 21 455–21 476. URL http://www.osapublishing.org/oe/abstract.cfm?URI=oe-23-16-21455. 21

VANDER-HYDE, D., C. AMRA, M. LEQUIME, F. MAGAÑA-SANDOVAL, J. R. SMITH et M. ZERRAD. 2015, «Optical scatter of quantum noise filter cavity optics», *Classical and Quantum Gravity*, vol. 32, 13, doi:10.1088/0264-9381/32/13/135019, p. 135 019. URL https://doi.org/10.1088/0264-9381/32/13/135019. 24

YAMAMOTO, H. 2015, «Mirror profile and intracavity field profile», G1500262-v3 LIGO/Caltech. 21

Chapter 3

Material and methods for the defect study

Contents

3.1 Introduction

In this chapter, the principle of the instruments used for the defect study are explained in details. For the characterization of point defects, two different instruments are used. The detection of defects is done with profilometers (coupled with modern image processing to determine their number, shape, and size) and the scattering measurements with a scatterometer. The instruments are installed in an ISO 3 clean room of the laboratory in order to minimize sample contamination by particles present in the air and take advantage of the active seismic isolation. ISO 3 means that there are at most 1000 particles ≥ 0.1 µm in a cube of 1 m^3 (see Table 3.1). The clean room environment prevents dust particles from contaminating the surface, these would create additional scattered light and possibly be mistaken for defects.

Class	Maximum Particles/m³						FED STD 209E equivalent
	≥0.1 um	≥0.2 um	≥0.3 um	≥0.5 um	≥1 um	≥5 um	
ISO 1	10	2					
ISO 2	100	24	10	4			
ISO 3	1,000	237	102	35	8		Class 1
ISO 4	10,000	2,370	1,020	352	83		Class 10
ISO 5	100,000	23,700	10,200	3,520	832	29	Class 100

Figure 3.1: ISO Cleanroom Standards and classifications.

3.2 Optical profilometer : Micromap

The Micromap is an optical profilometer built in 1999 in order to study the surface roughness of the mirrors. This commercial instrument has been modified at the request of the laboratory by adding a defect detection feature.

3.2.1 General description of the instrument

The Micromap optical profilometer, see Figure 3.2a, is a Nikon interferometric microscope. It is composed of a focusing column (150 mmn of useful travel) on which is mounted the Nikon modular support (25 mm of focusing travel) which contains an illumination module equipped with a 50 W tungsten-halogen source and a 2/3" CCD camera, with a resolution of 640 x 480 pixels, selected for its performance in linearity and signal to noise ratio. A multi-lens turret is mounted on an electric piezo wedge for phase shift, can be equipped with up to 4 objectives. An adjustment plate in X and Y and tilt allows the positioning and optimization of the number of interference fringes. The whole instrument is mounted on an active damped table to be isolated from vibrations.

3.2.2 Principle of the instrument

The most important step to do before performing a defect scan is the focus mapping. This procedure allows the creation of a focus plane based on the focus on a certain number of points (depending on the the surface diameter to be scanned). This step is crucial because it will allow the instrument to see the defects and to detect them in the plane. After this step, the instrument is able to measure defects, with size within 1 and 15 microns, and provide a defect map of the sample with the defects number, type and location on the sample. Defects maps are done by assembling fields of 400x400 pixels. Detection is based on 256 gray levels, a detection threshold can be set in order to be able to overcome background noise and stray light. The Micromap illuminates in the dark field (the angle of the exit cone is 45° and therefore the darkfield lighting follows this angle, see Figure 3.3) with light in green over 560 nm ± 50 nm wavelength range and then detects the light scattered

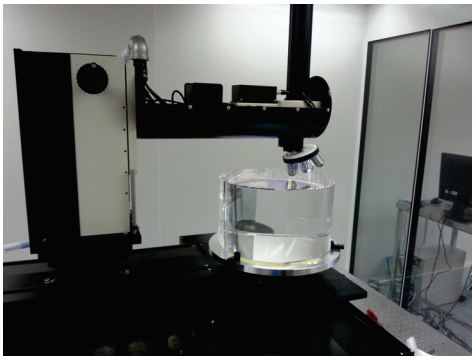

(a) Profilometer in the cleanroom of LMA

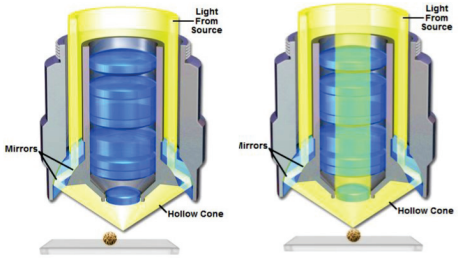

(b) Dark filed lens schematic

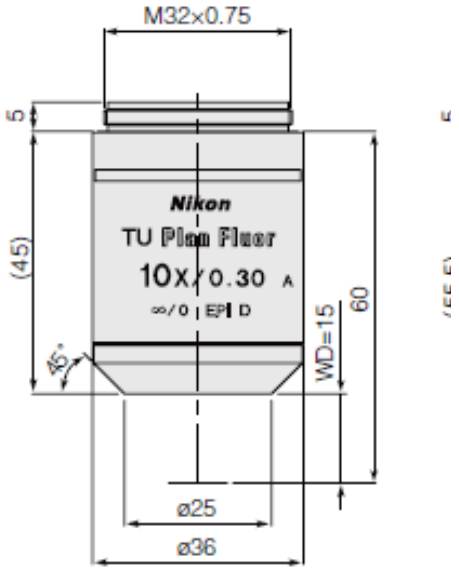

CFI TU Plan Fluor
BD 10×

(c) Lens schematic

Figure 3.2: In (a) Picture of the profilometer in the cleanroom of LMA credit LMA/CNRS, (b) the dark field objective schematic credit Olympus and (c) the dark field lens schematic.

Table 3.1: **System specifications for the camera.**

Name	CCD
Model	Hitachi
Sensor	CCD
Sensor type	2/3"
Resolution	640 (H) x 480 (V)
Pixel size	13.0 µm x 13.0 µm
Image buffer (MB)	?
ADC (Bit)	8
FPS full res	?
Quantum at 550 nm (%)	?
Temporal dark noise (e^-)	?
Saturation capacity (e^-)	?
Dynamic range (dB)	?
Absolute sensitivity threshold (e^-)	?
size (mm) (including connectors)	?
Mass (g)	?
Binning	yes

by the imperfections of the sample and collected by the objective (see Figure 3.2b). The pixel size is about 1.28 µm.

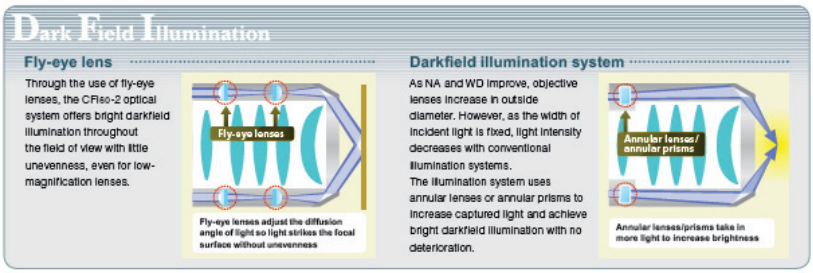

Figure 3.3: Exemple of the dark field principle.

The Micromap does not measure the size of each defect but only categorize them in three classes. In the defects map in Figure 3.4, each color pixel has a distinct meaning :

- Black : no measurement in the fields was taken (the edge of a circle).
- White : no defect was detected so the image was not saved.
- Blue : in this pixel, one or more defects with size larger than 5-6 microns (also called "areas") were detected. It should be noted that, on average, the largest defects observed did not exceed 15 microns.
- Red : in this pixel, defects with size smaller than 5 microns ("point defects") were detected. The image is more populated by point defects than any other kind of defects.
- Green : in this this pixel, one of more scratch-type defects or deformed defects that have a more longitudinal shape were detected.

In this thesis we are only interested by the point defects.

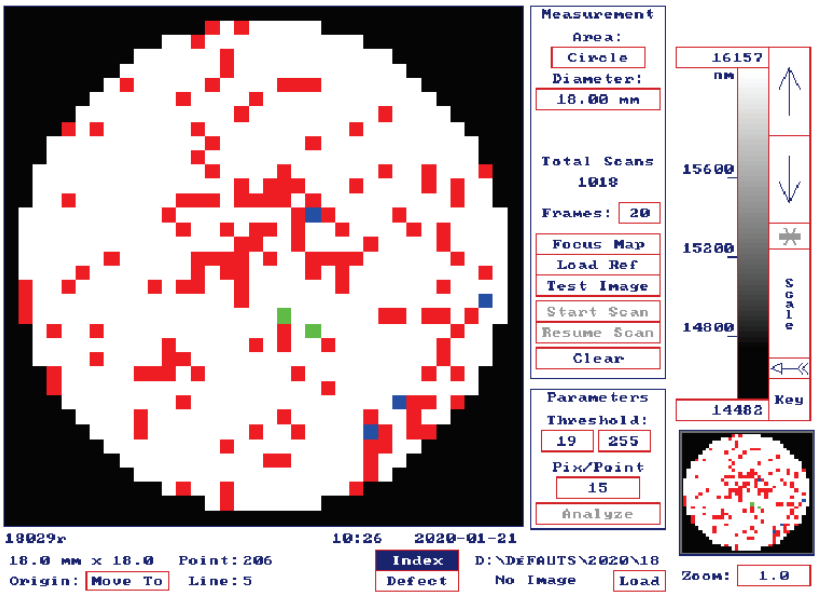

Figure 3.4: Exemple of defect map given by the instrument.

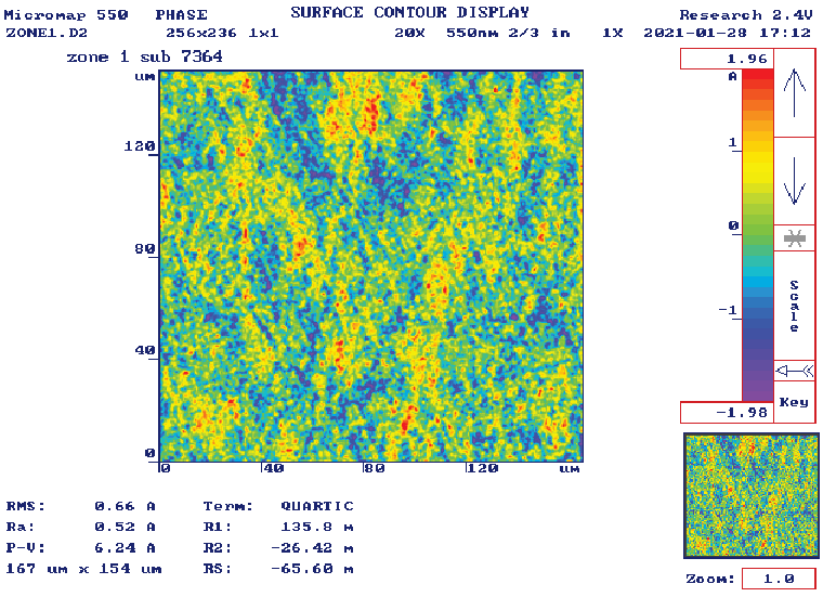

Figure 3.5: Exemple of roughness measurement

3.2.3 Measurement method

For defect measurements, the scan does not cover the entire surface of the sample. At the LMA, the bare substrates are mounted on aluminum holders to hold them in the coating machine during deposition (see figure 3.6). It has been shown that such sample holder pollutes the surface.

Indeed, as shown in figure 3.7, there is a strong pollution near the edge related to the mounts after the coating deposition. To overcome this problem, the defect mapping does not scan the entire surface of the coating but a smaller diameter sufficient to avoid this effect. Thus in the case of this study the measurements are limited to an area of ∅ 18 mm diameter centred on the 1 inch sample (∅ 25.4 mm).

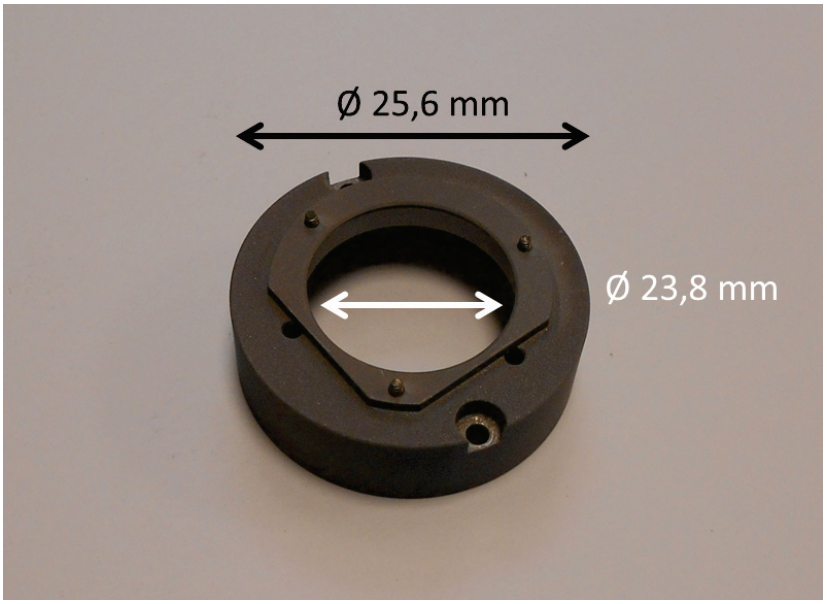

Figure 3.6: Photo of one inch mount used to make the coating depositions.

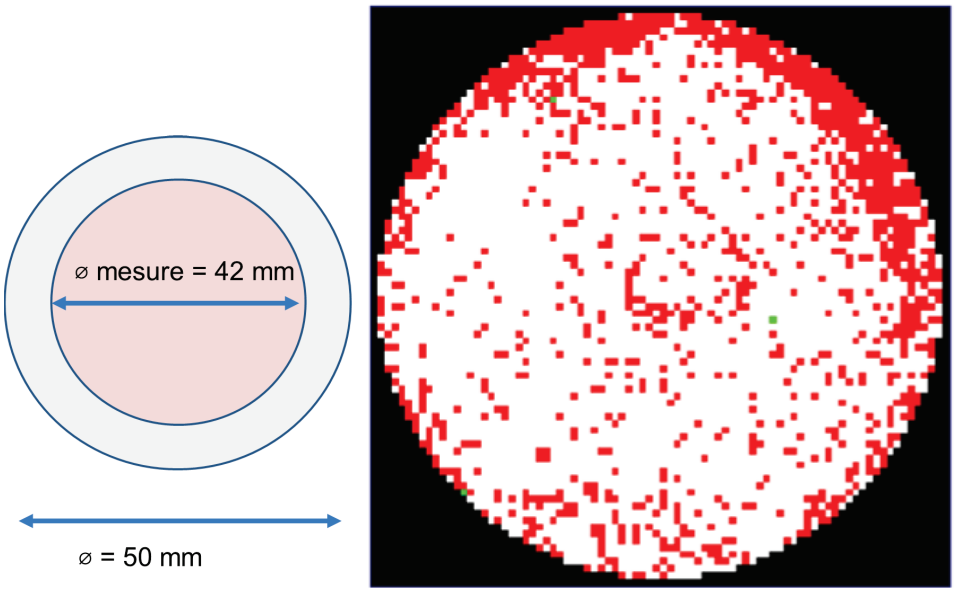

(a) (b)

Figure 3.7: In (a) a schematic of diameter scan of a sample. In (b) an example of contamination due to edge effects. For a sample of ∅ 50 mm the mapping of defects made on ∅ 42 mm clearly shows the defects present in edge.

It is worth mentioning that this effect is also observed on larger samples such as the Ad-

vanced Virgo Input Mirror (∅ 50 mm). The figure 3.8 shows a measurement area at the edge of an Advanced Virgo Input Mirror. It clearly shows the impact of the mount and the distinction between the "clean" area which is far from the edge and the "polluted" area (see more detail in section 4.3.7).

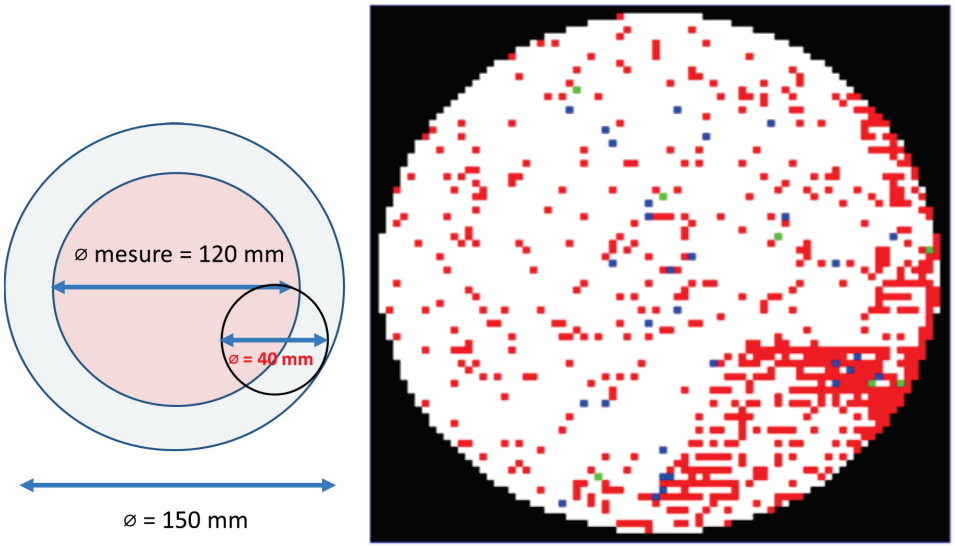

(a) (b)

Figure 3.8: The measurement is a ∅ 40 mm defect map made on the edge of a ∅ 150 mm mirror. In (a) a schematic of diameter scan of the miror. Typically the defect map is done on ∅ 120 mm but for the illustration the measurement was done between 120 and 150 mm. In (b) an example of contamination due to edge effects.

3.2.4 Characterization of the instrument

Micromap measurements are very sensitive to the environment. It is necessary to work in a cleanroom in order to minimize the pollution of the samples and to ensure isolation from mechanical noise. Indeed the focus of the system is very sensitive to vibrations due to the various manipulations or activities which also take place in the cleanroom. In this section the most critical parameters will be described.

Threshold

The Micromap built-in processing software considers a pixel or a group of pixels as a defect if the intensity is above a threshold called $threshold_{\mu map}$ value. The setting of this $threshold_{\mu map}$ is defined by the user and is highly critical : false defects will be detected if the value is too low and defects will be missed is the value is too high. Figure 3.9 shows the number of detected defects, for a sample measured with different threshold values. We usually set the $threshold_{\mu map}$ value at 20, three units higher than the background signal of the image. The figure shows that when changing the threshold value between 19, 20 and 21, the defects couting can vary by 30 to 40%.

The threshold needs to be tuned for a kind of sample : silica/tantala monolayer or multilayers.

In Table 3.2, we present the adjustment of Micromap. For the four samples of each materials we have the same level of background signal. SAYAH et collab. [2021].

For the study, it was decided to choose the same $threshold_{\mu map}$ for Ta_2O_5 and SiO_2. We notice that there is no influence of the layer thickness on the contrast level. The average background noise level is the same for the four thicknesses of the same material. The only significant difference is about the light level for the focus map: it is lower for the Ta_2O_5 because it reflects more than SiO_2.

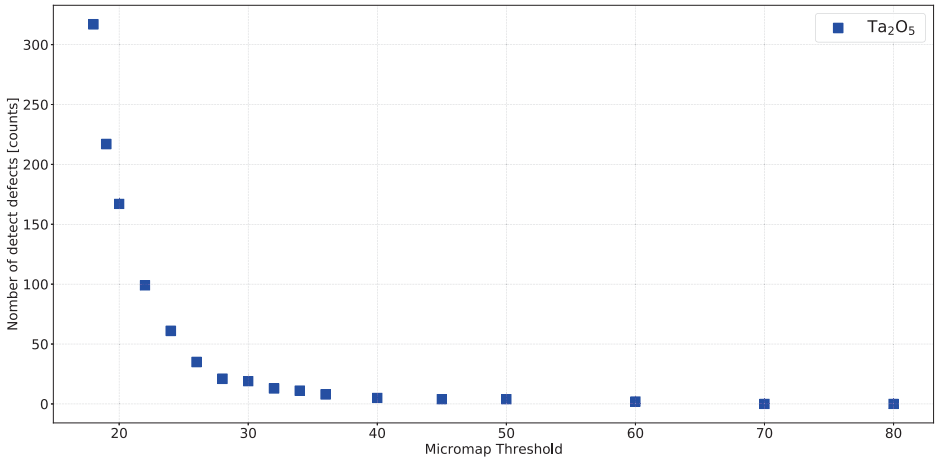

Figure 3.9: Figure of number of defects detected in function of Micromap Threshold measured with the thinnest sample of Ta_2O_5.

Table 3.2: **Contrast setting of the two materials according to the different thicknesses.**

Material	Thickness (nm)	Threshold$_{\mu map}$ (grey level)	Background signal level
SiO_2	523	19	16.2
	1005	19	16.1
	1550	19	16.2
	2053	19	16.3
Ta_2O_5	543	19	16.4
	1083	19	16.5
	1626	19	16.6
	2167	19	16.6

Repeatability and reproductibility

The repeatability of the measurement has been studied to assess the uncertainties and to better understand the instrument. The successive measurements of repeatability presented in table 3.3 have been done without dismounting the sample from the instrument. For a series of 10 measurements, the sample was washed only once before the test. Whereas the reproducibility of the measurement is based on the comparison measurements made at different times with the sample dismounted and remounted from the sample holder. For each measurement, the sample was disassembled, cleaned and a new focus card was done. The results of reproducibility measurements are presented in table 3.4. A high repeatability and reproductibility is mandatory to have a high precision measurement.

Table 3.3: **Repeatability of measurement of the number of detected defects with the Micromap to verify the stability of the measurement. A series of 10 reapetability measurements was done per sample of Ta_2O_5 and SiO_2. The median and standard deviation of the number of detected defects are shown.**

Sample	1	2	3	4	5	6	7	8	9	10	Median	Standard deviation
18036	112	49	62	54	55	59	75	66	99	53	60.5	21.1
18030	127	109	93	115	93	97	105	76	91	95	96	14.3
18032	147	139	147	150	145	139	137	142	147	139	143.5	4.5
18031	172	168	185	172	170	180	190	163	163	178	172	9
18028	50	59	60	59	101	60	81	107	93	99	70.5	21.6
18026	86	85	106	95	110	64	93	77	102	82	89.5	14.1
18029	187	187	161	180	187	207	170	184	186	183	185	12
18027	2159	2132	2036	1877	1781	1914	1800	1989	1805	1927	1921	135.1

Table 3.4: **Reproductibility of measurement of the number of detected defects with the Micromap to verify the stability of the measurement. Series of 10 measurements were done on one tantala sample D20077 PL7468. The median and standard deviation of the number of detected defects are shown.**

Sample	1	2	3	4	5	6	7	8	9	10	median	Standar deviation
D20077 PL7468	4	9	13	10	6	12	12	15	8	5	9.5	3.5

Activity in cleanroom

As a consequence of the observations made on the repeatability and reproducibility measurements, several tests have been done on the impact of attendance in the cleanroom on the measurements Figure 3.10. The test was performed on the thinnest sample of tantalum monolayer (D20077 PL7468), containing few defects. In this case the detection is fast and the measurements could be repeated several times in a working day.

We define four activity levels in the cleanroom as follows :

- **Null :** There was no one in the cleanroom.
- **Low :** Very low attendance with only 2 people working far from the Micromap or working quietly.
- **Medium :** There were 2 people present close to the Micromap.
- **High :** 4 people working loudly and close to the Micromap.

We observed that the attendance in the cleanroom and noise around the instrument has a clear impact on the detection defects. Statistically between the Low and High activity levels, the median of the detected defect decreases by 16% whereas the standard deviation increases by a factor 4. The activity in the vicinity Micromap impacts strongly both the precision and accuracy of the detection. It is important to notice that the aim of our study is to precisely quantify the defect density and to lose even 10% of accuracy on a sample is a great loss for the study. These tests have also shown that during the acquisition of the focus map, the disturbances around the Micromap are much more critical than during the detection step. Indeed, an error on a measurement of the focus map will induce a defocus and then damages the image quality. The defects will not be resolved and obviously not detected. While a focus map made in optimal conditions without disturbances will be better.

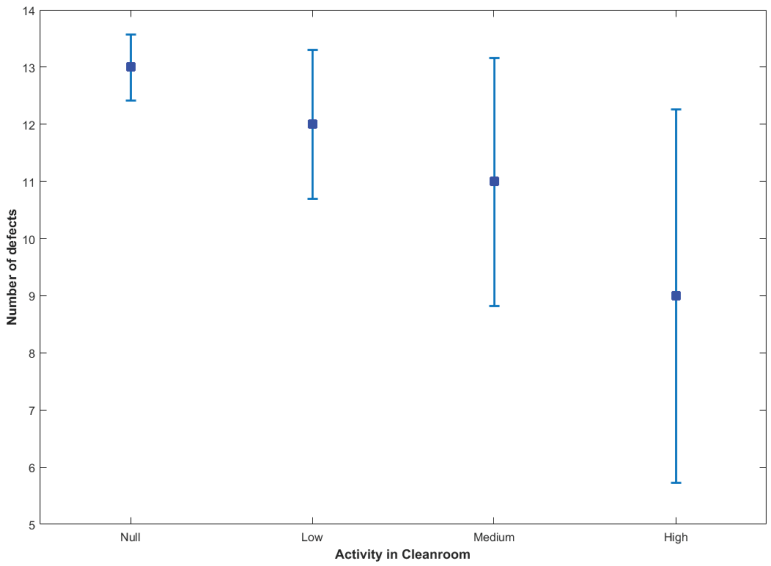

Figure 3.10: The effects of attendance in the cleanroom on detection defects measurements. The blue points are the medians of several series of measurements carried out in four conditions: null, low, medium and high affluence around the Micromap.

3.3 EOTECH profilometer

In order to be able to measure larger surfaces such as the future Advanced Virgo and Advanced LIGO mirrors with ∅ 550 cm, a new profilometer was needed. Moreover, the aging Micromap was reaching its limits in terms of quality of the camera, the wear of the motorized tables, and mainly the obsolescence of the control software (e.g. incompatibility of the drivers with recent computers). So it was necessary to develop a new instrument by adding new options to be much more efficient. The company EOTECH COMPANY was in charge of developing the instrument.

3.3.1 General description of the instrument and characteristics of the components

The figure 3.11 is a picture of the new instrument installed in the clean room. The system consists of different elements :

- Motorized X and Y moving tables : The tables chosen for this project are of the same brand as the ones that were supplied with the Micromap system at the time. This choice is justified by some important criteria: The normal load (1,470 kg normal load and 200 kg axial load), the precision, and the life of the mechanism.

- A support plate for the samples
- A displacement column Z with a carriage mounted on a rail
- Motorized cylinder for Z adjustment
- Measuring head type Optosurf including : a CCD camera Figure 3.12, Nikon illuminator light and dark background, LED source, 100 µm PZT motor, 5 position motorized turret, interferometric objectives DI 10X, 20X and 50x and a dark field objective 10X

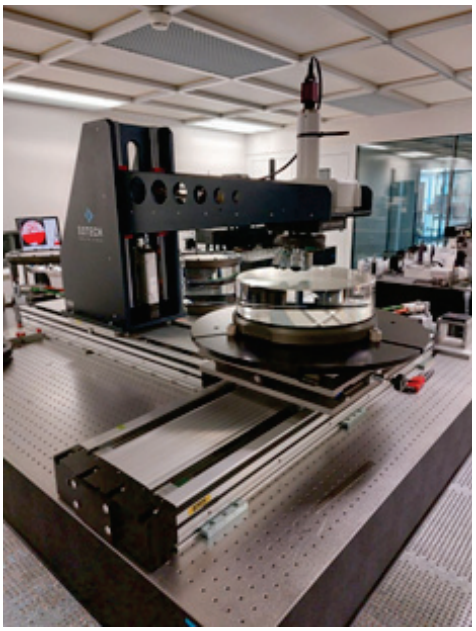

Figure 3.11: Profilometer EOTECH installed in the cleanroom at LMA.

Table 3.5: **Characteristics of the 10X Dark Field MUE 42100 (TU Plan fluor BD).**

Grossisement	10X DF
Measuring surface	760 x 760 µm
Working Distance	15 mm
Focal length	20 mm
Physical depth of focus	3.06 µm
Numerical aperture	0.30

Camera

CMOS sensors have made huge progress in recent years and offer superior performance to CCDs. The choice fell on the G507, a Mako version and which offers an exceptionally low noise level (Table 3.6).

3.3.2 Principle

The principle of the defect detection is the same of the old Micromap and a focus map is also needed. The detection is based on the diffraction of light produced in a dark field (grazing light) by a particle or a defect. The detection of defects with the Eotech profilometer is done in 2 steps called "detection" and "classification". These 2 steps are completely decorrelated from each other. The detection step provides images of the surface. The software allows to save a ".PNG" image

Figure 3.12: Camera mako G-507.

Table 3.6: **Caractéristiques de la caméra**

Name	Mako
Model	G-507
Sensor	Sony IMX264
Sensor type	CMOS
Resolution	2464 (H) x 2056 (V)
Pixel size	3.45 µm x 3.45 µm
Image buffer (MB)	64
ADC (Bit)	12
FPS full res	23.7
Quantum at 550 nm (%)	65
Temporal dark noise (e^-)	2.7 µm
Saturation capacity (e^-)	10600
Dynamic range (dB)	72.0
Absolute sensitivity threshold (e^-)	2.7
size (mm) (including connectors)	60.5 × 29.2 × 29.2
Mass (g)	80 (with C-Mount)
Binning	yes
RoI/AoI	yes

without compression of each measurement field without losing the pixel values of the sensor even if no defects were detected. The image is binarized with a threshold calculated as the quantile at 30% of the image pixel gray values to which we add an additional offset called "Threshold Shift". After detection, we obtain a map (see (a) in Figure 3.13) with colored pixels :

- In Green : the sum of the detected pixels (on the surface) does not exceed the threshold.
- In Red: the sum of detected pixels (on the surface) has reached the threshold.

The classification step is the analysis of the recorded images. The raw image is transformed into a "surface", i.e. the intensity becomes a height of value between 0 and 255, ignoring all values below the "Threshold". The classification of a measure is done by selecting the elements present on the resulting surface.

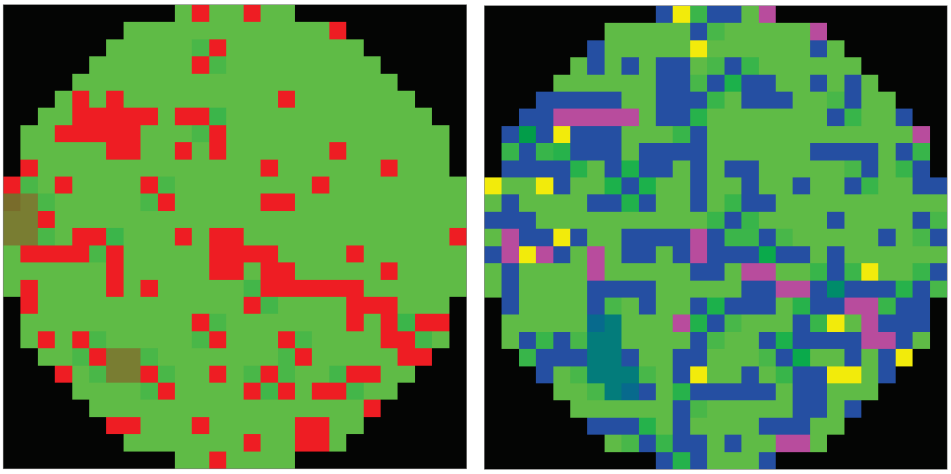

(a) Detection Step (b) Classification Step

Figure 3.13: Two defect maps obtain with Eotech profilometer with in (a) defect map obtained after the detection step and in (b) the second defect map obtained after the classification step.

After scanning the total area, the software analyzes the binarized images and classifies the detected defects into 3 different categories "small", "medium" and "big". The sizes of the different classes were determined based on the sizes of the old Micromap converted into surface : the minimum surface is 20 μm^2 and the maximum surface is 100 μm^2. The classification of a measurement is done by selecting the elements present in the surface :

- Small : a defect is considered "Small" if its area is between the area of a pixel and the "Minimum surface" of 20 μm^2.
- Medium : a defect is considered "Medium" if its surface is between the "Minimum Surface" 20 μm^2 and the "Maximum Surface" 100 μm^2.
- Big : A defect is considered as "Large" if its surface is included between the "Maximum surface" and the surface of the measurement 100 μm^2.

The status of the measurement is defined by the worst class detected. (If both "Small" and "Medium" defects are detected in the measurement then the measurement will be considered as "Medium"). See defect map (b) of Figure 3.13.

- Green : No defect in the measurement has been classified (either the defects are smaller than the minimum area or all the defects have an intensity lower than the " Threshold " or there is no defect).
- Blue : The biggest defect detected in the measurement is of class " Small ".

- Yellow: The largest defect detected in the measurement is of class " Medium " (it may or may not contain a defect of class " Small ").
- Magenta: The largest defect detected in the measurement is of class "Large" (it may or may not contain a defect of class "Small" and/or "Medium")

For this study, all measurements were done with camera 8 bits and binning x2 (Figure 3.14). It corresponds to 256 grey levels, a resolution of 1024 x 1024 pixels with a field of 700 µm x 700 µm and a pixel size of 0.7 µm after binning.

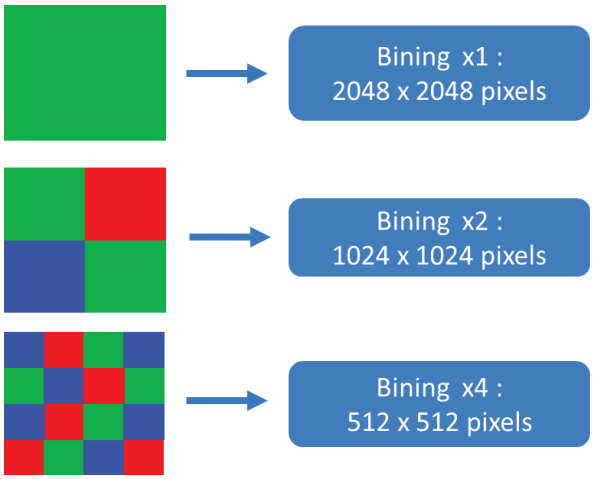

Figure 3.14: Pixel Binning proposed by the software.

3.3.3 Brief characterization of the instrument

A brief characterization took place to estimate the ideal threshold setting. Figure 3.15 shows the number of defects detected as a function of the threshold values. The figure obtained is similar to the Figure 3.9 obtained with the old Micromap. The number of detected defects decreases when the threshold is increasing. However, we observe a saturation in the detection of excess defects for threshold values below 23. For threshold values above 220, the detection tends to 6 defects which are certainly due to the noise of the camera. In view of the tests carried out the optimal threshold is 23.

To estimate the errors of Eotech profilometer instrument, repeatability tests were performed on a blank substrate without coating 3.16. If we compare the two defect map made with a rotation of 180°, we see that the fields containing defects are consistent. Then large tests were done with D20077R PL7468 sample, tantala monolayer sample. This is the same sample used for repeatability on the old Micromap (see section 3.2.4). Two series of repeatability and reproducibility measurements were performed on the instrument. Between the 2 series of repeatability we have a difference. On average we obtain for the first serie 162 defects detected with a standard deviation of 6 and for the second serie 159 defects with a standard deviation of 6. On a series of 10 measurements, the average value obtained is a variation from 167 to 153. That is to say 14 difference defects for the reproducibility and 6 difference defects for the repeatability. We have mainly differences observed on the scratches detection. The counting is different because of the new orientation of the sample but the two value are closed.

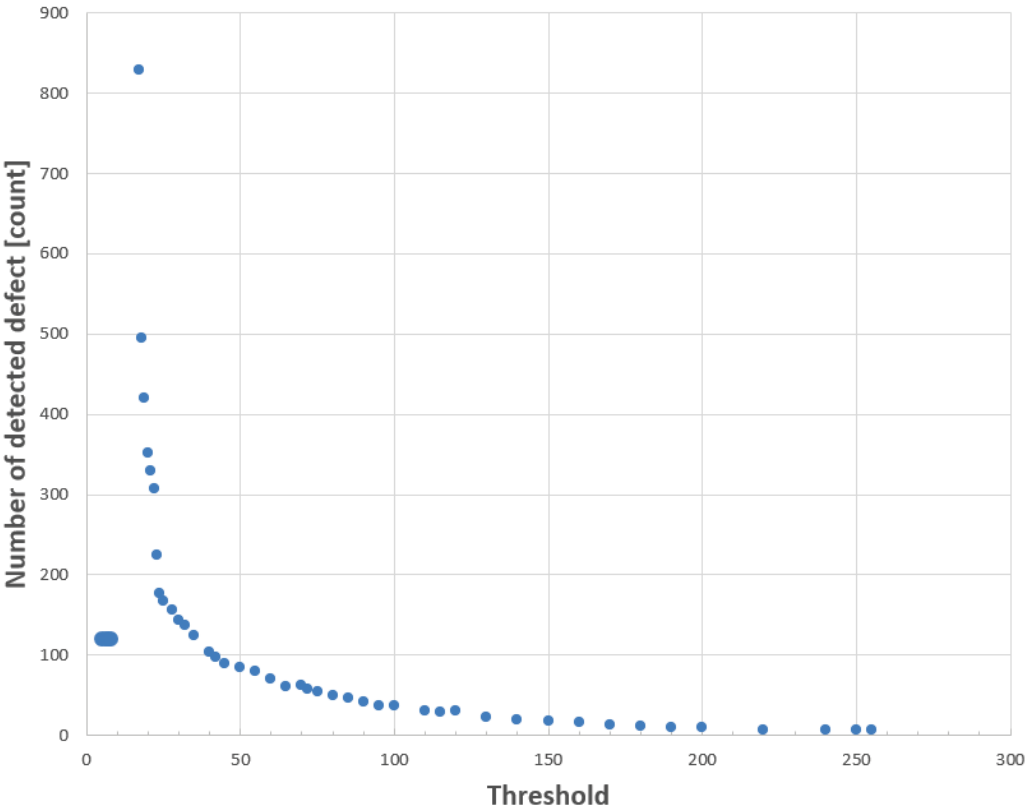

Figure 3.15: Number of detected defects as a function of the threshold.

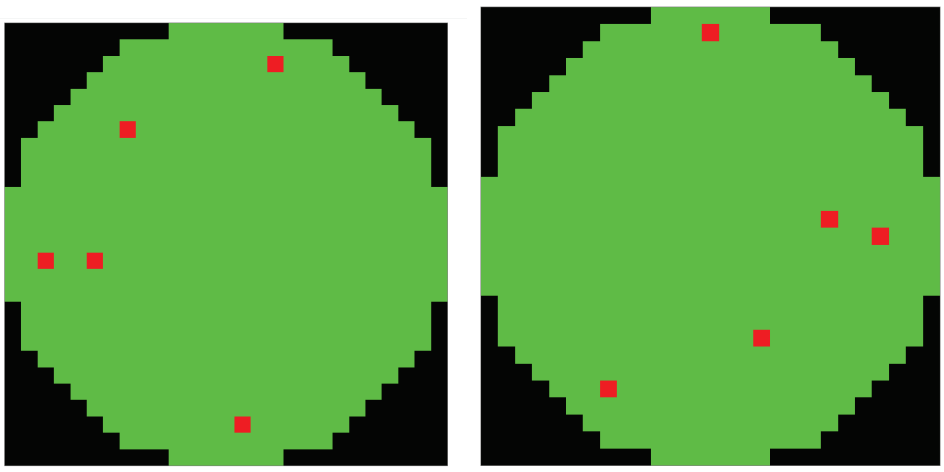

(a) (b)

Figure 3.16: Defect map of one sample measured twice. In (b) the sample is rotated 180∘.

3.4 Performances and Image processing

The built-in Micromap software does not provide the size of each defect, other than the information that it is within 1 and 5 micrometers. Moreover, it has been shown that the counting of the instrument is influenced by the cleanroom environment and the threshold value set. Thus to remedy this problem, it was decided in a first approach to post process the output images of the Micromap with a home-made image processing code.

3.4.1 Micromap algorithm

Scanning the surface sample over ∅ 18 mm diameter with the Micromap corresponds to 1018 measurement over single fields of 513 x 513 µm. The figure 3.17 is an example of a randomly chosen measurement field to illustrate. This measurement field corresponds to 400 x 400 pixels with a pixel size of 1.2825 µm.

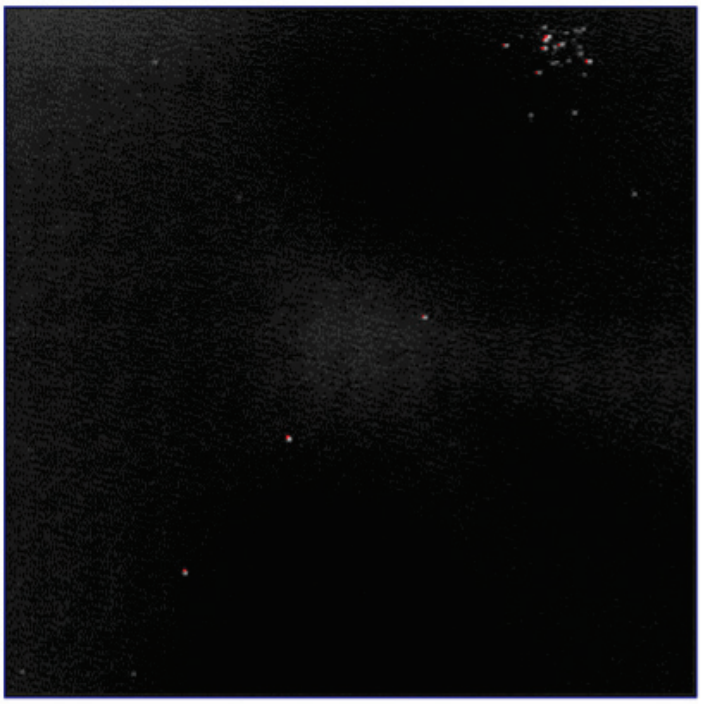

Figure 3.17: Exemple of an screenshot image given by the Micromap showing a 513 µm x 513 µm image field. The point defects are in white and only the defects marked in red were detected by the Micromap.

After several measurements, and inspecting the images by eye, it was noticed that the counting of the instrument algorithm is not necessarily correct. The bias on defect detection by the instrument has been estimated to be of the order of 20% to 30% of losses depending mainly on the choice of the $threshold_{\mu map}$ value. On the top of the figure 3.17 there are many defects marked in red that are detected and others that are not. In addition to the uncertainty of the counting by the instrument, obtaining information on the individual size of the defects has become a necessity for this study. The Micromap software saves only the field images in which at least one defect has been detected, so it is not possible to work on all the 1018 fields but only a part of them. The image has 480 x 640 pixels, and three color channels for each pixel. The color channels are coded between 0 and 65535 (more details in section 3.3.2. We first normalize the color levels.

3.4.2 Blob log algorithm

Defect detection

A first solution, called *"Blob log"*, has been developed in collaboration with Colin Bernet from IP2I. The goal was to improve the counting accuracy of the point-defects and determine their radius (by assuming a circular shape). The software is a Python code using the Laplacian of the Gaussian algorithm (LoG), as implemented in scikit-image library VAN DER WALT et collab. [2014] which allows after image processing to circle all the defects present on the image field. The LoG algorithm is based on a convolution of the image with 2D Gaussian functions with variable widths σ to give a scale space representation.

$$\mathrm{LoG}(x,y) = -\frac{1}{\pi\sigma^4}\left[1-\frac{x^2+y^2}{2\sigma^2}\right]e^{-\frac{x^2+y^2}{2\sigma^2}} \tag{3.1}$$

The process is repeated with Gaussians of different widths, in order to determine the radius of the detected defects by selecting for each one the most adequate Gaussian to maximize the Laplacian - the idea being, for a large defect, to prefer a large Gaussian covering the whole defect to a fine Gaussian centered on its brightest point. The main parameters of the detection are therefore the range of Gaussian widths used, whose bounds we will call σ_{max} and σ_{min}, as well as the number of widths considered, and the amplitude threshold $\mathrm{threshold}_{blob}$ below which no defect will be taken into account.

Image processing

We remind that the tiff images provided by the Micromap are defined in RGB colors, then converted to grayscale. After conversion, the image has only 1 color channel per pixel (although the images are diplayed with a given colormap). The formula used for the conversion of the red (R), green (G) and blue (B) pixels values SCIKIT is :

$$\mathrm{Y} = 0.2125\mathrm{R} + 0.7154\mathrm{G} + 0.0721\mathrm{B} \tag{3.2}$$

Before undergoing the defect detection step, the grayscale images are preprocessed with a high-pass filter LEGRAND [2020] to remove some background patterns as shown in the figure 3.18. The method uses a discrete Fourier transform of the raster image. It allows to isolate the patterns dominated by a certain range of frequencies. These patterns - stray light reflections - are due to the light of the Micromap and are visible on most of the images. The low frequency features are removed quite efficiently and the background looks much more uniform. After this step, the defect detection start on filtered image.

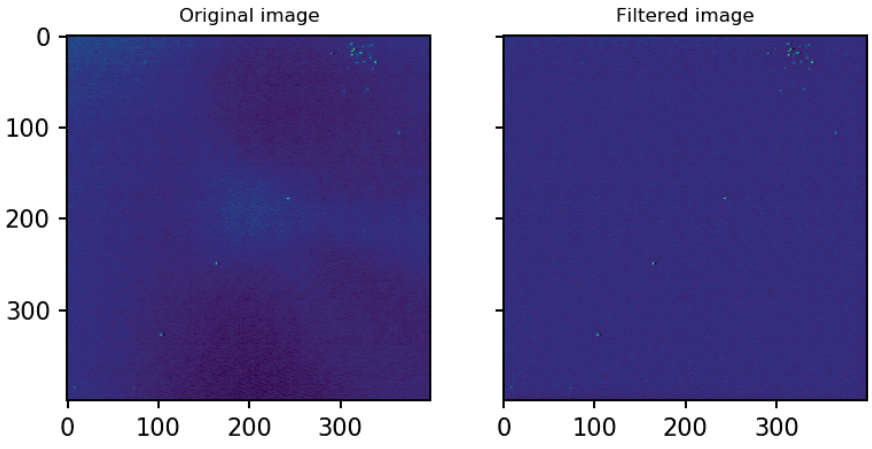

Figure 3.18: A Micromap image field represents 513 µm x 513 µm. On the left the original image convert to grayscale according to the relation given above and on the right the filtered image.

For a defect detection, there is an important parameter $threshold_{blob}$ to set. If the parameter $threshold_{blob}$ is too low, any irregularity on the image background is likely to be considered as a defect despite its low intensity on the image after convolution.

Since the Micromap images are highly noisy, this can lead the program to detect a drastic number of excess defects called "ghost defect".

With a similar behaviour as depicted in section 3.2.4, an example effect of choosing an inappropriate threshold value (either too low or too high) is presented in Figure 3.19.

The σ_{min} and σ_{max} parameters also have to be constrained with care. If the parameter σ_{min} is too low, the algorithm will use very fine Gaussian distributions, for which the influence of the points around their center will be very weak during the convolution, and will therefore make the difference between a bright point in a bright area and a bright point in a dark area. In addition, the Gaussian is created with amplitude inversely proportional to its radius - so that the order of magnitude of the convolution product always remains the same - which can also lead to divergences when the radius is too small. Finally, if the parameter σ_{max} is too high, the very large Gaussians are likely to consider a bright region of the image background as an excess defect.

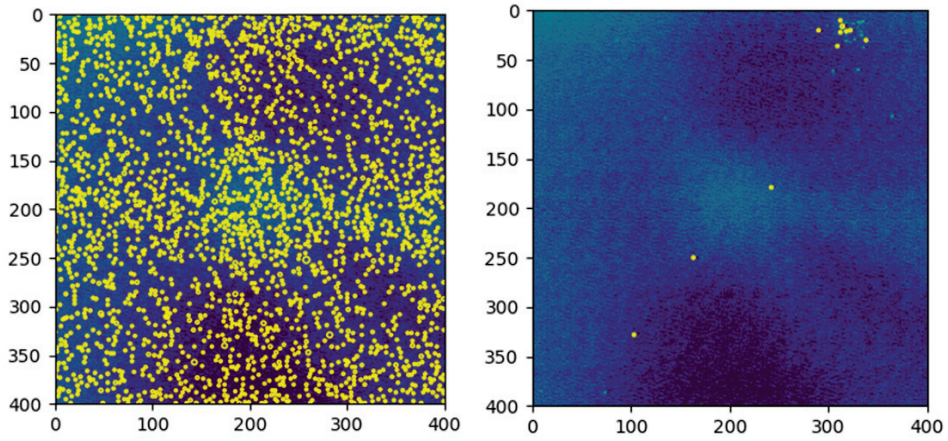

Figure 3.19: Two examples of poor defect detection. (a) has a detection threshold that is too low, the algorithm detects defects at every point in the field (b) has a detection threshold that is too high, resulting in low or excess defect detection in some cases.

Automation of the detection

The threshold to be used for defect detection has been optimised. Figure 3.20 shows that the detection rate is very high for low threshold values, before reaching a plateau and presenting the same number of detections for a wide range of thresholds. A subsequent comparison with the results obtained by the naked eye indicates that this plateau generally corresponds to the correct value. The plateau can be easily detected automatically through the computation of the derivative. The optimal threshold value has been arbitrarily defined as the centrer of the plateau. The error on the threshold is then linked to the width of the plateau.

Calibration

The second step was to refine the detection and to automate the detection thanks to a threshold chosen automatically. From a study based on a batch of images, the optimal $threshold_{blob}$ value appears to be linearly dependent on the median of grey scale values of the pixels for the full image.

By fixing the values of σ_{min} and σ_{max}, we were to able to use the linear relationship between the optimal $threshold_{blob}$ and the median value of an image, on the basis of which we were able to obtain a clean detection on the set of images.

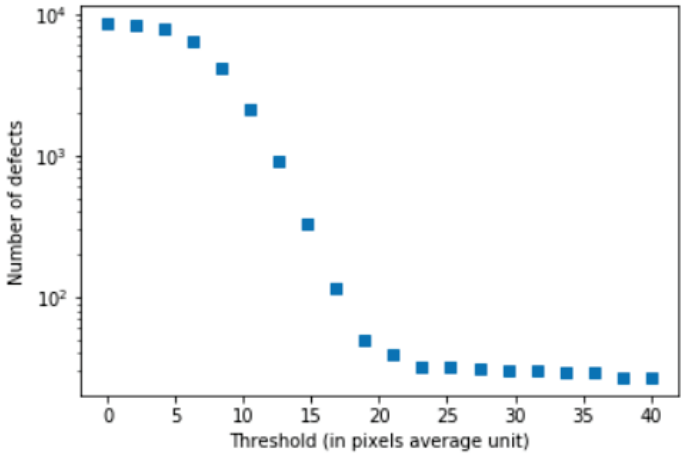

Figure 3.20: Number of detected defects as a function of the $threshold_{blob}$ value. Number of detected defects according to the detection threshold used for one image.

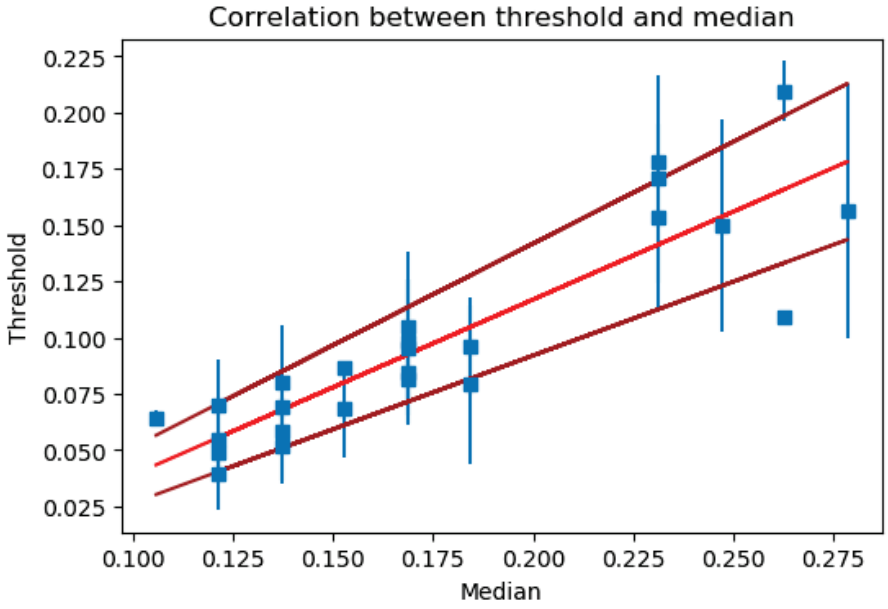

Figure 3.21: Threshold as a function of the image median showing the linear relationship between the ideal detection threshold (chosen as the mean value of the plateau) and the median of the image in red. The brown curves represent the relationships as a function of the thresholds taken at the beginning and end of the plateau.

The figure 3.22 shows the comparison of the detection of the algorithm of the instrument and *Blob log* algorithm. Defects detected by the built-in Micromap software are marked by a red dot, while defects detected by the *Blob log* algorithm are highlighted by yellow circles. The *Blob log* algorithm appears to be much more reliable than the buil-in Micromap one.

However, the detection is dependent on the threshold which itself depends on the image. We need to make a calibration which requires a lot of time (2h to one day depending on the batch of images and the number of defects). In addition, the presence of a pattern in the background is problematic and requires filtering, which is very resource and time consuming. That is why we switch to SEP.

However, the images background is sometimes affected by patterns that are not cleanly removed by our simple filtering procedure. Inspired by the observation that the images we are considering present several analogies with pictures of the sky, we have investigated the usage of image processing tools developed for astronomy, in order to profit from the sophisticated image background treatment and the robustness of reviewed and widely used codes.

3.4.3 SEP algorithm

In order to further improve our image analysis, a second code was developed based on SEP, a Python version of Sextractor (Source-Extractor) detailed in BERTIN, E. et ARNOUTS, S. [1996]. The SExtractor program is used in astronomy for objects detection to classify sources from astronomical images thanks to an efficient algorithm. It is an open source software, containing a Python library named *SEP - (Python library for Source Extraction and Photometry)*. The figure 3.23 shows the algorithm workflow. The complete analysis of an image is done following these several steps

- Background estimation : The first step is the estimation of the background image. The SEP library has a function to estimate the background of the image. This estimation is very useful because it allows to detect even the defects which have a weak intensity. To be able to detect the faintest objects and also to measure accurately their fluxes, we need to have a precise estimation of the background level in any place of the image, like a “background map” as shown in Figure 3.24. To obtain an estimate of the image background, SEP makes a first pass through the pixel data, computing an estimator of the local background in each mesh of a grid which covers the whole frame using Lutz's algorithm LUTZ [1980]. In this evaluation, each pixel value is assumed to be the sum of a background component, the brightness of the object contained in the pixel and the brightness from possible nearby objects.

- Detection : The detection step is performed on the background-subtracted image. The threshold$_{sep}$ parameter is the threshold used for detection. A defect is detected if one or more pixels have their gray value higher than the threshold$_{sep}$·*err*, with *err* the standard deviation of the image gray values. After scanning all the batch image, we obtain the catalog of detected defects (objects), the defects information (positions, sizes distributions) which will be used for the detection of scratches and the threshold value used in the function that will output a text file with the properties of the series of images.

- Scratch detection : sometimes a scratch on the surface of the sample is counted as multiple aligned defects (see Figure 3.26), that need to be removed from our samples under study, as we want to focus here on point defects. A scratch detection method based on the Hough transform has been added under the function *Scratch-detector*. The Hough transform is a pattern recognition technique used in image processing to detect lines in images M. NIXON [2008]. The principle of the *Scratch-detector* function is the following : creation of a dual space of the same dimension as our image, a line of equation $y = ax + b$ in real space will be converted into a point of coordinates (a,b) in dual space and in a point of coordinate (x,y) in real space will be a line of equation $b = ax + y$ in dual space (see Figure 3.25). By using polar coordinates we can link our dual space to the real space, the lines becoming sinusoids. The different lines (or sinusoids) in the dual space will intersect at a point whose coordinates

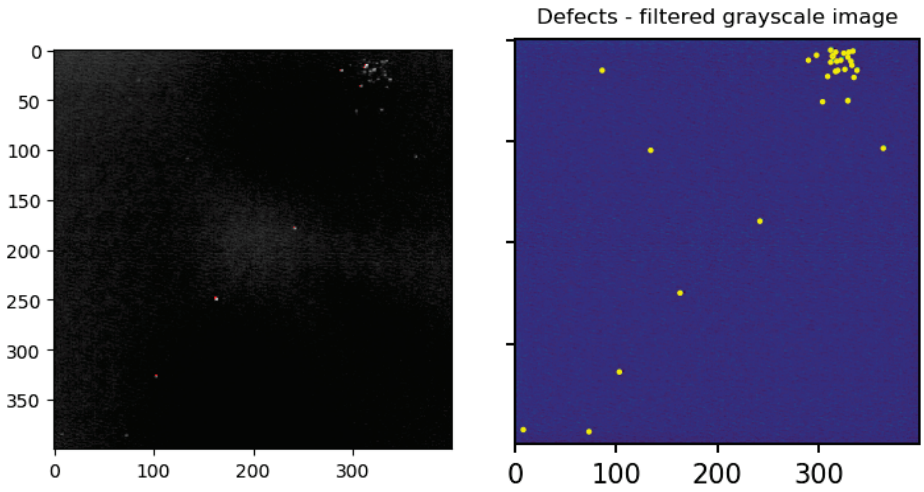

(a)

(b)

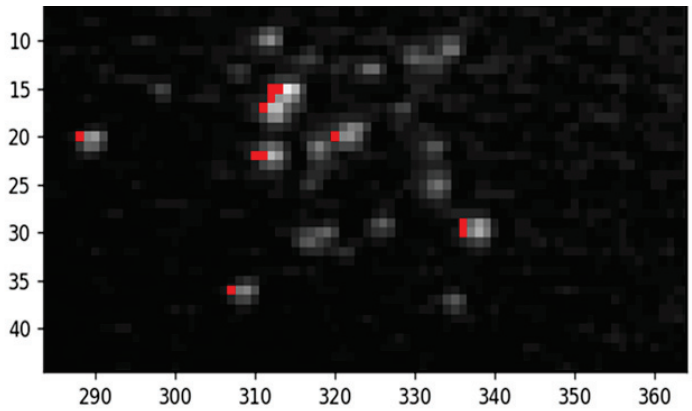

(c)

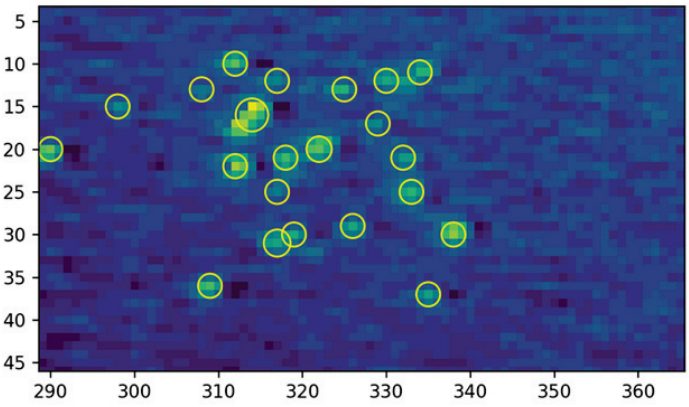

(d)

Figure 3.22: Image post-processing. In (a) the image given by the Micromap with some defects detected marked in red and other not. In (b), the post processing image analysed with the algorithm and all the defects cercled in yellow. In (c) a zoom is made on the cluster on the top right area.

will be the parameters of the line in real space passing through the points concerned. If less than 5 aligned defects are detected, it is very unlikely that a scratch is present (all the images used for testing had scratches with at least 8 defects). However, if the program detects more than 5 collinear defects, the probability of having a scratch is no longer negligible and a manual verification of the image is triggered. The defects associated to the scratch are not considered in further analysis.

- Photometry : SEP offers the possibility to estimate the apparent magnitude of an object. In our case, this function allows us to have information on the defects lumonisity.

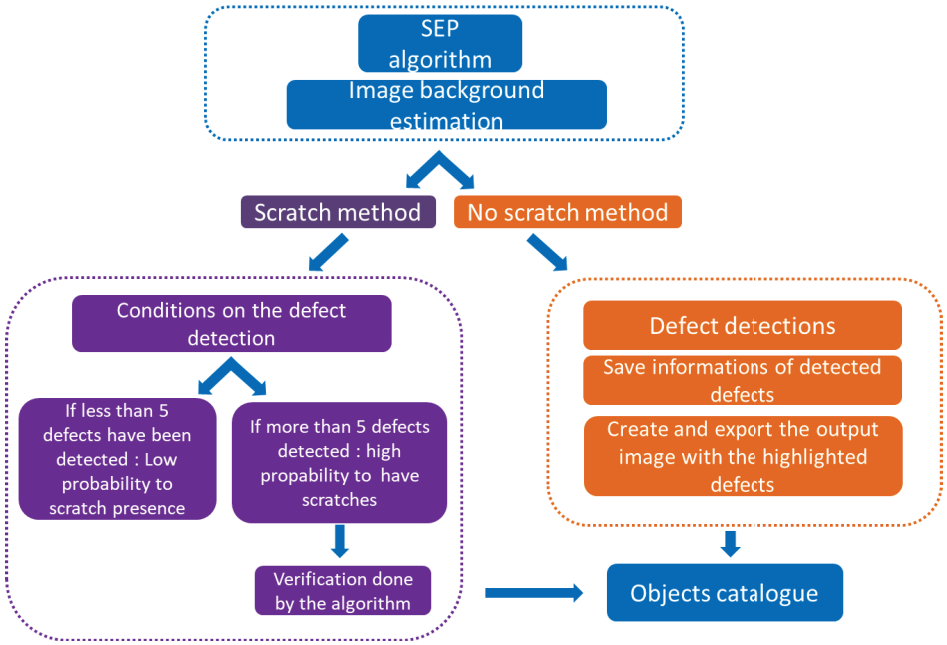

Figure 3.23: Layout of the main SExtractor procedures. Dashed arrows represent optional inputs.

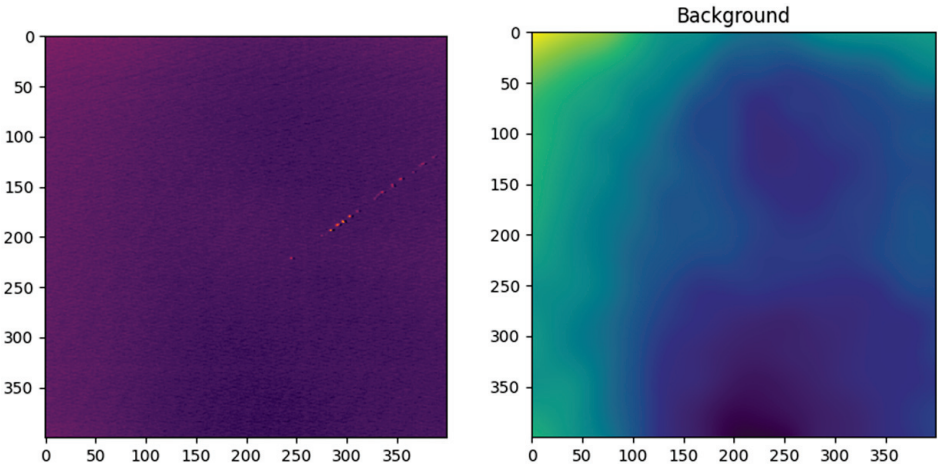

(a) (b)

Figure 3.24: Background estimation of an image in (a) the image and (b) the background map image after estimation.

Performance evaluation of SEP

The performance of the SEP code for the detection of defects on the Micromap images has been evaluated on simulated images (where true defects are inserted at known positions, over a typical

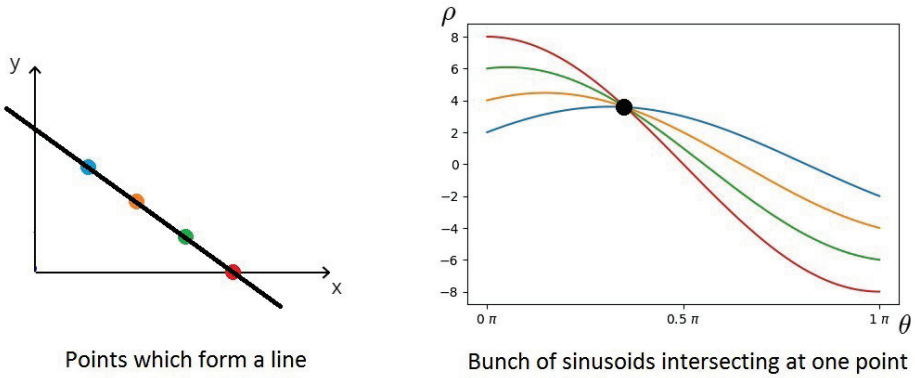

Figure 3.25: Exemple of the Hough transform.

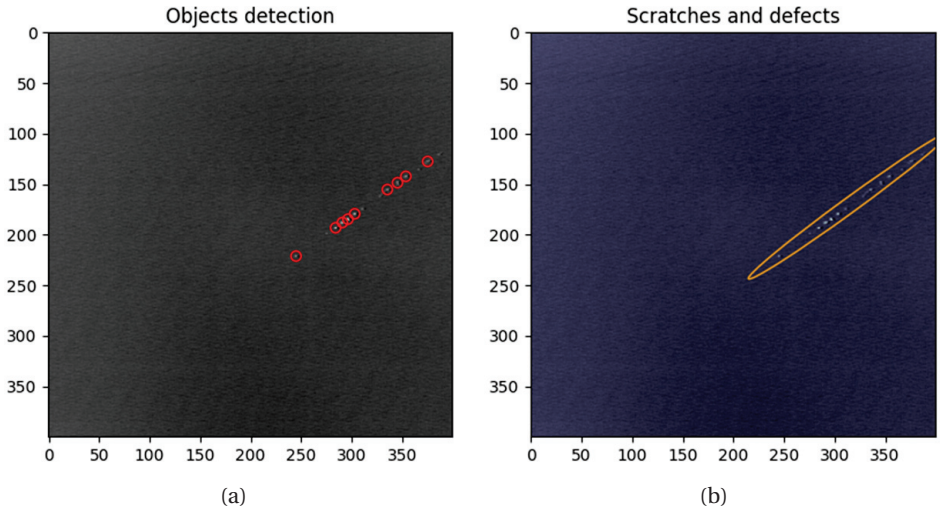

(a) (b)

Figure 3.26: Analysis of an image with a line of several aligned defects. Without the *Scratch-detector* function, the defects present are counted as defects (left) and thanks to the function the defects are detected as a scratch.

image background), in terms of efficiency and reliability. Two parameters are defined: the "match" is the fraction of real defects that are detected by the algorithm (a detected defect is considered matched to a real one if their distance is less than 3.5 pixels), and the "fake" is the number of defects that SEP will detect that are not matched to any true defect, divided by the total number of real defects in the image.

To evaluate the uncertainty on the match, we use the Clopper-Pearson method for efficiency error evaluation CLOPPER et PEARSON [1934] that is implemented in Python SCIPY.

For the uncertainty on the "fake", we assume the number of fake defects (b) and true defects (a) independent, and consider their Poisson uncertainties :

$$\Delta(\frac{a}{b}) = \sqrt{(\frac{\Delta a}{b})^2 + (\frac{a^2}{b^2}\Delta b^2)} \tag{3.3}$$

Figure 3.27 presents the evolution of the match (red) and the fake (blue) as a function of threshold$_{sep}$. For low values of threshold$_{sep}$, we have a high match, which is logical because almost all fakes are matched for low values of threshold$_{sep}$. You can notice the arrows on the fakes curve (in blue) at threshold$_{sep}$ equals to 1 and 1.5. This is because the fake values are very high (threshold$_{sep}$=1, the fake is at 1460.4 and threshold$_{sep}$=1.5, the fake is at 102). We then see that as threshold$_{sep}$ increases, the match and the fake decreases. The uncertainties are acceptable, we can also see that when we have a match approaching 100% there is no error bar upwards, which was expected. For low values of threshold$_{sep}$, a high number of fake defects is detected, and the "fake" is higher than unity. For a value of threshold$_{sep}$ around 2, the algorithm is able to ensure a 90% defect detection efficiency, for a fake rate of about 10%. After a preliminary study of the images, of much higher quality, produced by the eotech machine we have chosen threshold$_{sep}$ = 10.

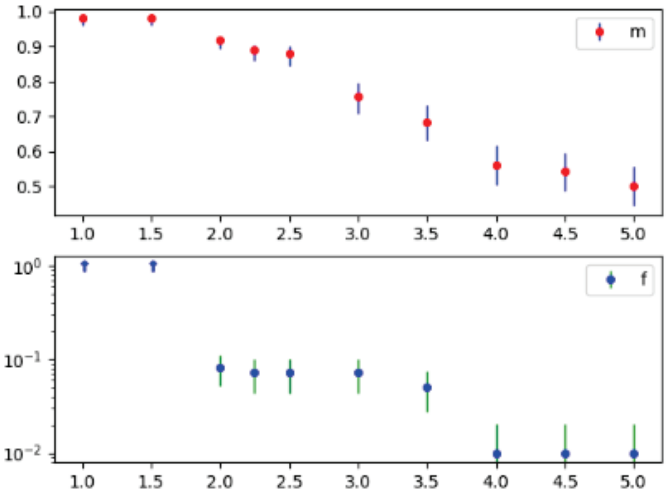

Figure 3.27: Estimation of the errors on the number of matches (top) and fakes (bottom) with respect to the SEP algorithm.

3.4.4 Comparison of the different algorithms detection

In order to evaluate the performance of the defect detection algorithms, repeatability and reproductibility measurements have been performed. First, a micropolished substrate coated with Ta_2O_5 layer was measured 100 times in order to know about the distribution of the defect count by

the Micromap, Blob-log and SEP. To estimate the correct count for the sample, a PhD user counted all the defects present on the batch of images. The figure 3.28, is presenting the results of the different counts Micromap, Blob log, SEP and PhD user. Supposing that the correct defect detection corresponds to the PhD user counting, the correct answer lies on the black line. The closer the points to this line, the better the algorithm. In this case SEP algorithm has the best matching.

The standard deviation from the black line for the different algorithm was calculated and we obtain : $\sigma_{Micromap} = 7$, $\sigma_{Bloblog} = 4{,}5$ and $\sigma_{SEP} = 3$. This confirms the robustness of the SEP algorythm.

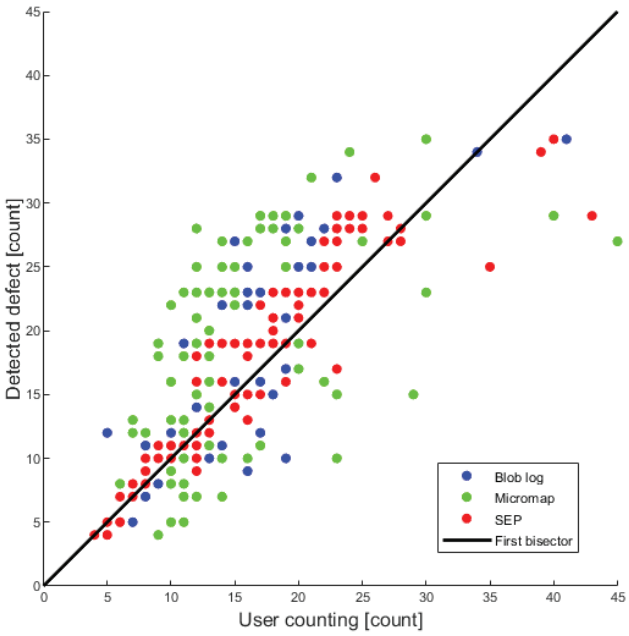

Figure 3.28: Comparison of the repeatability of the different detection algorithm.

3.5 Scatterometer : CASI

The scattering light is measured by a C.A.S.I. Scatterometer (Complete Angle Scan Instrument) from SMS (ex T.M.A. (USA)). It is the only commercial device of this type currently in Europe 3.29a. This instrument composed by a laser and a detector allows to measure the reflection, specular transmission of light and the scattered light at different scattering angles. The instrument offers the possibility to use different wavelengths of source laser such as 633 nm and 1064 nm but our measurements are made at 1064 nm, the same wavelength used in LIGO and Virgo interferometers.

3.5.1 Principle of the instrument

Scattering measurements are made by illuminating the sample with a laser at variable incidences between -80° and 80° with a step of 1° (Figure 3.30).

To determine the scattering of a sample, a function has been defined to represent it rigorously : the Bidirectional Reflectance Distribution Function (BRDF), a bidirectional quantity related to the incident light power 3.31. It is defined as the ratio of the total energy diffused per unit solid angle and the incident energy as follows STOVER [2012].

$$\mathrm{BRDF} \simeq \frac{dP_s/d\Omega_s}{P_i cos\theta_s} \simeq \frac{P_s/\Omega_s}{P_i cos\theta_s} \tag{3.4}$$

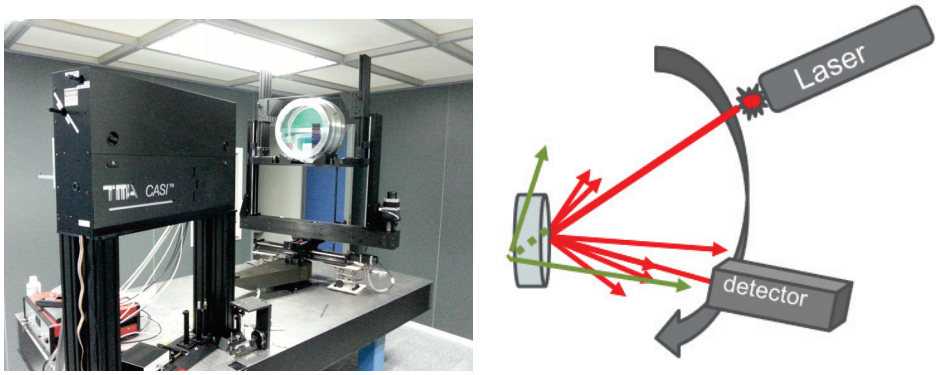

(a) Scatterometer in the cleanroom at LMA (b) Principle of the instrument.

Figure 3.29: Picture of the scatterometer in the cleanroom at LMA (a) and the principle schematic (b). The red rays are those reflected by the front face of the sample and the green rays are reflected by the back face

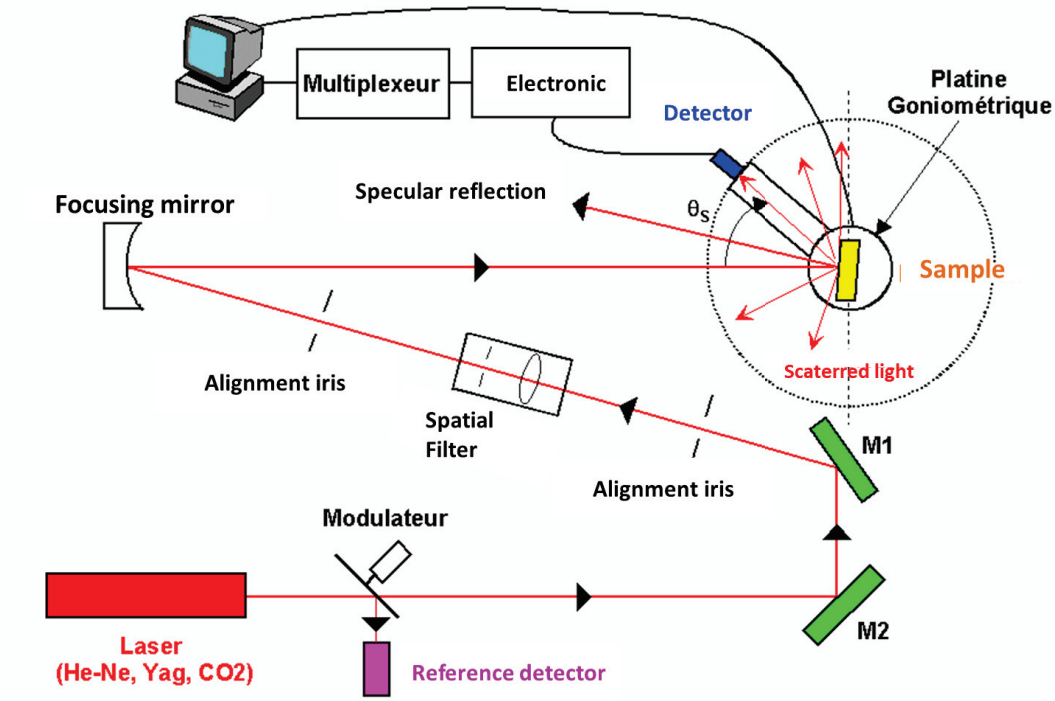

Figure 3.30: Principle of the measurement with CASI.

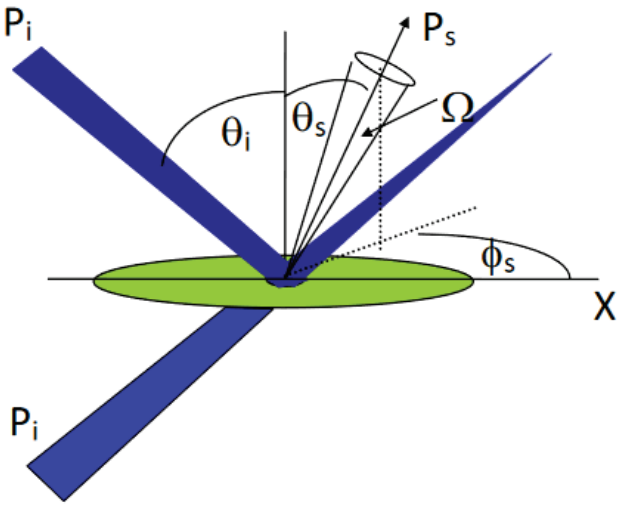

Figure 3.31: Standard spherical coordinates are used to define the geometry for the definitions of BRDF and BTDF (Bidirectional scattering transmission function).

Measuring the angular variation of the BRDF is one of the possibilities offered by the scatterometer. In this configuration, the sample is fixed and the detector rotates about the sample in the plane of incidence. To have a better estimation of the scattering light of defects a scattering map of the sample is done. The detector is fixed at a well defined position and the sample moves in its plane), see Figure 3.33. We obtain an average value of the BRDF which gives a much more realistic idea of the scattering of a mirror.

At LMA, there is a chart calculation allowing to convert the measured BRDF average values into an average diffusion value in ppm. In a quality approach and to be sure that the value given by this chart is correct, measurements of BRDF with a sweep at all angles (-80° to 80°) to have the shape of the BRDF have been performed on tantalum monolayers confirming that the average diffusion value obtained from the conversion of the measured BRDF returns the correct values. Indeed, the shape of the BRDF depends on the scattering source, i.e. the layer. The calculation of the scattering from the BRDF is done using the Total Integrated Scattering (TIS) :

$$\mathrm{TIS} = \frac{\int \mathrm{P}_{scattered}}{\mathrm{P}_{reflected}} \tag{3.5}$$

After the measurement of the BRDF (Figure 3.32), the scattering value is obtained by integrated the piece of the right curve after the specular TIS which gives X ppm.

As explained in section 3.2.3, the measurements are made on a ∅ 16 mm diameter to avoid unwanted reflections due to polluted edges. Knowing that the spot of the laser is 2 mm; the scanned diameter was reduced from ∅ 18 to 16 mm, as a precaution to avoid the effects of edges. The CASI has a major limitation that does not allow us to have the diffusion at different angles and in each point. We are not equipped with such an instrument at the LMA but the Fresnel Institute of Marseille have an instrument capable of making such measurements. An instrument called SALSA (Spectral and Angular Light Scattering characterization Apparatus) exists at the Fresnel Institute of Marseille Lequime et collab. [2018], allowing to measure in the whole angular domain and simultaneously in each point the BRDF.

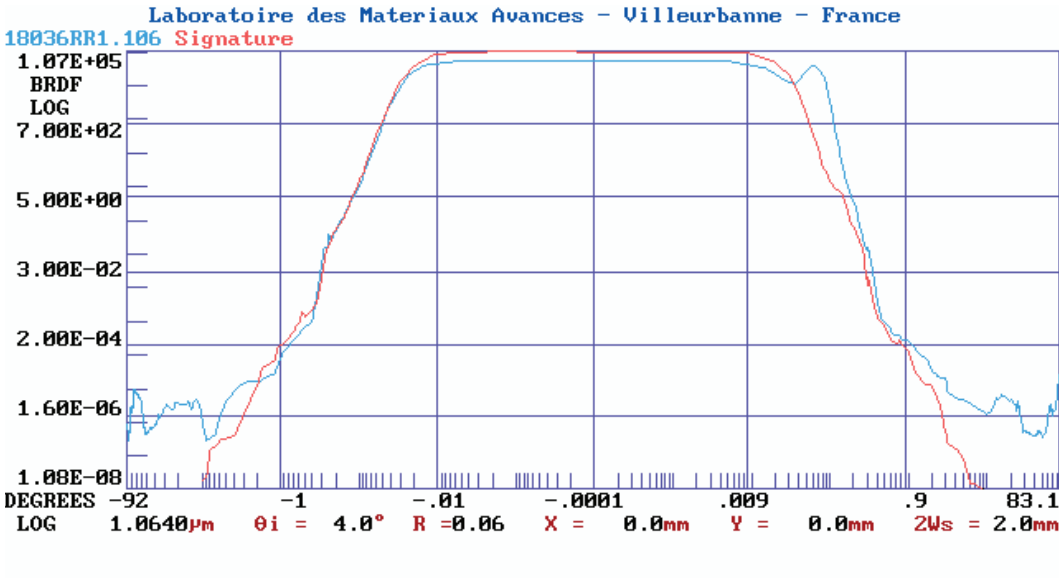

Figure 3.32: BRDF measurement on a defect-free area of a silica sample. The red curve is the detector signal and the blue curve is the BRDF of the sample. The peak observed at -0.4° corresponds to the reflection of the back face.

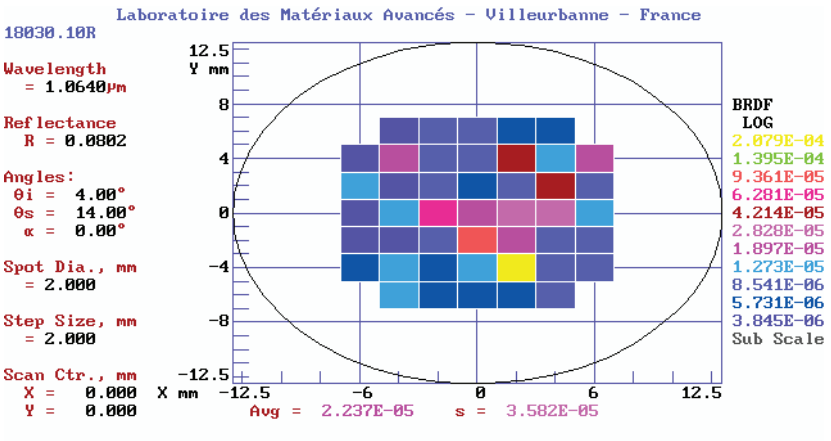

Figure 3.33: Example of a scattering map of a monolayer sample with the CASI.

3.6 Measurement protocol

For the measurements used in this study, a precise experimental protocol was established. To be sure to study and scan only the point defects present in the thin films, the protocol (detailed in Figure 3.34) was the following steps :

Before annealing :

- Substrates are cleaned before coating deposition ≈ 12 mn per sample
- Coating deposition is done for ≈ 24h (in the DIBS machine for exemple)
- Samples are cleaned after deposition (front side) ≈ 6 mn per sample
- Measurement with Micromap for defect scan ≈ 1h30 mn for one sample
- Samples are re-cleaned after defect scan (front and back side) ≈ 12 mn per sample
- Measurement with CASI for scattering map ≈ 1h for two samples
- Cleaning front and back side samples ≈ 12 mn per sample
- Annealing samples in oven at 500°C ≈ 48h

After annealing :

- Samples are cleaned after annealing (front side) ≈ 6 mn per sample
- Measurement with Micromap for defect scan after annealing ≈ 1h30 mn for one sample
- Samples are re-cleaned after defect scan (front and back side) ≈ 12 mn per sample
- Measurement with CASI for scattering map ≈ 1h for two samples

The cleaning and the measurements on the different instruments are done sample by sample. It is not possible to parallelize the steps except for the thermal annealing. For a 1” inch sample, it should be noted that it takes approximately over one week to achieve all the different steps.

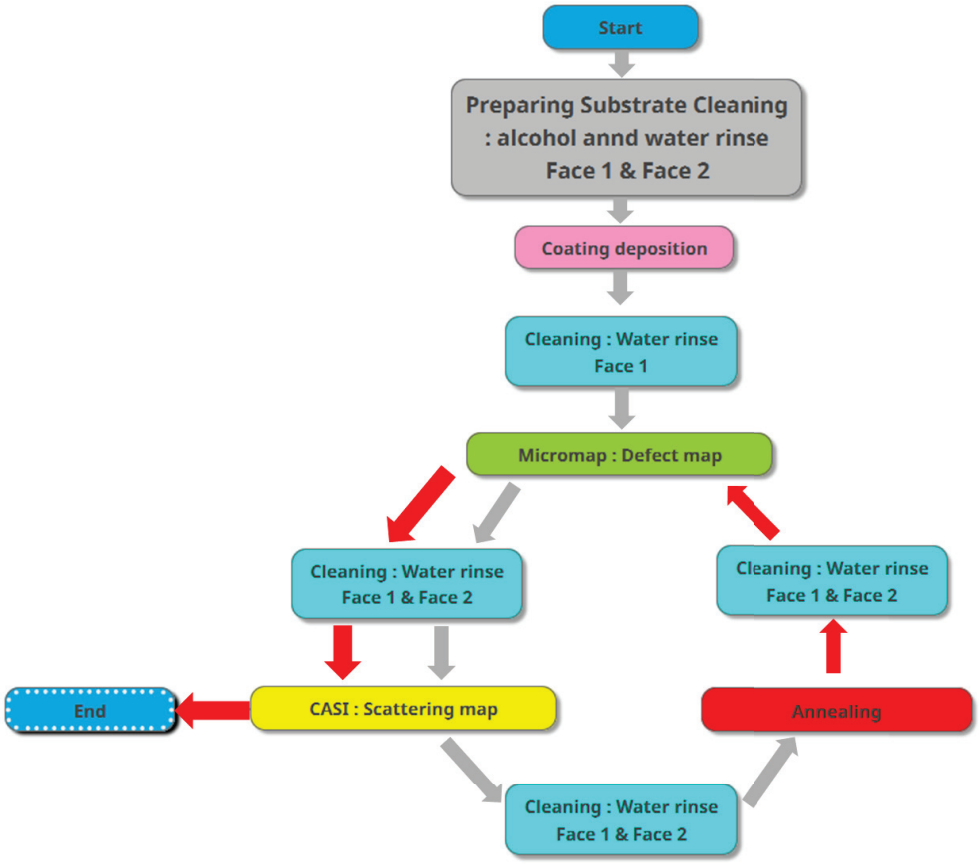

Figure 3.34: Diagram presenting the experimental protocol established for the study of defects. The grey arrows correspond to the first part of the measurements, the steps to be taken before annealing and the red arrows to the second part of the measurements, the steps to be taken after thermal annealing.

3.7 Summary

This chapter mainly presents the LMA instruments that were used in this study, notably the optical profilometers and the scatterometer. In particular, profilometers have been characterised to understand how the defect detection can be optimized. A code has been developed to allow a more accurate analysis of the results. Then the miticulous experimental procedure has been detailed to be sure that handling manipulation can not damage sample surfaces and add defects.

3.8 References

BERTIN, E. et ARNOUTS, S. 1996, «Sextractor: Software for source extraction», *Astron. Astrophys. Suppl. Ser.*, vol. 117, 2, doi:10.1051/aas:1996164, p. 393–404. URL https://doi.org/10.1051/aas:1996164. 54

CLOPPER, C. J. et E. S. PEARSON. 1934, «The use of confidence or fiducial limits illustrated in the case of the binomial», *Biometrika*, vol. 26, 4, doi:10.1093/biomet/26.4.404, p. 404–413, ISSN 0006-3444. URL https://doi.org/10.1093/biomet/26.4.404. 58

COMPANY. URL https://eotech.fr/, 1, ZI du fond des prés 91460 Marcoussis - France. 44

LEGRAND, F. 2020, «Transformée de fourier d'une image», URL https://www.f-legrand.fr/scidoc/docmml/numerique/tfd/tfdimage/tfdimage.html, informatique Appliquée aux Sciences Physiques. 51

LEQUIME, M., M. ZERRAD et C. AMRA. 2018, «Breakthrough spectrophotometric instrument for the ultra-fine characterization of the spectral transmittance of thin-film optical filters», *Opt. Express*, vol. 26, 26, doi:10.1364/OE.26.034236, p. 34 236––34 249. URL http://opg.optica.org/oe/abstract.cfm?URI=oe-26-26-34236. 61

LUTZ, R. K. 1980, «An Algorithm for the Real Time Analysis of Digitised Images», *The Computer Journal*, vol. 23, 3, doi:10.1093/comjnl/23.3.262, p. 262–269, ISSN 0010-4620. URL https://doi.org/10.1093/comjnl/23.3.262. 54

M. NIXON, A. A. 2008, *Feature extraction and image processing*, Academic Press. 54

SAYAH, S., B. SASSOLAS, J. DEGALLAIX, L. PINARD, C. MICHEL, V. SORDINI et G. CAGNOLI. 2021, «Point defects in ibs coating for very low loss mirrors», *Appl. Opt.*, vol. 60, 14, doi:10.1364/AO.415462, p. 4068–4073. URL http://www.osapublishing.org/ao/abstract.cfm?URI=ao-60-14-4068. 41

SCIKIT. URL https://scikit-image.org/docs/stable/auto_examples/color_exposure/plot_rgb_to_gray.html. 51

SCIPY. URL https://docs.scipy.org/doc/scipy/reference/generated/scipy.stats._result_classes.BinomTestResult.proportion_ci.html. 58

STOVER, J. C. 2012, *Optical Scattering: Measurement and Analysis, Third Editions*, CRC press, doi:10.1117/3.975276. 59

VAN DER WALT, S., J. L. SCHÖNBERGER, J. NUNEZ-IGLESIAS, F. BOULOGNE, J. D. WARNER, N. YAGER, E. GOUILLART, T. YU et THE SCIKIT-IMAGE CONTRIBUTORS. 2014, «scikit-image: image processing in python», *PeerJ*, vol. 2, doi:10.7717/peerj.453, p. e453, ISSN 2167-8359. URL https://doi.org/10.7717/peerj.453. 51

Chapter 4

Coating Point Defects

Contents

4.1 Introduction

Even if few point-like defects can be present on the substrate as was shown previously in chapter 2, it is mainly the deposition process that adds defects in the coating. Their presence has been a well known problem for several years and it is becoming a limiting factor for future detectors. The point defects can be the origin of the extra-loss observed in Advanced LIGO and Advanced Virgo YAMAMOTO [2015]. The goal of this study is to understand the mechanisms that creates them and find the handles to reduce them.

The creation of defects during the deposition process was also observed in other deposition techniques like physical vapor deposition (PVD) PANJAN et collab. [2020], electrodeposition, plasma polymerization, chemical vapor deposition (CVD) and magnetron sputtering HULTMAN et collab. [1988]; PETROV et collab. [1992]. Another team has studied the formation of neutral particles clusters, using gold and metals sputtering. They have obtained interesting results by studying the defects with mass spectroscopy techniques KING et collab. [2009]; WUCHER et WAHL [1996].

The reduction of particle contamination during the IBS deposition process has been investigated by producing two coating machines one standard and the other with a separator coil. The result shows that the separation process has a positive impact on the defect density. A reduction of a factor three of particle contamination by the bent magnetic separator was observed in comparison to the conventional IBS process MALOBABIC et collab. [2015].

Another study has explained how particle contamination (clusters between 3 and 30 µm) can occur during IBS sputtering. Particles from the ion beam can deviate from their trajectories, bounce and be dragged in the direction of the ion flow and thus deposit on the surface of the substrate WALTON et collab. [2003]. It has been observed that the smallest particles are the most deflected.

In KNOLLENBERG et collab. [1995], tests have been made by installing a optical fiber in various positions near the chamber floor to observe particles generated by the ion gun. The amount of particles sputtered during deposition is found to vary with the type of the target material. It was observed that there is a higher level of contamination in SiO_2 than in Ta_2O_5 probably related to the stress and the thermal conductivity of the materials.

Several teams have tried to understand the origin of defects in the various existing deposition processes, finding that the deposition technique plays a crucial role in the generation of defects. In this chapter, we present the series of tests that have been performed on the laboratory coating machine deposition in order to study the impact of different parameters related to the deposition process.

4.1.1 Point Defect Taxonomy

We work on amorphous layers with imperfections of various types. For the purpose of this PhD thesis, all imperfections below 5 µm present in thin films are referred to as point defects. Defects can be present either on the surface of the substrate, at the substrate-layer interface, in the thin film or on the surface of the thin film. Figure 4.1, shows a schematic view of a sample on which there are the various kinds of imperfections. The size of the defects varies on average from 1 to 15 microns.

Several types of point defects have been identified until now and can be classified in different categories PANJAN et collab. [2020] :

- Nodular defects : considered as the most common type of growth defects (Figure 4.2).
- Flake defects : High defect size whose growth that protrudes above the surface of a thin film (Figure 4.4).
- Droplet defects : they are very common in the coatings deposited by cathodic arc deposition technique and in sputter deposition process their formation appear in smaller scale (Figure 4.3).

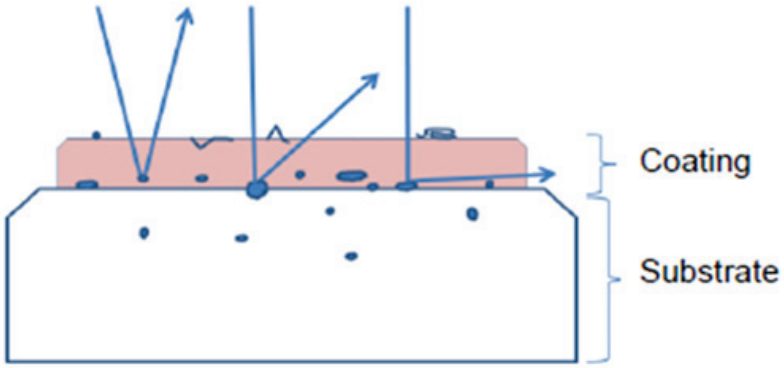

Figure 4.1: Schematic of a typical sample. The two inclined edges represent the chamfer. We can see the different types of imperfections which are dust or layer defects.

- Hole -like defects : this kind of defects appears below the surface of the thin film and with different shape (Figure 4.5).
- Pinhole defects : the most common defect in PVD thin films. This kind of defect are discontinuities in the coating microstructure in form of thin holes having a micron size diameter (Figure 4.5).
- Crater-Like defects : this defects are due to external forces during or after coating deposition or during cleaning (Figure 4.6).
- Foreign seed particles : Seed particles can be caused by dust, debris, polishing residue and impurities. They remain on the substrate surface after mechanical pretreatment (Figure 4.7).

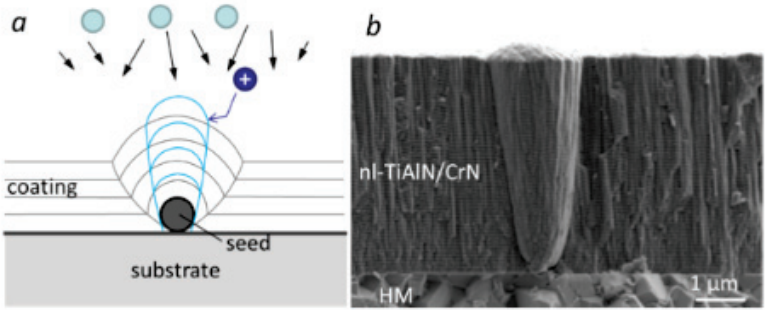

Figure 4.2: Scheme of a conical and parabolic nodule cross-section; the shape mainly depends on the flux distribution of the incoming atoms (a); fracture cross-section SEM image of a typical nodular defect with rather straight vertical walls in the nl-TiAlN/CrN hard coating prepared by magnetron sputtering (b) PANJAN et collab. [2020].

In our measurements, we classify defects based on our observation :

- Scratches which are sometimes due to the polishing or to a bad handling of the optics. There are different types of scratches :
  - Cracking of the coating due to internal stress in coating (Figure 4.8 a)
  - Scratch on the substrate that is revealed by the coating (Figure 4.8 b)
  - Scratches due to poor handling or to the installation of the substrates in the chamber (Figure 4.8 c)
- Inhomogeneities of the layer Figure 4.8 d)

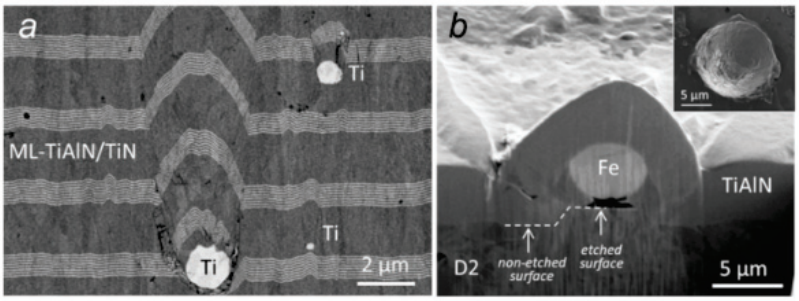

Figure 4.3: FIB cross-section image of a buried droplet formed in the multilayer TiAlN/TiN hard coating prepared at the company KCS Europe from Germany by cathode arc deposition technique (a). Fe-based droplet built in the TiAlN hard coating sputter-deposited on D2 tool steel substrate (b). The distinct step beneath the Fe droplet proves that it arrived on the surface of the substrate at the beginning of the ion etching PANJAN et collab. [2020].

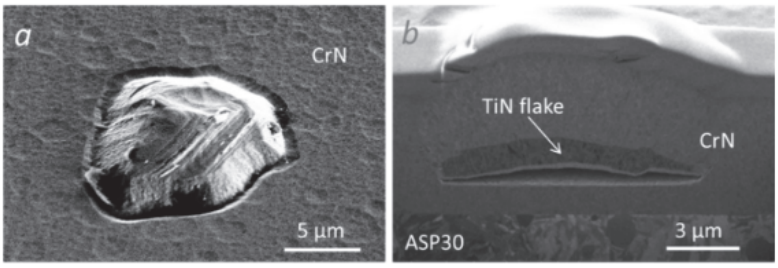

Figure 4.4: Top view SEM image (a) and FIB cross-section image (b) of flake defects in CrN hard coating prepared by evaporation using thermionic arc PANJAN et collab. [2020].

- Dust that settles due to a non-clean environment, or handling even with gloves (Figure 4.8 e)

On the other hand, large scratches or holes of size between 5 to 15 microns are visible by eye. As for the defects inside the layers, the smallest ones are only visible optically with a binocular microscope but some, medium or a little bigger, are visible to the naked eye.

4.1.2 Selection of the substrate

The choice of the substrate is a key element of the study. As they all already contain a certain number of defects before deposition, it is important to choose the substrate with the lowest defect density and the best surface roughness to get closer to a perfect surface. In addition, the presence of scratch residues after polishing could imply a multiplication of the defects during the thin film deposition. In table 4.1, we present the characteristics of different kinds of substrates for the study. Compared to Coastline, Heraeus substrate present more defects and a higher roughness.

Table 4.1: Comparaison of two fused silica substrate quality to be choosen for the study.

Substrate quality	Roughness Å RMS	Defect Density [defect/mm²]
Standard polishing Heraeus	> 1Å RMS	0.09
Superpolished Coastline	0.5 ÅRMS	0.04

Based on the measurements of roughness and defects density, the Coastline substrates have been chosen for all the studies presented in this PhD work.

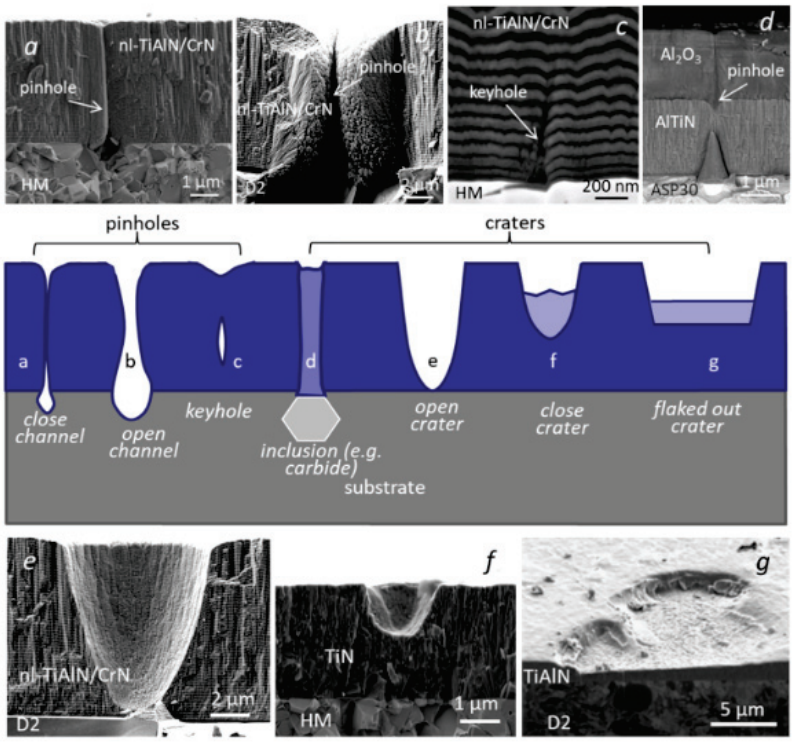

Figure 4.5: Schematic overview of different shapes of hole-like defects in PVD coatings: (a) pinhole at the site of a pit in the substrate; (b) open pinhole; (c) closed pinhole (keyhole); (d) pinhole that appeared at the site of a shallow crater formed during ion etching of ASP30 tool steel substrate; (e) crater formed due to the expulsion of a nodular defect; (f) a crater that does not extend through the entire coating; and (g) crater of irregular shape formed by detachment of flake defects. FIB and fracture cross-sectional SEM images of typical hole-like defects in PVD hard coatings prepared by magnetron sputtering (coating type : nl-TiAlN/CrN, CrN, TiAlN) and by evaporation using thermionic arc (coating type:TiN) are added PANJAN et collab. [2020].

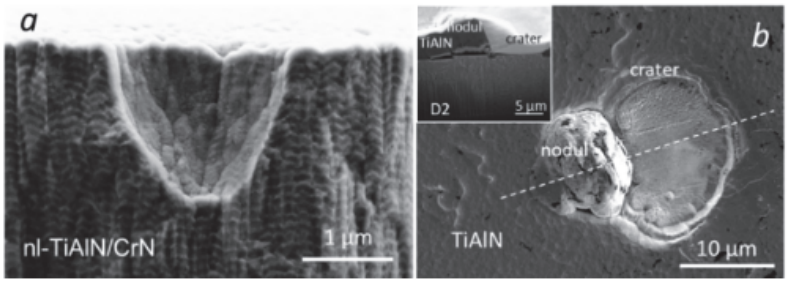

Figure 4.6: Crater-like defect left by the detachment of a nodule in sputter-deposited nl-TiAlN/CrN hard coating (a) and combination of flake and nodular defects in sputter-deposited TiAlN coating (b) PANJAN et collab. [2020].

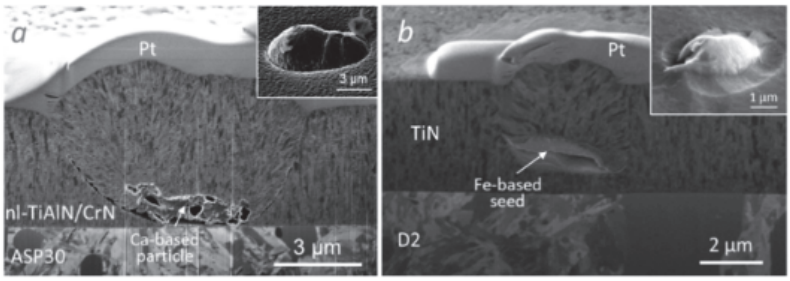

Figure 4.7: Top-view SEM (insets) and FIB images of nodular defects originating from Ca-based and Fe-based seeds. Nanolayer nl-TiAlN/CrN (a) and TiN (b) hard coatings were prepared by sputtering and evaporation using a thermionic arc, respectively PANJAN et collab. [2020].

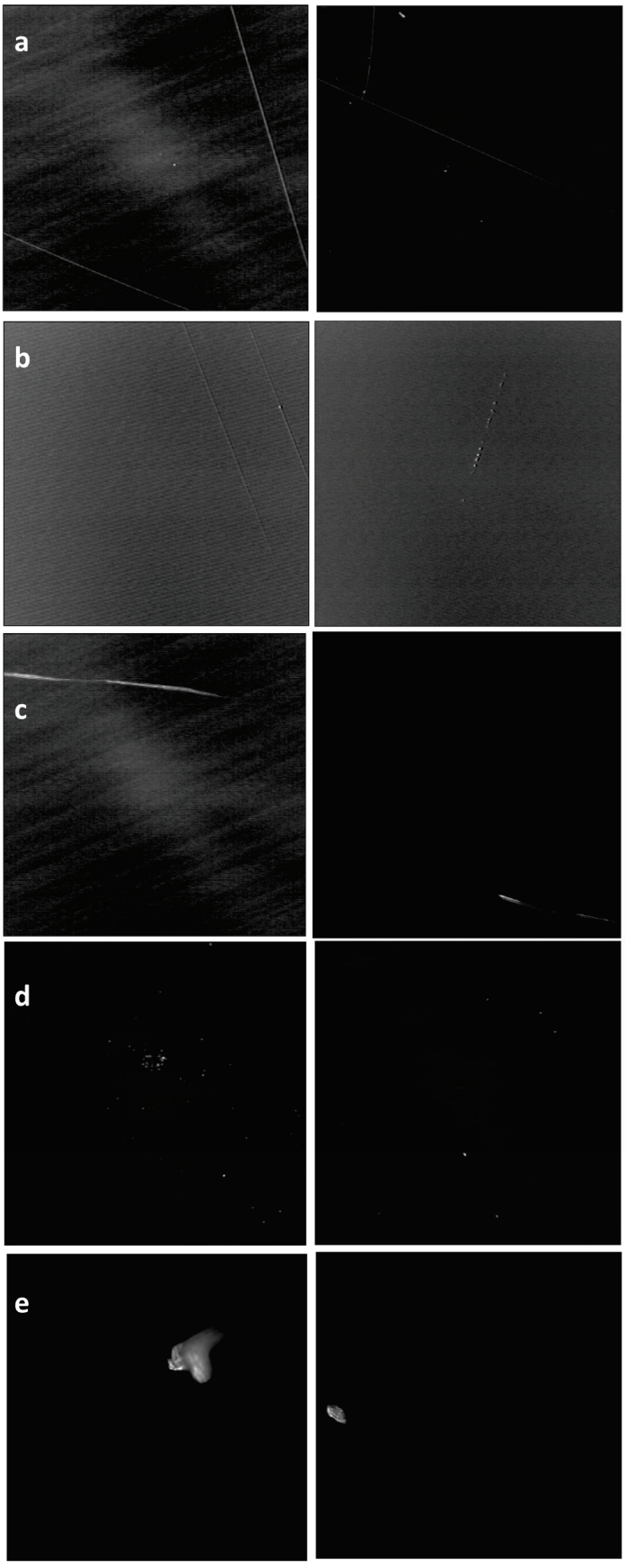

Figure 4.8: Examples of kind of scratch which appeared after coating deposition observed on different samples with the Micromap profilometer. Images dimensions are 513 µm x 513 µm.

4.1.3 Table of samples

There were two measurement campaigns of coating deposition: the very first preliminary tests carried out in the DIBS machine and then a second, in-depth one with further tests in DIBS and GC machine. For a better understanding of the manuscript, all the samples used for the PhD work are summarized in the Table 4.2 for the preliminary study and in Table 4.3 for the in-depth one.

Table 4.2: **The table lists, for each sample used, the coating machine, and the coating material and layer thickness.**

Coating machine	Material	Thickness (nm)	RUN	Sample
DIBS	Ta_2O_5	562.5	18028	PL4117
		1134.5	18026	PL4091
		1665.4	18029	PL4126
		2231.8	18027	PL4087
DIBS	SiO_2	524.8	18036	PL4151
		1005	18030	PL4151
		1550.6	18032	PL4161
		2053	18031	PL4159

Table 4.3: **List of samples with the coating machine, the coating material, the layer thickness, the coating run number and the sample ID. In some cases, the coating was deposited on several substrates in the same run, to produce equivalent samples: this information is given in the columns "RUN" and "Sample".**

Coating machine	Material	Thickness (nm)	RUN	Samples
DIBS	Ta_2O_5	0	D20036	PL7393
		128	D20077	PL7466 PL7467 PL7468 PL7469
		256	D21002	PL7366 PL7372 PL7376 PL7464
		512	D21001	PL7391 PL7394
		1027	D21040	PL9184 PL9188
		1513	D21036	PL8677 PL8712
		2017	D21037	PL9229
GC	Ta_2O_5	0	GC ghost	PL10089
		144	C21101	PL9246 PL9247 PL9248 PL9251
		284	C21103	PL9256 PL9255 PL9253 PL9252
		568	C21100	PL9203 PL9213
		1125	C21104	PL9259 PL9261
		2833	C21102	PL9234 PL9235
GC	$Ti:Ta_2O_5$	122.5	C21074	PL9189 PL9190 PL9191 PL9201
		300	C21060	PL8692 PL8695 PL8699 PL8824
		495.1	C21063	PL9262 PL9245
		965.2	C21075	PL9210 PL9211
		2378.6	C21077	PL9205 PL9207

DIBS Parameter	Material	Thickness (nm)	RUN	Samples
Ib	Ta_2O_5	≈ 1000	110 mA	D21056 PL9257 PL9238 PL9254
			180 mA	D21057 PL9507 PL9510 PL9512
			200 mA	D22001 PL9534 PL9550 PL9551
			250 mA	D21058 PL9505 PL9504 PL9501
Vb	Ta_2O_5	≈ 1000	450 V	D22002 PL9555 PL9595 PL9599
			600 V	D22004 PL10098 PL10100 PL10108
			800 V	D22003 PL10107 PL10110 PL10113
			1000 V	D22001 PL9534 PL9550 PL9551

4.2 Study of the layer thickness influence on the defect density

In this section, the first results concerning the influence of the layer thickness on the defect density are presented. The coating deposition of the different thicknesses were made in the DIBS machine.

4.2.1 Preliminary study

The preliminary study was the occasion to check hypotheses based on the measurements of the first Advanced Virgo mirrors. In particular, that the number of defects increased with the thickness of the layer. The preliminary study is documented in a publication SAYAH et collab. [2021]. In order to understand the behavior separately for the two materials constituting the Advanced Virgo (and LIGO) mirrors stack, we have produced, in the DIBS machine, Ta_2O_5 and SiO_2 coating samples separately, with four different thicknesses each. The same deposition parameters have been used for both materials (same ion beam energy, same ion beam current and same sputtering angle), these are presented in Table 4.4. All the results of the preliminary study were obtained with the Micromap measurements. The error bars represent the repeatability uncertainties.

Table 4.4: **Coating parameters.**

Material	Ib (mA)	Vb (V)	Vacc (V)	Ie (mA)	θ (°)	Ar source sccm	Ar RFN sccm	O2 sccm
Ta_2O_5	200	1000	200	250	45	12	5	20
SiO_2	200	1000	200	250	45	12	5	16

Figure 4.9 shows the evolution of the number of defects as a function of the layer thickness for both materials. In both cases the defect density increases with the layer thickness. However, the behavior is different for the 2 materials. The defect rate of SiO_2 varies linearly with the thickness see Figure 4.9a, while it follows a power law for Ta_2O_5, see Figure 4.9b. In addition, at equivalent thickness, the number of defects present in SiO_2 is approximately 10 times lower than Ta_2O_5. The first hypothesis, to explain the non-linear evolution of the defect rate as a function of the thickness of Ta_2O_5, was a creation of defects due to particles that would be detached from the walls of the chamber as successive coating deposition runs were made. However, the SiO_2 deposition series was done after the Ta_2O_5 deposition series without cleaning the chamber. Therefore we should have observed the same phenomenon on the SiO_2.

The second hypothesis to explain Ta_2O_5 behaviour is that it could be the consequence of processes thermally activated during the deposition. Indeed, the deposition temperature of silica layers is the same for all layers but the deposition is quite long compared to tantala. For this reason, the substrate temperature was in a steady state during most of the deposition time while for the tantala the temperature was possibly evolving during deposition.

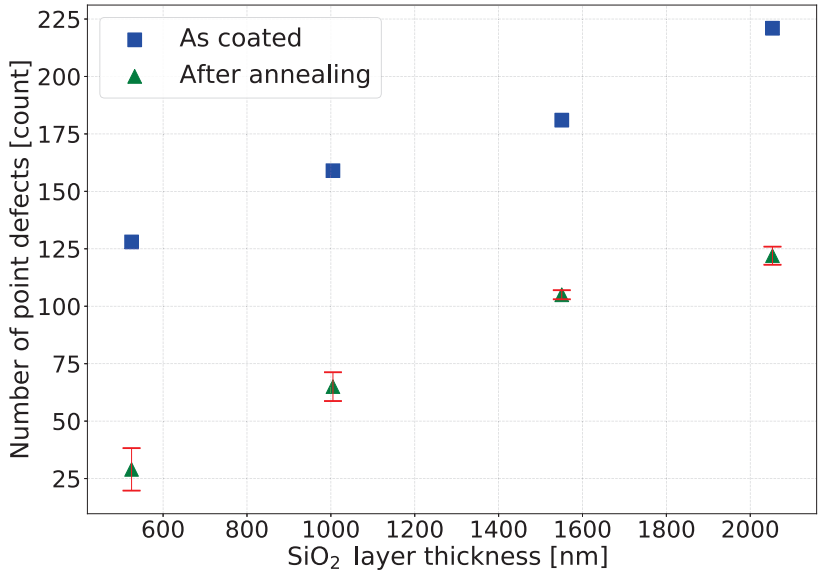

(a)

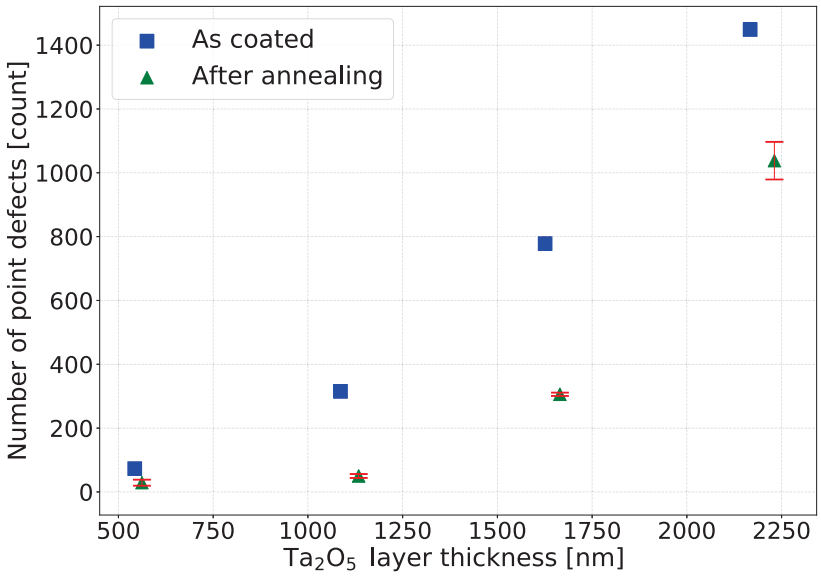

(b)

Figure 4.9: Number of point-like scatterers in SiO2 layers (a) and Ta2O5 (b) as a function of the layer thickness. Results are shown for materials as coated (in blue) and after annealing (in green) measured with the Micromap. The measurements were repeated and the markers show the average values, while the error bars show the region containing 90% of the results. Measurements before annealing were not repeated.

4.2.2 In-depth study

All the results presented in this section were obtained with EOTECH profilometer. Following the results obtained in the preliminary study, a more in-depth study was conducted, focusing on Ta_2O_5, in order to maximise the statistics, since this material has the highest defect density. For statistical reasons, several samples were produced per run for more reliability and in order to verify the trend of the power law with respect to the thickness (Figure 4.9). For all the results in the following, the error bars represent the spread of the measurements when performed on different samples. The results in this section are obtained on samples with deposition runs performed in the DIBS machine. Once the machine was under vacuum, the substrate was preheated for 3 hours to reach a steady state before starting the sputtering process. As shown in Figure 4.11, the temperature reached by the surface is about 145°C. Figure 4.10, shows the defects number as a function of the thickness. Within statistical uncertainties, the trend is consistent with a linear behaviour. For Ta_2O_5 samples having undergone a longer pre-heating phase, the dependence of the number of defects on the layer thickness is then confirmed to be consistent with a linear one, and with the results obtained on SiO_2 samples in the preliminary study.

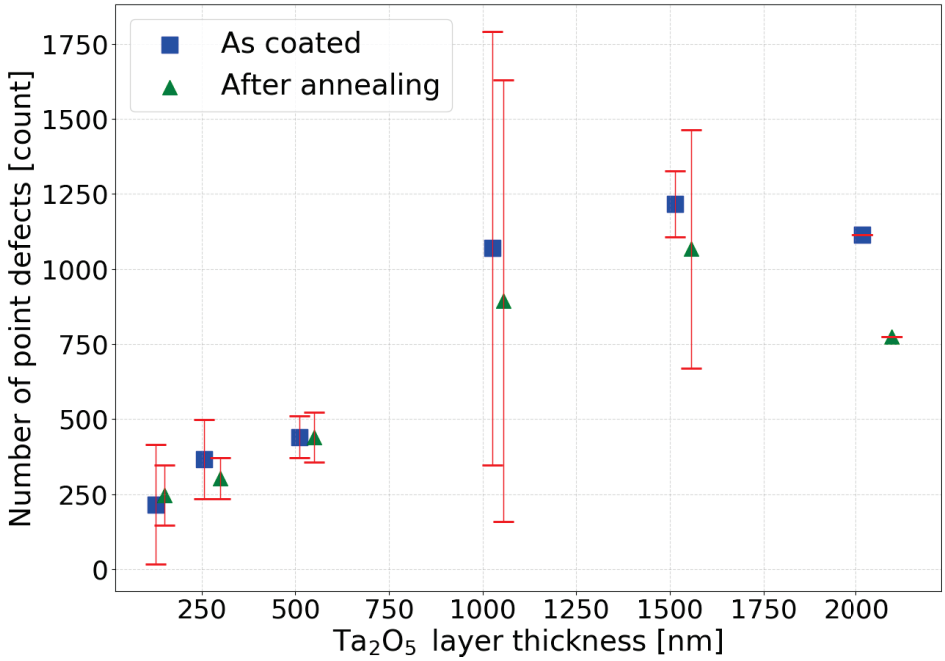

Figure 4.10: Number of defects in Ta_2O_5 processed in the DIBS coating machine. Blue point represent the median of point defects presents in each runs before annealing. The point (0;0) represent a "ghost deposition". That means one sample was put in to the chamber in the same conditions of others runs (under vaccum and preheating) but without sputtering any material.

The different trend between both Ta_2O_5 samples batchs is not well explained by the deposition temperature. Actually between a pre-heat of 1.5h and 3h the surface temperature increased from 135°C to 145°C (see figure 4.11). But during this pre-heating we measured a significant variation of the water residual content in the chamber. Indeed, additional measurements made in the DIBS allowed to measure the amount of water vapor present in the chamber as a function of time (see Figure 4.12). Between 1.5 hour and 3 hours, the water content decreased by a factor of 2. This can certainly impact the pressure into the chamber and lead to a better vacuum quality. Besides, the problem of water vapor in silica layers is well known and leads to structural defects in the silica NUCCIO [2009].

This second hypothesis can explain better the trend behaviour obtained in the preliminary study, where for Ta_2O_5 the equilibrium temperature in the chamber at the time of deposition had not been reached. Pure tantala depositions have been also performed in other machines, as will be discussed in Section 4.3.4, leading to a compatible conclusion.

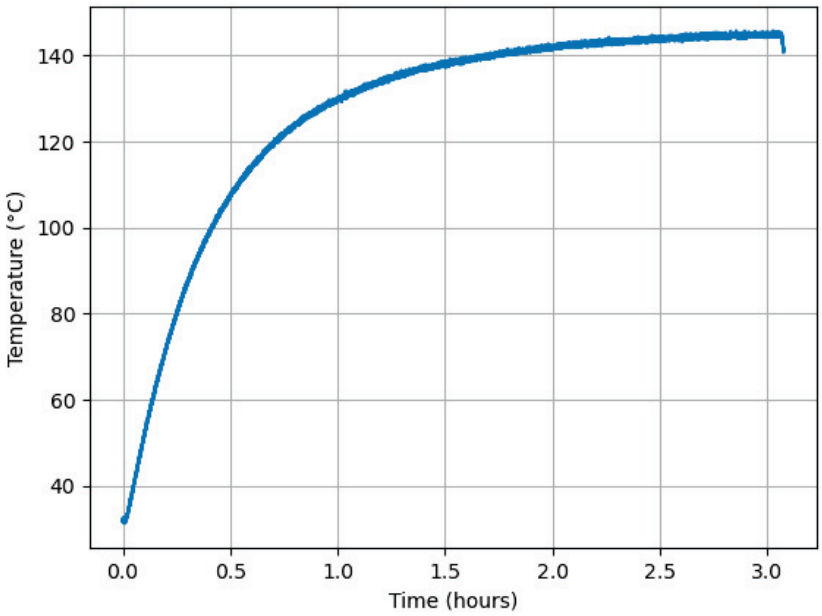

Figure 4.11: Curve representing the temperature during coating deposition into the chamber as a function of time in hours.

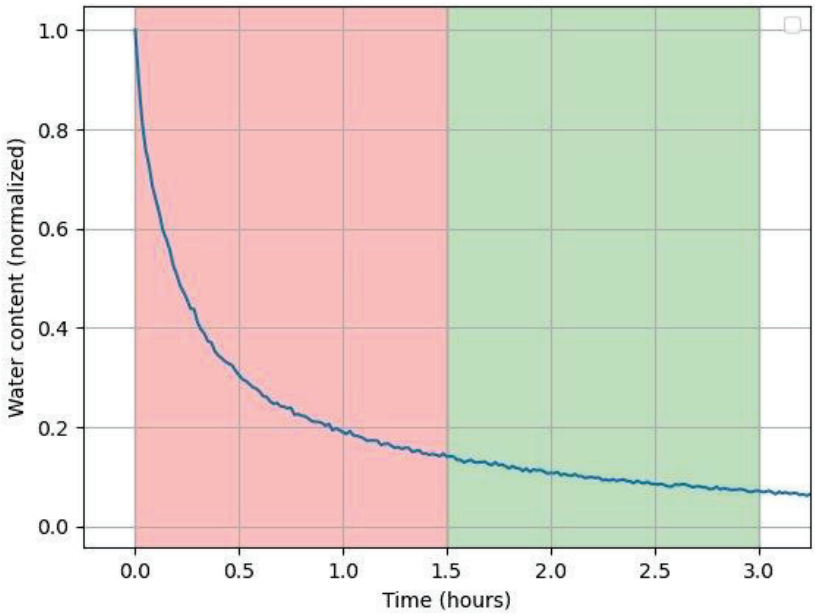

Figure 4.12: Curve representing the water vapour quantity in the coating chamber. The red zone corresponds to the preheating phase of the chamber (1.5 hours) with the infrared lamp and the green zone corresponds to the preheating during 3 hours.

4.3 Influence of other parameters during deposition

In this section, different parameters have been modified to study their influence during or after deposition on the defect density. The results are based on the tantala samples produced for the in-depth study.

4.3.1 Influence of the Annealing

All samples are placed in an oven for thermal annealing after deposition. This is a heating cycle that can change the characteristics of a material. The annealing allows in particular to eliminate or reduce the mechanical strain in the layer related to the growth, but also to obtain the formation of a favorable structure (a better homogeneity, a better stochiometry adjustment and a strong reduction of the optical absorption of the layers) GRANATA et collab. [2020].

As an example, the Ta_2O_5 and SiO_2 samples were annealed at 500°C. It can be seen from the graphs showing the number of defects as a function of thickness, Figure 4.9, that annealing clearly decreases the defect rate, by 50% for Ta_2O_5 and about 40% for SiO_2, but that the curves retain their trends observed before annealing. The comparison between the thickest layer shows that the defect rate for Ta_2O_5 decrease from 1449 to 1038 and SiO_2 from 221 to 122.

In view of these results, the effect of the number of subsequent annealing was investigated. Samples were annealed under the same conditions as the first annealing at 500°C and in the same oven. The SiO_2 deposition series performed on DIBS underwent a second annealing.

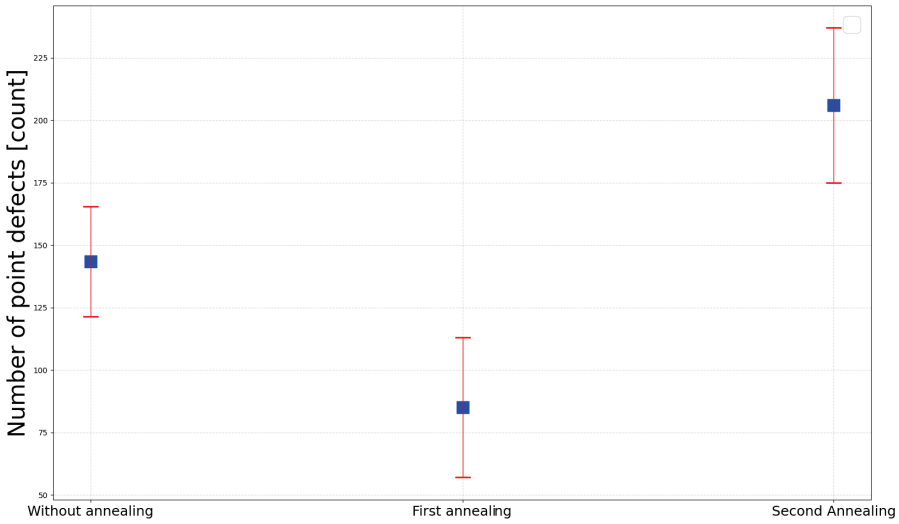

Figure 4.13: Influence of two annealing on the number of defects on SiO_2 monolayers samples.

A similar test was performed on Ta_2O_5 DIBS samples. The Table 4.5 and Figure 4.14 present the results for two samples which were annealed. The figure 4.15 shows the spatial distribution of detected defect after the first and the second annealing. Contrary to what was observed for SiO_2, in Figure 4.13, in this case a second annealing does not seem to increase the number of defects present in the coating. But the defect number does not evolve. The curative aspect of the annealing, in terms of reducing the number of defects is visible only after one annealing.

4.3.2 Influence of the substrate temperature

In section 4.3.1, we have seen the effect of the preheating of the coating machine on the number of defects. Here we study the effect of a direct heating of the substrate using a high temperature deposition system. The coating machine DIBS has a heating substrate holder that has been tested to measure the impact of the substrate temperature on the creation of point defects (Figure 4.16). The substrate is heated with heating ramp for approximately 3 hours and up to 3 different temperatures.

Table 4.5: Results of the number of thermal annealing on the number of defects on two Ta_2O_5 samples of 500 nm thickness.

Sample	Before annealing	After annealing 1 [defect/mm²]	After annealing 2
D21002R PL7464	508	345	259
D21002R PL73762	336	315	370
Median	422	330	314

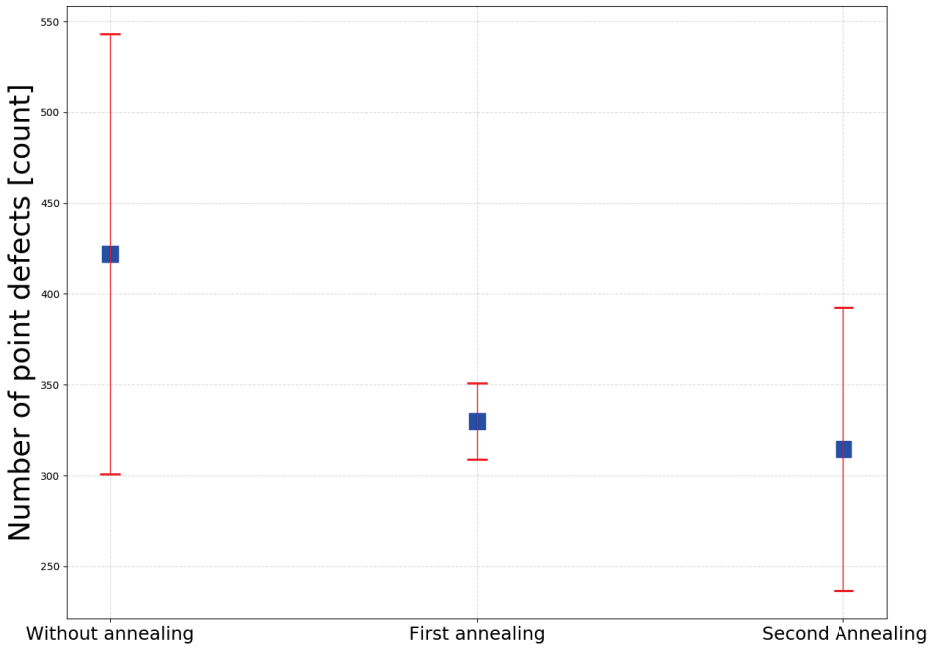

Figure 4.14: Influence of two annealing on the number of defects on Ta_2O_5 sample (D21002R).

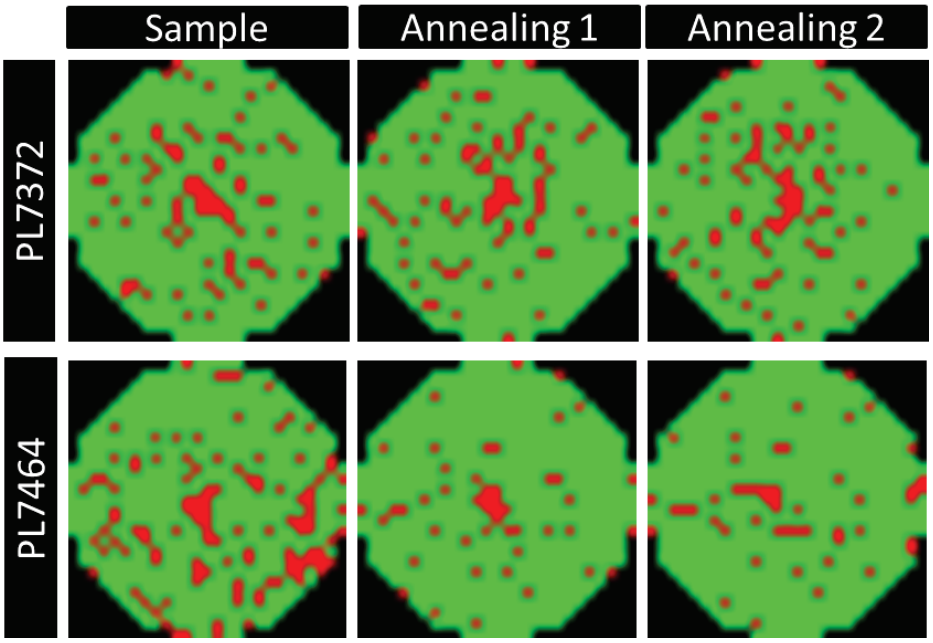

Figure 4.15: Mapping of sample D21002R PL7262 showing the effect of the number of annealing on the number of detected defects.

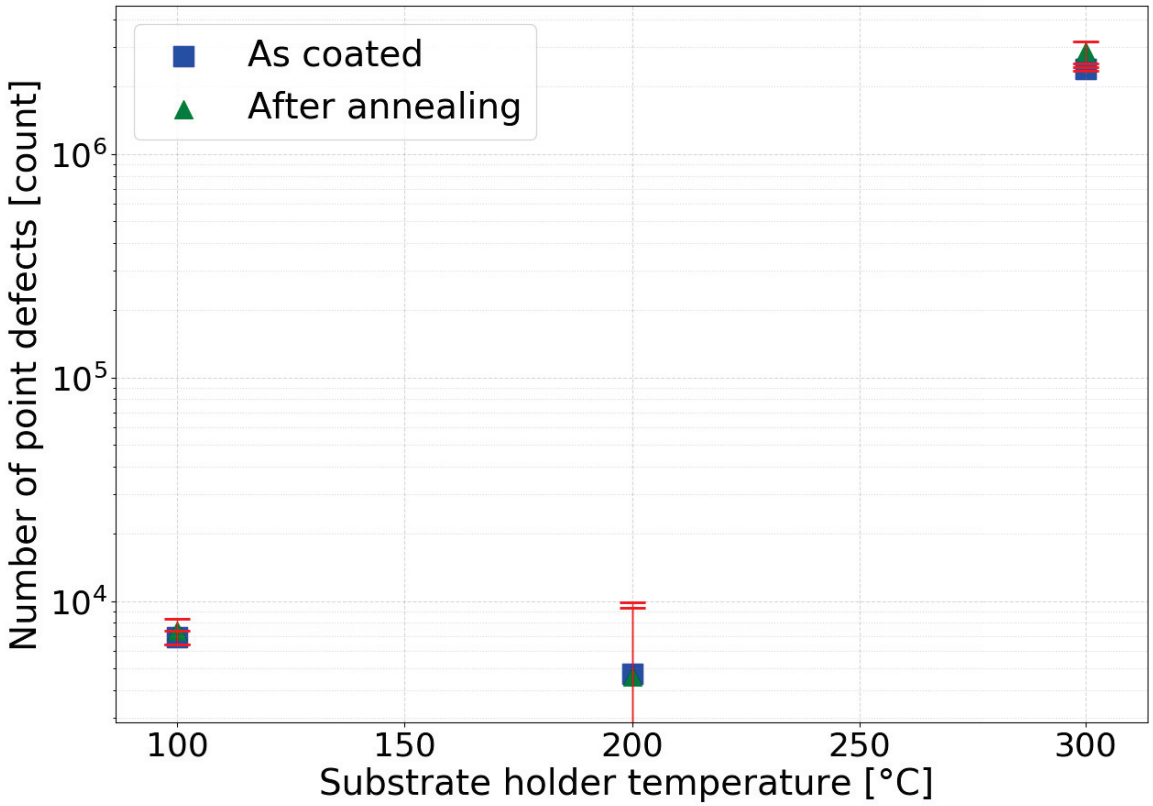

Figure 4.16: Number of defects in Ta_2O_5 layers as a function of the temperatures of the heating substrate holder. Note the logarithmic y-axis scale, needed to account for the number of defects for the highest temperature sample.

For this study, the thickness of the deposited layer has been fixed to 1000 nm in order to see the impact of the substrate temperature only and not a variation because of the thickness, see Figure 4.18. Three runs were performed at three different temperatures 100°C, 200°C and 300°C and only two substrates per run. The heating of the substrate at 100°C and 200°C appears to produce deposition of similar quality, apart from the surface of the coating deposited at 200°C having a roughness with RMS 0.92 Å, compared to 0.77 Å for the one at 100°C . On the other hand, the coating deposited on a substrate with temperature 300°C is highly degraded. Indeed the sample presents a deteriorated roughness (Figures 4.17 and 4.19,) with an RMS value of 3.59 Å, and an increase in the number of defects of two orders of magnitude. To the naked eye, the sample appears brownish (see Figure 4.18).

Figure 4.17: Three pictures (513 µm x 513 µm) of one sample of each RUN after deposition with the Heating substrate holder with 3 increasing temperatures 100°C, 200°C and 300°C. For the third one, the high roughness is clearly visible.

Figure 4.18: Pictures of the samples at the exit of the coating chamber. At 100°C the samples are transparent but at 200°C and 300°C the samples are more and more brownish.

In order to check if it was the substrate surface roughness that was modified, the substrate roughness was measured before and after the ghost deposition performed after heating for 3 hours at 300°C (Table 4.7) : substrate that has underwent the whole procedure without the deposition (pumping down, heating, venting) to see the impact of the machine conditions machine on the point defects rate. It was found to have an RMS about 0.6 Å before and 0.7 Å after, confirming that the high temperature affects the coating roughness and not the substrate. On the other hand, the number of defects is a factor 10 larger, suggesting that the heating procedure reveals underlying substrate defects.

Table 4.6: Information about deposition runs with the high temperature system.

Temperatures [°C]	Roughness [Å RMS]	Defect Density before [defect/mm²]	Defect density after [defect/mm²]
100	0.77	27	29
200	0.92	19	18
300	3.59	9445	11298

Table 4.7: Characteristics of the test sample measured before and after the "ghost deposition".

Substrate	Roughness [Å RMS]	Defect Density [defect/mm²]
Before "ghost deposition"	0.64	0.016 (4 defects)
After "ghost deposition"	0.76	0.19 (49 defects)

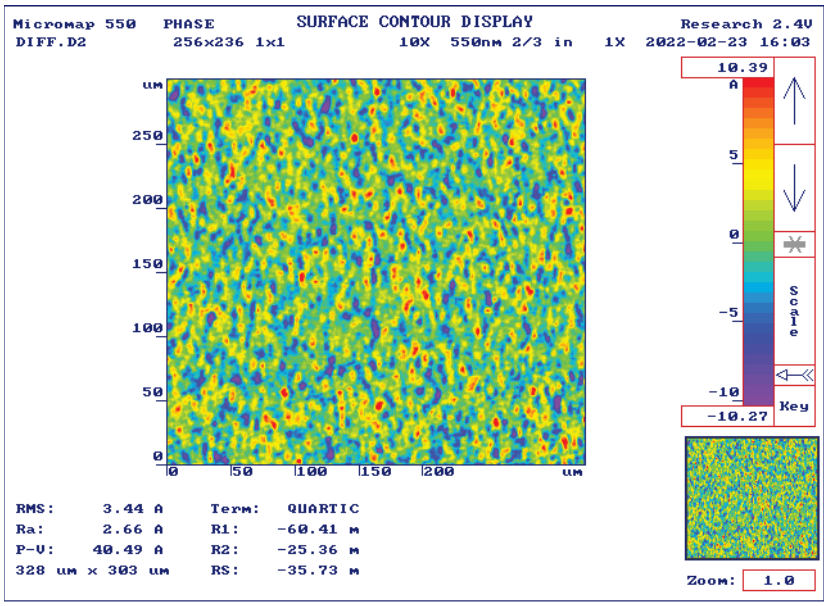

Figure 4.19: Roughness cartography of an area of the sample at 300°C.

4.3.3 Influence of the beam intensity I_B and the voltage V_B

Others parameters affecting the coating deposition procedure have been modified : the intensity of the beam V_b which represent the atoms energy sent by the source and I_b the voltage of the beam which represent the number of projectiles per unit of time.

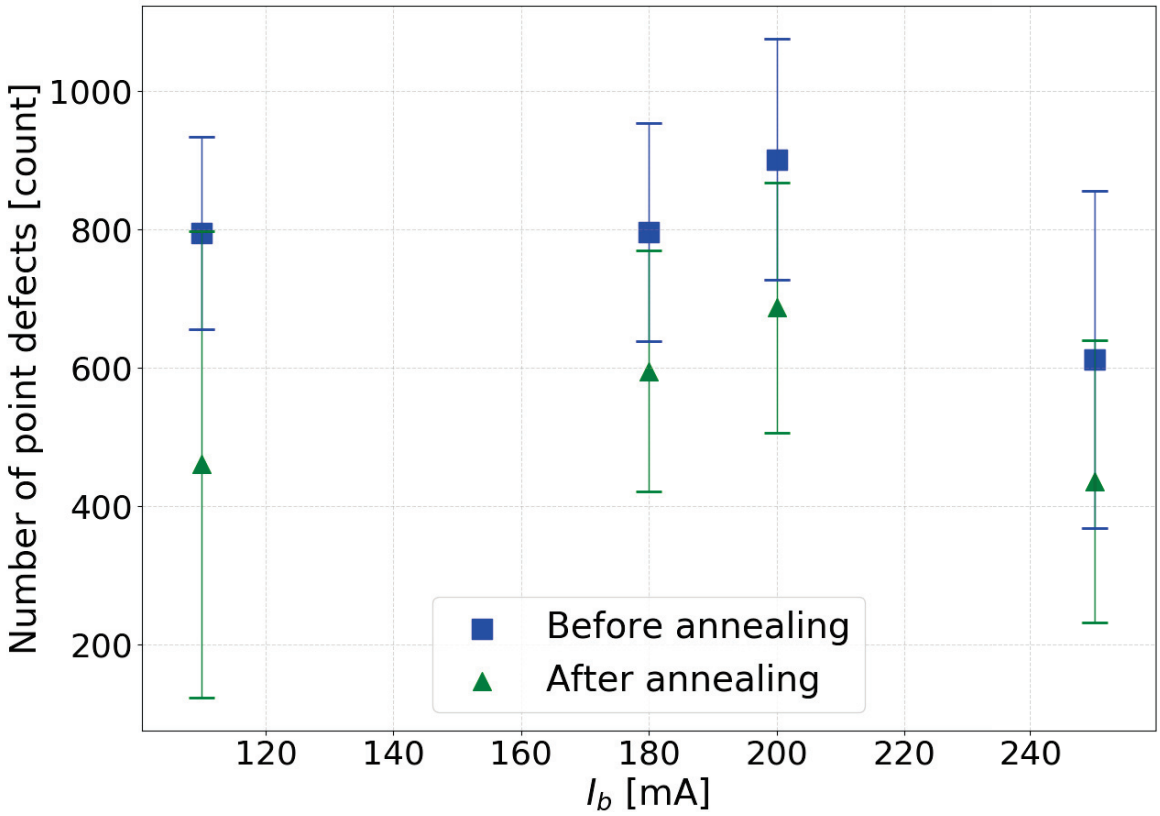

Figure 4.20: The number of defects in Ta_2O_5 layers as a function of the intensity.

Four coating runs were made with 4 different I_b values at 100 mA, 180 mA, 200 mA and 250 mA with a thickness fixed at 1000 nm. To increase the statistics and improve the analysis of these point defects, 3 substrates are placed in the machine for each run. The figure 4.20 shows the number of point defects, before and after annealing, in Ta_2O_5 as a function of the intensity. The points represent the median of the 3 samples. The number of point defects seems to remain constant with the intensity of the beam. In first approximation, the variation of the ion beam current impacts the deposition rate: higher the ion current, higher the deposition rate. From Figure 4.20, the creation of defects does not seem to be linked to the deposition rate. Besides, there is no change in roughness but the layer of samples becomes brownish and therefore absorbs in the visible range, which can interfere with the counting of defects done with the profilometer.

Concerning V_b, 3 coating runs have been done at 500 V, 1000 V and 1250 V with 3 substrates per run. The figure 4.21 presents the point defects number as a function of the voltage. As can be seen, the point defects number increases with the voltage of the beam.

The hypothesis that the increase of the number of defects with the value of V_b is due to the deposition speed is contradicted by the observation that the number of defects does not evolve with I_b, also affecting the deposition speed BUNDESMANN et NEUMANN [2018]. In addition to changing the deposition rate, V_b allows to change the energy of the sputtered particles. We used the SRIM (Stopping and Range of Ions in Matter) ZIEGLER et collab. [2010] software simulation to calculate the ions energy distribution of particles as a function of parameters V_b. The Figure 4.22 presents the number of defects as a function of the ions energy. The linear trend observed clearly shows that the energy of the sputtered particles has an effect on the number of defects created during deposition process.

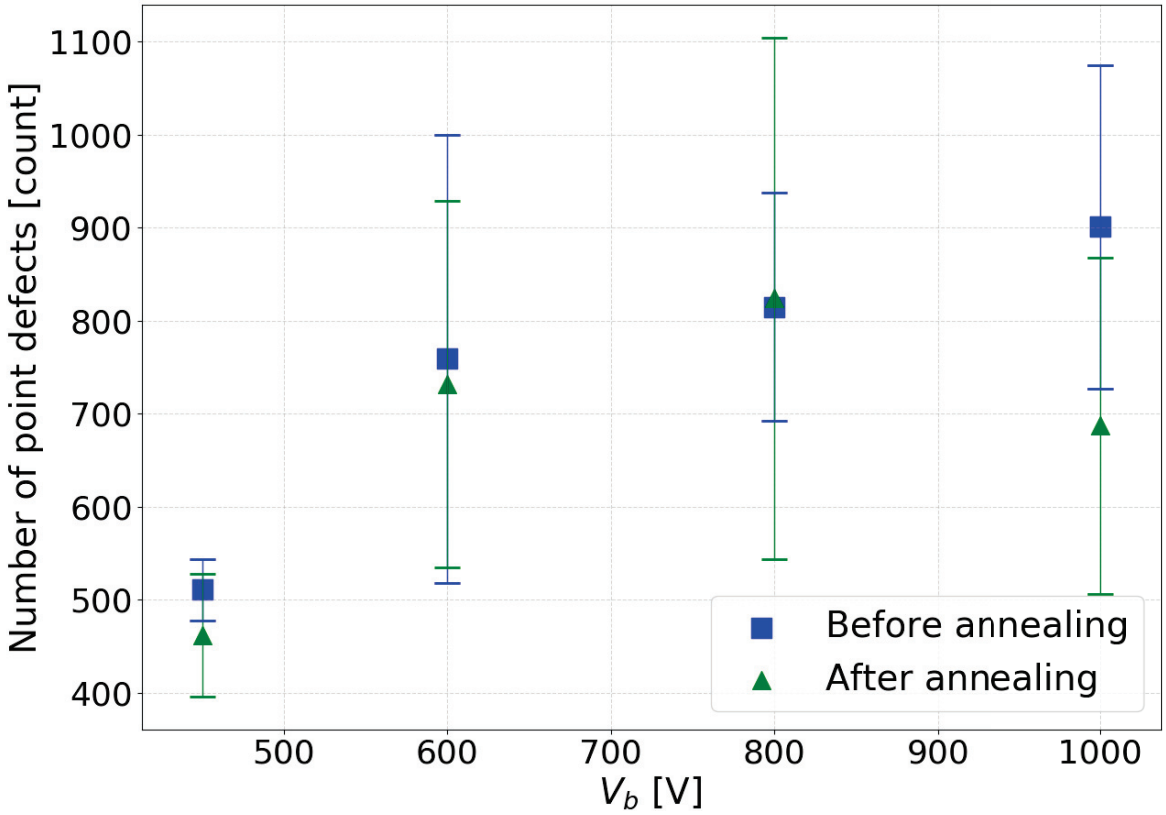

Figure 4.21: The number of defects in Ta_2O_5 layers as a function of the beam voltage.

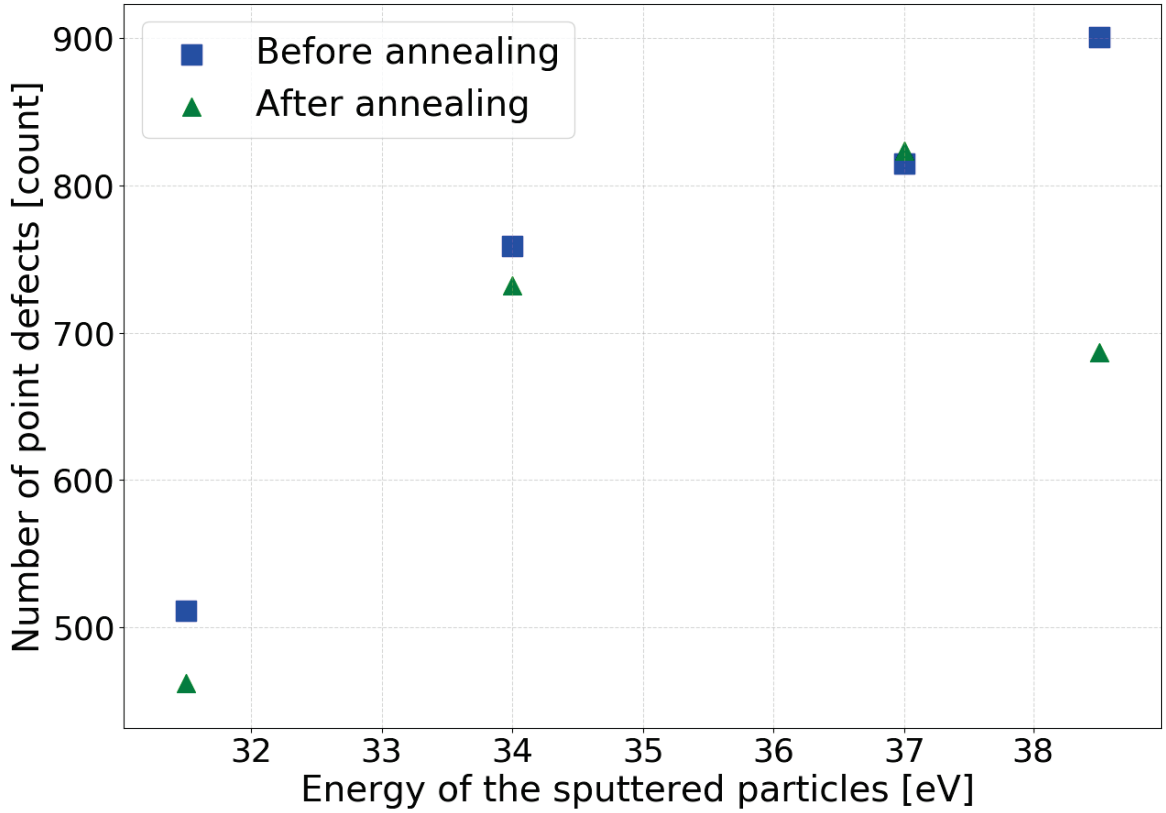

Figure 4.22: The number of defects in Ta_2O_5 layers as a function of the ion energy.

4.3.4 Influence of the deposition chamber : DIBS - GRAND COATER

For better understanding the influence of the coating machine on the defects generation, coating depositions were made in the large machine to compare with the DIBS results. The first comparison was focused on Ta_2O_5. Figure 4.23 shows that the amount of point defects present in the DIBS series is significantly higher than those of the large machine Grand Coater (GC). Between the two thickest sample of DIBS and GC there is a factor of 3. This difference can be explained by the size of the coating machines. As a reminder, the size of the DIBS machine is 0.5 m^3 while the GC is about 10 m^3. The deposition parameters are different as well. Compared to DIBS, the target-substrate distance is 2 times larger in the GC and the distance shutter-substrate also. These are probably parameters that can induce a quantitative difference in the defect rate.

Apart from the difference in the overall number of defects, the general trend of dependence on the layer thickness observed in the samples coated in the GC is consistent with the one observed in samples coated in the DIBS (Figures 4.24 and 4.25), with one exception. In Figure 4.24, the number of defects observed for the fourth thickness is not aligned with the trend and is very high compared to the others. It is worth mentioning that the production of the samples has started with these ones. The coating machine had been cleaned just before starting the run. It has often been observed that the more runs the machine makes, the lower the defect rate. Sputtered material coats the metallic walls and liners of the chamber and overlay dust or particles that could otherwise come off and pollute the deposition.

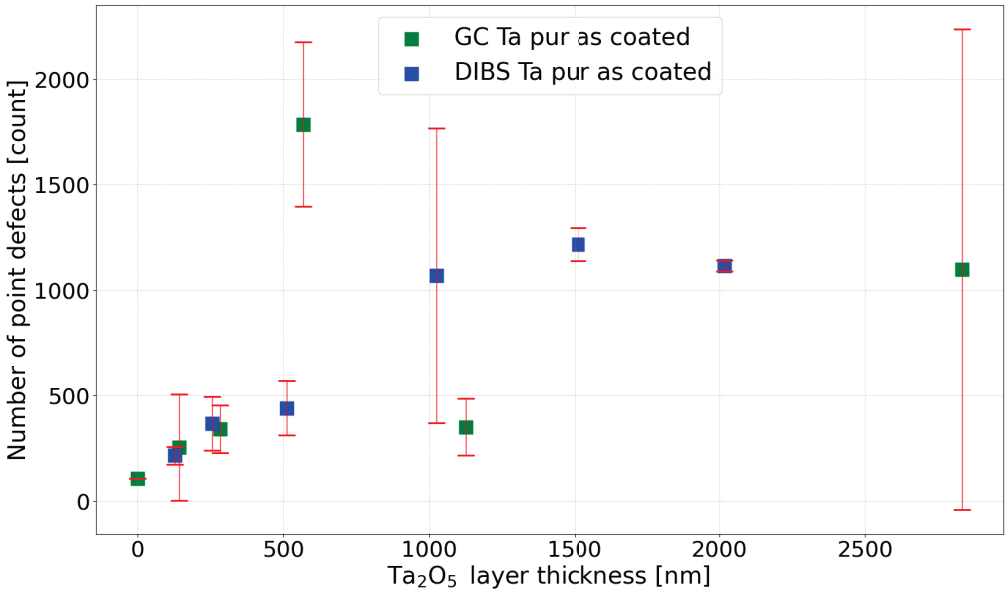

Figure 4.23: Number of point defects in Ta_2O_5 layers as a function of the layer thickness in the DIBS and in the GC machines.

4.3.5 Influence of the doping

The large mirrors of the gravitational wave detectors are stacks of silica and titanium-doped tantalum (Ti:Ta_2O_5) GRANATA et collab. [2020]. For reasons of availability and accessibility to the machines, the PhD work has been started with pure tantala. In order to better understand and characterize this material, samples with coating of titanium-doped tantalum have been made in the GC. In figure 4.25, which presents the number of defects in Ti:Ta_2O_5 as a function of thickness. The evolution of the number of defects with thickness appears to be comparable.

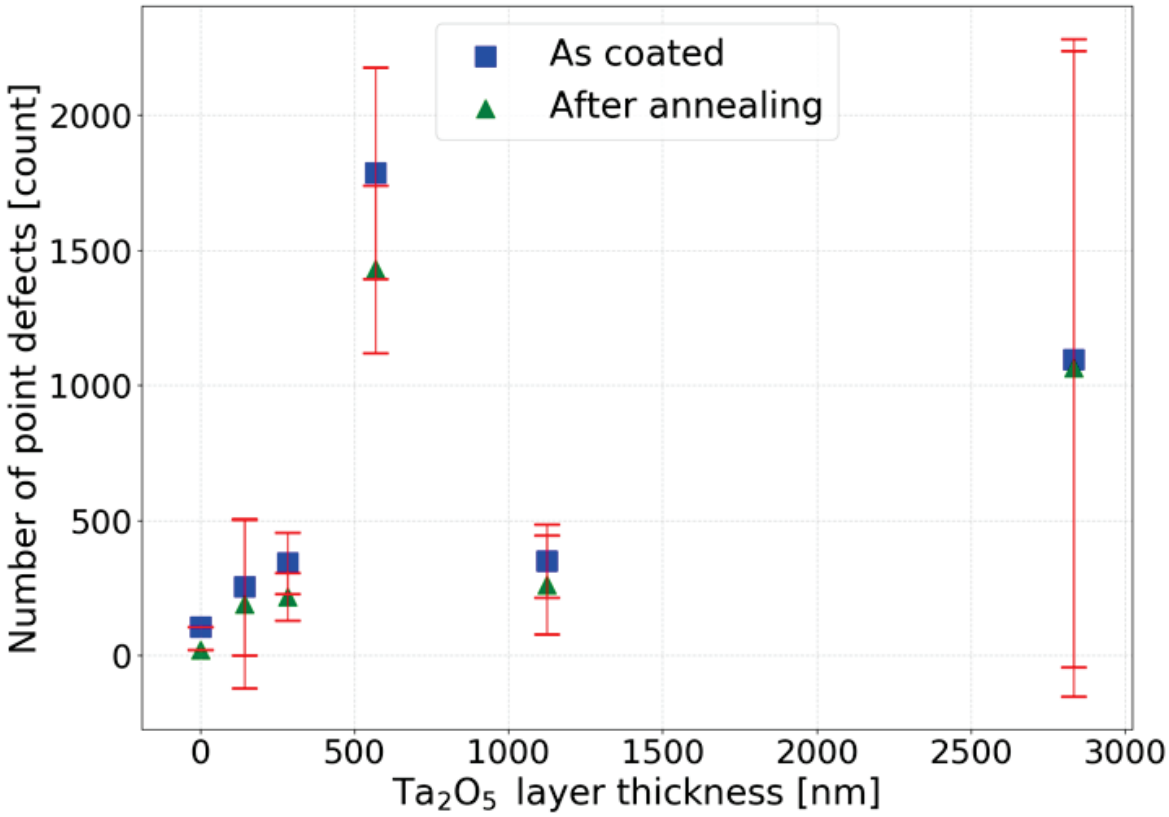

Figure 4.24: Number of point defects in Ta_2O_5 layers as a function of the layer thickness processed in the GC coating machine.

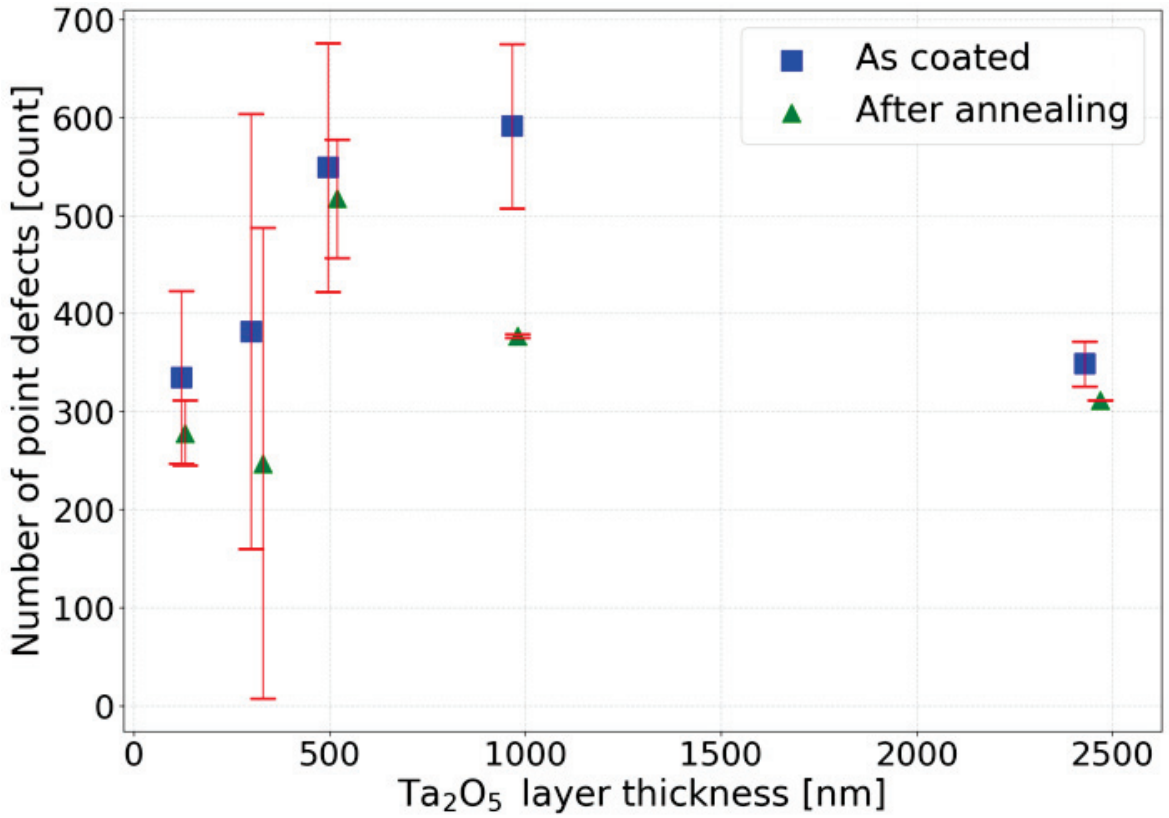

Figure 4.25: Number of point defects in pur Ta_2O_5 pure and titania doped tantala layers as a function of the layer thickness processed in the GC coating machine.

4.3.6 Influence of the substrate

In all results of the in-depth study, a large spread of defect densities has been observed over several samples of the same run (represented by the error bars in all figures). Given these observations, one can wonder what is the impact of the choice of the substrate before coating on the defect creation. To better understand the effect, four substrates without coating were measured before and after annealing. The results are shown in Table 4.8. The average number of defects is 58 before annealing and 13 after annealing.

To explain the spread in number of defects, it is likely that there is a native contribution from the substrate because the choice of substrate is done randomly. In addition, the several steps of substrate manipulation by the operators (cleaning, mounting in the frame, loading inside the coating machine) can have a critical impact on the surface condition before coating.

Table 4.8: Number of defects on bare micropolished substrates before and after annealing.

Substrate	Before annealing	After annealing
Substrate 1	60	14
Substrate 2	81	12
Substrate 3	57	23
Substrate 4	41	9

4.3.7 Influence of the sample mount

It was showed in section 3.2.3 that the area near the edge of the substrate has a higher defect density than elsewhere. The point is to understand if the holder itself has an impact on the defect formation. A test was conducted on three 1 inch substrates mounted in 3 different holders spaced by 10 cm the ones from the others in the GC :

- LMA holder : sandblasted aluminium frame
- Electropolished stainless steel
- Industrial process

The standard aluminum frame - (LMA process), an aluminium frame (industrial process) and a stainless steel frame - (electroplished). Figure 4.28, shows the distribution of defects for the three cases. The mount has a clear impact on the total number of defects. The mount that generates the most defects is the standard mount used at LMA whereas the mount treated with the process 3 allow a reduction of the number of defects by a factor of 5. The process 2 mount is in-between with a reduction of about 60%. The median defect size is about 0.9 µm for the three mounts, as shown in Figure 4.27, and the mount does not seem to have any effect on the size distribution.

Thanks to this study, the frame used at LMA was updated, leading to an increase in coating quality.

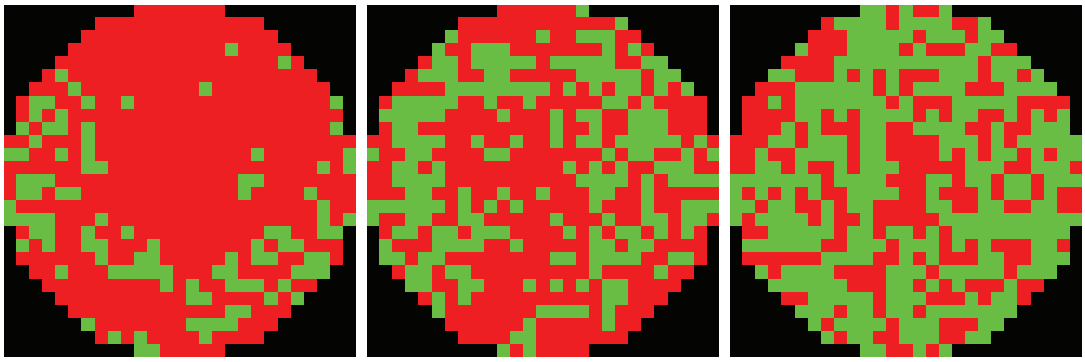

(a) (b) (c)

Figure 4.26: Defect map of the three mirrors samples done with three different mounts in the GC machine. In (a) LMA process in (b) electroplished process and (c) Industrial process.

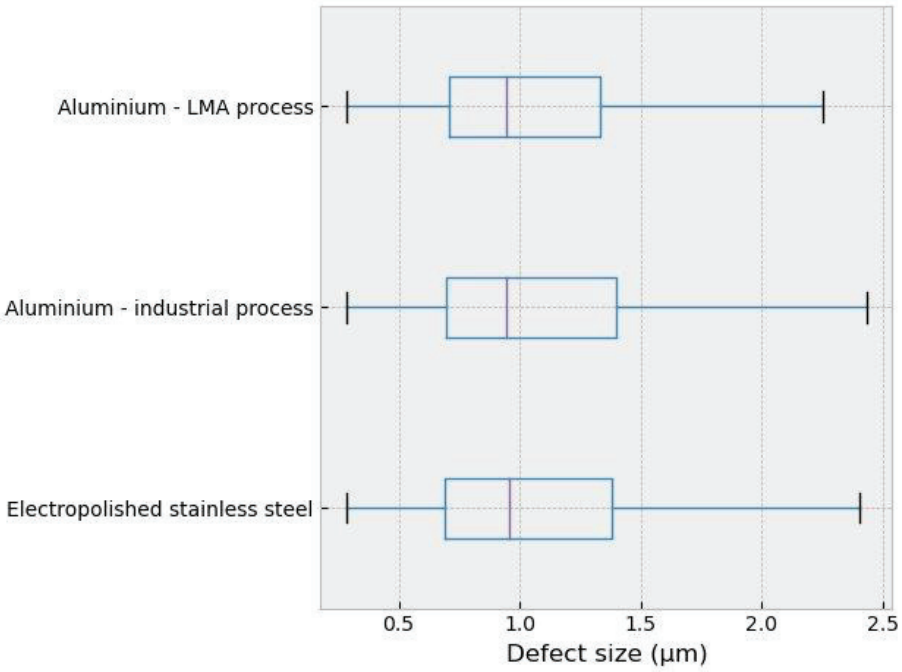

Figure 4.27: Defect size for the three sample mount after annealing.

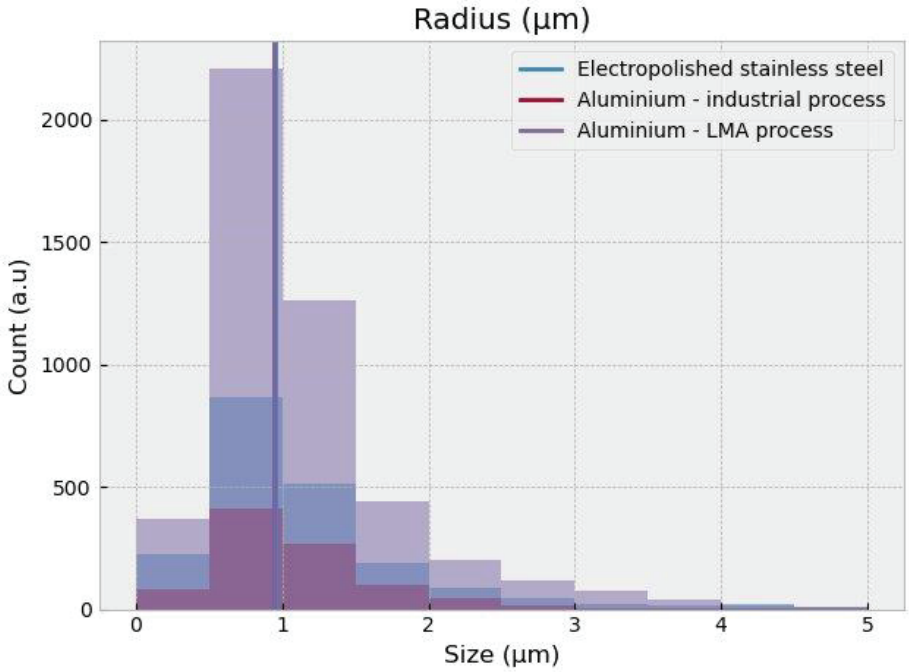

Figure 4.28: Defect size for the the different mount using three different process.

4.4 Study of Defect Sizes

Thanks to the offline image processing developed specifically for this study and documented in in Chapter 3, the defect size information of each defect detected by the instrument has been extracted SAYAH et collab. [2021].

4.4.1 Preliminary study

Figure 4.29 shows the distribution of defect sizes of the thickest samples of Ta_2O_5 and SiO_2 produced for the preliminary study before and after annealing. The distributions have been normalized to ease the shape comparison. The peak visible at 1.8 µm on the histogram is due to the limit of the image pixel size which is about 1.25 µm. All defects smaller than the pixel size are found in this bar. Before annealing the median defects size is about 3.5 µm for SiO_2 and 3.2 µm for Ta_2O_5. After annealing, the median defects size is 3.66 µm for SiO_2 and 2.96 µm for Ta_2O_5, with a 68% probability region of [3.04, 4.26] µm and [2.37, 3.48] µm, respectively, showing that the defects size is lower for Ta_2O_5 than for SiO_2.The 95% probability regions are quite large, because of the limited statistics, and do not allow quantitive comparisons. Also, the annealing seems to slightly lower the defects size for Ta_2O_5, while the opposite is observed for SiO_2. But still, the number of defects in the SiO_2 is low and do not allow drawing quantitative conclusions. The results are obtained with the *Blob log* algorithm (see Section 3.4.2).

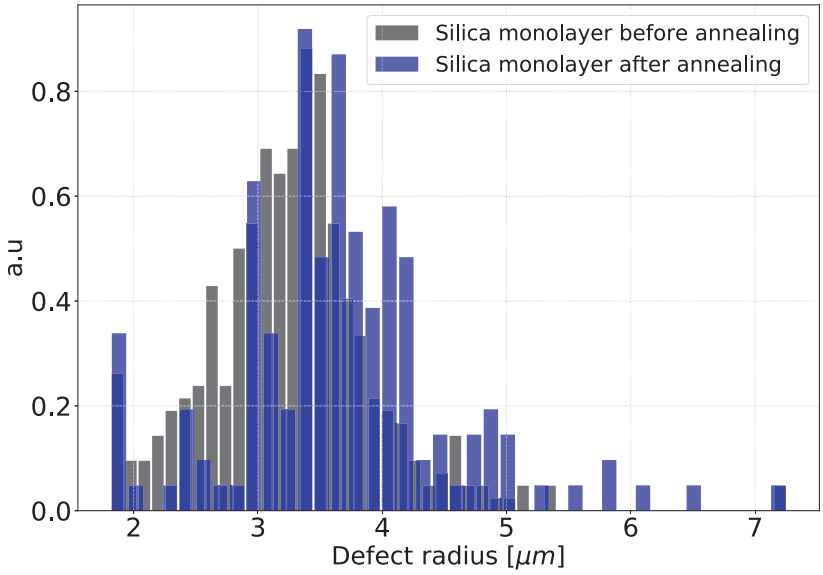

(a)

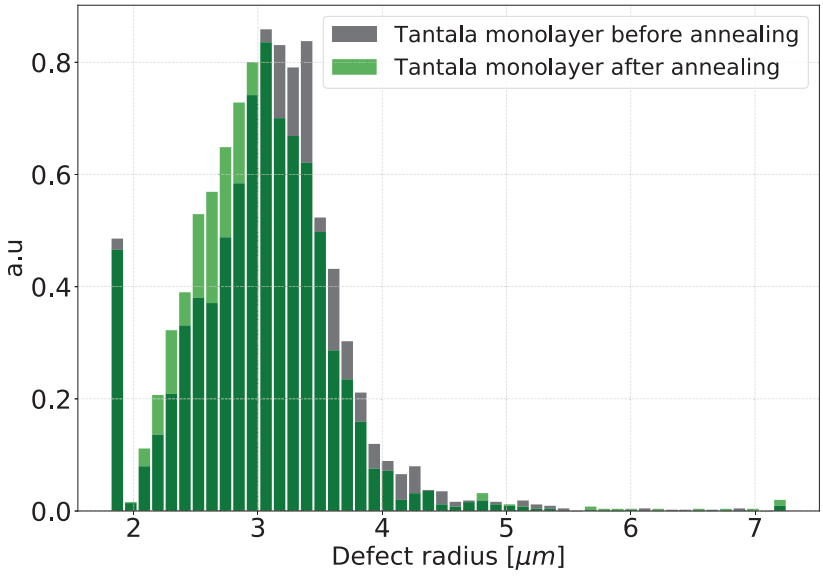

(b)

Figure 4.29: Defect size for the thickest samples of the two materials, SiO_2 (a) and Ta_2O_5 (b), before and after annealing. The distributions have been normalized to ease the shape comparison

4.4.2 In-depth study

The study of the size of the defects was repeated on the new samples produced in the DIBS machine, taking advantage of the higher statistics.

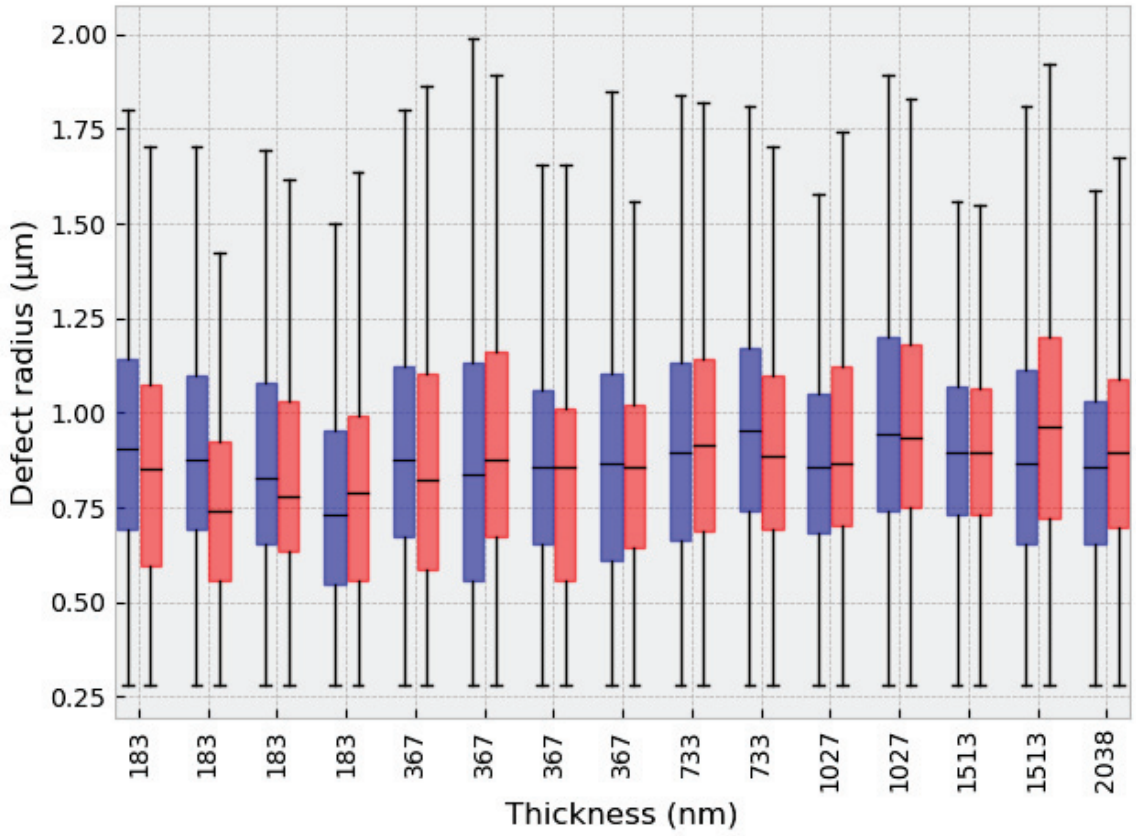

Figure 4.30: Defect size for the Ta_2O_5 before annealing (in blue) and after annealing (in red) as a function of the sample thickness in the DIBS machine.

Figures 4.30, 4.32 and 4.33 show the defect sizes for the samples of Ta_2O_5 deposited in the DIBS, Ta_2O_5 deposited in the GC, and Ti:Ta2O5 deposited in the GC, respectively. For each sample, the median is shown, together with the 68% and 90% confidence intervals, before (blue) and after (red) annealing. The median seems to be constant around 0.85 and 0.92 µm in the three cases, and the annealing has no statistically significant effect. To increase the statistics, and under the hypothesis that the defect size does not depend on thickness, all defect sizes for the samples coated in the DIBS machine are shown in Figure 4.31. The median size is 0.9 µm before annealing with a 68% probability region of [0.57, 1.25] µm and 0.91 µm after annealing with a 68% probability region of [0.57, 1.26] µm. This confirms that defect size is not dependent to the layer thickness and is not affected by the annealing. These results are obtained with the SEP algorithm. A better resolution of the images produced by the Eotech machine with respect to the Micromap, together with a sligthly different definition of the size between the *Blob log* and the SEP algorithms can explain the difference in evaluated median defect size.

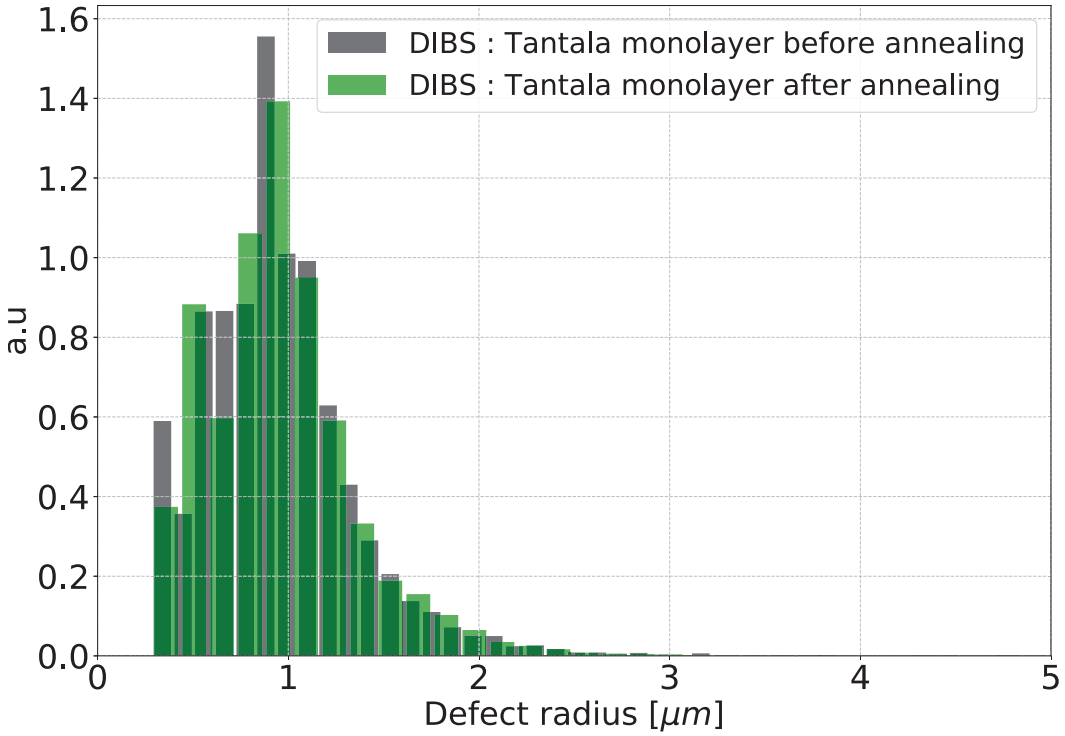

Figure 4.31: Defect size for all samples produced in the DIBS with the standard parameters (I_b = 200 mA, V_b=1000 V, Ta_2O_5 monolayer) before and after annealing. The distributions have been normalized to ease the shape comparison.

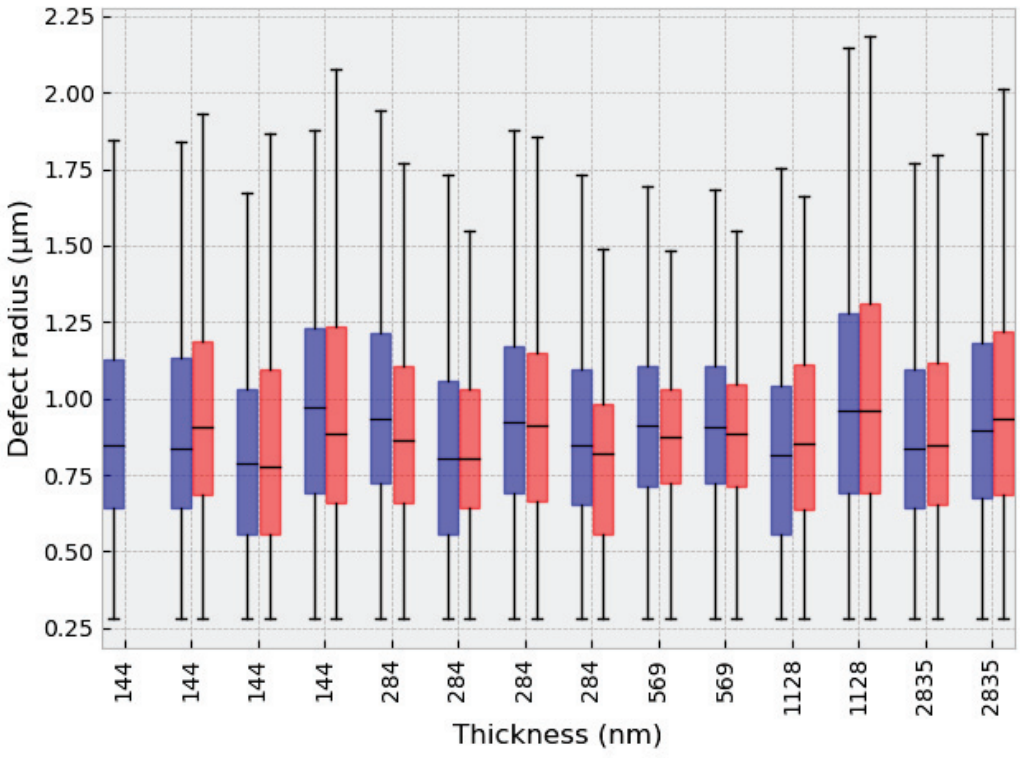

Figure 4.32: Defect size for all Ta_2O_5 samples produced in the GC machine with the standard parameters before annealing (in blue) and after annealing (in red).

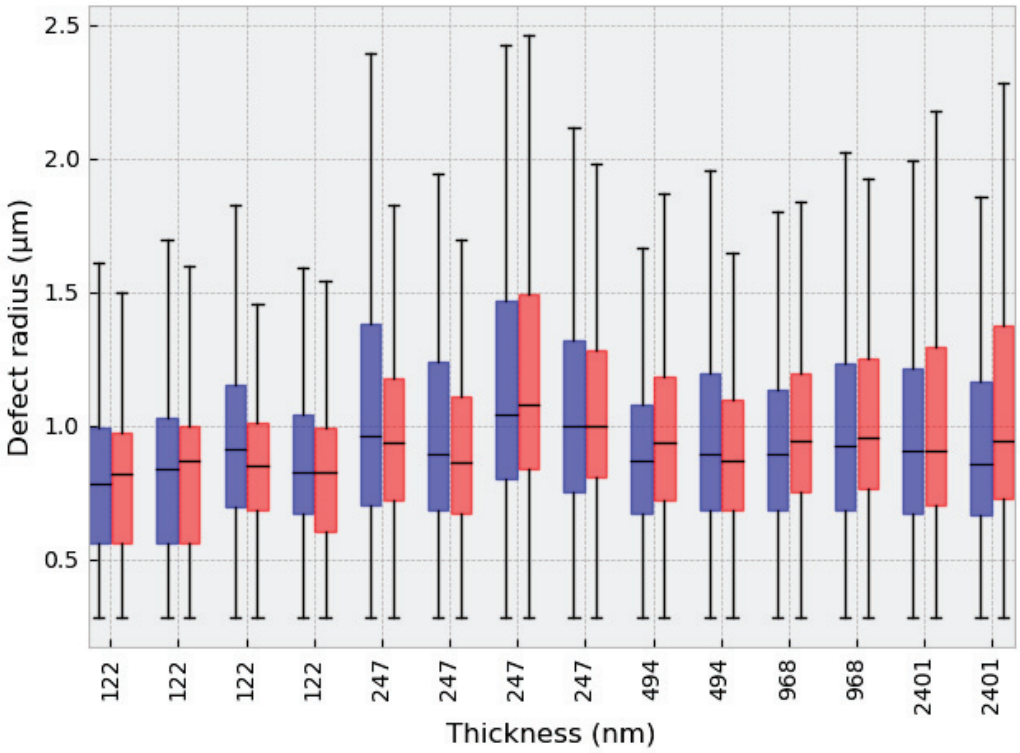

Figure 4.33: Defect size for all titania doped tantala samples produced in the GC machine with the standard parameters before (in blue) and after annealing (in red).

4.5 Summary

It has been observed that monolayers of tantala and silica present a lot of point defects likely related to the thickness and to the materials. Tantala monolayers have a higher defect density compared to silica monolayers of about a factor two. For the two materials, the density of point defect seems to increase with the layer thickness as it has been shown in section 4.2. This results has been observed on the two coating deposition machines (the DIBS and the GC). Different coating deposition parameters have been tested to identify their impact on the defect density. The thermal annealing has a positive influence on the defect density reducing them about 20 to 30% on tantala layers and 40% to 50% on silica layers. However, thermal annealing does not seem to impact the size of the defects. Finally, we have developed dedicated algorithms to determine the size of each detected defect and to compare the median of size defects according to the material and to the coating deposition machine.

4.6 References

BUNDESMANN, C. et H. NEUMANN. 2018, «Tutorial: The systematics of ion beam sputtering for deposition of thin films with tailored properties», *Journal of Applied Physics*, vol. 124, 23, doi: 10.1063/1.5054046, 231102. 84

GRANATA, M., A. AMATO, L. BALZARINI, M. CANEPA, J. DEGALLAIX, D. FOREST, V. DOLIQUE, L. MERENI, C. MICHEL, L. PINARD, B. SASSOLAS, J. TEILLON et G. CAGNOLI. 2020, «Amorphous optical coatings of present gravitational-wave interferometers», *Classical and Quantum Gravity*, vol. 37, 9, doi:10.1088/1361-6382/ab77e9, p. 095 004. URL https://doi.org/10.1088/1361-6382/ab77e9. 79, 86

HULTMAN, L., B. JOHANSSON, J. SUNDGREN, L. C. MARKERT et J. E. GREENE. 1988, «Ar incor-

poration in epitaxial tin films deposited by reactive magnetron sputtering in mixed ar/n2 discharges», *Applied Physics Letters*, vol. 53, 13, doi:10.1063/1.100014, p. 1175–1177. URL https://doi.org/10.1063/1.100014. 68

KING, B., I. VERYOVKIN, J. MOORE, W. CALAWAY et M. PELLIN. 2009, «Formation of neutral clusters during sputtering of gold», *Surface Science*, vol. 603, 5, doi:https://doi.org/10.1016/j.susc.2009.01.027, p. 819–825, ISSN 0039-6028. URL https://doi.org/10.1016/j.susc.2009.01.027. 68

KNOLLENBERG, R. G., D. LONG et S. LOPEZ. 1995, «An in-situ fiber optics sensor for monitoring particle microcontamination during an ibs optical coating process», dans *Optical Interference Coatings*, Optica Publishing Group, p. TuB6. URL http://opg.optica.org/abstract.cfm?URI=OIC-1995-TuB6. 68

MALOBABIC, S., M. JUPÉ, P. KADKHODA et D. RISTAU. 2015, «Towards a magnetic field separation in ion beam sputtering processes», *Thin Solid Films*, vol. 592, doi:10.1016/j.tsf.2015.05.016. 68

NUCCIO, L. 2009, *Diffusion of small molecules in amorphous SiO2: effects on the properties of the material and on its point defects*, thèse de doctorat, University of Palermo. 77

PANJAN, P., A. DRNOVŠEK, P. GSELMAN, M. ČEKADA et M. PANJAN. 2020, «Review of growth defects in thin films prepared by pvd techniques», *The Coatings*, vol. 10, p. 447. 68, 69, 70, 71

PETROV, I., L. HULTMAN, J. SUNDGREN et J. E. GREENE. 1992, «Polycrystalline tin films deposited by reactive bias magnetron sputtering: Effects of ion bombardment on resputtering rates, film composition, and microstructure», *Journal of Vacuum Science & Technology A*, vol. 10, 2, doi:10.1116/1.578074, p. 265–272. URL https://doi.org/10.1116/1.578074. 68

SAYAH, S., B. SASSOLAS, J. DEGALLAIX, L. PINARD, C. MICHEL, V. SORDINI et G. CAGNOLI. 2021, «Point defects in ibs coating for very low loss mirrors», *Appl. Opt.*, vol. 60, 14, doi:10.1364/AO.415462, p. 4068–4073. URL http://www.osapublishing.org/ao/abstract.cfm?URI=ao-60-14-4068. 75, 90

WALTON, C. C., P. A. KEARNEY, J. A. FOLTA, D. W. SWEENEY et P. B. MIRKARIMI. 2003, «Understanding particle defect transport in an ultra clean sputter coating process», dans *Emerging Lithographic Technologies VII*, vol. 5037, édité par R. L. Engelstad, International Society for Optics and Photonics, SPIE, p. 470 – 481, doi:10.1117/12.484970. URL https://doi.org/10.1117/12.484970. 68

WUCHER, A. et M. WAHL. 1996, «The formation of clusters during ion induced sputtering of metals», *Nuclear Instruments and Methods in Physics Research Section B: Beam Interactions with Materials and Atoms*, vol. 115, 1, doi:https://doi.org/10.1016/0168-583X(96)00153-X, p. 581–589, ISSN 0168-583X. URL https://www.sciencedirect.com/science/article/pii/0168583X9600153X, atomic Collisions in Solids. 68

YAMAMOTO, H. 2015, «Mirror profile and intracavity field profile», G1500262-v3 LIGO/Caltech. 68

ZIEGLER, J. F., M. ZIEGLER et J. BIERSACK. 2010, «Srim – the stopping and range of ions in matter (2010)», *Nuclear Instruments and Methods in Physics Research Section B: Beam Interactions with Materials and Atoms*, vol. 268, 11, doi:https://doi.org/10.1016/j.nimb.2010.02.091, p. 1818–1823, ISSN 0168-583X. URL https://www.sciencedirect.com/science/article/pii/S0168583X10001862, 19th International Conference on Ion Beam Analysis. 84

Chapter 5

Scattered light

Contents

5.1 Introduction

The subject of this work is to study the point defects present in the coating of mirrors for gravitational waves detectors, as they are a source of scattered light, inducing a loss of sensitivity. The study of scattering by coatings has been an active field for many years, especially for physics experiments requiring very low loss optics BENNETT et MATTSSON [1989]; STOVER [2012]. For our analysis, a large set of samples has been produced, with different characteristics. Chapter 4 describes the measurement of the density and size of point defects in these samples. This chapter concerns the same samples studied in Chapter 4, and is dedicated to the measurement of their scattered light.

Before presenting the results, the scattered light is introduced together with the typical observables used to quantify it. In addition, we present simulated results of the light scattered by a defect, in a simplified scenario.

5.2 Theory of Light Scattering by point defects

5.2.1 Principle

Light is described as an electromagnetic wave, composed of an electric field and a magnetic field whose variations are described by Maxwell's equations MACLEOD [2010]. The theory of electromagnetism at the first order AMRA [1994a,b] allows to describe the diffusion of light by optical stacks in the case where the roughness is low compared to the wavelength of the incident light. The model describing light scattering by interference filters is detailed in AMRA et collab. [2021]. The light scattered in a particular direction (θ, ϕ) by a surface is given by the formula below :

$$I(\theta,\phi) = \sum_{i,j} C_{ij}(\theta,\phi)\alpha_{ij}(\theta,\phi)\gamma_{ij}(\theta,\phi) \tag{5.1}$$

where $I(\theta,\phi)$ designates the scattered intensity at a particular direction (θ,ϕ) of space (θ the angle measured from the normal to the sample and ϕ is the polar angle as shown in Figure 5.1).

The intensity I can also be represents by the scattered light ($d\phi/d\Omega$) per unit solid angle (sr^{-1}), and is often related to the BRDF, as introduced Chapter 3, by the formula

$$I(\theta,\phi) = \frac{d\phi}{d\Omega} = \mathrm{BRDF}(\theta,\phi)cos\theta \tag{5.2}$$

The wave vectors $\vec{k}^-$ and $\vec{k}^+$ of the scattered light in reflexion and transmission, are defined in Figure 5.1 as :

$$\vec{k^-} = \frac{2\pi n_0}{\lambda}\begin{Bmatrix} sin\theta cos\phi \\ sin\theta sin\phi \\ -cos\theta \end{Bmatrix} \tag{5.3}$$

$$\vec{k^+} = \frac{2\pi n_s}{\lambda}\begin{Bmatrix} sin\theta cos\phi \\ sin\theta sin\phi \\ cos\theta \end{Bmatrix} \tag{5.4}$$

with n_0 the refraction index of the incident plane and n_s the refraction index of the scattered plan. $C_{i,j} = C_i\ \overline{C_j}$ represents a design-dependent optical factor whose calculation depends on the origin of scattering (surface or bulk) AMRA [1993], polarization of light, and illumination and observation angles

$$C^-(\theta,\phi) = C^-(\theta) = \frac{1}{2}\left(\frac{2\pi n_0}{\lambda}\right)^2\left[cos^2\theta_0|q_s|^2 + |q_p|^2\right] \tag{5.5}$$

$$C^+(\theta,\phi) = C^+(\theta) = \frac{1}{2}\left(\frac{n_s^3}{n_0}\right)\left(\frac{2\pi}{\lambda}\right)^2\left[cos^2\theta_s|q_s|^2 + |q_p|^2\right] \tag{5.6}$$

With

$$q_s(\theta) = j\Big(\frac{2\pi}{\lambda}\Big)2n_0(n_0 - n_s)(n_0 cos\theta_0 + n_s cos\theta_s)^{-1} \tag{5.7}$$

$$q_p(\theta) = j\Big(\frac{2\pi}{\lambda}\Big)2n_0(n_0 - n_s)(\frac{n_0}{cos\theta_0} + \frac{n_s}{cos\theta_s})^{-1} \tag{5.8}$$

α_{ij} is a cross-correlation term between defects at surfaces (i) and (j) or between defects within bulks (i) and (j); and γ_{jj} is the irregularity spectrum that depends only on the microstructure of surfaces or bulks:

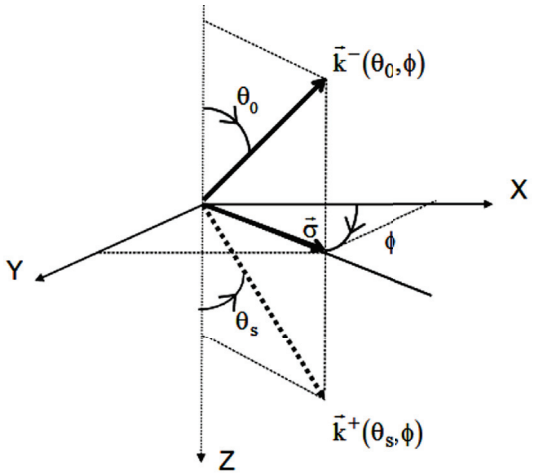

Figure 5.1: Definition of scattering angles θ and ϕ.

For the surface model, γ_{jj} is the roughness spectrum of interface *j*. If $h_j(r)$ designates the interface profile of layer *j* and $\hat{h_j}(\sigma)$ is its Fourier transform, the roughness spectrum can be written as

$$\gamma_{jj} = \frac{4\pi^2}{S}\left|\hat{h_j}(\sigma)\right|^2 \tag{5.9}$$

where *S* represents the illuminated area and $\frac{\sigma}{2\pi} = \frac{sin(\theta)}{\lambda(cos\phi, sin\phi)}$ is the spatial frequency of the defect that creates a scattered wave at direction (θ, ϕ).

Note that in American nomenclature, the scattering intensity $I(\theta, \phi)$ is called Angle-Resolved-Scattering (ARS). It is this quantity that we will use in the following. The formula for ARS when light is incident on the surface at nonnormal nonincidence is defined as :

$$\text{ARS} = \frac{dP_S}{P_i d\Omega} = \frac{\frac{1}{2}\sqrt{\frac{\epsilon_0}{\mu_0}}E^2.dS_\Omega}{P_i \frac{dS_\Omega}{r^2}} \tag{5.10}$$

where P_i is the incident power, $dP_s/d\Omega$ is the power scattered per solid angle, *E* the electric field amplitude in far field approximation, *r* the radius of the projection hemisphere and ϵ is the dielectric constant of the surface. The unit of this quantity is the inverse solid angle (sr^{-1}). The ARS is also related to the BRDF with this formula :

$$\text{ARS} = \text{BRDF}(\theta, \phi) cos\theta \tag{5.11}$$

5.2.2 Scattering from localized defects

The scattering model is now extended to the case of discrete irregularities. We still consider the equation (5.1) and we assume that the height of surface defects is much less than the illumination

wavelength and that the relative variation of the refractive index in the bulk defect is much smaller than unity. From MAURE et collab. [1996], the defects are assumed to have a circular cross section parallel to the main interface (see Figure 5.2).

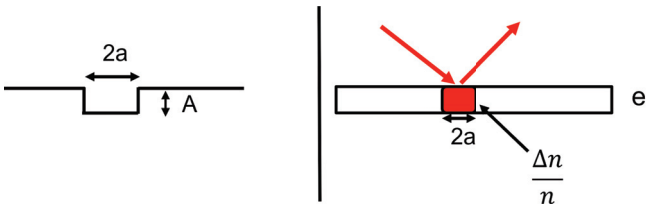

Figure 5.2: Scattering model of a localized defect at the interface (left) and of localized defect present in the bulk (right).

The irregularity spectrum is expressed in terms of the Bessel function of order 1 (J1) as follows:

- For a surface defect of amplitude A_j and radius a_j at the interface (j) (figure 5.2, left):

$$\Upsilon_{jj} = \frac{A_j^2}{S} a^4 \left| \frac{J_1(\sigma a)}{\sigma a} \right|^2 \tag{5.12}$$

- For a bulk defect of radius a_j and a relative index inhomogeneity $\frac{\Delta n_j}{n_j}$ in the whole depth of layer (j) (figure 5.2, right):

$$\Upsilon_{jj} = \frac{l}{S} \left(2\frac{\Delta n}{n} \right)^2 a^4 \left| \frac{J_1(\sigma a)}{\sigma a} \right|^2 \tag{5.13}$$

This work focuses on bulk defects present in the coating. In the case of a unique defect, angular scattering curves present oscillations in the θ angular range. The minima occur at scattering angles θ, which are approximately given by

$$\sigma a \approx m\pi \Rightarrow sin\theta \approx m\frac{\lambda}{2a} \tag{5.14}$$

These angles correspond to the zero values of the Bessel function J_1. The number of lobes depends on the ratio λ/a of the light wavelength to the defect radius a.

5.3 COMSOL Simulation

This section describes the results of simulations of the light scattered by a single isolated defect. This is a simplified case that does not describe completely what we have measured in the laboratory. For the samples studied in this thesis, although we were able to determine the single defects size, it was impossible to measure the light scattered by one isolated defect. Also, the chemical nature of the defect being unknown, we miss the information on the Δn. Nevertheless, simulations are fundamental to understand the expected trends, even if in a ideal case. This is only a first step in the development of a simulation tool in the laboratory.

The simulations were performed using COMSOL Multiphysics, a cross-platform finite element analysis, solver, and multiphysics simulation software MULTIPHYSICS [1998]. COMSOL allows us to define the coating material, the defect size and height, its position in the layer and its refraction index.

5.3.1 Data sets

All the data and parameters used for the simulation are summarized in the Table 5.1.

Table 5.1: **Global definitions and parameters used for the simulation.**

Name	Value	Description
w	6 [µm]	width of physical geometry
h_{layer}	873 [nm]	Layer thickness
h_{subs}	20 [nm]	substrate thickness
na	1	Air Refractive index
nl	1.45	Layer Refractive index
nb	3.9	Substrate Refractive Index
nd	1.537	Defect Refractive index
λ	1064 [nm]	Wavelength
ϕ	0	Azimuthal angle of incidence
θ	0	Polar angle of incidence
I_0	1 [MW/m^2]	Intensity of incident field
hd	0 [nm]	height of defect

5.3.2 Reference case

In the case of several defects, one should take into account their respective size distribution, their positions, their respective inhomogeneities, as well as the interference between the waves scattered by each defect. For our study we have chosen to simulate a simple case that we will call reference case in which we consider only one isolated defect. The geometry has been simplified for computing resources reasons.

The simulated simplified case of our problematic study consists of one monolayer of Ta_2O_5 on a silica substrate with only one defect inside the layer (see Figure 5.3). The aim of the simulation is to help us understand how point defects scatter light, depending on the layer thickness and the defect refraction index and size. All the parameters are presented in Table 5.1.

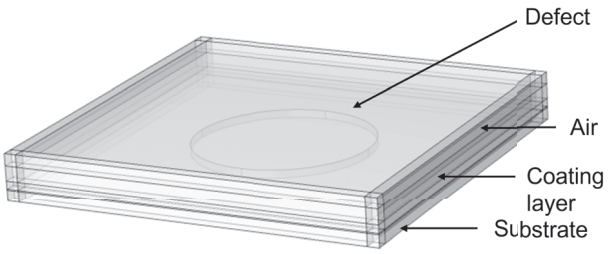

Figure 5.3: 3D view of the simulated sample. One isolated silica defect inside a tantala monolayer on a silica substrate.

The simulated parameters are 1.5 µm radius defect with a refractive-index of 1.45. In Figure 5.4, we show the ARS as a function of the angle for the reference case. Thanks to the theory, we can verify the concordance of the results by calculating the expected structure with lobes (see Equation (5.14)). In the reference case, the position is about 20° which is consistent with the value obtained in Figure 5.4.

5.3.3 Impact of the material

As we still do not know the chemical nature of the defect, we have chosen to simulate the behavior of the defect as a function of the material : silicon, tantala and silica. The Table 5.2 presents the data of the different materials.

Figure 5.5 present the ARS for three defects of different material as a function of θ. The figure shows that, in Ta_2O_5 layer, a silicon or silica defect would scatter similar amounts of light, while the

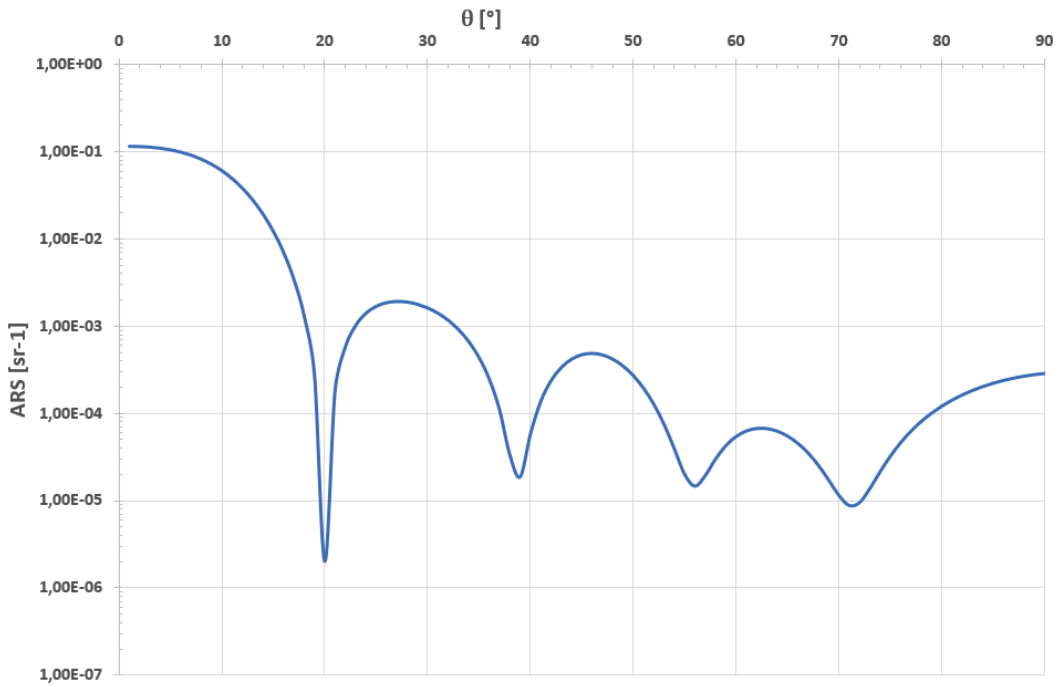

Figure 5.4: Calculated ARS as a function of θ for the reference case of a 1.5 µm radius defect present at the surface of a Ta_2O_5 layer deposited on a silica substrate. The defect thickness is equal to 125 nm in a layer of 130 nm.

light scattered by a Ta_2O_5 defect is two order of magnitudes smaller, at all angles. The lobe pattern of the computed ARS for the tantala defect in tantala layer is quite suprising. Indeed, the layer is homogeneous in this case and no scattering should occur. The position of the lobes indicates a defect radius of about 6 µm what corresponds to the cell dimension of the finite-elements model. This seems to be an artefact of the numerical simulation.

Table 5.2: **Global definitions and parameters used for the simulation.**

Material	Refraction index	coefficient
Silicon	n = 3.9766	k = 0.030209
Ta_2O_5	n = 2.0356	
SiO_2	n = 1.4582	

5.3.4 Impact of defect diameter

In the simulation we varied the radius of the defect from 0.5 µm to 2.5 µm. These values were chosen because they correspond to the smallest and largest defects classified as point defects by the optical profilometers. Figure 5.6 shows the ARS as a function of angle θ. The scattered light can differ by a factor 1000 between the largest and the smallest defect radius, with larger defects scattering more light.

As presented in section 5.2.2, light scattering theory provides a relationship between the light scattering and the size of a defect MAURE et collab. [1996]. Equation (5.13) confirms the impact of the defect size on the scattering. In realistic cases, the total scattering will depend on the number of defects, their distribution and their size.

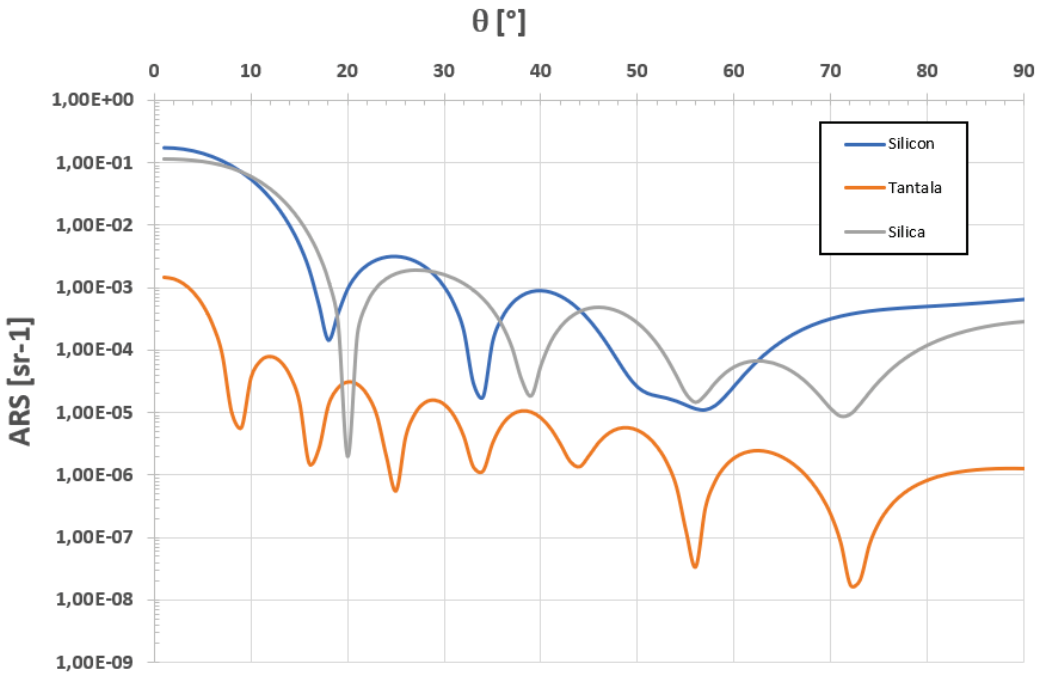

Figure 5.5: Simulated ARS as a function of θ for different material defect : silicon in blue, tantala in orange and silica in grey. The defect is in a Ta_2O_5 layer and the defect radius size is about 1.5 µm.

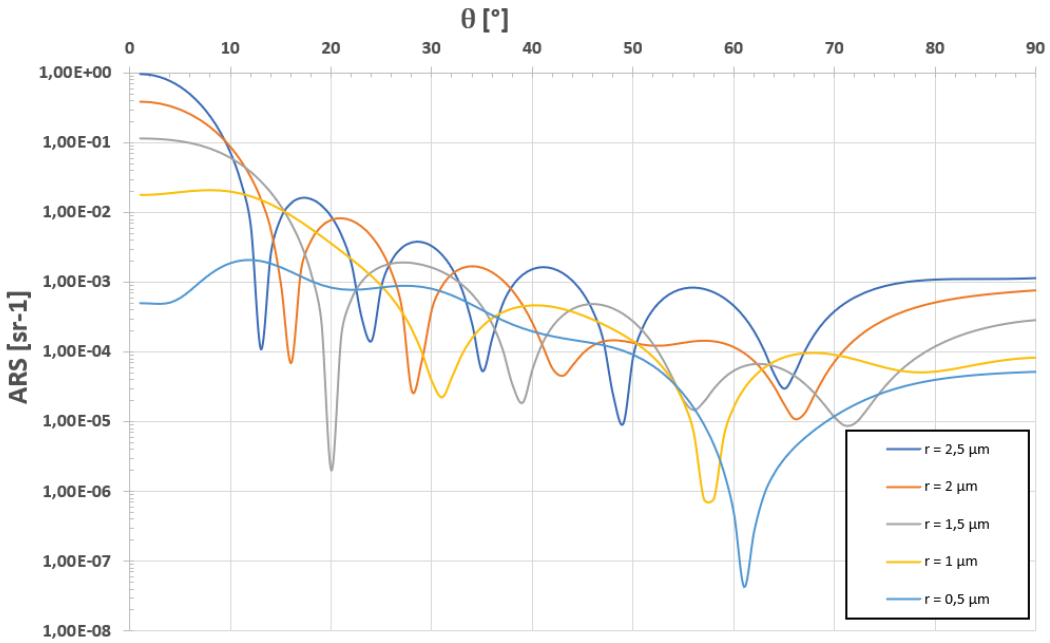

Figure 5.6: Simulated ARS of a different defect radius as a function of θ. In this case the simulation varies the size of Ta_2O_5 defect inside a Ta_2O_5 layer. The defect thickness of the defect is equal to 130 nm.

5.3.5 Impact of the location of the defect in the layer

Although the optical profilometers used in our study do not allow us to know the exact position of the defect in the thin films, its effect on the scattered light has been studied in simulations. In order to know the impact of the defect position in the layer on the scattered light, different positions of defect were simulated (see Figure 5.7) : on the substrate surface (at the bottom of the layer), in the middle of the layer, near the coating surface (flush with the surface) and on the coating surface.

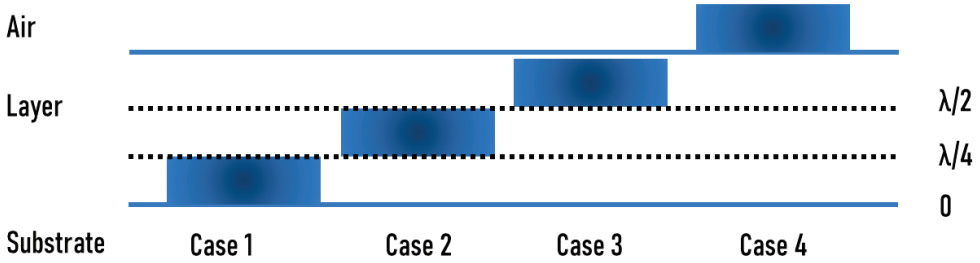

Figure 5.7: Scheme of the 3 different defect positions simulated.

Figure 5.8, displays the simulated ARS of a different defect position in the layer as a function of θ and shows that there is not much difference between the different cases below 30°. At higher angles, the ARS show deviations reach about 2 or 3 orders of magnitude. Concerning the fourth case, it seems that a defect on the surface of the coating have less impact at large scattering angle than a defect embedded in the layer.

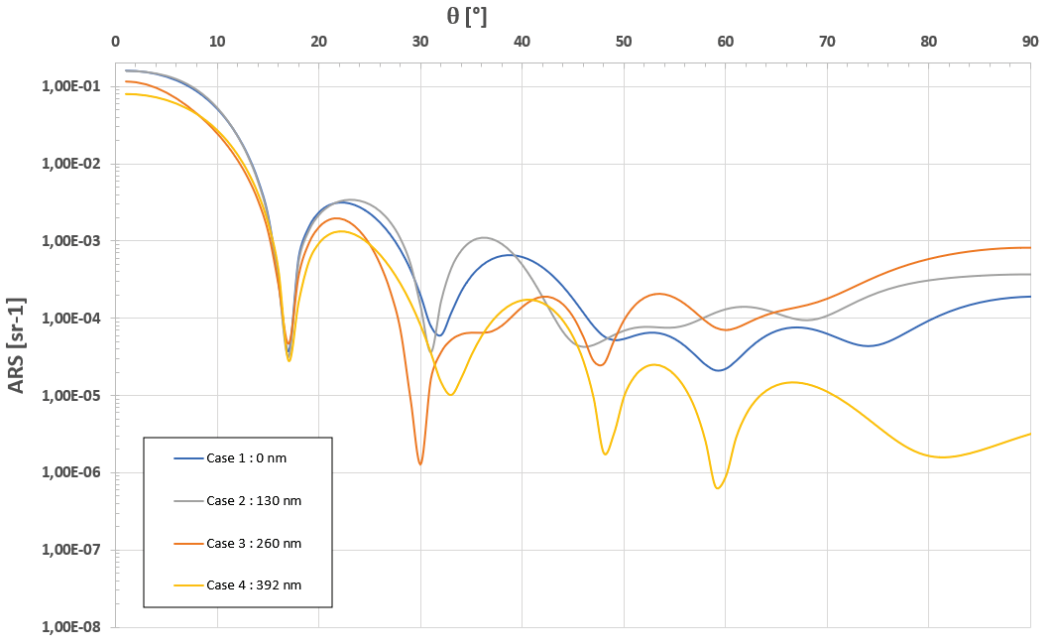

Figure 5.8: Simulated ARS of different positions of a defect of a radius 1.5 µm and index inhomogeneity of 1.45 in a layer thickness of 392 nm.

5.3.6 Impact of the thickness of the defect

The profilometers allow to measure the height of the defect only if it has an effect on the surface. If there is a hole or a bump then we can make a topographic measurement of the defect. This manipulation has to be performed by hand on each individual defect and is not done systematically. For practical reasons, this parameter was not measured.

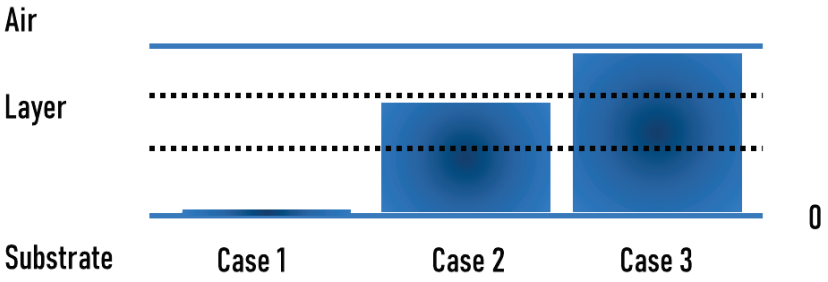

Figure 5.9: Scheme of the 3 different defect thicknesses simulated.

Nevertheless, the impact of the thickness of the defect was studied in the simulations. As shown in Figure 5.9, three cases were considered : 0 nm, 2/3 of the layer thickness and the whole layer. When the thickness of the defect is quasi-null or equal to the layer, the ARS are similar. Conversely, when the thickness is 2/3 of the layer the ARS is one order of magnitude lower (Figure 5.10).

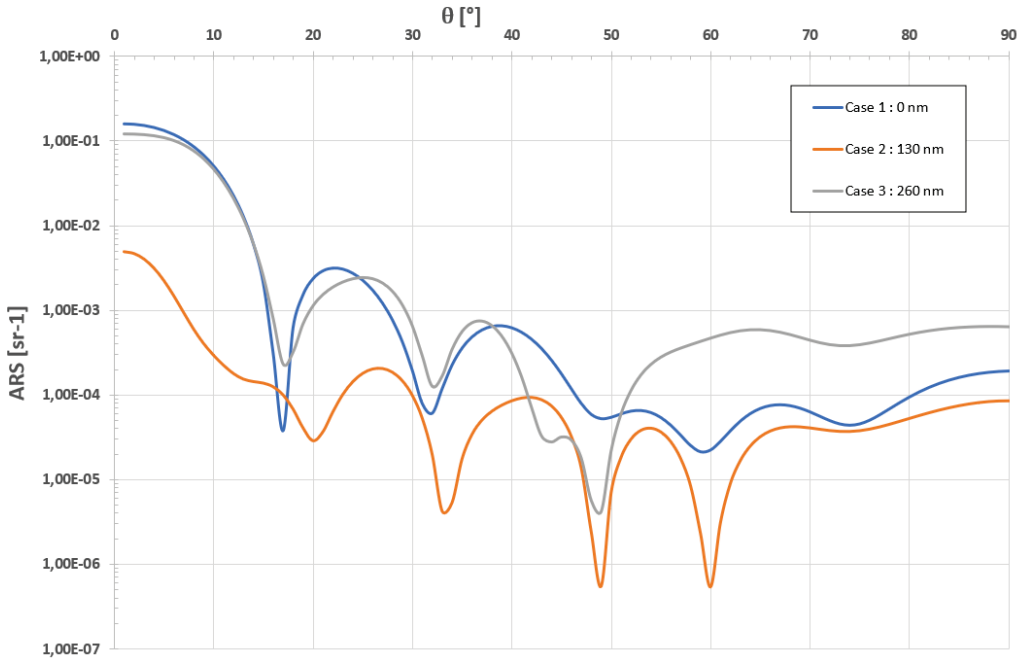

Figure 5.10: Simulated ARS of different thickness of defects inside a Ta_2O_5 layer.

The thickness of the defect has a strong impact on the ARS. This may suggest that we could have a weaker defect detection on the profilometers. Defects in the layers have a weakened scattering level at large angles. Since the measurements are made at 45°, they may not be detected.

5.4 Scattered Light from Point Defects

To evaluate the scattered light from defects we show two BRDF curves in figure 5.11, measured on two End Mirrors of Advanced Virgo. The red curve is representative of an area with a high density

of defects while the blue curve represents the BRDF of an area with few defects. It is between 4° and 66° that the difference is the most visible. We can see that at high concentration of defects, the value of the BRDF is $5.5{\cdot}10^{-6}$ sr^{-1} which corresponds to a light scattering of 4 ppm and at low concentration of defects the value of the BRDF is $1.8{\cdot}10^{-6}$ sr^{-1}, that is to say 1.2 ppm. Thus, the scattering is multiplied by a factor 3. We notice an offset between the 2 curves. This observation is made on a real mirror, and by choosing two regions with highly different defect densities, so it does not necessarily represent the simpler case of monolayers produced for this study.

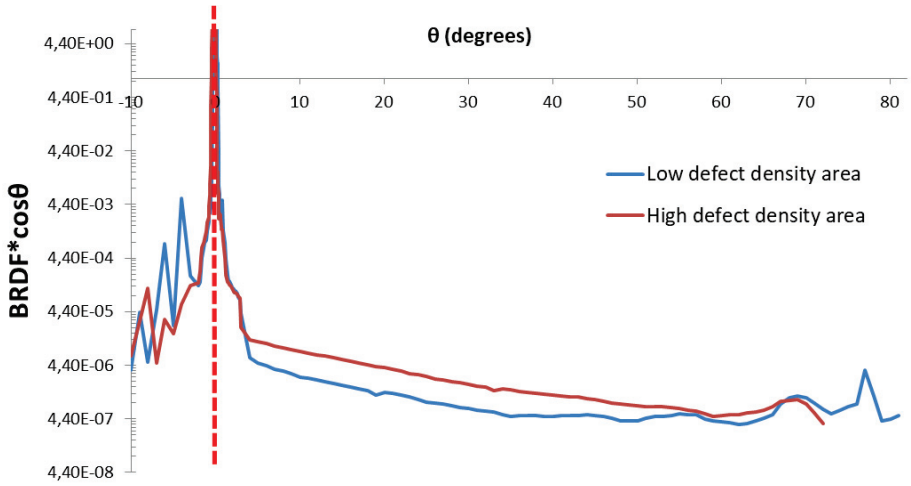

Figure 5.11: ARS curves corrected by the cosine of the scattering angle as a function of the scattering angle. The specular reflection, shown in dashed line on the figure, corresponds to the angle of 4° at which we place to illuminate. The specular reflection is clearly visible at -4°.

5.4.1 Preliminary study

As seen in Chapter 4, the samples used for the preliminary study were measured with the scatterometter by performing scattering map. The results are summarized in Table 5.3.

Table 5.3: **Scattered light and defect density measurement for each material after annealing according to their layer thickness. One Coastline substrate without coating has been measured to compare the scattering value with the different samples.**

Material	Thickness (nm)	Defect density (def/mm^2)	Scattering (ppm)
Substrate	0	0.04	3
SiO_2	523	0.14	5.1 ± 1.2
	1005	0.32	4.5 ± 0.6
	1550	0.52	9.4 ± 0.5
	2053	0.61	11.5 ± 1.6
Ta_2O_5	543	0.12	5.8 ± 0.8
	1083	0.25	5.3 ± 0.2
	1626	1.52	5.2 ± 0.5
	2167	5.16	11.6 ± 0.1

To quantify the impact of the defects on the scattered light, we measured the 8 samples with the CASI after annealing. At that time the idea of measuring the scattering light of the samples before annealing had not been exploited. The protocol was to measure only after annealing as it was done on the large optics used by the LIGO and Virgo interferometers. Figure 5.12 shows the scattered light of the two materials as a function of the layer thickness. Ta_2O_5 coating seems

to have a stable scattering for the first three thinnest layers that increases for the thickest one. The thickest SiO_2 sample has a scattering of $1.37{\cdot}10^{-5}$ sr^{-1} whereas the thinnest one $1{,}06{\cdot}10^{-5}$ sr^{-1}. Similarly, for Ta_2O_5 samples, the thinnest sample scatters $9.31{\cdot}10^{-6}$ sr^{-1} while the thickest, $2{,}19{\cdot}10^{-5}$ sr^{-1}. While there is a factor 10 on the number of defects between the thickest sample of silica and tantala, the scattered light is comparable. This tends to show that the scattered light does not depend highly on the defects number, or that the defects present in the layers of Ta_2O_5 scatter less light than the defects present in the SiO_2. In addition, the distribution of the electric field being different in the two materials could also affect the scattered light. The error bars shown in the results of the preliminary study are only determined with repeatability measurements. Since then, we have realised that such uncertainties can be underestimated, as other factors, for example the quality of the substrate, can impact the spread of the measurements. For this reason, in the in-depth studies, several samples for each deposition configuration were produced.

It is worth mentioning that the uncoated substrates used in this study have an optical scattering level below $4.2{\cdot}10^{-6}$ sr^{-1}. So the thin layer coating and particularly the addition of defects contribute to the scattered light. To verify the constant scattered light of the lower thicknesses, a simulated deposition coating on a substrate called "ghost deposition" has been done. The so-called ghost deposition refers to a sample where the substrate was put in the IBS machine under the normal deposition conditions, but no deposition was performed, and for this reason is treated as a sample with null thickness. We notice that the scattered value measured is consistent with the value measured on raw substrate (within typical repeatability uncertainties, although the value being slightly lower can also be explained by small fluctuations in the substrate quality).

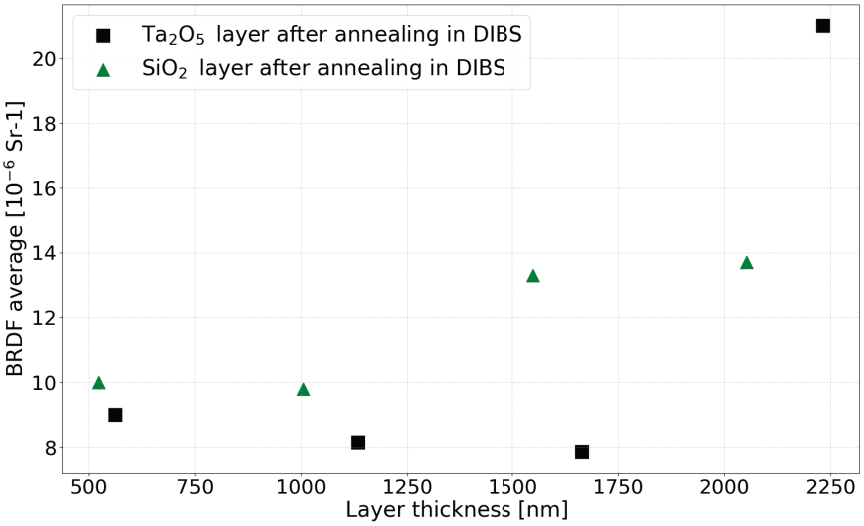

Figure 5.12: Scattered light for the two materials, Ta_2O_5 and SiO_2, as a function of the layer thickness after annealing. Note that the results were obtained by scattering mapping and not by measuring BRDF at all angles.

5.4.2 In-depth study

In comparison to the preliminary study, the scattering light of the new samples produced in the DIBS were measured before and after annealing. In addition, as shown in Table 4.3, several samples have been produced for each configuration. For all the results, the error bars represent the spread of the measurements performed on different samples.

5.4.3 Influence of the thickness

The light scattered by the samples produced in the different DIBS and GC machines was systematically measured before and after annealing.

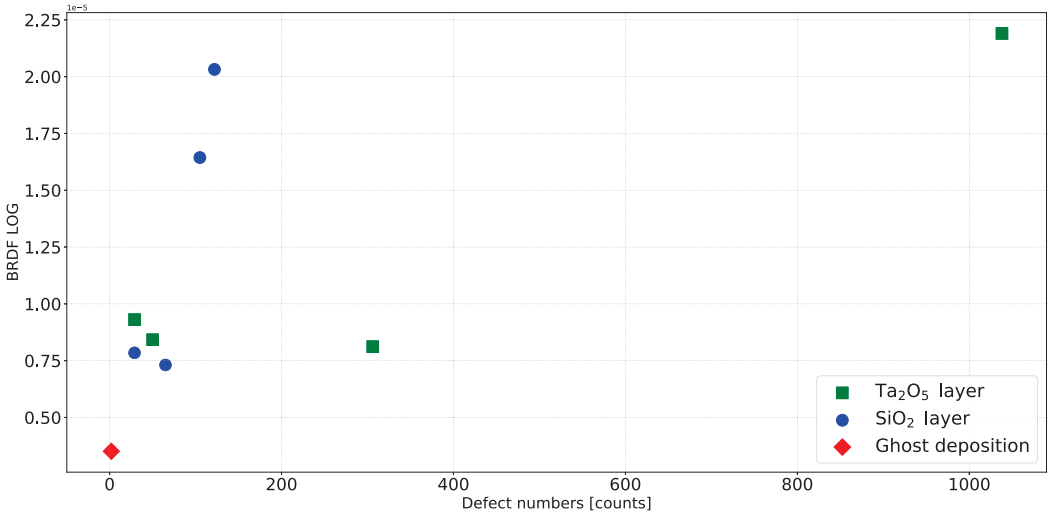

Figure 5.13: Scattered light for the two materials, Ta_2O_5 and SiO_2, as a function of the number of defects. The ghost deposition represent a sample where the substrate was put in the IBS machine under the normal deposition conditions, but no deposition was performed is consistent with the value measured on raw substrate. Measurements done at 10° detector.

Figure 5.14, Figure 5.15 and Figure 5.16 show the scattered light as a function of the layer thickness. In the 3 cases, DIBS - GC pur Ta - GC doped Ta, the trends are similar. While we had observed that the number of defects increases with the layer thickness, the level of scattering light for each thickness seems to be constant. In addition, the metrology could be an explanation. The spot size is 2 mm in diameter. The contribution of the defect signal may not be significant enough.

The annealing appears to have a positive effect on both defect density (as shown in the previous Chapter) and the scattered light.

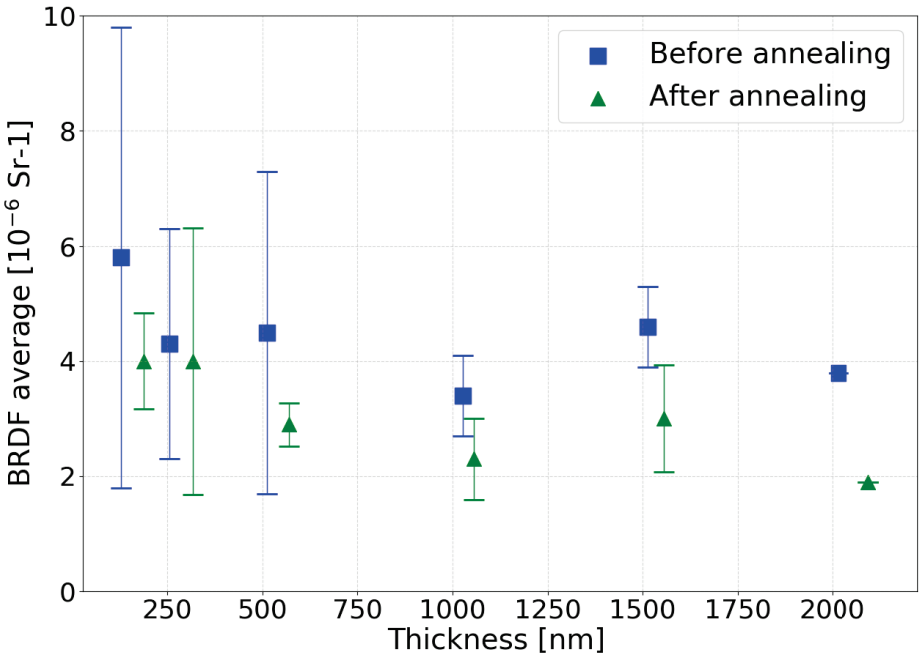

(a)

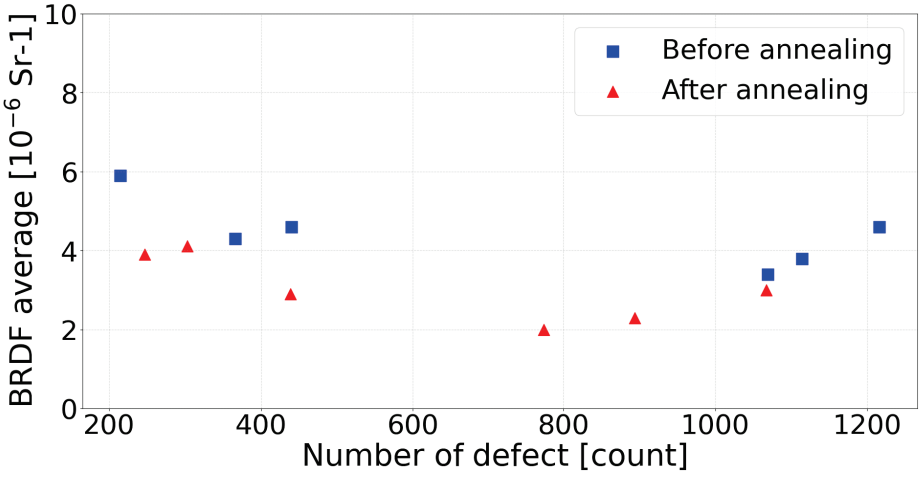

(b)

Figure 5.14: Scattering values of the tantala coatings produced in the DIBS as a function of the thickness before and after annealing. Measurements done at 10° detector.

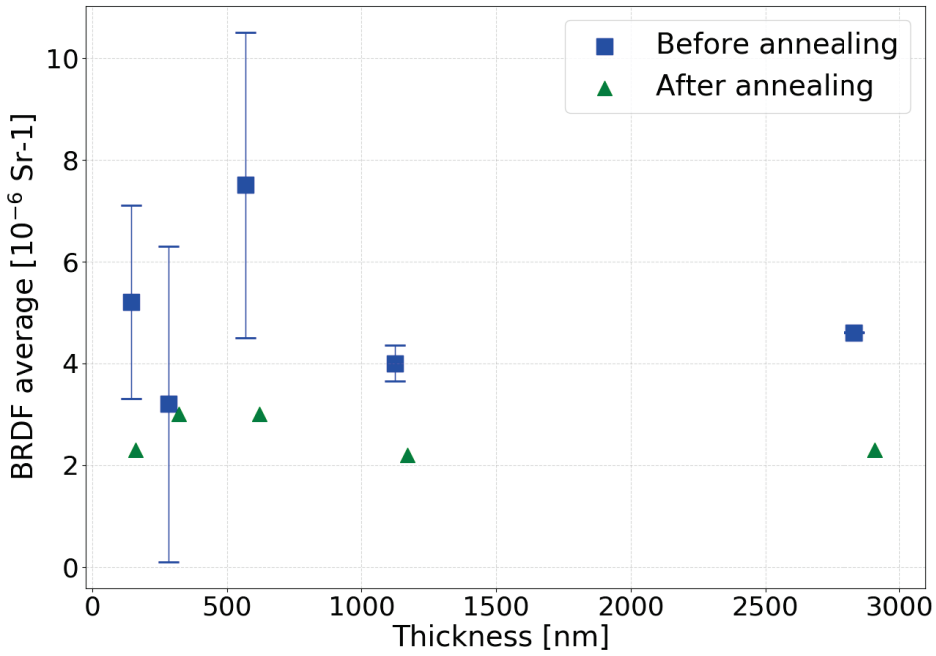

(a)

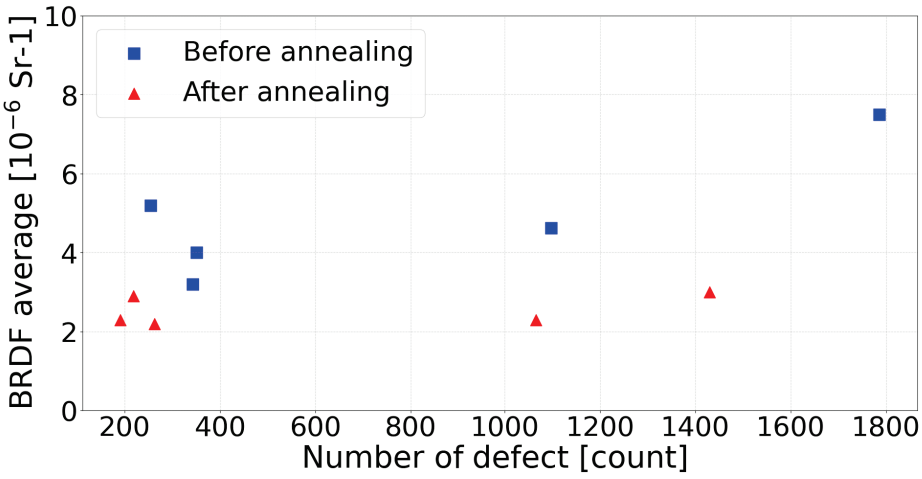

(b)

Figure 5.15: Scattering values of the tantala coatings produced in GC as a function of the thickness before and after annealing in (a) and the scattered values as a function of the number of detected defects in (b).

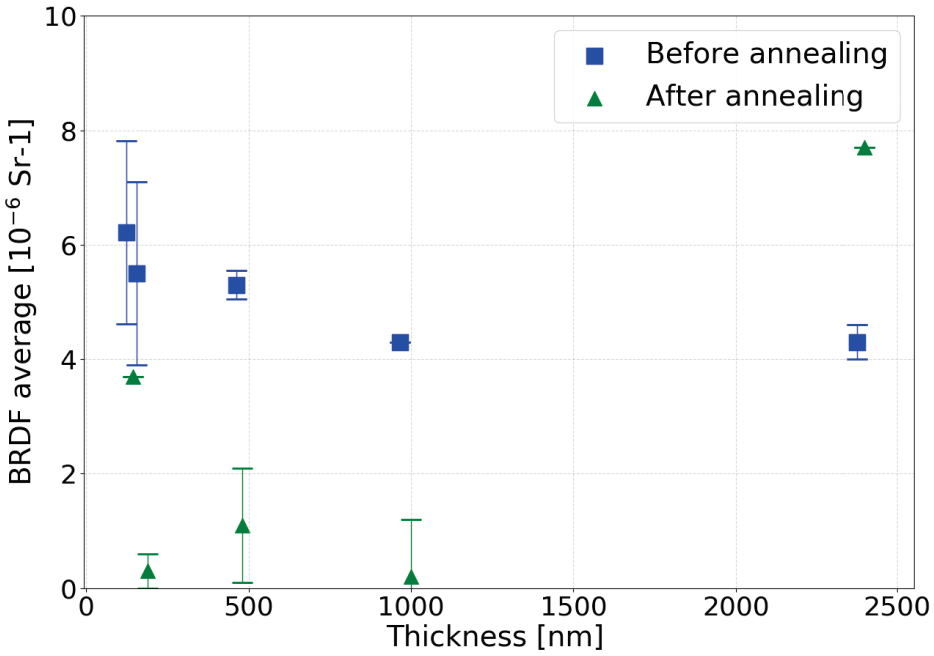

(a)

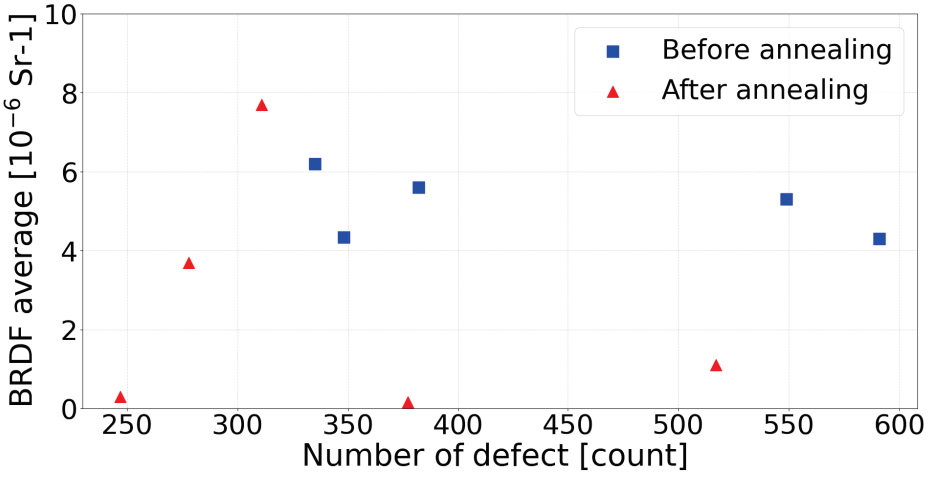

(b)

Figure 5.16: Scattering values of the doped tantala coatings produced in GC as a function of the thickness before and after annealing and the scattered values as a function of the number of detected defects in (b).

5.4.4 Influence of the Annealing

The light scattered by the samples dedicated to the study of the influence of multiple subsequent annealings was measured before and after the 2 thermal annealing procedures (see Table 5.4). Figure 5.17 shows the scattering level as a function of the number of annealing. While we had seen in chapter 4, that the second annealing has no major impact on the density of defects, it seems that the effect is visible on the amount of scattered light.

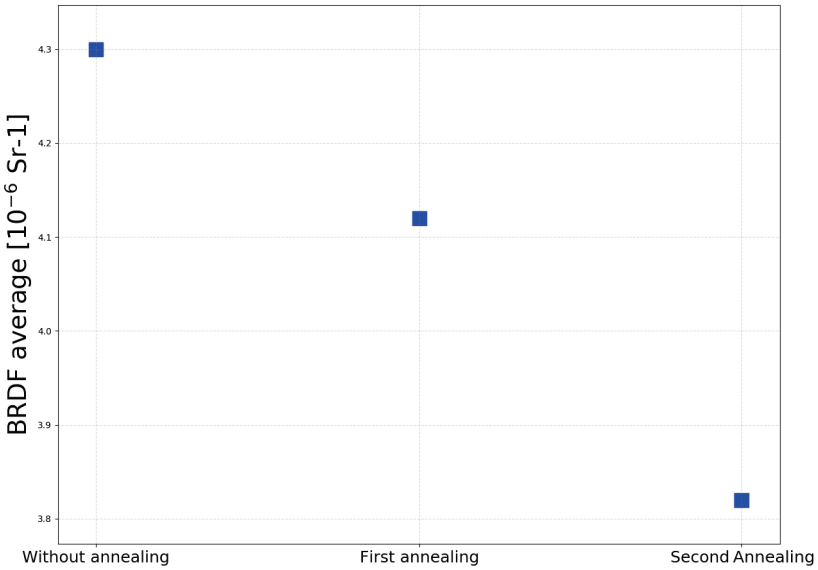

(a)

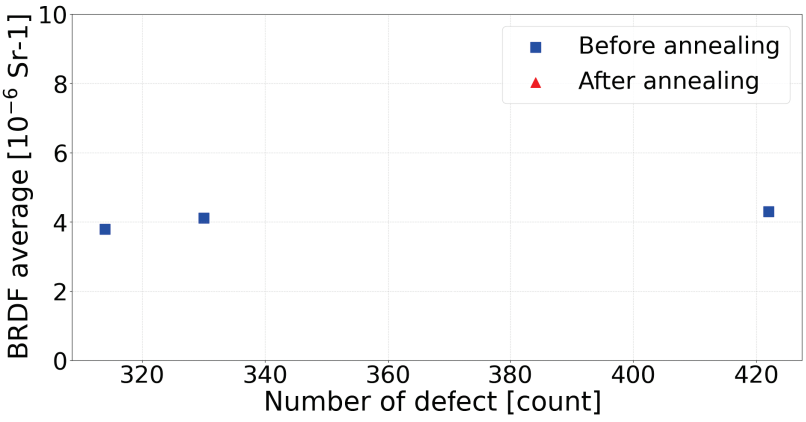

(b)

Figure 5.17: Scattered light level of run D21002 as a function of the number of thermal annealing in (a) and the scattered level of the same run as a function of the number of detected defect in (b).

The post-deposition annealing has well-known mechanical and optical effects on thin films. First it reduces the compressive strain of films coated by IBS, thanks to a redistribution of the material in the film MACLEOD [2010]. At the same time, this process induces both a decrease of the refractive index and an increase of the layer thickness that is in agreement with a decreased density of the film GRANATA et collab. [2020]. Moreover, some structural changes have been recently highlighted in sputtered silica films that could improve the mechanical quality factor of the material GRANATA et collab. [2018]. Thermal treatment has clearly several effects on thin films and the results indicate that it seems to act as a cure for the optical scattering.

In our study, we show the annealing affects the scattered light, the number of defects and the surface roughness. From there, we need to understand why and how the magic happens. The initial hypothesis related to the preliminary study was that the defects change in size with annealing by reducing their size. However, due to the small number of samples we could not draw any con-

Table 5.4: Results of the number of thermal annealing on the number of defects on two Ta_2O_5 samples of 500 nm thickness.

Sample	Before annealing	After annealing 1 [defect/mm²]	After annealing 2
D21002R PL7464	508	345	259
D21002R PL73762	336	315	370
Defect median	422	330	314

clusion. On the other hand, the deeper study, with more statistics, shows that the annealing had no influence on the size of the defects. The reduction of the scattering after annealing is consistent with the results published by CAPOTE et collab. [2021]. They also reported that defects disappear during annealing under vacuum and this is probably due to the presence of water, dust, or other contaminants that evaporate during the heating.

5.4.5 Influence of the substrate temperature

As explained, the samples deposited with the heated substrate show rough surfaces due to heating during coating deposition. In this case, Figure 5.18 shows that thermal annealing increases the scattered light.

5.4.6 Influence of the beam intensity I_b and the voltage V_b

We have seen in the previous chapter that the parameter I_b and V_b could influence the deposition speed and the energy of the sputtered particles. Figure 5.19 and Figure 5.20 show that the scattered light is not influenced by the value of I_b and V_b used during deposition. Also in this case, the results show that the level of scattering decreases after thermal annealing.

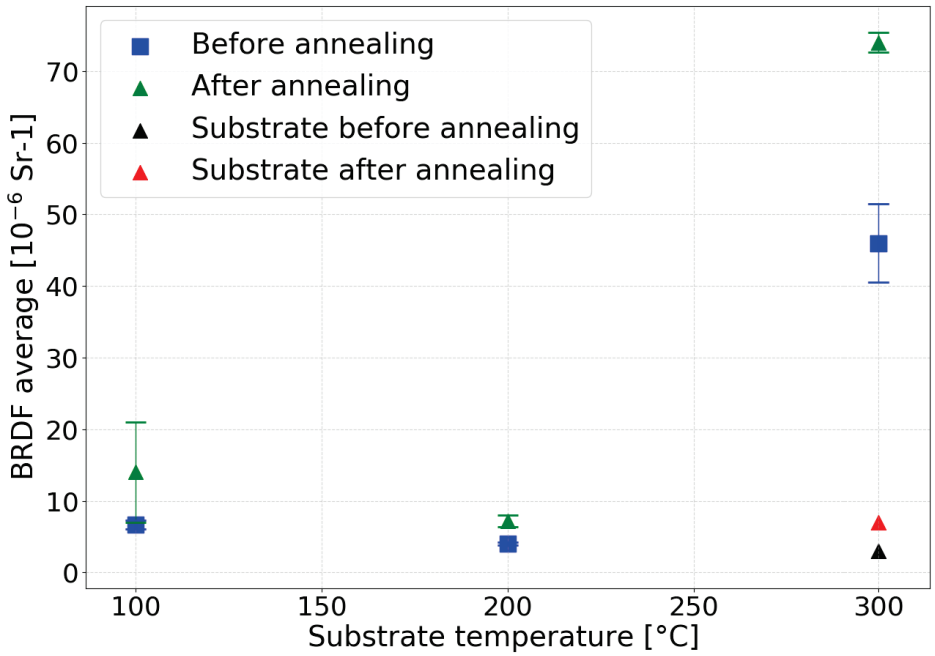

(a)

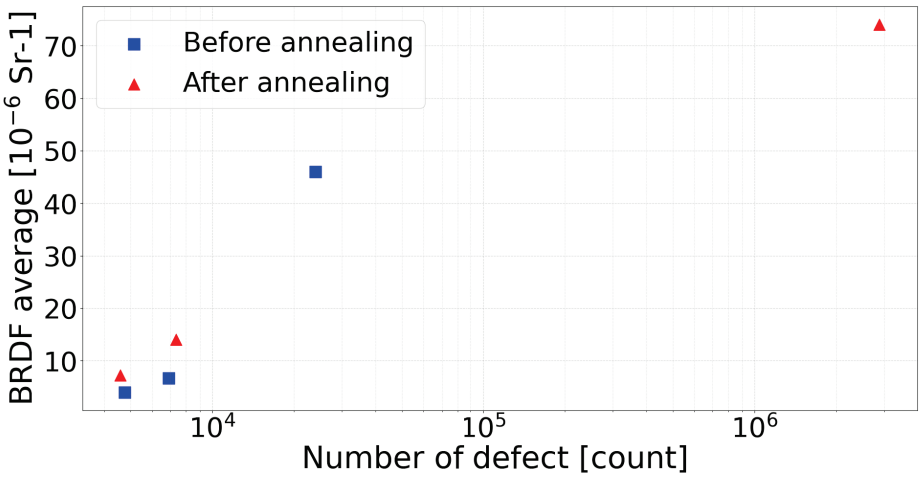

(b)

Figure 5.18: Scattered light level of the sample holder runs as a function of the substrate temperature in (a) and the scattered level of the same run as a function of the number of detected defect in (b).

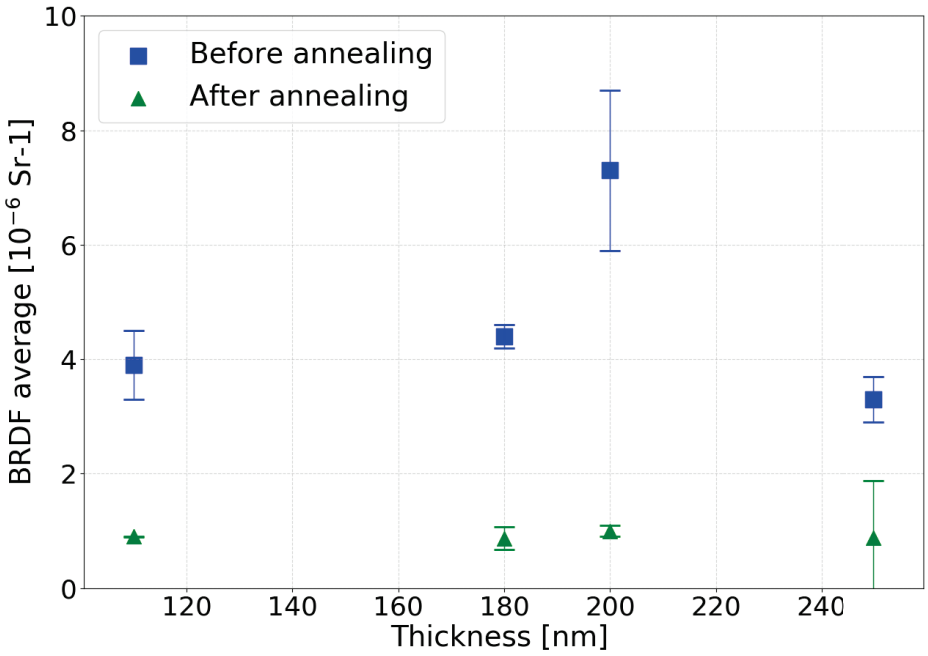

(a)

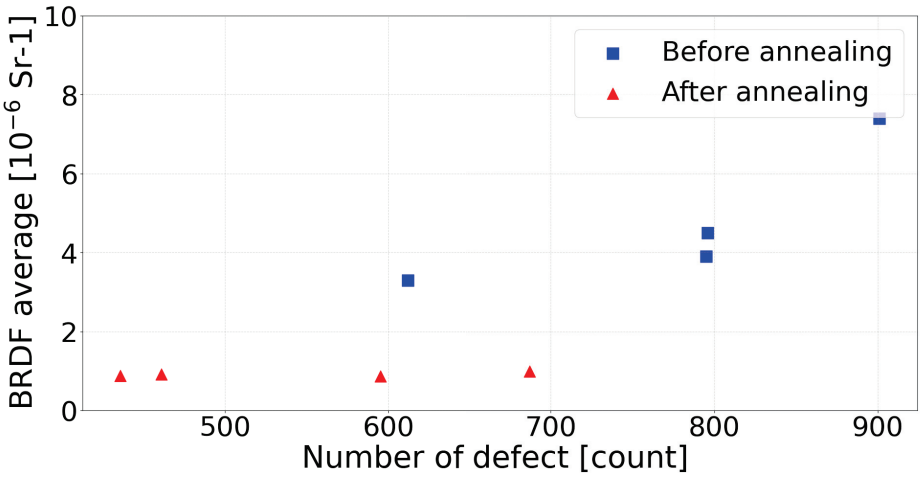

(b)

Figure 5.19: Scattered light as a function of I_b in (a) and the scattered level of the same run as a function of the number of detected defect in (b).

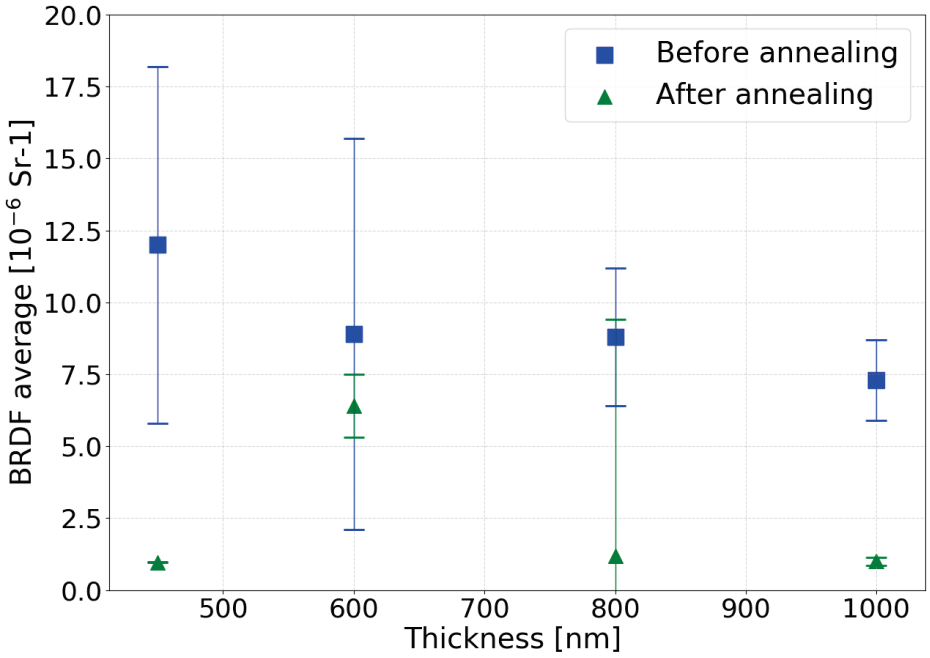

(a)

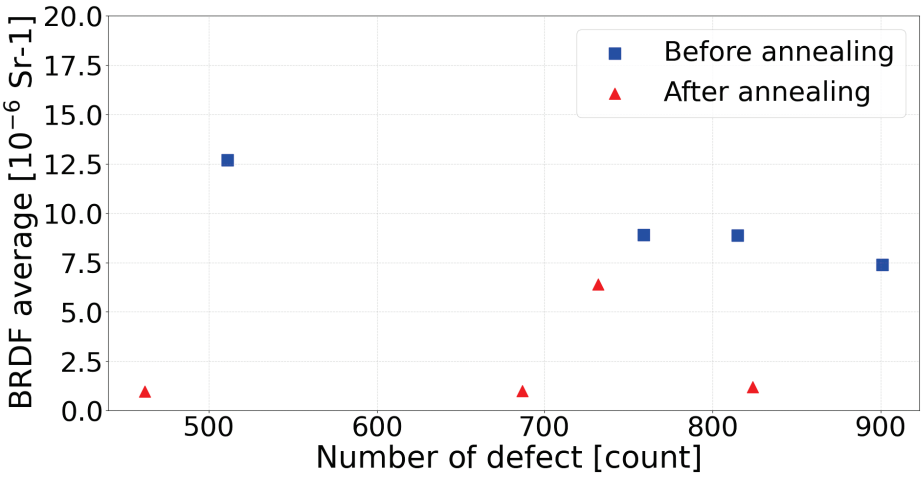

(b)

Figure 5.20: Scattered light as a function of V_b in (a) and the scattered level of the same run as a function of the number of detected defect in (b).

5.5 Summary

In this chapter we have explored a simulation tool to understand the defects behaviour. Obviously, this desserves further developments to provide a full simulation of a real mirror under realistic conditions.

Moreover, all the figures presented in this part from Figure 5.14 to Figure 5.20 presenting the BRDF average values as a function of the number of detected defects, confirm that there is no correlation between the amount of light scattered and the density of defects present in the layers. This conclusion is consistent with the observation from O2, that the LMA metrology is not adapted to measure the total scattered light the mirrors would generate in the interferometer. On the other hand, in the vast majority of cases we have observed that annealing, in addition to reducing the number of defects (most often), also reduces the scattered.

5.6 References

AMRA, C. 1993, «First-order vector theory of bulk scattering in optical multilayers», *J. Opt. Soc. Am. A*, vol. 10, 2, doi:10.1364/JOSAA.10.000365, p. 365−−374. URL http://opg.optica.org/josaa/abstract.cfm?URI=josaa-10-2-365. 98

AMRA, C. 1994a, «Light scattering from multilayer optics. i. tools of investigation», *J. Opt. Soc. Am. A*, vol. 11, 1, doi:10.1364/JOSAA.11.000197, p. 197–210. URL http://opg.optica.org/josaa/abstract.cfm?URI=josaa-11-1-197. 98

AMRA, C. 1994b, «Light scattering from multilayer optics. ii. application to experiment», *J. Opt. Soc. Am. A*, vol. 11, 1, doi:10.1364/JOSAA.11.000211, p. 211–226. URL http://opg.optica.org/josaa/abstract.cfm?URI=josaa-11-1-211. 98

AMRA, C., M. LEQUIME et M. ZERRAD. 2021, *Electromagnetic Optics of Thin-Film Coatings: Light Scattering, Giant Field Enhancement, and Planar Microcavities*, Cambridge University Press, doi:10.1017/9781108772372. 98

BENNETT, J. M. et L. MATTSSON. 1989, «Introduction to surface roughness and scattering 2nd edition», *J. Opt. Soc. Am. A*, , 2, doi:10.1364/1557521085. URL https://opg.optica.org/books/bookshelf/Intro_Surface_Rough_Scatter.cfm. 98

CAPOTE, E. M., A. GLECKL, J. GUERRERO, M. REZAC, R. WRIGHT et J. R. SMITH. 2021, «In-vacuum measurements of optical scatter versus annealing temperature for amorphous ta2o5 and tio2:ta2o5 thin films», *J. Opt. Soc. Am. A*, vol. 38, 4, doi:10.1364/JOSAA.415665, p. 534–541. URL http://opg.optica.org/josaa/abstract.cfm?URI=josaa-38-4-534. 113

GRANATA, M., A. AMATO, L. BALZARINI, M. CANEPA, J. DEGALLAIX, D. FOREST, V. DOLIQUE, L. MERENI, C. MICHEL, L. PINARD, B. SASSOLAS, J. TEILLON et G. CAGNOLI. 2020, «Amorphous optical coatings of present gravitational-wave interferometers», *Class.Quant.Grav.*, vol. 37, 9, doi:10.1088/1361-6382/ab77e9, p. 095 004. URL https://hal.archives-ouvertes.fr/hal-02317325. 112

GRANATA, M., E. COILLET, V. MARTINEZ, V. DOLIQUE, A. AMATO, M. CANEPA, J. MARGUERITAT, C. MARTINET, A. MERMET, C. MICHEL, L. PINARD, B. SASSOLAS et G. CAGNOLI. 2018, «Correlated evolution of structure and mechanical loss of a sputtered silica film», *Phys. Rev. Materials*, vol. 2, doi:10.1103/PhysRevMaterials.2.053607, p. 053 607. URL https://link.aps.org/doi/10.1103/PhysRevMaterials.2.053607. 112

MACLEOD, H. A. 2010, *Thin-film optical filters*, CRC press. 98, 112

MAURE, S., G. ALBRAND et C. AMRA. 1996, «Low-level scattering and localized defects», *Appl. Opt.*, vol. 35, 28, doi:10.1364/AO.35.005573, p. 5573–5582. URL http://opg.optica.org/ao/abstract.cfm?URI=ao-35-28-5573. 100, 102

MULTIPHYSICS, C. 1998, «Introduction to comsol multiphysics®», *COMSOL Multiphysics, Burlington, MA, accessed Feb*, vol. 9, p. 2018. 100

STOVER, J. C. 2012, *Optical Scattering: Measurement and Analysis, Third Editions*, CRC press, doi:10.1117/3.975276. 98

Chapter 6

Chemical analysis of point defects

Contents

6.1 Introduction

The characterization of point defects in optical thin films is not sufficient to understand what generates them and how they scatter the light. The most important information missing in this study to have a global vision of the phenomenon is the chemical nature of these defects. In order to remedy this, different chemical analyses have been performed during this thesis using Raman spectroscopy, Scanning Electron Microscopy coupled to an EDX probe (MEB-EDX), Laser-Induced Breakdown Spectroscopy (LIBS) and Atomic force microscopy (AFM). These attempts have shown the complexity of identifying these defects with state-of-the-art instruments but also the enormous time needed to make such measurements.

All the chemical measurements were done on the preliminary study samples.

6.2 Table of samples

The samples used for the chemical analysises are listed in Table 6.1.

Table 6.1: **The table lists, for each sample used, the coating machine, and the coating material and layer thickness.**

Coating machine	Material	Thickness (nm)	RUN	Sample	Substrate
DIBS	Ta_2O_5	1122,2	18026	NN	µHeraeus
		1665.4	18029	PL4126	µC
		2231.8	D21037	PL9223	µC
DIBS	SiO_2	1005	18030	NN	Ti Pastille (SF11)

6.3 RAMAN analysis

As a first attempt, we used the Raman spectrometer available at the Institut de Physique des Deux Infinis (IP2I) and the one available at the Institut Lumière Matière (ILM) (instrument detailed in COILLET [2017]. Raman spectroscopy, is a non-destructive technique that allows access to the structure of the material at short and medium distance. It is based on the radiation-matter interaction and corresponds to the inelastic scattering of light (monochromatic and intense) by the material. In the case of Stokes Raman scattering (the most probable), the scattered photon has less energy than the incident photon because it has given up part of its energy in the form of a phonon LONG [2002]. In this work, all the Raman spectra correspond to the Stokes Raman scattering.

The set of spectra was obtained with a short distance x100 objective, whose numerical aperture is 0.95 (aperture angle of the objective allowing the rays to enter). The larger is the angle the better is the resolution.

6.3.1 Study of defect-free area

Since the thin film deposition were made on fused silica substrates, it is important to identify the spectroscopic signatures of the silica in order to interpret the spectra. The Figure 6.1 presents the Raman spectrum of the fused silica glass substrate (Suprasil 300). In the low frequency band, we find the Boson peak at 60 cm^{-1}. This is typical of disordered materials and corresponds to an excess of vibrational density of states compared to the Debye theory. We have an asymmetric band around 440 cm^{-1}, called Main Band (MB), which correspond to the Si-O-Si angle bending mode HEHLEN [2010]. We observe also 2 narrower bands at 490 (called D1) and 600 cm^{-1} (called D2). We also observe 3 bands, wider, in the high frequency range which are 800, 1060 and 1200 cm^{-1} corresponding to LO-TO asymmetric Si-O stretching modes of the Si-O-Si bond COILLET [2017].

Concerning the second material used, Ta_2O_5, Figure 6.2 presents the Raman spectrum of amorphous Ta_2O_5. The characteristic feature of Ta_2O_5 is the main band at 680 cm^{-1}. It corresponds to the vibrations due to the displacements of the oxygen atoms.

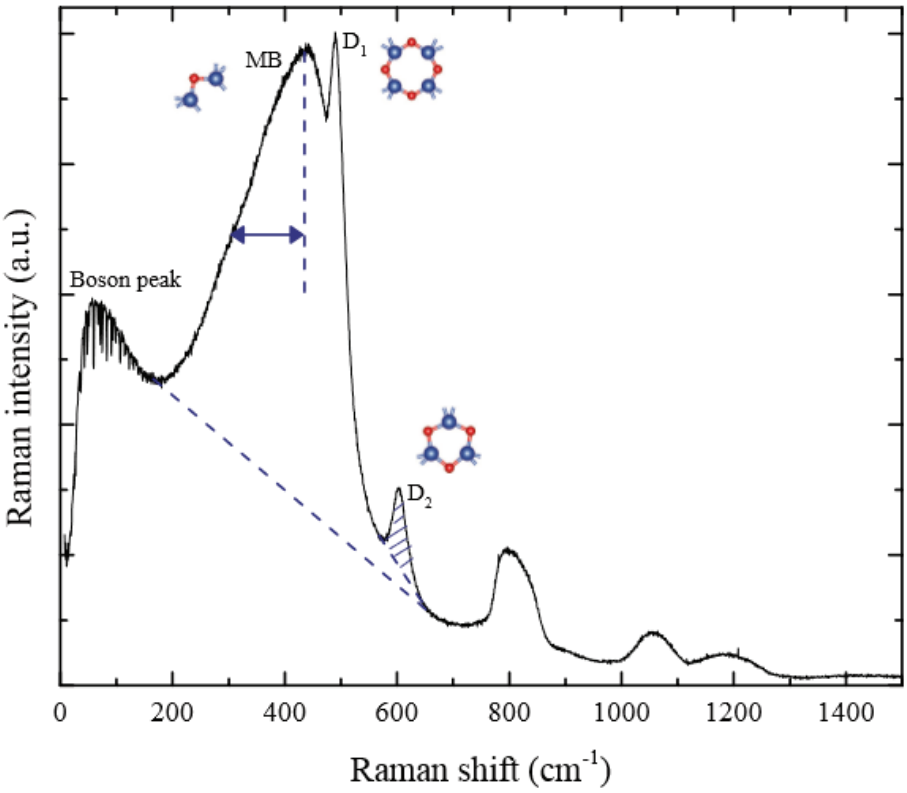

Figure 6.1: Raman spectrum of fused silica glass COILLET [2017].

6.3.2 Post-deposition annealing

In this section, we observe the samples before and after annealing. Note that the coating deposition parameters are the same for the two samples. As we have already seen, annealing has a significant effect on the defect density. This led us to analyze by Raman spectroscopy, the thin layers of the samples before and after annealing. To understand the difference between the two spectra, we compare the position of the bands present before annealing and their new position after annealing.

For the substrate without deposition, Figure 6.3, we notice that after annealing, the D1 band is shifted a few cm^{-1} towards the low frequencies. The SiO_2 deposition, shown in Figure 6.4, shows that annealing lowers the level of the spectrum in the high frequencies. This observation is consistent with a readjustment of the stochiometry carried out by annealing during which the material is reoxidized. For the Ta_2O_5 deposition, in Figure 6.5, shows that there is no modification of the structure at short distance. The emission is higher towards low and high frequencies. It seems that there is no impact of annealing on the Ta_2O_5.

6.3.3 Study of point defects in silica and tantala monolayers

To obtain the spectra of the defects we focused on a defect and considered the use of a certain laser power. Depending on the wavelength used, the penetration depth changes. The red wavelength has a deeper penetration depth so it probes a larger part of the substrate. The blue wavelength has a shorter penetration depth so it probes a thin part of the thin layer, which allows to get rid of a part of the substrate and to have the signature of the defect. In order to probe a volume of the

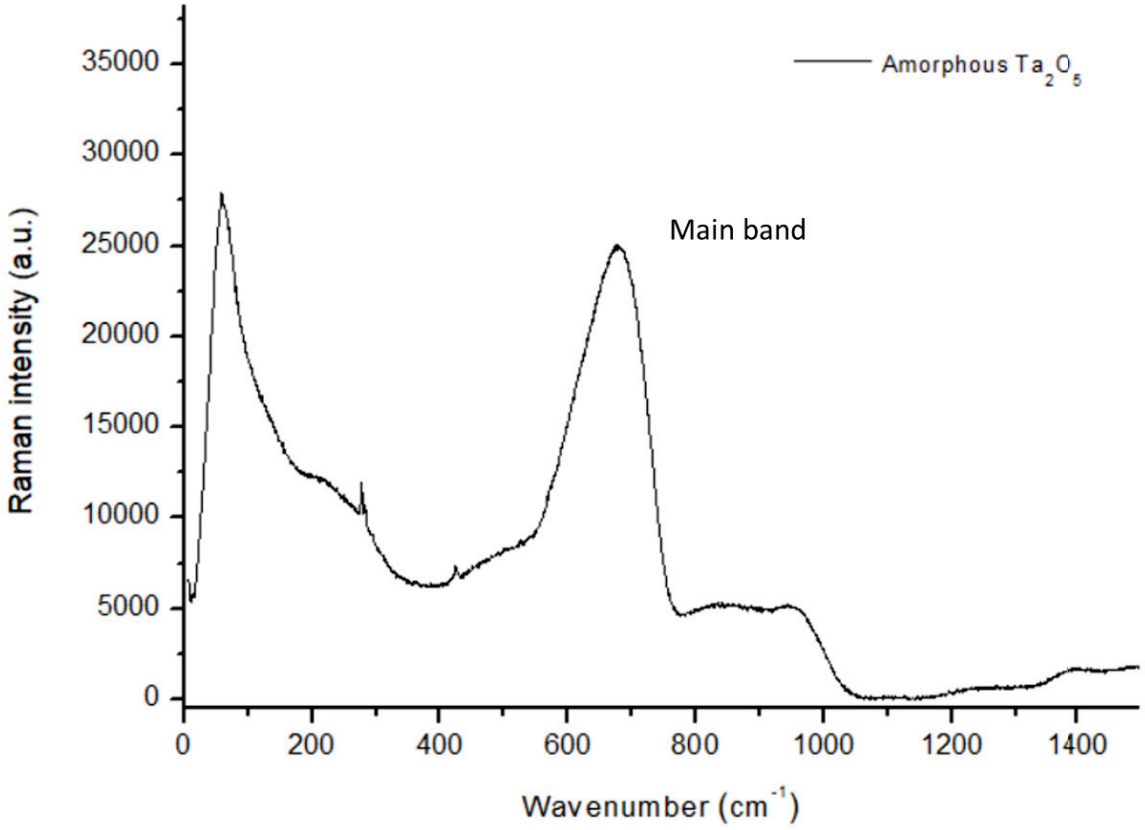

Figure 6.2: Raman spectrum of tantalum pentoxide Ta_2O_5 COILLET [2017].

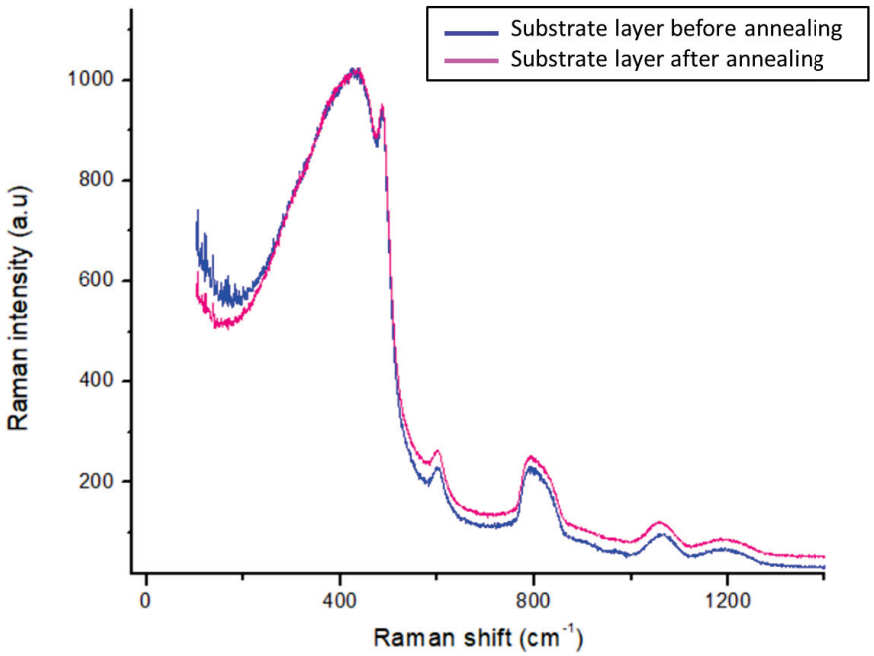

Figure 6.3: Spectrum of the substrate without coating deposition before (blue) and after annealing (red).

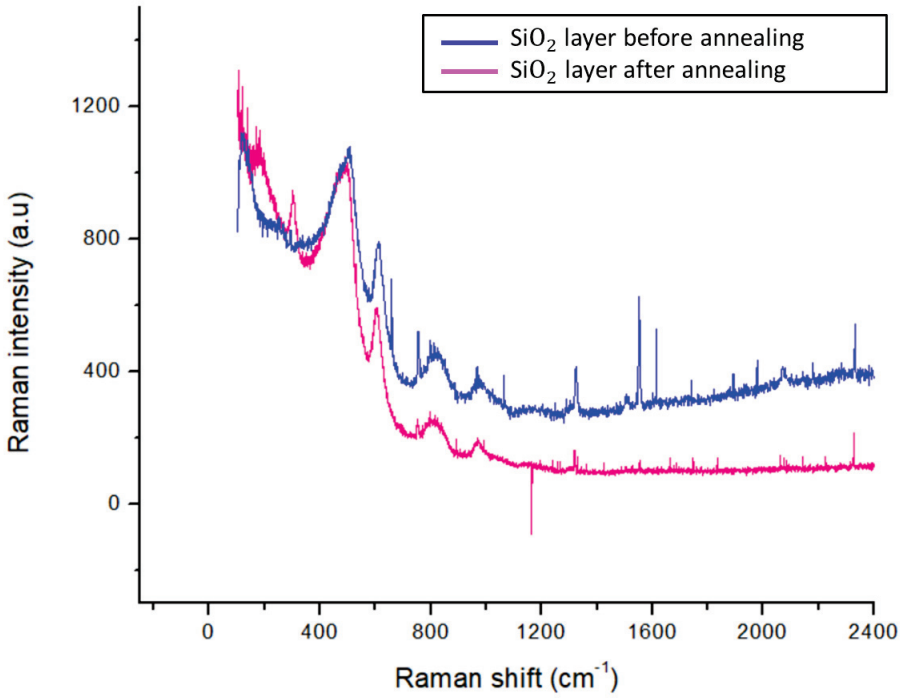

Figure 6.4: Spectrum of 18030 sample : SiO_2 on silica substrate before and after annealing.

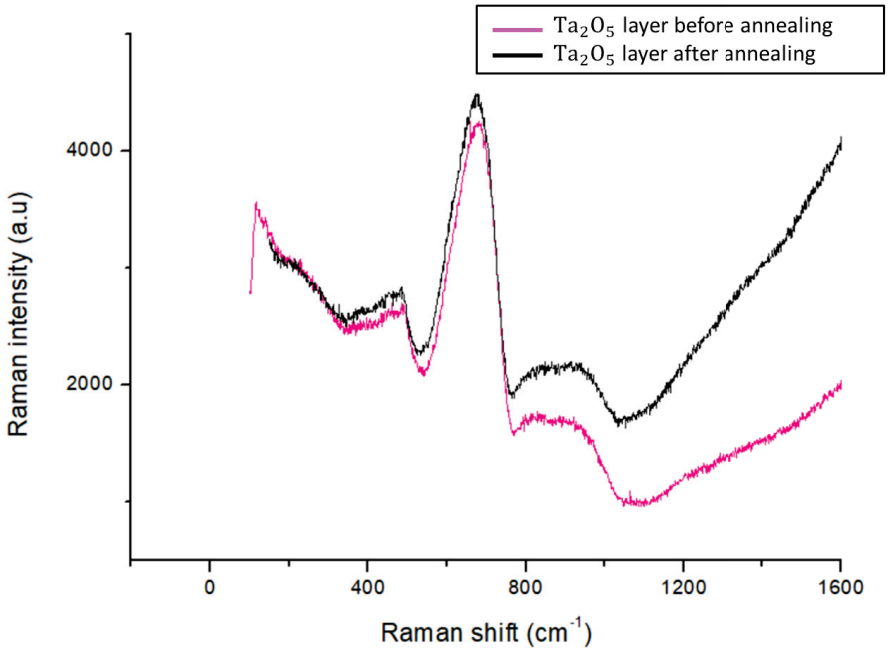

Figure 6.5: Spectrum of 18026 sample : Ta_2O_5 on silica substrate before and after annealing.

layer as small as possible, we decided to use the shortest wavelength available at laboratories to perform the measurements, 450 nm.

6.3.4 Ta_2O_5 defects

The Figure 6.6, shows an example of localized defects in the coating. These 3 defects are the most common in the layers. They have an irregular shape, a dark color and a size of about 5 microns. However, the measured spectra are not the same (see black and purple curves in Figure 6.7).

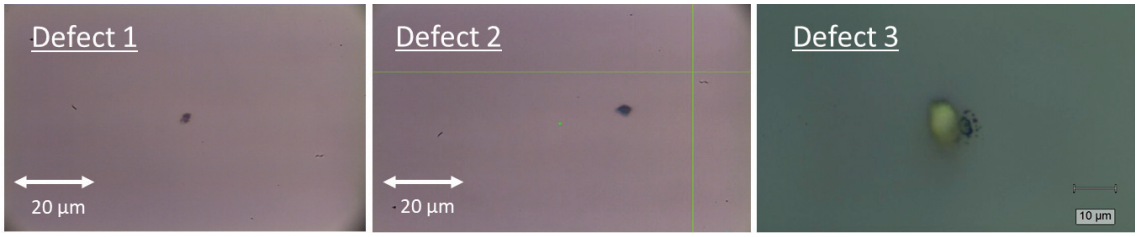

Figure 6.6: Raman pictures of defects 1, 2 and 3 in Ta_2O_5 layer (sample 18026).

As shown in Figure 6.7, several defects have the same Raman signal of the layer which indicates that they have the same structure. On the other hand, some defects like the pink and yellow spectra do not show either the main Ta_2O_5 peak or the Boson peak. If we compare these spectra with the Raman spectrum of the anatase phase of TiO_2 (red curve), the Raman peaks (indicated by the arrows) coincide with those observed on these defects. This indicates that the layer contains TiO_2 whose origin could come from a pollution of the sputtering target or from a contamination of the oven by coating depositions made at LMA containing Titania. The only potential source that could explain this result would be the thermal annealing in which samples containing Ti are also annealed. However, it is well known that defects are already present in the layers before thermal annealing so contamination by the oven is unlikely to be the main source.

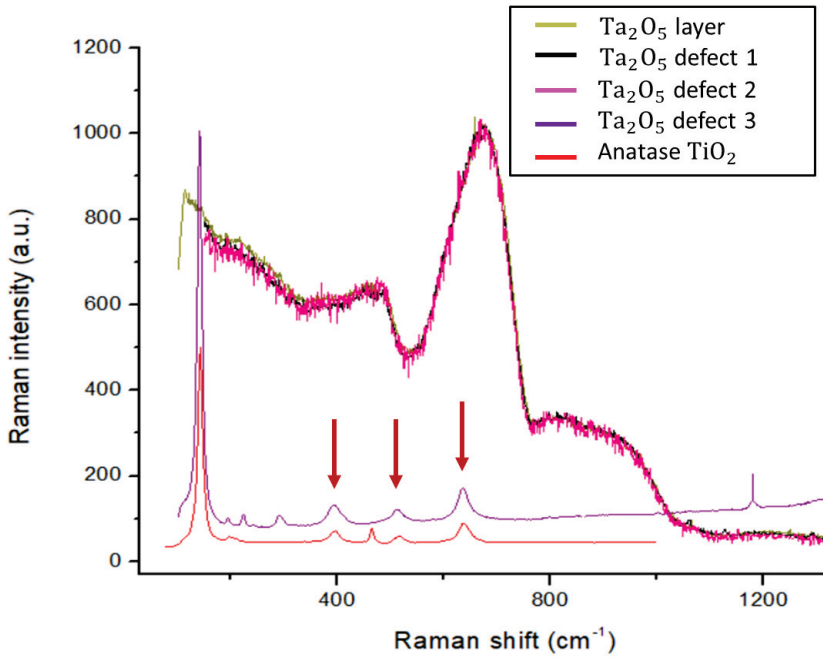

Figure 6.7: Raman spectra of Ta_2O_5 on an annealed sample. The green curve shows the spectrum of the layer without a defect, the black pink and purple curves shows respectively spectrums of defect 1 2 and 3 and the red curve shows the spectrum of anatase TiO_2.

6.3.5 SiO_2 defects

The Ta_2O_5 has a higher effective cross section than the SiO_2 corresponding to a higher intensity of the Raman signal. The main band of the Ta_2O_5 is very high compared to the one of the silica so a layer of SiO_2 on silica is impossible to probe the layer with Raman spectrometer. For the Raman measurements, the SiO_2, in order to screen us from the substrate signal, deposition were carried out on substrates containing a tantalum coating (6.8). Thus, we could point out several defects present in the SiO_2 thin film. We have chosen to present only a few interesting spectra allowing to understand the structure of these defects.

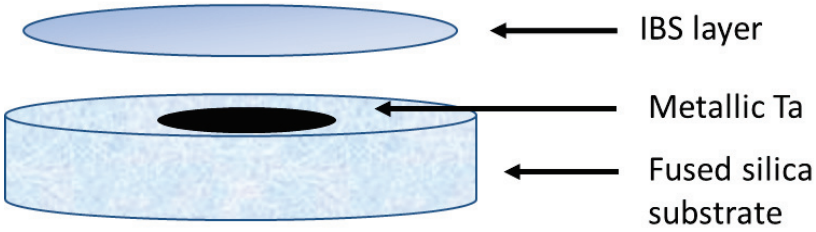

Figure 6.8: A simplified scheme of a sample ∅ 25.4 mm used only for Raman measurements of sample 18036 to differentiate the silica layer from the silica substrate. A thin film is deposited by IBS on a fused silica substrate with a Tantalum coating.

Figure 6.9 shows a picture of 2 defects in SiO_2 layers that were used to obtain the 2 spectra in Figure 6.10.

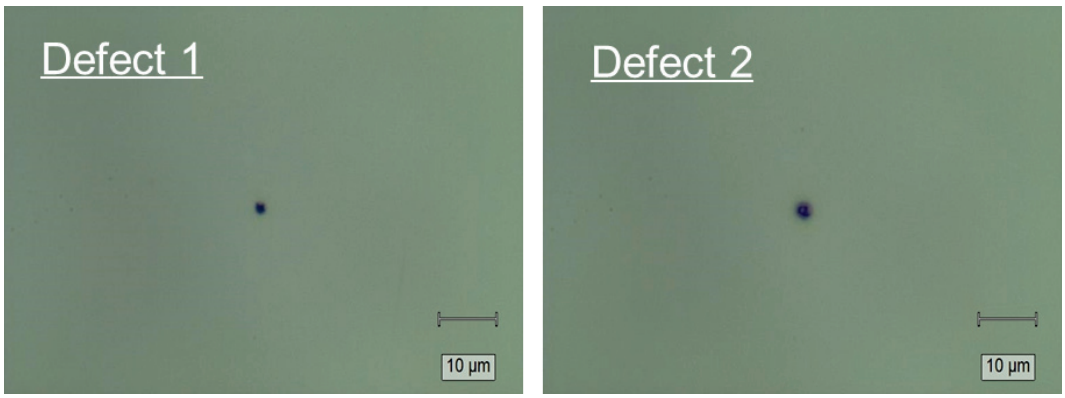

Figure 6.9: Pictures of defects taken with the Raman spectrometer on samples of SiO_2.

The blue color spectrum, which appears to be emission, shows the 2 peaks D1 and D2 of the silica. Even if we do not know the structure of this defect, the defect is visible when using 2 different excitation wavelengths, confirming Raman scattering. The green curve, showing the spectrum of defect 2 in the layer, is similar to the spectrum of Ta_2O_5 seen in Figure 6.2. This can be due to a dust particles that fell on the surface was not removed during cleaning or the deposition. So even if these 2 defects are very close from a cosmetic point of view, they are very different in their structure.

6.3.6 Classification of defects

By comparing all the defect spectra obtained, we can see that there are 3 families of defects :

- Intrinsic defects: these are generally SiO_2 or Ta_2O_5 defects. These defects are generated during the deposition inside the coating chamber. They are related to the bad arrangement of the sputtered particles on the surface of the substrate.

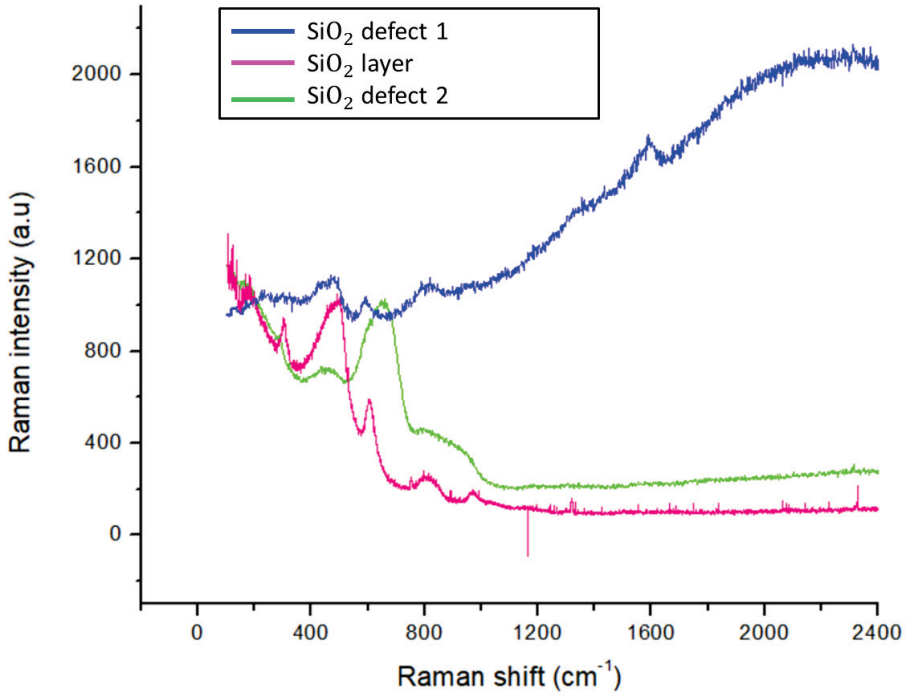

Figure 6.10: Raman spectra of a Ta_2O_5 layer and defect on an annealed sample 18030. The blue curve shows the spectra of defect 1, the pink curve shows the spectra of Ta_2O_5 layer without defect and the green curve the defect 2 spectra.

- Dust type defects: Particles can be deposited on the thin layers. This phenomenon can be related to the lack of cleanliness during the measurements, during the deposition and or to the pollution of the thermal oven.
- Luminescence type defects: these defects whose origin is unknown for the moment, emit in the high frequencies.

The Raman reveals some very interesting things. The defects come in part from the materials that make up the coating. Most of the targeted defects show the same spectrum as silica or tantalum.

However, in the SiO_2 layers, other defects show spectra completely different from the Raman spectra of silica. We can assume that these are particles or polishing residues that would have probably been deposited on the substrate or during the IBS deposition. We worked with two different wavelengths (532 nm and 633 nm) and some signatures are present for both, which means that it is indeed Raman scattering.

Concerning the Ta_2O_5 layers, by comparing the spectra with that of the crystallized TiO_2, we observe the signature of anatase on the Ta_2O_5 layers after annealing. Indeed, the thermal furnaces of the LMA are used for different kinds of coating, therefore, they see different kinds of samples, including coating containing titanium. It is not impossible that we have a contamination in the oven that could induce particle deposition on our samples after annealing but not before.

6.4 SEM EDX analysis

The second investigation was to measure the samples using the MEB-EDX in the laboratory Matériaux Ingénierie et Science (MATEIS) of the Institut National des Sciences Appliquées (INSA) in Lyon. The measurement test was done on the 18029R sample (Ta_2O_5 monolayer of thickness 1665.4 nm). A scanning electron microscope (SEM) is a type of electron microscope, operating under vacuum, that produces enlarged images (nanometer resolution) by scanning the surface with a focused

beam of electrons. This beam generates an ionization of the atoms which, by de-exciting, emit a photon X whose energy is characteristic of the emitting atom GOLDSTEIN et collab. [2003]. This is energy dispersive microanalysis (EDS), in which the X emission is processed electronically. The energies of the peaks present are determined and they are automatically compared with an X emission file of known energies . Depending on the chosen detector, the imaging mode is defined. The SEI detector (secondary electron imaging) collects secondary electrons to observe reliefs and thus obtain information on the morphology. The second detector BEI (backscattering electron imaging) collects backscattered electrons which are sensitive to the atomic number.

6.4.1 Preparation of the sample

In this test, two regions were analyzed on the cross-section of a piece of the sample (8 mm x 4 mm x 4 mm cube) in which defects are seen using the backscatter electron detector (BSE): region 1 and region 2. Other sites were identified but only reliable results (from a point of view of signal to noise ratio, etc.) were kept. If we observe a contrast at the level of the layer it means that we have a difference in chemical composition (i.e. a difference in atomic number). The brighter appear the areas, the heavier are the detected elements. We can also have a contrast which is due to the topography, meaning to the presence of dust on the sample. In the preparation of samples, the surface was polished (ionic polisher ILION) so we know that the layer is flat. The contrast observed cannot be attributed to a dust deposited on the sample, as this would give a signal with the BSE detector but also with the secondary electron detector (SE), which is not the case for the analyzed defects.

6.4.2 Analysis of defects in region 1

Figure 6.11 shows one of the two analyzed regions, presenting a defect, along with a measurement of its size. The mappings shown in Figure 6.12 and 6.13 correspond to the same area of interest as shown in Figure 6.11. Figure 6.12 shows "raw" mappings, where we count the number of X-rays with an energy in a given range, including noise contribution. On the other hand, Figure 6.13 shows the elemental maps on which the name of the element and the line used are indicated.

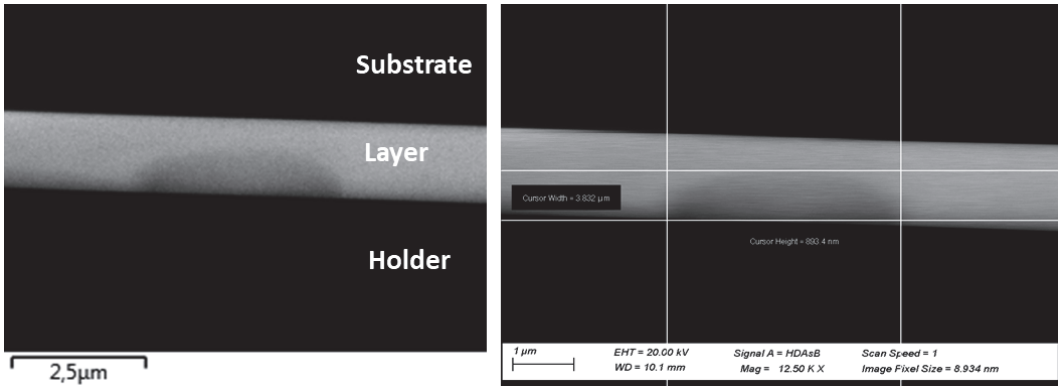

Figure 6.11: Field of view of region 1 with 2 defects visible captioned with the position cursor to determine the size of the defect.

The SiKα1 peak is superimposed with a tantalum line. When two elements have X-ray superimposed, the maps are not representative because we mix the contributions of the two elements. We can deconvolute the contributions (see the "Ta %at map" and "Si %at map" in Figure 6.12) but we introduce noise, and as a result, the silicon mapping is not significant (see Figure 6.13). Interestingly, there is a clear enrichment of aluminum and carbon on the bottom edge of the layer, which corresponds to the surface of the layer. Carbon was used in deconvolution because carbon is always present in the analyses due to various contaminations during preparation and observation. This seems to indicate that the detected defect is rich in aluminum.

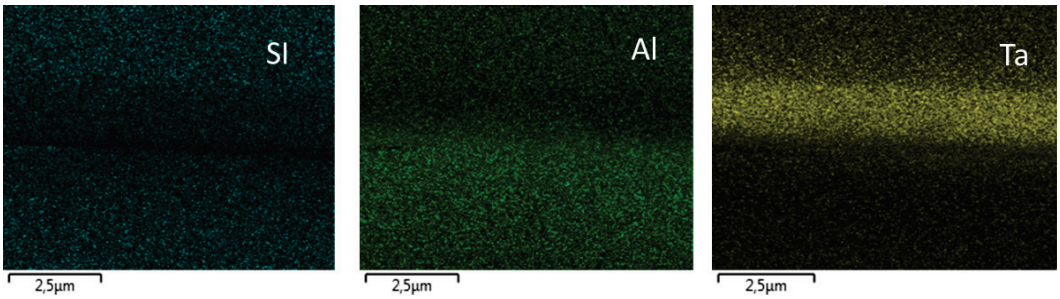

Figure 6.12: Three raw maps of the elements detected on the field of view in Figure 6.11.

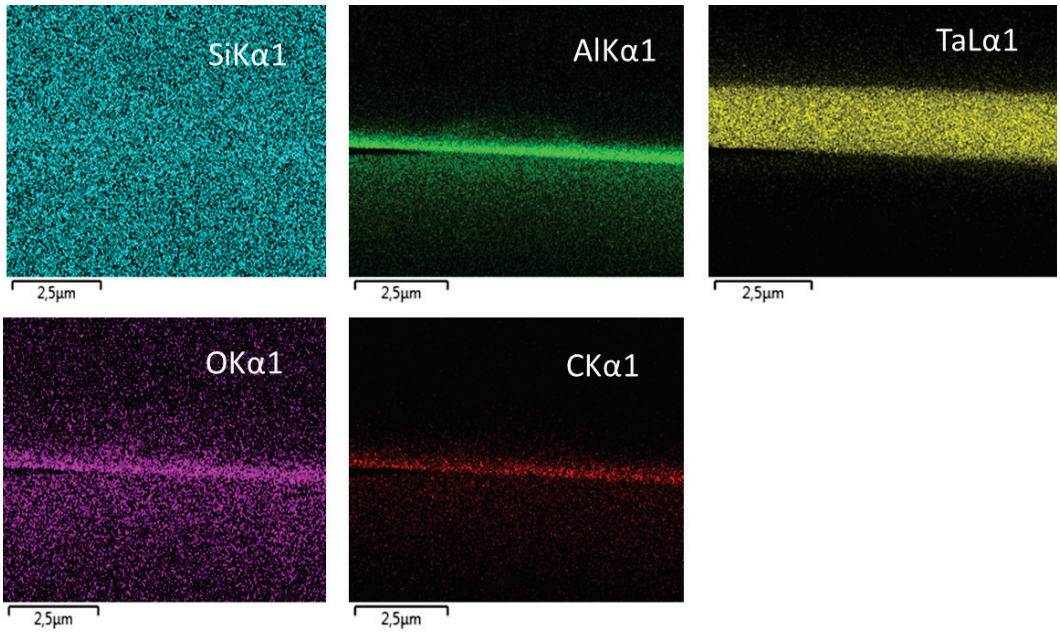

Figure 6.13: Quantitative maps (arbitrary units) of the elements detected on the field of view in Figure 6.11.

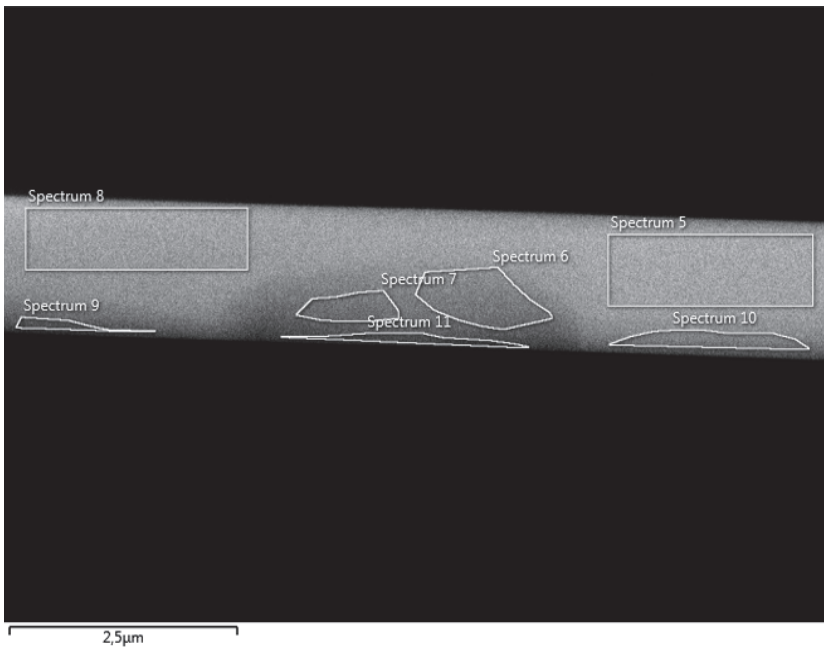

Figure 6.14: This image shows the different areas analyzed to obtain the spectra in Figure 6.15.

Table 6.2: Quantitative data of element concentrations in atomic percent (atomic %) region 1.

Spectrum	Spectrum position	O at.%	Al at.%	Si at.%	Ta at.%	Total at.%
5	Layer	27	6	9	58	100
7	Inside the defect	34	15	8	43	100
9	Defect left	38	33	55	23	100
10	Layer surface	38	28	6	28	100
11	defect surface	38	31	6	25	100

To more accurately determine possible aluminum enrichment at the defect and at the surface of the layer, energy spectra were acquired on particular areas of the sample. The spectra are given in Figure 6.15 and the associated area in 6.14. The data in Table 6.2 gives the concentrations of the elements in atomic percent (atomic %).

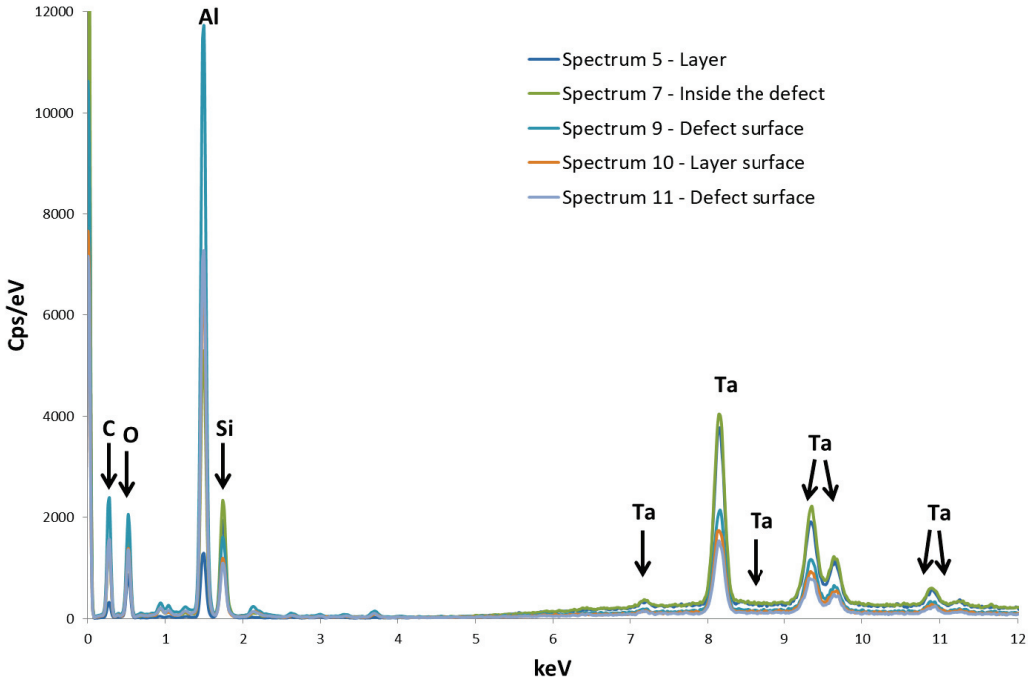

Figure 6.15: Spectra of the different areas analyzed on the field of view (layer and defects).

6.4.3 Analysis of defects in region 2

On this area, Figure 6.16, two defects are visible : a small one on the right and a larger one on the left. The Figure 6.17 shows the associated maps with the distribution elements scanning and in Table 6.3 the quantitative element concentrations. The Figure 6.19 and 6.18 shows spectrums of the different zones analyzed on the region 2.

6.4.4 Other analyzed defect region

Another region was analyzed in Figure 6.20. We can notice the presence of another type of defect which is not on the surface contrary to the first 2 sites analyzed. The presence of 2 rather circular defects is visible deeper in the layer. Their size of ≈ 600 nm and their shape suggest argon bubbles that could be trapped in the layer. The analysis showed the presence of argon but due to a poor signal to noise ratio the study could not be conclusive.

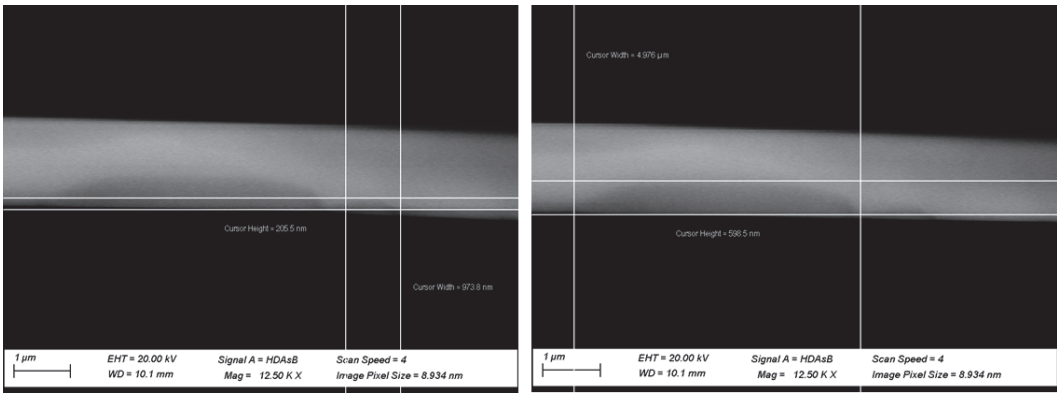

Figure 6.16: Field of view of the new site measurement in region 2 with the size of the 2 visible defects.

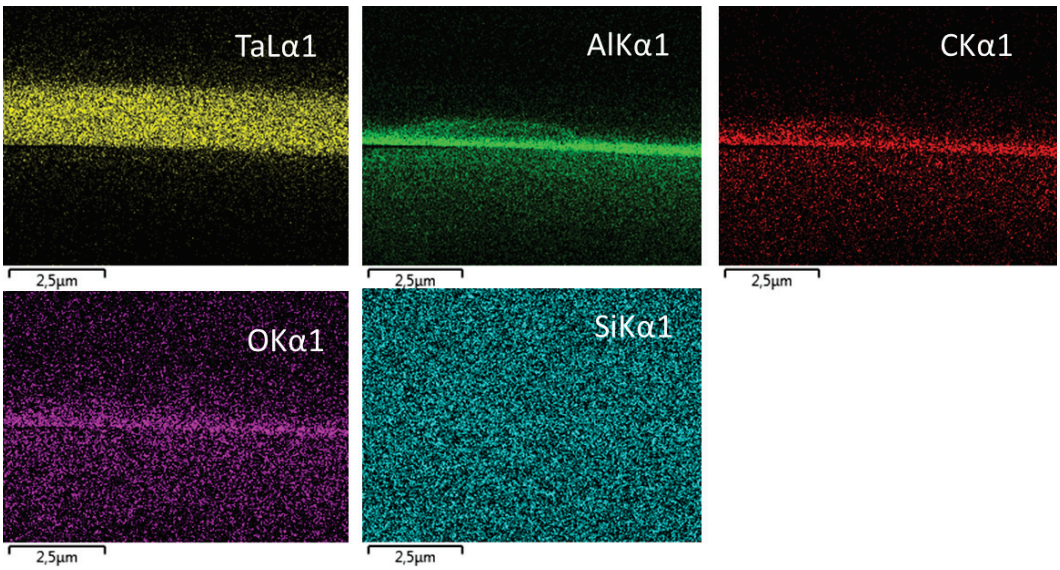

Figure 6.17: X maps corresponding to the SEM image Figure 6.16 showing the distribution of Ta, Al, C, O and Si.

Table 6.3: Quantitative data of element concentrations in atomic percent (atomic %) of region 2.

Spectrum	Spectrum position	O at.%	Al at.%	Si at.%	Ta at.%	Total at.%
30	Surface layer	43	39	4	14	100
31	Defect surface	42	37	5	15	100
32	Inside the defect	42	23	6	29	100
33	Depth layer	40	9	8	43	100
34	Inside defect	41	38	5	15	100

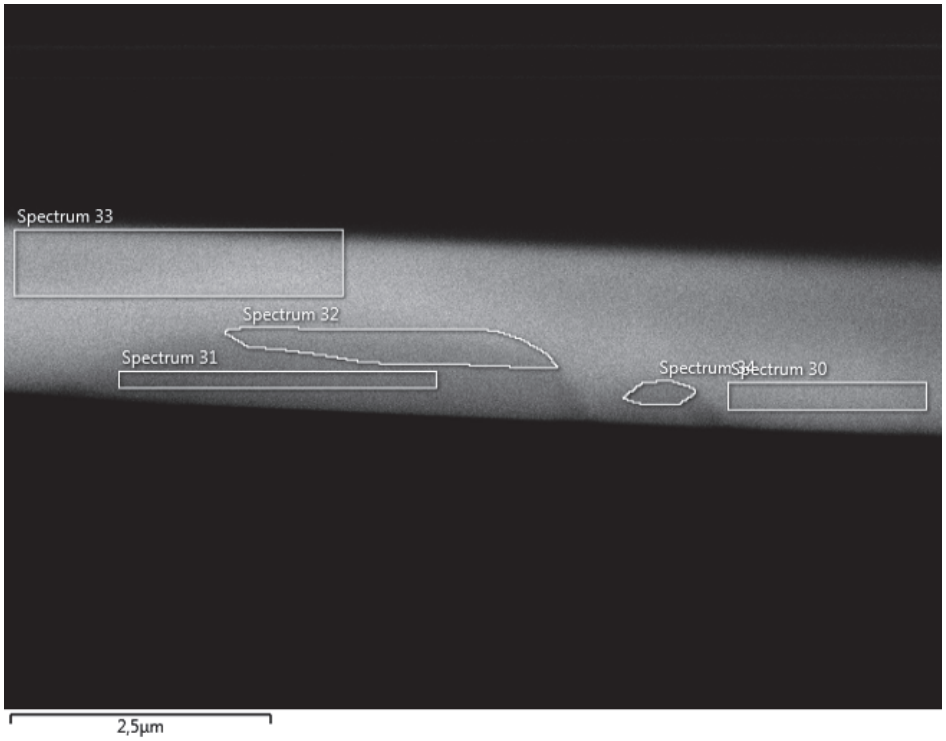

Figure 6.18: This image shows the different areas analyzed to obtain the spectra in Figure 6.19.

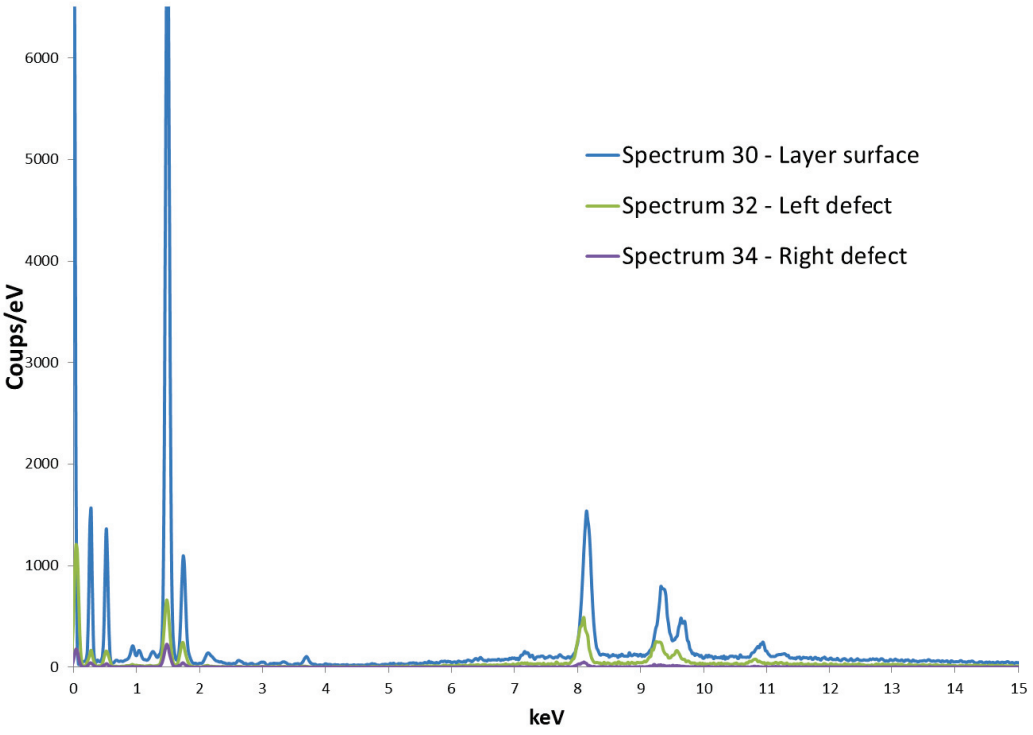

Figure 6.19: Spectra of the different zones analyzed of region 2.

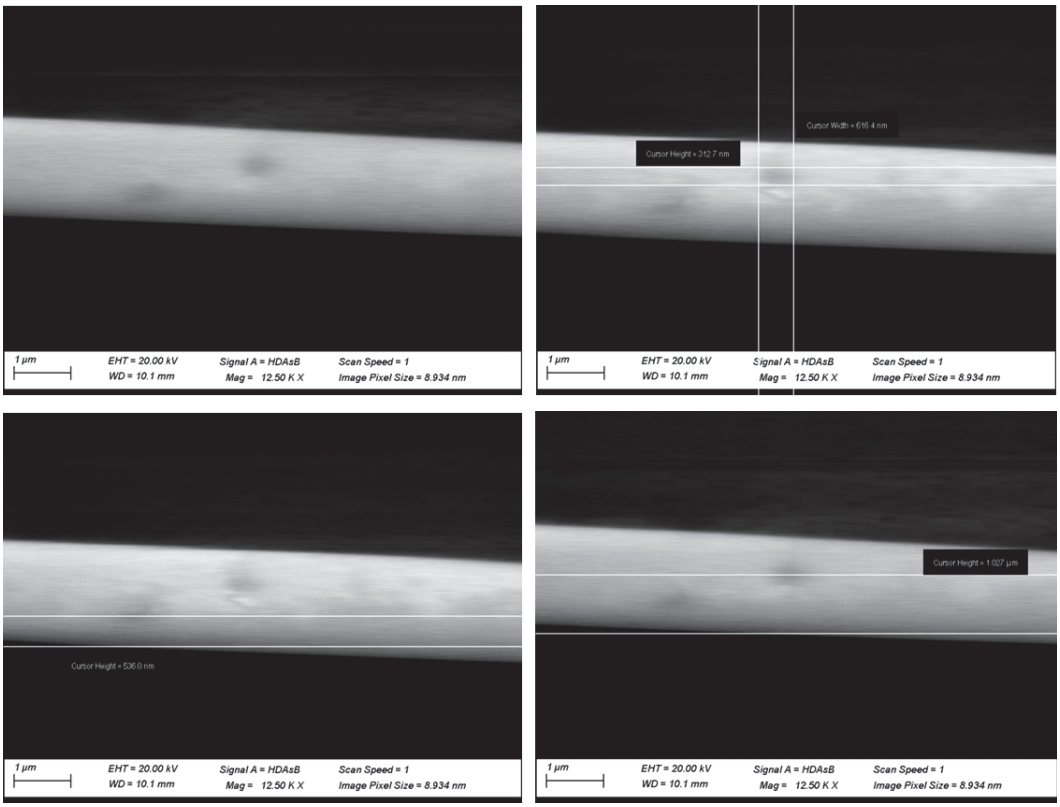

Figure 6.20: Field of view of another site being analyzed. The other 3 pictures show the size of the defect and its distance from the surface of the layer.

6.4.5 Discussion

We show different Figures 6.11,6.16 and Tables 6.2,6.3 for both regions. To summarise, the quantification of the spectra in the region 1, allows to confirm a strong presence of aluminum and silicon everywhere in the layer. For silica, the content is between 5 and 10 atomic % in the whole layer. For aluminum, we have 6% atomic in the layer with an increase in surface to 31% atomic. The defect has an intermediate quantity of 15%. We also observe an oxygen enrichment at the defect 35% and up to 40% at the surface of the layer. This could be consistent with the tantalum oxide and aluminum oxide formulas.

The analysis of region 2 confirms the presence of aluminium in significant quantities. In view of the maps, Figure 6.17, it would appear that the aluminium forms a thin layer on the surface of the sample.

The SEM measurements are conclusive and prove to be very relevant to consider new measurement campaigns. The quantifications are consistent:

- In the core of the tantalum layer (spectra 5, 8, 33), we have an aluminum concentration of about 6-7% (at.)
- On the surface (spectra 9, 10, 11, 30, 31, 34), the concentration of Alu is rather 34-35% (at.)
- In the defects (spectra 6, 7, 32), we have an intermediate aluminum concentration: about 17%.

In view of these results and the maps, the main conclusion is the observation of a thin layer of aluminum on the surface of the layer. Inside the deposition chamber, the shutter, the chamber wall protections and the mounts containing the substrates being composed or covered entirely with aluminium, it is not impossible to have such a contamination at the level of the layer.

6.4.6 Limits of the study

These measurements are very limited for our purpose. Despite the good will and time spent on the preparation of the samples, the study could not be continued after the first results presented above. The main difficulties limiting our observations are listed below. The layers and the substrate are transparent and the defects are optically visible by illuminating the back side. Moreover, for an observation, a small cube of sample in transverse section of 4 mm x 4 mm x 4 mm is needed. The probability to find defects on such a thin section (surface = 1.3 mm) is very low. Subsequently, it was tried to locate the defects visually before making a SEM observation without cutting them and making marks with a diamond tip. However, observing them from above in visible light was not conclusive either because the defects were not found.

6.5 Alternative SEM measurements

The second test on SEM analysis were done in Centre Technologique des Microstructures (CTμ) of University Lyon 1. We choose Ta_2O_5 sample 18029 after annealing (see Table 6.1). To increase our chances of seeing defects, a thin layer of carbon was deposited using a small deposition machine by evaporation. The carbon layer which is homogeneous on the surface allows to make it conductive. This alternative has been thought to avoid cutting the sample and to observe directly the defects on the surface.

6.5.1 Defect in region 1

Figure 6.21 shows an area of the sample in wich we found a defect and in the Table 6.4 the element concentrations in atomic percent in the defect and in the layer. Note that this defect is much smaller than expected (less than 1 μm) but it coincides with the median of defect detected with the Eotech profilometer. The results show that this defect is Ta defect but contains significant quantities of Cu and Fe about 10% and 18% respectively. This could be explain by the the presence of stainless steel inside the coating machine of DIBS and by the backing plate which is in copper.

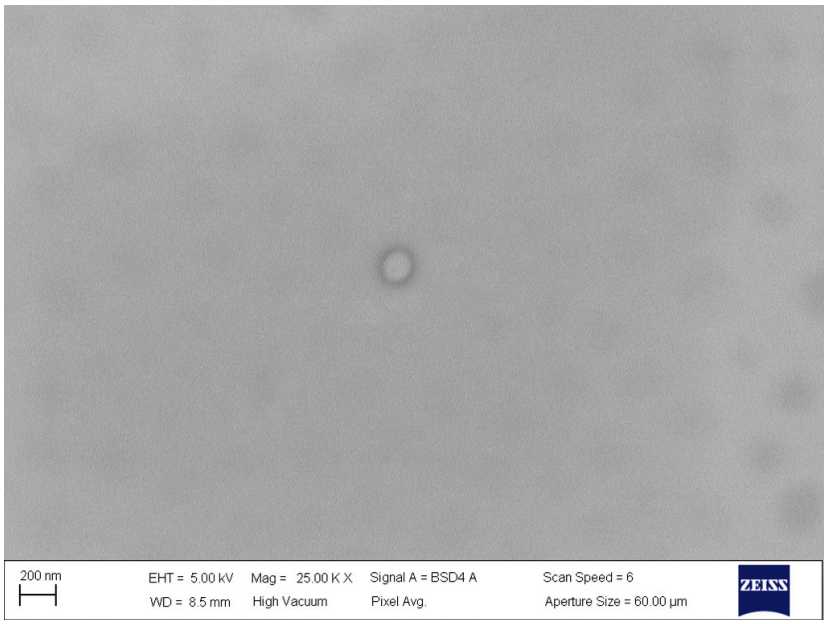

Figure 6.21: Field of view showing one defect present on a tantala layer.

Table 6.4: Quantitative data of element concentrations in atomic percent (atomic %).

Description	B at.%	O at.%	Si at.%	Ar at.%	Fe at.%	Cu at.%	Ta at.%	Total at.%
Defect	5.02	10.81	0.68		17.95	10.43	55.10	100
Layer	4.96	12.99	0.71	1.7			79.64	100

6.5.2 Defect in region 2

Figure 6.22 shows another defect and the map associated in Figure 6.23. The results suggest that it is also a tantalum defect probably due to a stoichiometry problem.

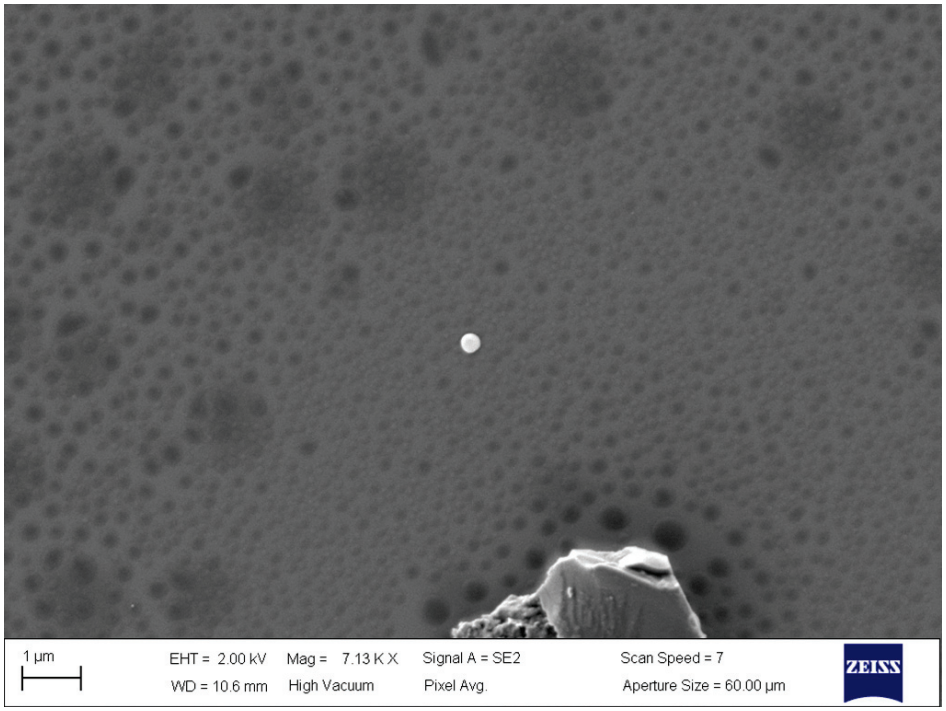

Figure 6.22: Field of view with one white defect in the center.

Table 6.5: Quantitative data of element concentrations in atomic percent (atomic %).

Description	B at.%	O at.%	Si at.%	Ar at.%	Fe at.%	Cu at.%	Ta at.%	Total at.%
Defect	4.79	9.46	0.94	0.75	22.54	25.06	36.45	100
Layer	2.95	13.07	0.74	1.33			81.91	100

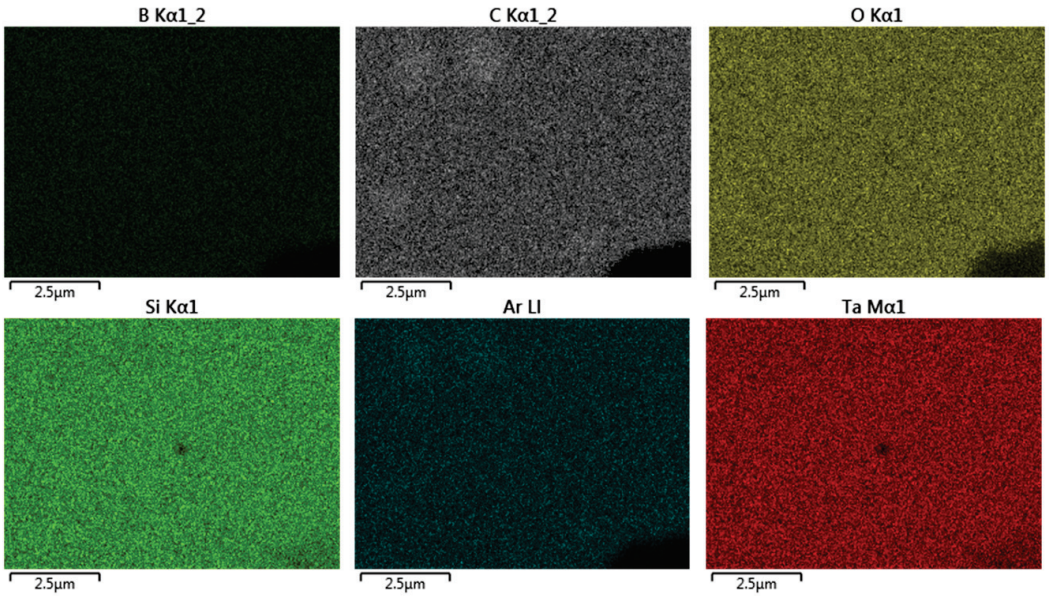

Figure 6.23: Pictures of the selected defect in the center of the image.

6.6 LIBS analysis

The third technique used was the Laser-Induced Breakdown Spectroscopy (LIBS) imaging at ILM in Lyon Motto-Ros et collab. [2020]. This technique consists in focusing a laser pulse on the surface material. The strong illumination causes heating and then leads to vaporization in the form of a plasma. By deexciting, the ejected atoms and ions emit photons, whose wavelength allows to identify the elements present and whose intensity is proportional to the concentration of the emitting atoms. We deduce the elemental composition of the material.

The test was performed on the sample D21037 PL9223 Figure 6.24.

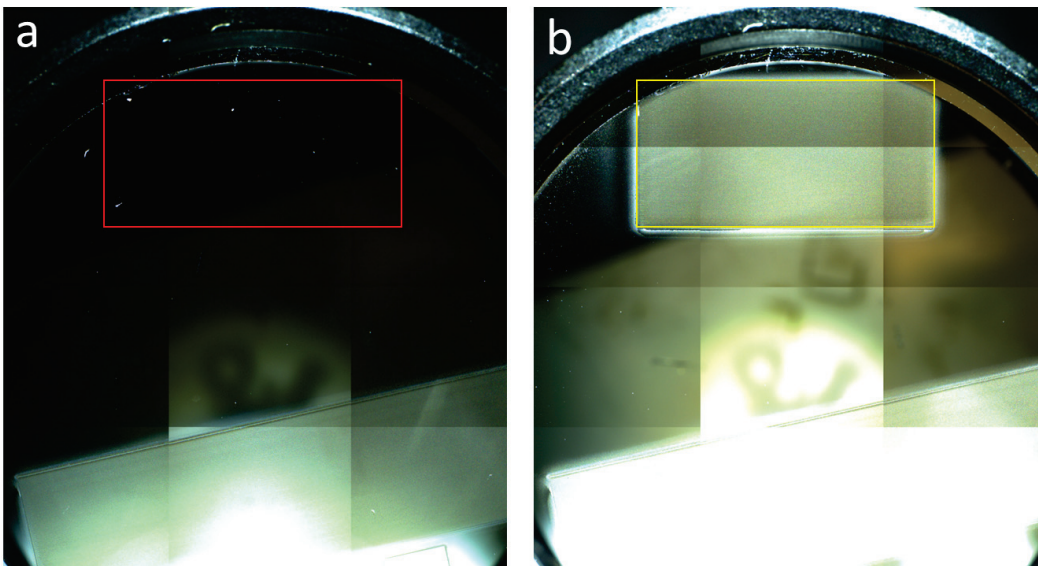

Figure 6.24: In (a) the scan area before analyse. The rectangular zone represent 800x400 with 14 µm of resolution. In (b) the same scan area after analysis.

A defect mapping was done on Micromap before doing a LIBS scan. The idea was to be able to superimpose the two maps but the test revealed the complexity of finding defects in the area of interest despite the defect map done on the Micromap (certainly not accurate enough for the size of the scan possible at the LIBS).

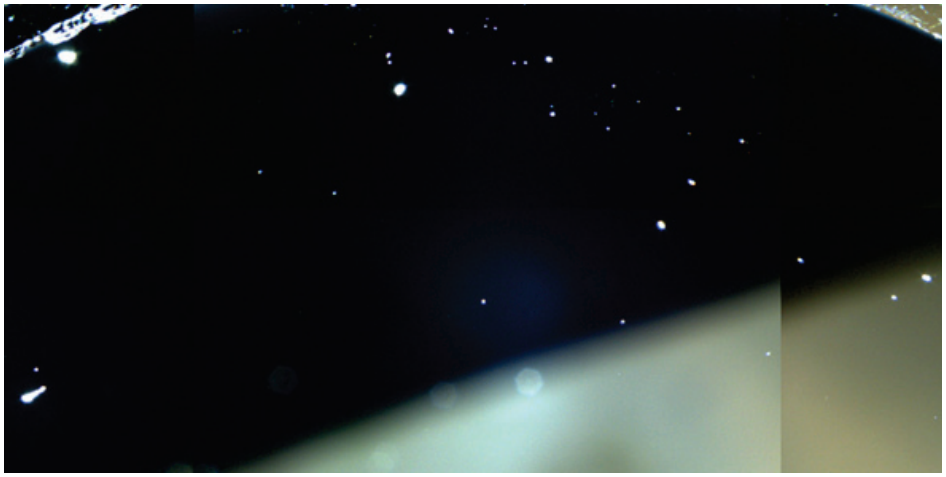

Figure 6.25: Picture of the interest zone. A zoom of (a) see in Figure 6.24; All bright points are probably dust.

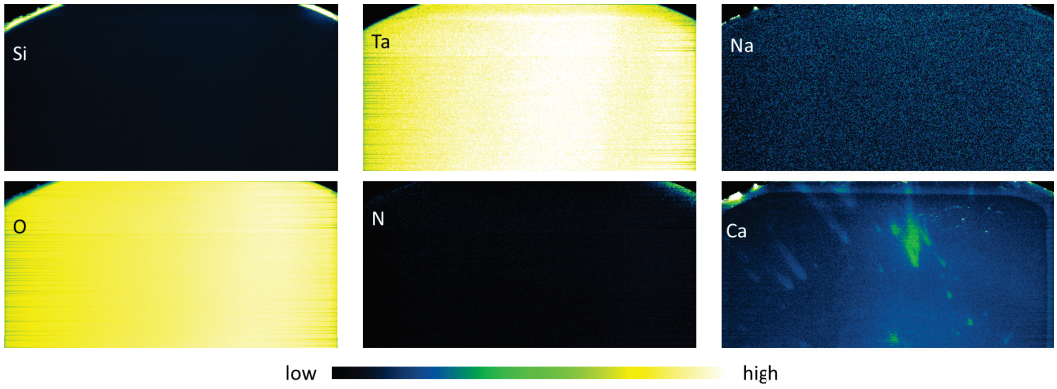

Figure 6.26: Maps of the elements detected on the field of view in Figure 6.24 (a).

The Figure 6.26, presents the maps of the region seen in Figure 6.25. The detection has been optimized on Ca and Na (centered on the most intense lines of these 2 elements). The image of Na seems noisy but it seems to have a signal at the level of the detection limit. The same was observed for Ca but with a distribution giving more confidence (however it was difficult to say if this comes from a possible contamination).

To understand these results a test was performed on a substrate without coating (µC PL7364) to confirm this. It turns out that there was a measurement artifact related to the instrument and no real defect could be found.

6.7 AFM analysis

Tests of Atomic Force Microscopy (AFM) measurement were carried out at the Plateau d'imagerie et microscopie (Platim) de l'Ecole Normale Supérieure (ENS) de Lyon. In addition to seeking to know the chemical nature of the defect, it was interesting to scan in depth the layers to know the localization of the defects inside the layer. The idea was to see if they could be imaged by Z-stacking, in order to answer a recurrent question from our colleagues to which we can not provide an answer currently. For this purpose, different machines of AFM have been tested (a Bruker Catalyst) coupled to an inverted microscope, and a JPK Nanowizard III stand alone (with a basic optic on top), bioth allowing to perform topography measurements. There were no conclusive results. These tests showed, also for the AFM technique, the difficulty of identifying defects. It is necessary, in a first step to locate the defects very precisely, to make sure the analysis focus on them.

6.8 Summary

Attempts to find the defects chemical nature using different techniques have revealed to be very complex and require technical skills, dedicated machines and meticulous preparation. In addition to the possible contaminations linked to the deposition process, the different analysis techniques are not done in a cleanroom environment, although it has been demonstrated that contamination/particles are a troublesome category of defects that induce scattered light.

The RAMAN technique is interesting but probes a large part of the layer in addition to the defect. With MEB AFM and LIBS, we have seen the limits of the technique related to our problem: defects are optically visible but when observed with electronic miscroscopes the defects become difficult or impossible to detect. This is why an interesting solution to consider in the future would be to add to the Eotech profilometer a new lens called LensAFM, a small AFM for custom integration NANOSURF. This system on the Eotech profilometer will allow to detect defects with the dark field detection and then to measure their morphology by switching on the AFM objective. Thanks to this solution, the detected defects will be the known defects and there will be no doubt about possible dust contamination because the working environment will be the cleanroom.

6.9 References

COILLET, E. 2017, *Structural characterization of thin non-crystalline layers for low thermal noise optic*, Theses, Université de Lyon. URL https://tel.archives-ouvertes.fr/tel-01626513. 120, 121, 122

GOLDSTEIN, J., J. GOLDSTEIN, D. NEWBURY, D. JOY, P. ECHLIN, C. LYMAN, E. LIFSHIN, L. SAWYER, O. JOY et J. MICHAEL. 2003, *Scanning Electron Microscopy and X-Ray Microanalysis: Third Edition*, Scanning Electron Microscopy and X-ray Microanalysis, Springer US, ISBN 9780306472923. URL https://books.google.fr/books?id=ruF9DQxCDLQC. 127

HEHLEN, B. 2010, «Inter-tetrahedra bond angle of permanently densified silicas extracted from

their Raman spectra», *Journal of Physics: Condensed Matter*, vol. 22, doi:10.1088/0953-8984/22/2/025401, p. 025 401. URL https://hal.archives-ouvertes.fr/hal-00528017. 120

LONG, D. A. 2002, *The Raman effect: a unified treatment of the theory of Raman scattering by molecules*, vol. 8, Wiley Chichester. 120

MOTTO-ROS, V., V. GARDETTE, L. SANCEY, M. LEPRINCE, D. GENTY, S. ROUX, B. BUSSER et F. PELASCINI. 2020, «LIBS-Based Imaging: Recent Advances and Future Directions», *Spectroscopy*, vol. 35, p. 34–40. URL https://hal.archives-ouvertes.fr/hal-02998713. 135

NANOSURF. «Computer requirements for nanosurf products», URL https://www.nanosurf.com/downloads/Nanosurf-NaniteAFM-Brochure.pdf. 137

Conclusion

Scattered light is a major issue for future gravitational waves projects and space experiments using very low loss optics. In this thesis, an experimental study on the point defects in SiO_2 and Ta_2O_5 and their impact on the scattered light was conducted at LMA. Its main goal was to investigate the point defects origin by determining their distribution according to the materials, their size, their behaviour and their impact on the scattered light.

Thanks to a thorough samples production campaign and to systematic measurements, we can say that the defect density increases with the thickness of the layer whatever the material and the coating deposition machine. However, it was observed that even if the defect density increases with the thickness of the layer, there is no impact, measurable at LMA, on the amount of scattered light. Therefore no variation is seen on the scattered light, even though we would expect the diffusion to increase as well with the defect density.

The study of point defects that impact the performance of the gravitational wave detectors has led to the identification of several factors involved in the generation of defects in the layers in particular a dependence on the deposition parameter V_b. The energy of the sputtered particles appears to have an influence on the defect density created during deposition. It has been shown that thermal annealing also has an influence on the defect density by reducing it of about 20 to 30% on tantala layers, 40% to 50% on silica layers and generally reducing the scattered light. A second annealing does not seem to have such a significant impact. Improving the deposition process and thermal annealing are paramount if we want to reduce the amount of defects.

The use of certain materials is more conducive to the creation of defects (more defects on Ta_2O_5 monolayers than in SiO_2), but this does not necessarily imply an increase in scattered light as we have seen with Ta_2O_5 monolayers in the in-depth study.

The Micromap profilometer at LMA has been an essential instrument for the study of defects, allowing their detection, to determine the spatial distribution and the classification according to their sizes. The limits encountered with the Micromap, lead us to think and develop a new instrument, the Eotech profilometer, capable of better analyzing the surfaces thanks to a more powerful camera. The usage of the new instrument for the studies presented here allowed to validate its functioning and optimize it by adding new functionalities and improve the detection efficiency. An important development has been done on the image analysis software side as well. In particular, the development of the SEP algorithm for image processing allows for better defect quantification and noise subtraction, in order to reduce the dependence on the cleanroom environment.

Although the presence of defects was known and the scattered light characterised globally on mirrors for GW experiments, a systematic campaign of measurements as the one presented here has never been done before. This exploratory study unveiled the complexity of the subject and allows us to draw up a list of guidelines :

- The need to have a large number of samples in order to draw statistical conclusions. Concerning the deposition process, it would be necessary to repeat the runs of the same series of samples to have better results and make the runs one after the other.

- The substrate choice : a particular attention must be paid to the choice of the substrate. As demonstrated in chapter 4, substrates are randomly selected and some may contain numerous defects before coating deposition.

- The measuring instruments are sensitive to the cleanroom environment and the right conditions must be ensured to make the results reliable.
- The handling of the samples is an important step to be performed with all care, as it can alter the surface state.
- COMSOL simulation : to start the study a simple case was studied but for the continuation it would be interesting to develop the model and study the effect of the defects in the stacks.
- Improvement of the scatterometer : a particular care has to be given to metrology, a fundamental step for mirrors characterisation. In particular, our results show that the instruments available at LMA are not adapted for the study of these defects and that it would be necessary to proceed differently to measure the light scattered by the defects.
- The RAMAN measurements have shown interesting results about the defect and the layers signature. This technique provides additional information on the structure. Therefore, to determine the chemical composition of defects, it would be interesting to make further joint measurements of RAMAN and SEM-EDX.
- It is of paramount importance to understand the chemical nature of the defects, to determine how they are created during the deposition process. Such analyses are very complex and should be designed carefully. One of the most promising techniques appears to be SEM-EDX measurements.
- The AFM measurements were not conclusive for the study but a solution is envisaged to remedy this by adding to the Eotech profilometer a new lens called LensAFM. This will allow to have information about defects position in the layer.

As a conclusion, we present in this thesis the first systematic study of the microscopic and individual properties of point-like defects in the coatings of the mirrors for gravitational waves experiments. The thorough deposition campaign, together with systematic measurements, allow us to highlight the dependence of the defects density and scattered light on several deposition factors, as well as to understand better the metrology needed for such studies. As it is often the case for first exploratory studies, our work also reveals the richness of the subject and suggests many new ideas still to be explored.